UNIVERSIDADE DE LISBOA

INSTITUTO SUPERIOR TÉCNICO

Biradial turbine generator-set for off-grid OWC wave energy converters

Diogo Jorge da Costa Teixeira Neves Ferreira

Supervisor: **Doctor** Luís Manuel de Carvalho Gato

Co-Supervisors: **Doctor** João Carlos de Campos Henriques

Doctor Ana Maria de Pinho Ferreira da Silva Fernandes Martins

Thesis approved in public session to obtain the PhD Degree in

Sustainable Energy Systems

Jury final classification: **Pass with Distinction**

2024

UNIVERSIDADE DE LISBOA

INSTITUTO SUPERIOR TÉCNICO

Biradial turbine generator-set for off-grid OWC wave energy converters

Diogo Jorge da Costa Teixeira Neves Ferreira

Supervisor: **Doctor** Luís Manuel de Carvalho Gato

Co-Supervisors: **Doctor** João Carlos de Campos Henriques

Doctor Ana Maria de Pinho Ferreira da Silva Fernandes Martins

Thesis approved in public session to obtain the PhD Degree in

Sustainable Energy Systems

Jury final classification: **Pass with Distinction**

Jury

Chairperson:

Doctor Paulo Manuel Cadete Ferrão, Instituto Superior Técnico, Universidade de Lisboa

Members of the jury:

Doctor António Franco de Oliveira Falcão, Instituto Superior Técnico, Universidade de Lisboa

Doctor Hendrik Polinder, Faculty of Mechanical, Maritime and Materials Engineering, Delft University of Technology, Países Baixos

Doctor Bruno Pereiras García, Universidad de Oviedo, Espanha

Doctor Luís Manuel de Carvalho Gato, Instituto Superior Técnico, Universidade de Lisboa

2024

Resumo

Os conversores de energia das ondas para alimentação de sistemas elétricos sem ligação à rede são apontados como um possível motor para o desenvolvimento da Economia Azul. O presente trabalho doutoral tem como objetivo o projeto de um turbogerador, baseado numa turbina birradial, para conversores de energia das ondas do tipo coluna de água oscilante e para alimentar sistemas elétricos de corrente contínua isolados. Entrevistas a profissionais da monitorização marítima confirmam a aplicabilidade deste dispositivo. A relação entre a deflexão do escoamento nas pás diretrizes e no rotor da turbina é corrigida. Esta correção uniformiza o escoamento à saída do rotor, aumentado o rendimento da turbina fora das condições nominais de funcionamento. São projetadas novas pás diretrizes fabricáveis por calandragem para redução dos custos de fabrico. Estas pás demonstram um desempenho aerodinâmico superior a versões anteriores. É descoberta a deflexão nas pás diretrizes que maximiza o rendimento da turbina. Desenvolveu-se um novo método de projeto do rotor para reduzir o tamanho da turbina sem prejuízo do rendimento, para um dado amortecimento hidrodinâmico do conversor. Um gerador de ímanes permanentes e um retificador de díodos foram selecionados e caracterizados experimentalmente para analisar o rendimento, fator de potência e proximidade a condições de desmagnetização. A relação entre os parâmetros mecânicos e elétricos foram modelados com funções analíticas de ajustamento para utilização em projeto. O conversor de energia das ondas foi definido e modelado. Realizou-se o projeto de um conversor eletrónico de potência para regulação do funcionamento do turbogerador, do carregamento das baterias internas e da alimentação de cargas externas. Demonstra-se que os controladores evitam a sobre-corrente e o embalamento do turbogerador e que regulam eficazmente a potência do conversor. Considerando a operação ao largo do Porto de Leixões, estima-se uma potência elétrica disponível de 400W durante os estados de mar mais frequentes.

Palavras-chave: energia das ondas, coluna de água oscilante, turbina birradial, geração elétrica isolada, modelação numérica e experimental.

Abstract

Wave energy converters for powering off-grid electrical systems have the potential to support the development of the Blue Economy. The goal of the present doctoral research was to design a turbo-generator, based on a biradial turbine, for oscillating water column wave energy converters to power off-grid continuous-current electrical systems. Interviews with professionals of ocean monitoring equipment confirmed the applicability of this device. The relationship between the flow deflection in the turbine guide vanes and in the rotor was corrected. This correction increases rotor outflow uniformity, increasing the turbine efficiency outside nominal operating conditions. New guide vanes manufacturable by sheet bending were designed to reduce manufacturing costs. These vanes show improved aerodynamic performance compared to previous versions. The guide vane deflection that maximizes the turbine efficiency was found. A new rotor design method was developed to decrease the turbine size without penalizing its efficiency for a given converter hydrodynamic damping. A permanent magnet generator and a diode rectifier were experimentally characterized to assess efficiency, power factor and proximity to demagnetization regimes. The relationships between the mechanical input and the electrical output were modelled with analytical fitting functions for design use. The wave energy converter was defined and modelled. A power electronic converter was designed to regulate the turbo-generator operation, battery charging, and external-load supply. The controllers effectively avoid turbo-generator over-current and over-speed and regulate the converter output power. Considering the deployment site off the Port of Leixões, an electric power availability of 400 W is estimated during the most frequent sea-states.

Keywords: wave energy, oscillating water column, biradial turbine, off-grid power generation, numerical and experimental modelling.

Acknowledgments

As I prepare to submit my Ph.D. thesis, I can hardly believe how many years, experiences, and ups and downs have led to this moment. I am grateful to had the opportunity to contribute to science and technology in a field I'm passionate about. It wouldn't be possible to submit this work without the contribution of so many people, to whom I want to express my sincere gratitude.

I would like to begin by acknowledging the invaluable contributions of my advisors, Professors Luís Gato, João Henriques, and Ana Martins, whose support and guidance were essential to the success of this project. Their multidisciplinary expertise and unique personalities were instrumental in shaping this project from its inception and navigating through the most challenging moments.

I would like to extend my appreciation to Professor Luís Eça for his support and willingness to share his expertise and insights, even though he was not formally my advisor, SL.

I thank Professor Lei Zuo for having me as a visiting student in his group at Virginia Tech and for providing me with key concepts for my work.

I thank my esteemed companion, now Doctor Juan Portillo, who told me about a short course on the Lean Launchpad Method. Attending this course led me to my research topic, and eventually to collaborate with my co-advisors Ana Martins and João Henriques on the off-grid wave energy converter project. On the personal level, I look back fondly on our regular coffee breaks and lunches, which always provided me with good laughs and interesting conversations.

To Emeritus Professor Antonio Falcão, who unknowingly had me fascinated by turbomachines since I first read his lecture notes on the topic, and for founding the research group where I developed my work, I congratulate for a remarkable career.

I express my appreciation to Mrs. Maria José for providing continuous logistical and administrative support throughout my research, and for never succumbing to the "computer says no" mentality.

I thank Pedro Alves, our workshop technician, for the invaluable teachings in all things practical during the time we worked together.

I express my gratitude to Ari and Alexandre Martins from Usimeca Lda. for going above and

beyond their role as a supplier by demonstrating a sincere interest in my research and providing me with key design and manufacturing solutions.

To Ana Carrelhas I congratulate on the amazing and continuous effort to improve our lab.

To my new office companions, André Governo and Delfim Sá, I thank for listening to this old PhD student about his struggles to finish the thesis. I hope my advice will be useful.

I thank my first companions at the Wave Energy Group, affectionately nicknamed "Vadios das Ondas", for the wonderful memories and good times that helped me unwind after long days of work. I look forward to celebrating this thesis submission with them.

I also want to take this opportunity to thank my parents for their love, support, and encouragement throughout my academic journey. Their sacrifices, patience, and belief in me made me who I am.

I cannot conclude this note without expressing my sincere gratitude to Sofia, my girlfriend, who I met in the first year of my PhD and has been with me through the toughest moments of this journey. I couldn't have done it without her.

Contents

List of Tables

List of Figures

Chapter 1

Introduction

The Earth's oceans are a recognised key asset for human development. Some of its resources include food, raw materials and energy, but sustainability of the ocean, like of the majority of Earth's ecosystems, is under stress from pollution, declining biodiversity and climate change.

The Organisation for Economic Co-operation and Development (OECD) predicts that the ocean economy will double its size during the 2010-2030 period [1]. In 2010 ocean-based industries contributed with 1.5 trillion US dollars (2.5%) to global Gross Value Added (GVA) and 31 million direct full-time jobs. Offshore Oil&Gas and fishing will continue to grow, but the sectors expected to have the largest long-term growth are transportation, shipbuilding, ocean renewable energy, tourism, surveillance and safety, marine aquaculture and ocean renewable energy. In a business as usual scenario, it is expected that in 2030 ocean economy will grow to more than USD 3 trillion in GVA and to directly employ 40 million people.

Whether or not this economic development will be environmentally sustainable is up do debate. Yet, it is clear that sustainable development requires careful planning and technological breakthroughs in different areas. In 2013, the United Nations introduced the term *Blue Economy* [2] which has since been integrated in several development policies:

> *The Blue Economy conceptualises oceans as "Development Spaces" where spatial planning integrates conservation, sustainable use, oil and mineral wealth extraction, bioprospecting, sustainable energy production and marine transport. The Blue Economy breaks the mould of the business as usual "brown" development model*

> *where the oceans have been perceived as a means of free resource extraction and waste dumping; with costs externalised from economic calculations. The Blue Economy will incorporate ocean values and services into economic modelling and decision-making processes. The Blue Economy paradigm constitutes a sustainable development framework for developing countries addressing equity in access to, development of and the sharing of benefits from marine resources; offering scope for re-investment in human development and the alleviation of crippling national debt burdens.*

The European Commission has defined *a new approach for a sustainable Blue Economy in the EU* [3] as an integral part of the Recovery Plan for Europe [4], which is the largest stimulus program in EU's history, and the European Green Deal [5], that establishes a long-term, sustainable and resilient carbon-neutral economic model. Among other iniciatives, the *approach* promotes the coexistence and synergies of economic activities in the maritime space through the Maritime Spatial Planning, and proposes a series of actions to boost investment in research, skills and innovation, and mobilizes financing opportunities under the new European Maritime, Fisheries and Aquaculture Fund, and other EU Programmes, such as the Resilience and Recovery Facility.

One out of five EU regions are specialising in at least one domain related to the Blue Economy [6]. Smart Specialisation Strategy is a place-based approach characterised by the identification of strategic areas for intervention based on the analysis of economic potential and with wide stakeholder involvement. The Autonomous Region of the Azores, Portugal, is highlighted as a EU-Region Smartly Specialised in Blue Economy. The Azores is focused in thematic areas with high economic potential such as biotechnology and deep-sea mineral exploration, in environmental monitoring for the sustainable exploitation of these resources and in becoming an intercontinental platform for the knowledge of the oceans.

Portugal's Exclusive Economic Zone (EEZ), which is the 10th largest in the world, covers an extensive area of the North-East Atlantic. Accordingly, the Portuguese National Ocean Strategy for the period 2021-2030 [7] and the *Visão Estratégica para o Plano de Recuperação Económica de Portugal 2020-2030* [8] emphasizes the strategic value of the Atlantic for scientific, economic and cultural activities and the exploitation of its resources as national priorities. For Portugal to meet the challenges of growth and competitiveness of maritime economy within its strategic frameworks, it is fundamental to promote development of marine technology. The identified priority areas include decarbonization, renewable energy, energy security, advancement of science and technology, ocean industrialization and digitalization, and maritime safety and sovereignty.

Sensor data is essential for ocean management, scientific research, resource assessment and maritime surveillance. In turn, sensors are dependent on a power source. In offshore locations, it is usually the oceanographic or surveillance ship that employs them. Moored and drifting buoys with internal batteries are also used. Although their capital and operation costs are lower than ships, battery autonomy limits the employment of advanced sensors. Although increasingly common, data acquisition from satellite and aerial observation systems is also dependent on weather conditions and limited to the top of the water column. As such, the need to improve *in-situ* observation has been addressed [9]

Sensor buoys, are autonomous floating devices, equipped with sensors to collect and store data, and in some cases, with capabilities for processing and transmission in real-time. State-of-the-art sensor buoys are equipped with batteries and photovoltaic panels working as operation-extenders. However, this solution lacks in both autonomy and power. Despite recently hitting record low prices, small PV panels lack the power output on marine environments to enable the use of high power equipment. Battery replacement and maintenance requires specialized ships to collect, repair and re-deploy the buoy. These operations can be expensive and difficult due to weather conditions. A large network of buoys may require a fleet of maintenance ships. The sensor buoy market needs a new power-source that enables the use existing sensors more effectively, but as importantly, the implementation of more advanced sensors during longer periods of time [10].

Applied either as stand-alone battery chargers or as generation units in DC micro-grids, off-grid wave energy converters (WECs) are emerging as a potentially disruptive technology for remote ocean sensing [11–21]. Applications include observation platforms for scientific or surveillance purposes, charging stations for uncrewed underwater vehicles. Real-time monitoring and automation of offshore aquaculture farms is also proposed.

These applications can benefit from the abundance of wave energy in the maritime area under Portuguese jurisdiction [22, 23]. There is a predominant direction of wave propagation and low energy dissipation near the shoreline due to the favourable bathymetric gradient, particularly in the Azores.

Off-grid WEC's can presumably extend the operational time of state-of-the-art sensors, and change the type, volume, and cost of acquired data. An uninterruptible power supply allows higher sampling rates and real-time communication for traditional sensors. Moreover, high power sensors or machinery, typically operated from ships, could be used from a wave-powered buoy/platform. Namely autonomous vehicles (scientific, industrial or military) or surveillance radars or sonars. In this case, the operational costs of operating such devices could potentially be decreased, since a ship would then be used for deployment and recovery of the buoy/platform with its operation being done remotely from a command centre.

This thesis presents technical and scientific advancements in the creation of off-grid wave energy converters for ocean sensing. It aligns with both EU economic policy at the regional level and the UN's concept of a Blue Economy. Commercial off-grid wave energy converters may become a valuable addition to the marine observation and sensing market and provide a stepping stone towards the commercialization of grid-connected devices.

1.1 OWC wave energy converters

The conversion of wave energy into useful forms is a complex process that comprises various areas of engineering such as hydrodynamics, aerodynamics, hydraulics, structural analysis, materials, electronics, and control. Designing wave energy converters presents numerous challenges due to the variation of wave power across different time scales, including wave-to-wave variability (over a few seconds), sea state variability (over hours or days), and seasonal changes [24]. Another significant challenge is ensuring the survival of the converters during extreme conditions. During storms, the incident power can be one hundred times higher than in nominal conditions. Even in nominal conditions, converting the slow motion of waves into the high rotational speed of electrical generators (about 500 times greater) remains a challenge.

The multitude of concepts and designs of wave energy converters, in comparison to other

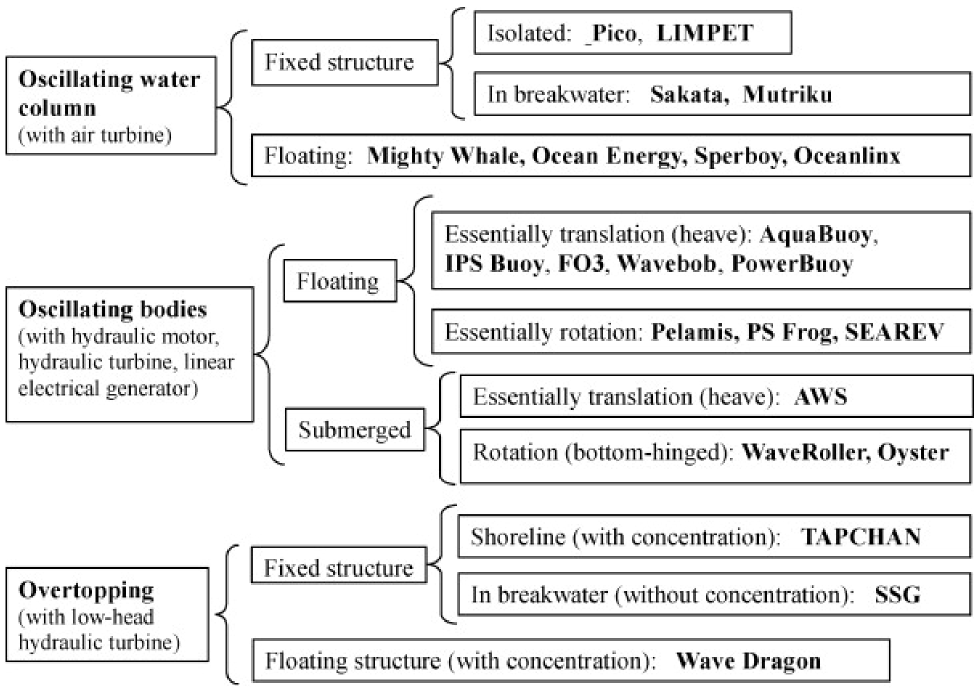

Figure 1.1: Wave energy technologies, adapted from [24].

ocean-based renewable energy sources such as tidal stream and marine currents, evidences lack of technological convergence within the field of wave energy [25]. WEC classification can be done based on the deployment location, such as onshore, nearshore, or offshore, or based on their underlying operating principle. A recent literature review [26] considers seven technological classes: attenuators, point-absorbers, oscillating water columns, overtopping devices, submerged pressure differential, bulge wave, rotating mass, and "others". The Ocean Energy Systems (under the framework of the International Energy Agency) uses a simpler three category classification: oscillating water columns (OWCs), oscillating bodies and overtopping devices, derived from earlier work [24]. Fig. 1.1 illustrates these technologies with examples of converters.

Due to harsh operating conditions and high commissioning and maintenance costs, system reliability is a priority for offshore equipment, especially in autonomous operation. OWCs are possibly the most simple and reliable concept for wave energy converters. There are no moving parts other than the rotors of an air turbine and conventional electrical generator, which are located above sea level [24, 27–29]. An OWC converter comprises a partly submerged concrete or steel structure, open below the water surface, inside which air is trapped above the free surface of the water. The oscillating motion of the internal free surface produced by the

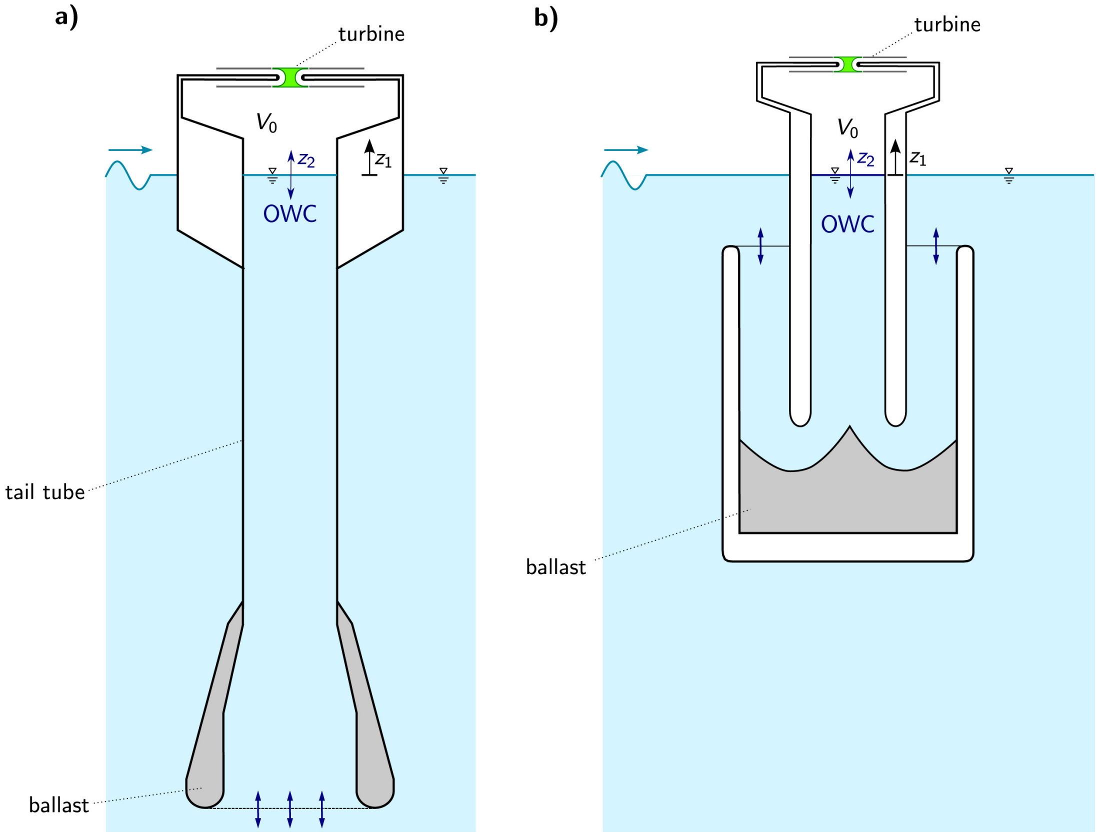

Figure 1.2: Cross-sectional views of OWCS: (a) spar buoy and (b) coaxial duct. Adapted from [30].

incident waves forces the air to flow through a turbine that drives an electrical generator [24]. Fig. 1.2 illustrates the cross-section of two floating OWC converters.

While other technologies are used for remote ocean sensing [31], the research work presented in this thesis deals exclusively with OWCs.

The first patent for a wave energy converter was filed in 1799 in Paris, France, by Pierre-Simon Girard. Based on the established categorizations, this device can be classified as an oscillating body converter [32]. The earliest documented oscillating water column was constructed by Bochaux-Praceique in Bordeaux, France in 1910 [32]. However, Yoshio Masuda is widely recognized as the father of modern wave energy due to his development of navigational buoys based on the OWC principle [24].

OWCs have been extensively studied for utility-scale power production [24, 33], but the last ten years saw few studies regarding this type of devices dedicated to off-grid applications.

A new method for design of OWCs with optimization of buoy hydrodynamics and turbine size was proposed [34]. The method was then used to design an OWC spar buoy and a coaxial duct for powering oceanographic sensors. Results show that the spar buoy outperformed the coaxial duct for similar sized devices. The spar buoy design was tested in a wave tank at 1:10 scale, for two wave climates and using an orifice plate as a turbine simulator [35]. It is concluded that operation in the Portuguese Atlantic west coast outperforms operation in the Mediterranean, off the coast of Sicily, with a annual mean pneumatic power of 1 kW and 0.4 kW, respectively, for a device with a diameter of 2.42 m and a draught of 8.44 m.

The design and 1:16 scale wave tank testing of an OWC spar buoy for powering a LiDAR systems was reported [36]. These systems are often used to assess wind speed in wind farms and require stable platforms for correct measurements but spar buoys are known to have large amplitudes of motion when in resonance conditions, which benefit power production. The researchers obtained a compromise design that complies with the stability requirement and provides adequate power production in resonance conditions.

An OWC BBDB for off-grid operation was numerically designed with a new wave-to-wire model [37]. The proposed design is expected to achieve a mean electric power output of 2 kW in the Portuguese north-west Atlantic coast. A model was tested in a wave tank at 1:120 scale [38]. Results illustrate the influence of wave direction and mooring line configuration over device performance. The resonant frequencies for heave and pitch and respective response amplitude operators were calculated.

A new concept for an OWC BBDB (Backward Bent-Duct Buoy) has been proposed [39], where two OWC ducts oriented in opposing directions jointly drive a single turbine that is isolated from the atmosphere. This design enables the capture of surge motion in both directions.

A novel buoy for wave profiling based on the OWC principle was presented [40, 41]. Instead of using the OWC chamber pressure to drive a turbine, the pressure is measured in order to characterize the incident waves. In this design, the sensors are powered by PV panels. The publications cover a 1:20 wave tank testing and a full-scale pre-deployment test.

Wave energy converters using the oscillating body technology (Fig. 1.1) have seen more development than OWCs for small-scale, off-grid energy production for sensing applications. In the last decade, notable advancements of the MBARI-WEC have been documented [42]. This WEC, designed by the Monterey Bay Aquarium Research Institute in Monterey, California, USA, utilizes an oscillating body mechanism and is equipped with a hydraulic motor. The

Smart Power Buoy, has been commercialized by Resen Waves, a company based in Lyngby, Denmark [43]. This device utilizes a direct mechanical drive system based on a flywheel and has the capability to produce a continuous electric power output of 300 W and a peak output of 600 W, starting at wave heights of 0.5 m. The dry mass of the Smart Power Buoy has been rated at a maximum of 350 kg. The PB3 PowerBuoy [44], produced by Ocean Power Technologies in New Jersey, USA, is one of the most notable commercial WECs for sensing applications. This device is an oscillating body WEC that employs a direct electric drive mechanism. According to the manufacturer, it has a peak electrical power output of 3 kW and an average annual electric power output of 350 W depending on location.

The key advantage of OWCs compared to oscillating bodies lies in the ability of the air within the chamber to serve as both a gear box and a spring without the use of mechanical components. The air chamber cross-sectional area variation between the water surface and the turbine increases the air flow velocity from several meters per second, at the water level, to tenths of meters per second, at the turbine inlet. This allows low-torque and high-speed operation of the electro-mechanical components. In contrast, oscillating bodies move at velocities similar to the motion of waves, causing high-torque and low-speed operation. The resulting high structural loads decrease the longevity of mechanical components such as gear boxes and generators. The spring-like effect of air compressibility minimizes impact forces and reduces fatigue problems, increasing reliability and lowering structural costs. Additionally, the placement of all mechanisms above the water level simplifies maintenance and reduces the risk of water impact during energetic sea-state conditions.

Even with its acknowledged benefits, extensive studies for utility-level generation [33], and the commercialization of Masuda's OWC navigational buoys in 1965, with some models in operation up to 20 years [24], development of oscillating water columns for off-grid systems is still lagging. The main drawback of OWCs is their modest power output caused by the low efficiency of the air turbines normally used [33].

1.2 Self-rectifying air turbines

Conventional turbines are designed to operate in unidirectional flow regimes, and in steady-state conditions for many applications. Under these conditions, high levels of efficiency and adequate power regulation have been accomplished across a range of applications such as hydro and steam power plants. However, for oscillating water columns, the primary challenge in turbine design and operation stems from the inherently irregular and bidirectional flow generated by the OWC, which is also dependent on the prevailing sea state.

Masuda's navigational buoys contained a rectification system to convert the bidirectional flow into a unidirectional one in order to drive a conventional turbine [45]. This approach requires using non-return valves, which results in substantial energy losses during the process. These losses are particularly pronounced due to the air flow velocities inherent to OWC systems. The required valve response time of approximately 1 second presents a significant challenge, particularly in high flow rate conditions. While valves could potentially be placed in the low-speed, high cross-sectional area of the chamber, this would result in a large, slow, and costly system.

New turbine designs that use unidirectional twin rotors have been recently proposed. With these turbines, each rotor extracts energy from one of the two OWC flow directions. In one publication, a valve system directs the flow to one of the rotors depending on the flow direction [46]. Alternatively, if no valves are used, unidirectional rotors choke the air flow when forced to operate in reverse mode, directing the flow trough the other rotor in direct mode [47]. Evaluation of these designs shows that windage losses on the closed/choked-conditions rotor, have a significant impact on the average cycle efficiency. Given their mechanical complexity and associated costs, these systems are not suited for low-power, off-grid OWC applications.

The majority of converters employ self-rectifying turbines, which can convert power while rotating in the same direction irrespectively of the OWC flow direction, due to their geometric design, i.e. transmitted torque is not sensitive to flow direction [29]. But as will be discussed next, these devices have their own shortcomings.

The Wells turbine is one of the most studied self-rectifying turbines. The simplest implementation consists of a monoplane rotor with symmetric airfoil-shaped blades placed in a central

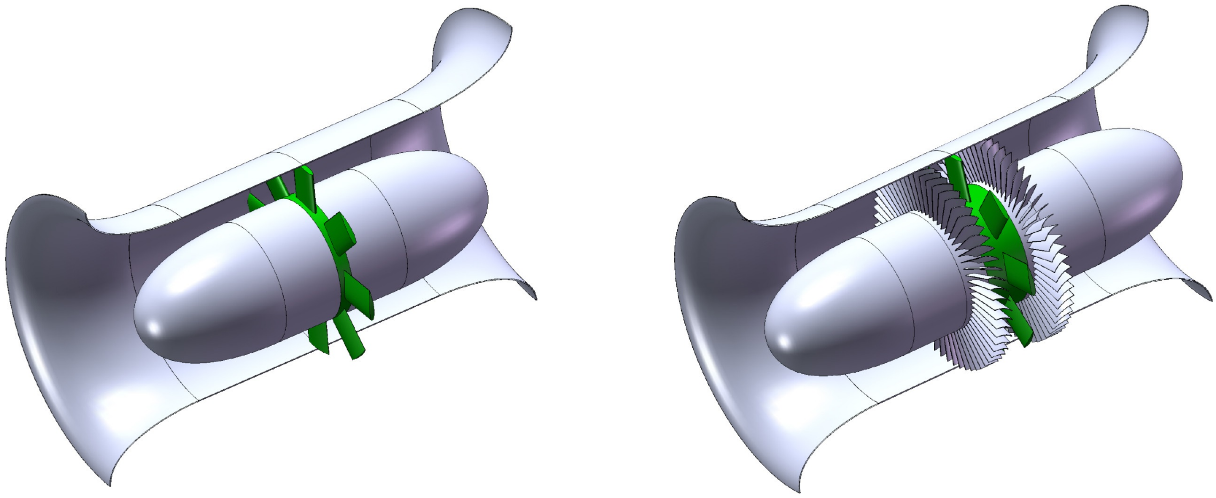

(a) Without guide vanes. (b) With guide vanes.

Figure 1.3: Three-dimensional model of monoplane Wells turbines with the rotor in green and the shroud partially removed. Adapted from Ref. [49].

hub, as depicted in Fig. 1.3a. This basic configuration can be augmented with the inclusion of guide vanes on either side of the rotor, as depicted in Fig. 1.3b. Additionally, biplane rotors, both counter-rotating and non-counter-rotating, as well as with mid-plane guide-vanes have also been proposed [48, 49].

The rotational speed of Wells turbines surpasses that of other self-rectifying turbine designs for the same application. As such, the rotor blade tip-speed must be carefully limited in design and operation, since it has the potential to induce shock-waves and excessive centrifugal stresses. Another well known characteristic is to have a linear relation between its pressure head and the flow rate under free-stall flow conditions. A peak efficiency of 75% was reported for a low-solidity monoplane design equipped with guide vanes [50].

Despite several improvements since it was first introduced, the Wells turbine remains known for having a narrow operating range with respect to the variation of OWC chamber pressure, which calls for the implementation of effective rotational speed controllers to maintain proper efficiency [51]. A sharp drop in efficiency occurs when the incidence angle of the flow over the blades exceeds the stall angle. Some proposed solutions include the implementation of pitch regulated blades, however, this approach adds significant mechanical complexity to the system, compromising its primary advantage of mechanical simplicity.

In off-grid applications, it is desirable to have a power generation unit capable of self-starting, i.e. with the ability to deliver power to unpowered systems or depleted batteries. Wells

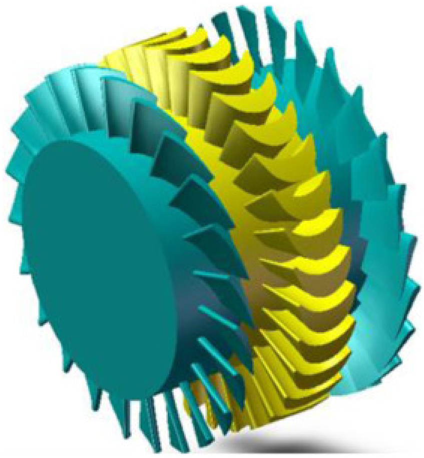

Figure 1.4: Unshrouded axial-flow impulse turbine. Adapted from Ref. [51].

turbines typically lack this capability because they do not generate stand-still torque from incoming flows, requiring an external power source to rotate the turbine up to generation speed [52]. This can be implemented by using the generator in motor mode and drawing power from a secondary source such as batteries or photovoltaic panels. Self-starting has been reported in high solidity turbines, but at the expense aerodynamic efficiency [53].

Axial impulse turbines [54] are the most popular alternative to Wells turbines. The rotor of these devices resembles those of the entry stage of axial steam turbines [55]. To ensure the turbine is insensitive to flow direction, the rotor geometry is symmetrical to a plane perpendicular to the rotation axis and is accompanied by rows of guide vanes on both sides, which are placed symmetrically to the said plane, as depicted in Fig. 1.4.

The efficiency curve of axial impulse turbines does not exhibit the sharp drop typical of Wells turbines since impulse rotors are more resistant to flow incidence. In contrast to the Wells turbine, a gradual decline for increasing values of the flow rate follows the peak efficiency [51]. This characteristic allows for a more forgiving speed controller and turbine operation at a reasonable efficiency even in the more energetic sea states. On the other hand, the peak efficiency of axial impulse turbines is severely limited by losses on the guide vanes downstream of the rotor, since these guide vanes are inherently misaligned with rotor outflow [54]. The flow losses at the outlet guide vanes aggravate when the flow deflection at the inlet guide vane is large but the associated noise emission is mild compared to the Wells turbine [56].

Several improvements to axial impulse turbines have been proposed, most notably to reduce losses in the downstream guide vanes. Two types of pivoting mechanisms have been proposed to place the guide vanes in a more benign position relative to the rotor outflow. Self-pitching guide vanes that flip under the action of the aerodynamic moments acting on them were studied and found to improve turbine efficiency [54]. An active mechanism consisting of a ring and articulated rods actuated by a servomotor was tested in a sea-trial with a prototype [57]. An interesting approach to reduce downstream guide vane losses is to substitute each guide vane row by multiple rows with lower solidity but providing the same inflow deflection. The objective behind this approach is to create unobstructed flow paths in-between vanes for the rotor outflow [58]. While losses in the downstream guide vanes were significantly reduced, the efficiency of the model turbine was penalized by the modest efficiency of the rotor used. On other approaches, an efficiency of 48.7% reported on a turbine with fixed guide vanes, with an efficiency gain of 2.2% over the reference case achieved by the using end plates in rotor blades [59].

Axial impulse turbines are mechanically more complex than Wells turbines but, by being able to generate stand-still torque [60], can feed an unpowered system without auxiliary power sources. Low noise emission might be an asset for operating in marine protected areas and for powering sensitive equipment such as sonars. Another interesting feature is that the relation between the pressure head and the flow rate is approximately quadratic, which implies that the rotational speed barely affects the OWC hydrodynamics, i.e. speed does not affect the wave-to-pneumatic energy conversion process [48].

The biradial impulse turbine was proposed in 2013 for bidirectional flow applications as an alternative to axial impulse turbines [61]. The geometry of a biradial rotor is also symmetrical about a plane perpendicular to the rotation axis since the flow is bidirectional. But contrary to axial impulse turbines, the rotor inlet and the outlet face the radial direction. The rotor is surrounded by sets of radial-inflow guide vanes and each set is designed to deflect one of the OWC flow directions, as with axial impulse turbines. The guide vane sets are connected to the corresponding rotor inlet/outlet opening by axisymmetric ducts with flat-disc walls. The turbine inflow is centripetal, while the outflow is predominantly centrifugal. A comparison between a biradial and an axial in the meridional plane is illustrated in Fig. 1.5 followed by a photo of each rotor in Fig. 1.6.

Biradial impulse turbines have the same inherent problem of axial impulse turbines with re-

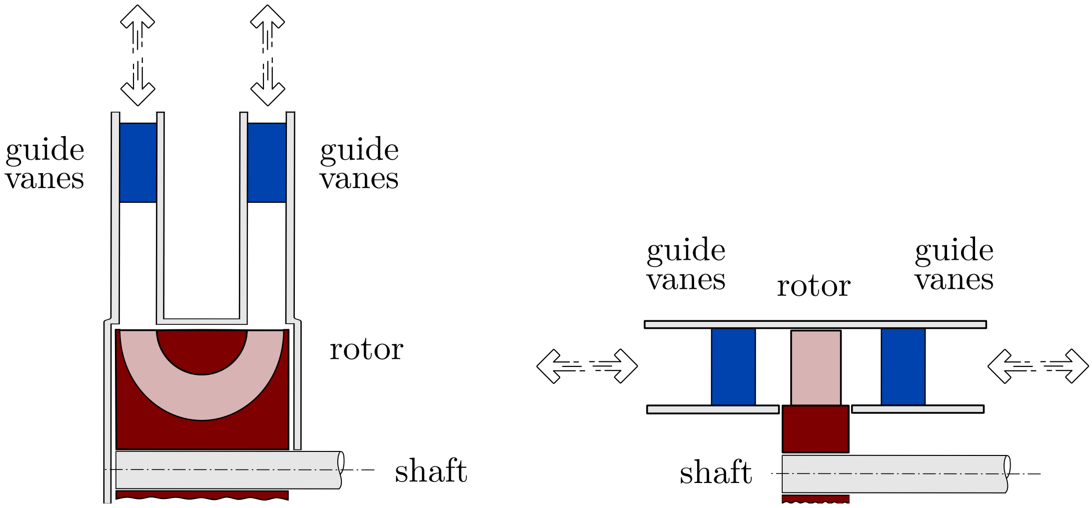

Figure 1.5: Biradial impulse turbine (left) and an axial impulse turbine (right) meridional plane representations.

Figure 1.6: Impulse rotors for self-rectifying air turbines: biradial rotor (left) [62] and axial rotor (right) [58].

spect to losses in the downstream guide vanes due to misalignment. The flow enters the turbine in the radially inward direction. Then it is deflected by the inlet guide vanes, receiving circumferential velocity (swirl) in exchange for a static pressure drop (apart from energy losses). The kinetic energy associated with the swirling flow is then converted by the rotor into mechanical energy, causing the flow to leave the rotor with little to zero circumferential velocity component, i.e., approximately in the radially outwards direction. As such, the outlet guide vanes are highly misaligned with the rotor outflow because they are designed to generate swirl for the flow entering the turbine from the opposite direction. The interaction between the rotor outflow with the misaligned outlet guide vanes generates flow separation and severe stagnation pressure losses.

Two design approaches derive from the opportunities presented by the rotor being biradial: the movable guide vane version (MGV) and the fixed guide vane version (FGV). In the MGV implementation, a mechanism is introduced that periodically removes the guide vanes from the flow channel by axial translation, avoiding contact between them and the rotor outflow, which is possible due to the axial compactness of the meridional channel [61]. This approach completely avoids losses in downstream guide vanes, resulting in a reported peak efficiency of 78% [62]. In the FGV implementation, the guide vanes are radially shifted from rotor in the design phase to promote rotor outflow deceleration in a diffuser before reaching the outlet guide vanes. While not eliminating them entirely, the stagnation pressure losses are proportional to the square of the outflow velocity and are thus mitigated [63]. The peak efficiency reported for the FGV version is 72% [64].

As with other impulse turbines, the biradial turbines exhibit a quadratic relation between the pressure head and the flow rate, self-starting capability and no sudden efficiency drops with varying flow rate in either MGV or FGV implementations [62, 64]. The noise emissions were also addressed and are significantly lower than the Wells turbine [65]. The efficiency of these early models is comparable to the highest efficiency of low-solidity Wells turbines and clearly superior to axial impulse turbines [51].

Despite being a recent design, the biradial turbines already reached important milestones. Namely the construction of a 30 kW prototype [66] that was tested under real-sea conditions at the BiMEP test-site [67], Spain, in the scope of the OPERA H2020 R&D Project [68]. First in the onshore Mutriku wave power plant [69] and then aboard the IDOM MARMOK-A-5 spar buoy [70]. The sea-trials at the Mutriku wave power plant showed that the prototype has an averaged peak efficiency 37% higher than the other turbines (biplane Wells) in operation at the same site. One of the most promising additions to this prototype was a high-speed safety valve which enabled a new peak-shaving control strategy. It consists on the fast and partial closure of the valve to adjust the flow rate across the turbine in response to pressure peaks. This strategy is effective in keeping the generator speed and electric power at the rated values in highly energetic sea states [66].

At the current development stage, biradial impulse turbines maintain all the advantages of axial impulse turbines over the Wells counterpart and improve on their only shortcoming, the low peak efficiency. Nevertheless, this added benefit comes at the cost of increased structural complexity due to its non-conventional geometry. It is an axially compact machine but a high radial-offset radius of the guide vanes with respect to the rotor can cause practical challenges.

As with many aspects of wave energy conversion, there is no technological convergence in turbines for OWCs. To the author's knowledge, no turbines, or variants of existing ones, have been specifically developed for off-grid OWCs. In this specific context, the strength of Wells turbines seem to be their mechanical simplicity, which is important to keep manufacturing costs low. The self-starting capability and forgiving control requirements of impulse turbines, seem to indicate that a simpler generator, power electronics and controller arrangement might be achieved compared with the Wells counterpart. Yet, it is not clear if the high efficiency of biradial turbines, with respect to the axial variant, compensates the added structural complexity in the context of off-grid devices. But the novelty of biradial turbines and the promising results demonstrated for grid-connected generation justifies their study in off-grid application. Lowering noise emissions could expand the potential applications of an OWC, and enhancing device longevity may be achieved by incorporating an effective shut-off valve.

1.3 Research objectives

From the discussion so far, a central question remains unanswered due to the lack scientific and technical data:

How can off-grid OWC WECs be designed and implemented
as a valuable solution for the Blue Economy?

Motivated by this question, the Wave Energy Group at Instituto Superior Técnico is actively developing an OWC wave energy converter to power off-grid systems. The research work leading to this thesis is an integral part of this effort.

Due to its interdisciplinary nature, the answer to the main research question exceeds the scope of a single doctoral research project in terms of both subject and time-frame. The objective for the research work presented in this thesis is to design and assess aerodynamic

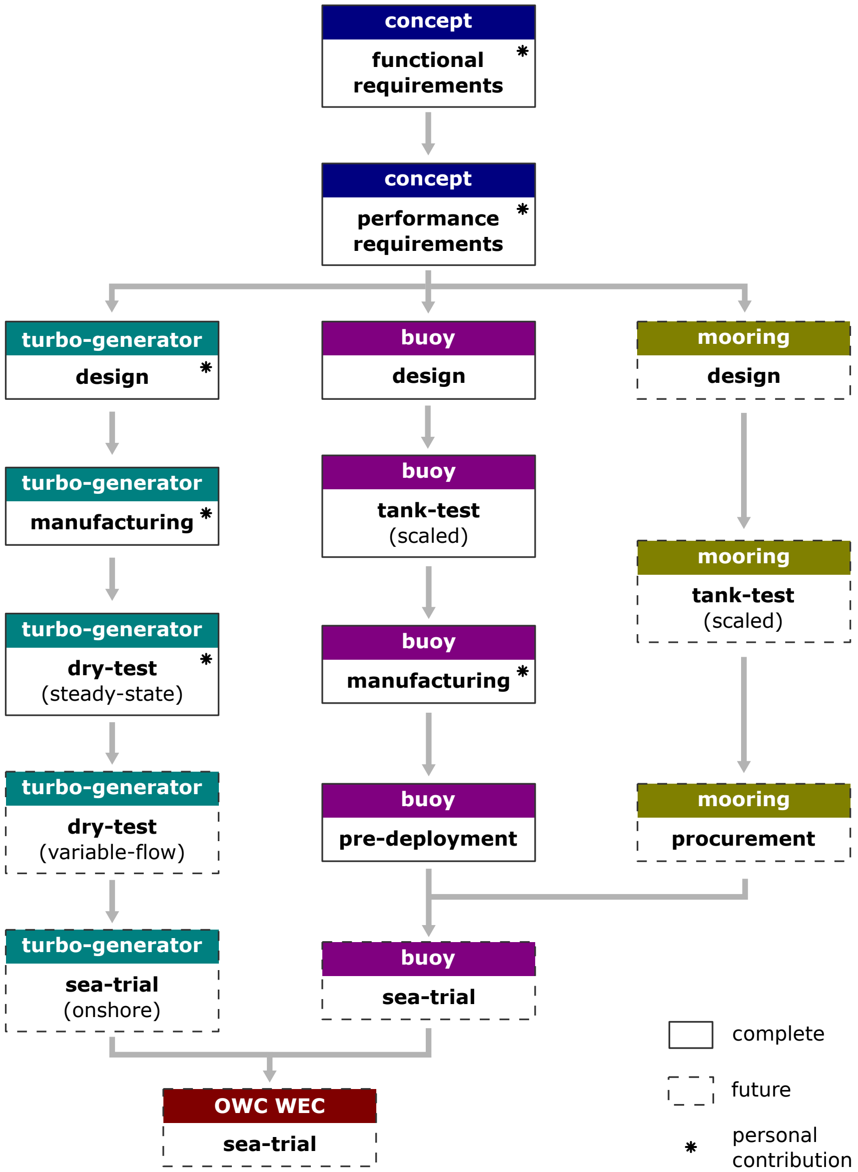

Figure 1.7: Instituto Superior Técnico's research work on off-grid OWC wave energy converters.

and electromechanical components for a turbo-generator based on the self-rectifying biradial impulse turbine. In itself, it is still a broad multidisciplinary topic covering aerodynamics, mechanical design, and electronics while having a strong interaction between the other areas within the broader research line.

IST's effort and its relation with the research work presented in this thesis is illustrated Fig. 1.7. The development of an off-grid OWC WEC starts with questions such as which systems can and should be powered by the WEC, what are their power requirements, how are they currently powered, what should be the target size of the converter and power output? Questions that can be summarized as:

What are the WEC's functional and performance requirements?

These are fundamental to frame the research work of the three main parts comprising the converter: turbo-generator, OWC buoy and mooring lines.

The core of this thesis are contributions to the turbo-generator research branch. Using the lessons learnt from the development of a grid-connected turbo-generator module as the starting point, successive improvements and adaptations to the specific context of off-grid generation are proposed. As such, the core of this thesis aims to respond to the following question:

How can the design tested in the OPERA project
be improved for off-grid generation?

To answer these questions specific research objectives were established:

- Implement design features that improve the aerodynamic efficiency of the turbine.
- Implement design features that reduce manufacturing costs of the turbine.
- Derive a turbo-generator design compatible with the OWC buoy.
- Define a generator and power electronic converter that addresses the specific functional requirements of off-grid generation.

1.4 Thesis structure

The thesis is structured into seven chapters, with each chapter addressing semi-independent questions and objectives. The remainder of this work is organized as follows.

Chapter 2 supports the objectives of the broader research line introduced on Chapter 1. It identifies the challenges faced by operators of ocean monitoring equipment and ocean-related data users in their daily activities trough a series of interviews. Moored data buoys were identified as crucial elements within ocean data value chains, yet concerns arise regarding the capability of their internal power supply to meet current demands.

Subsequent chapters deal with the detailed design of the biradial turbo-generator module.

Chapter 3 identifies a discrepancy between the expected operating conditions for achieving maximum efficiency and the actual conditions for which optimal efficiency is observed on the 30 kW prototype. Hypotheses to explain and mitigate these observations are raised and Computational Fluid Dynamics software is used to validate them.

In Chapter 4, the manufacturing process of the turbine guide vanes is identified as a possible cost reduction vector. A new design concept with more cost-efficient manufacturing is proposed and CFD coupled with evolutionary computation is used to obtain new geometries. A comparison is made between the new guide-vanes and those used in the 30 kW prototype. The optimum relationship between guide vane angles, rotor blade angles, and turbine efficiency is discussed.

Chapter 5 introduces modifications to the rotor design method of the 30 kW prototype with the aim of improving its aerodynamic efficiency. The chapter provides a detailed assessment of the impact of each design parameter on efficiency. Additionally, the chapter applies classic turbomachinery theory to reduce the turbine size while maintaining a fixed OWC damping constant. New rotor geometries are created based on the chapter's objectives, and their performance is assessed through CFD simulations.

Chapter 6 proposes and tests a permanent magnet generator and a diode rectifier for the off-grid wave energy converter. It presents the test-rig, testing procedure and the performance data taken under steady-state conditions. The results are post-processed for easy integration with wave-to-wire models aiming for component design and WEC performance estimation. Finally, practical aspects of operation, such as efficiency, power factor and risk of demagnetization are analysed and discussed.

Chapter 7 presents the design of a power electronic converter for off-grid direct-current power supply with the generator and rectifier assembly of Chapter 6. An oscillating-water-column wave energy converter with an internal battery bank is defined and simulated to derive the electronic converter parameters. Control strategies are devised to regulate the generator operation and the battery charging process.

Finally, Chapter 8 concludes the thesis by highlighting the main outcomes and contributions for the development of the IST's off-grid wave energy converter and proposes future research topics.

1.5 Publications

The following is a list of scientific publications that led to the present thesis.

Publications in international journals and conferences

- J.C.C. Henriques, J.C.C. Portillo, L.M.C. Gato, R.P.F. Gomes, D.N. Ferreira, A.F.O. Falcão, *Design of oscillating-water-column wave energy converters with an application to self-powered sensor buoys*, Energy, Volume 112, 2016, Pages 852-867, ISSN 0360-5442, doi: 10.1016/j.energy.2016.06.054.

- J.C.C. Portillo, D.N. Ferreira, J.C.C. Henriques and L.M.C. Gato, *Creating value in oceanography with wave energy converters: User needs*, Proceedings of the 12th European Wave and Tidal Energy Conference, 2017, Ireland.

- A.R. Maduro, L.M.C. Gato, J.C.C. Henriques and D.N. Ferreira, *Design and optimization of fixed guide-vanes arranged into concentric annular rows for a self-rectifying biradial air-turbine*, Proceedings of the 12th European Wave and Tidal Energy Conference, 2017, Ireland.

- D.N. Ferreira, L.M.C. Gato, L. Eça, J.C.C. Henriques, *Aerodynamic analysis of a biradial turbine with movable guide-vanes: Incidence and slip effects on efficiency*, Energy, Volume 200, 2020, 117502, ISSN 0360-5442, doi: 10.1016/j.energy.2020.117502.

- L.M.C. Gato, A.R. Maduro, A.A.D. Carrelhas, J.C.C. Henriques, D.N. Ferreira, *Performance improvement of the biradial self-rectifying impulse air-turbine for wave energy conversion by multi-row guide vanes: Design and experimental results*, Energy, Volume 216, 2021, 119110, ISSN 0360-5442, doi: doi.org/10.1016/j.energy.2020.119110.

- L.M.C. Ferro, D.N. Ferreira, L.M.C. Gato, *Influence of mesh quality and turbulence model on computation of two-dimensional flow on a volute of a biradial turbine*, Congresso Nacional de Engenharia Mecânica 2022, Teresina, Piauí, Brasil.

- D.N. Ferreira, L.M.C. Gato, L. Eça, *Efficiency of biradial impulse turbines concerning rotor blade angle, guide-vane deflection and blockage*, Energy, Volume 266, 2023, 126390, ISSN 0360-5442, doi: 10.1016/j.energy.2022.126390.

- L.M.C. Gato, D.N. Ferreira, D.O.C. Sá, *Biradial turbine rotor aerodynamic design and parametric analysis*, Energy Conversion and Management, Volume 278, 2023, 116651, ISSN 0196-8904, doi: /10.1016/j.enconman.2022.116651.

- D.N. Ferreira, L.M.C. Gato, J.C.C. Henriques, *Testing of a permanent magnet synchronous generator for off-grid OWC wave energy converters*, submitted to IEEE Transactions on Energy Conversion on July 2023.

- D.N. Ferreira, L.M.C. Gato, J.C.C. Henriques, *Preliminary design of an OWC wave energy converter battery charger*, Proceedings of the 15th European Wave and Tidal Energy Conference, 2023, Spain.

- G. Saha, D.N. Ferreira, N. Srikanth, L. Zuo, *Enhancing the efficiency of an axial impulse turbine with a diffuser*, Proceedings of the 15th European Wave and Tidal Energy Conference, 2023, Spain.

Patents

- A.F.O. Falcão, L.M.C. Gato, J.C.C. Henriques, D.N. Ferreira. *Energy conversion system for use in bidirectional flows and its method of operation*, Portugal, patent No. PT 109624 B, Instituto Nacional da Propriedade Intelectual.

Chapter 2

A survey on ocean monitoring systems

This chapter identifies and discusses challenges faced by operators of ocean monitoring equipment and ocean-related data users in their daily activities. The concept of operational oceanography and its infrastructure are introduced, along with the key sectors and stakeholders involved. The study comprises 42 semi-structured interviews with individuals from different sectors, including end-users from the tourism and transport industry, and end-users that also operate their own infrastructure, such as the oceanography, energy, and defence sectors. Common challenges such as availability and reliability of data from off-shore locations were identified. Moored data buoys allow measurements along the entire water column and the lowest level of the atmosphere. Reduced battery autonomy and lifespan, onboard photovoltaic panel failures, bio-fouling, sensor and transmitter failures were identified as the main limitations of these devices.

2.1 Objectives

Operational oceanography is an interdisciplinary field that uses advanced technologies and modelling techniques to provide real-time and near-real-time information on the state of the ocean and its interactions with the atmosphere and the geosphere. Examples of products/services derived from operational oceanography include weather forecasts, climate predictions, oil spill monitoring, fisheries management, and search and rescue operations. This field is rapidly evolving, driven by technological advances, growing demand for ocean-related services, and the need to address pressing societal and environmental challenges.

Metocean data users are present across various marine sectors, including the environment, energy, military, public safety, transport, and tourism. The environment sector focuses on monitoring and safeguarding the marine environment, maintaining sustainable fisheries and healthy marine ecosystems. The energy sector aims to enhance the efficiency and safety of its industries, mainly marine energy and Oil&Gas. The military sector aims to support control, planning, and day-to-day operations, while the public safety sector strives to avoid loss of life by monitoring metocean conditions, issuing alerts, and implementing necessary actions. The transport sector aims to improve offshore operations' efficiency, effectiveness, and safety, and finally, the tourism sector aims to aid the public in planning their leisure activities.

The Global Ocean Observing System (GOOS) is an international program that aims to publicly provide regular and accurate measurements of the ocean's physical, chemical, and biological properties [71]. It is a coordinated effort between governments, research institutions, and other stakeholders to gather and share ocean data in order to better understand and manage the world's oceans. GOOS uses a variety of tools, including satellites, *in-situ* measurements, and numerical modelling, to acquire and process data such as temperature, salinity and ocean currents, among many others. The Copernicus Programme is the European Union's Earth Observation Programme. As part of GOOS, it provides free, open, regular and systematic reference information on the European regional seas.

The GOOS relies heavily on over 30 satellites, however, their usefulness is limited by atmospheric conditions and by the impossibility to take measurements from deep inside of the water column. As such this data needs to me calibrated and complemented with *in-situ* measurements [9]. These are made using observing ships and vessels, moored and drifting buoys, and Argo profiling floats. The approximate inventory of Argo profiling floats is around 3000 units, observing ships and vessels are around 700, and there are around 1360 buoys deployed in the ocean [72]. Fig. 2.1 summarizes the exiting techniques for *in-situ* data acquisition. The existing sensor buoys often include solar panels and batteries whose autonomy and power output is insufficient for the even more modern sensor applications [10]. As such, alternatives to overcome

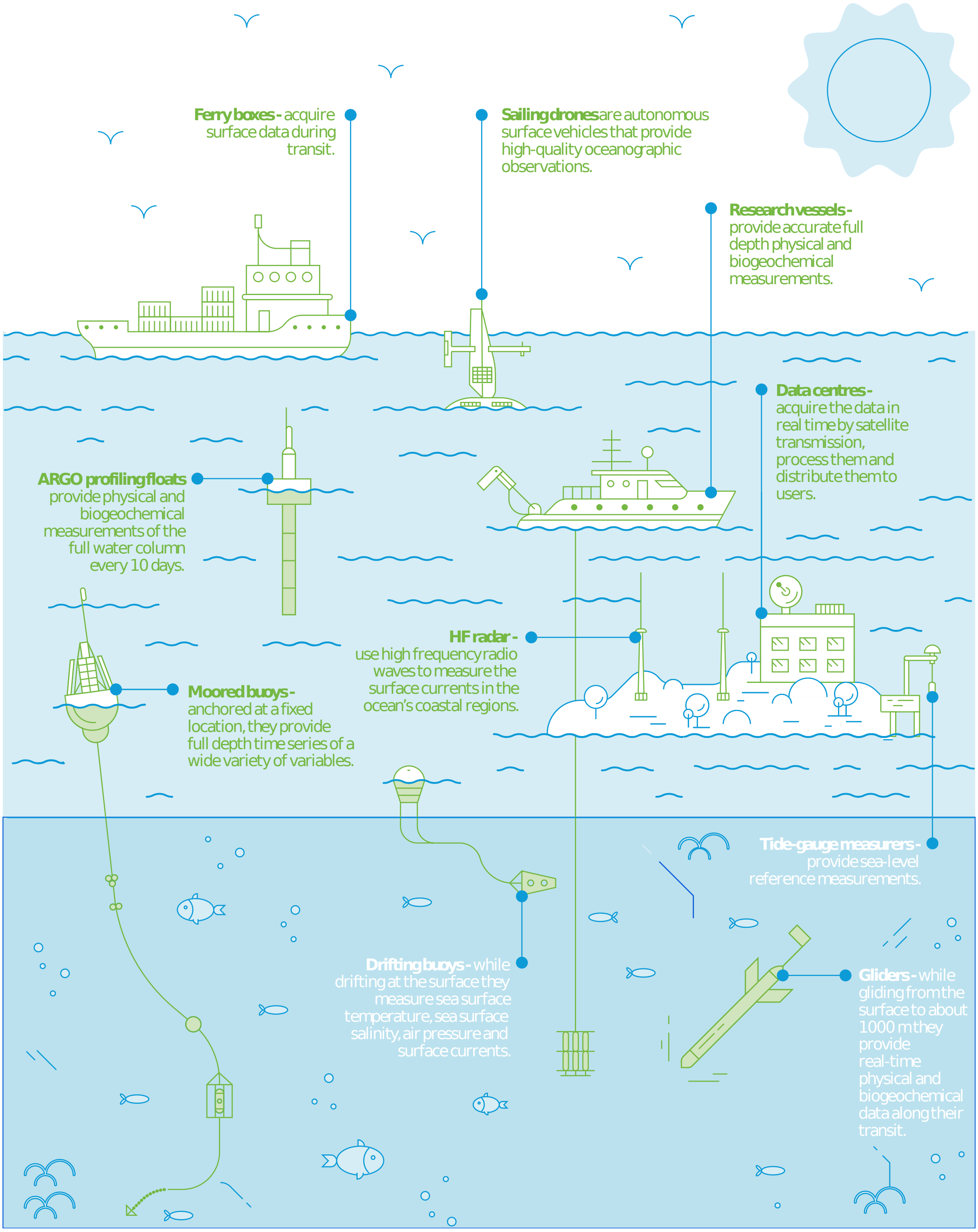

Figure 2.1: *In-situ* observation techniques for operational oceanography. Adapted from [73]

the current power limitations of data buoys are of great importance for the future of the GOOS.

The objectives of this present Chapter are: (i) to recognize the challenges encountered by users of oceanographic monitoring equipment and professionals using ocean-related data in their daily work, and (ii) to gain insights into the practical limitations of the employed equipment."

2.2 Methods

The data source are open-ended questions focused on the daily tasks of monitoring equipment and metocean data users. Interviews were done face-to-face, when possible, or remotely, otherwise.

Interviewees were selected based on their activity sector and relation to offshore operations. It is helpfully to distinguish between three types of oceanographic data users [74]:

- Operational-intermediate-service-providers and end-users rely on regular and systematic data and information to facilitate their activity. These users require information throughout the life cycle of their products, including strategic planning, exploration, design of solutions, and day-to-day operations. For instance, an offshore oil and gas companies in the design of a facility and in the plan for drilling activities.

- Policy end-users require operational data and information to support the creation of effective legislation, guaranteeing the safety of life and property while safeguarding the environment. This data is equally crucial for overseeing compliance with the laws and evaluating policy efficacy. For example, when optimizing the implementation of a policy aimed at reducing harmful pollutant concentrations, scenario modelling is essential to project future trends and assess the potential impact of measures. Additionally, long-term monitoring becomes indispensable to ensure the policy accomplishes its intended objectives.

- Scientific end-users rely on high-quality data output as a base for scientific advancement. Regular and sustained data sets are used to understand ocean-related physical, chemical, and biological processes, including its influence on weather and climate.

The following sectors were covered in forty two interviews: twenty-one from the energy sector (fourteen from renewable and seven from Oil&Gas), seven from environment sector, four from tourism, three from defence, three from fisheries, three from public safety, and one from transport. Regarding the energy sector, especially from the Oil&Gas, individuals from Europe and America were interviewed. For the rest of sectors, individuals were mostly from Europe.

Data analysis followed a qualitative approach looking for common problems and desired features for data buoys.

2.3 Results

The main interview outcomes are presented here in a per-sector basis.

Oceanography

This group comprises companies and institutions related to operational oceanography. These may be operators, end users and/or value-added intermediaries. Interviewees highlighted that long-term deployment of moored data buoys is becoming increasingly difficult. The main challenges to overcome are the onboard power management due to the ever increasing demands of new applications, failures in power, transmission and measuring systems due to bio-fouling, and the increasing operational costs of support ships.

Interviewees confirmed that state-of-the-art monitoring buoys are powered by batteries and, in some cases, incorporate photovoltaic (PV) panels for autonomy extension. Small wind turbines are rarely used due to failure under extreme weather conditions. The effectiveness of PV panels and their capability to endure long term deployment is limited by a number of factors: power production is proportional to surface area, which is limited on a buoy, and is weather dependent; efficiency is reduced by dirt, salt and animal deposits; and there is no power production during the night. Battery lifespan is allegedly reduced in buoys with PV panels and a high number of sensors.

In addition, interviewees reported that data records are often missing due to temporarily power shortages. This occurs more frequently in winter and can last several days. The occurrence of cloudy and rainy days, and failures due to extreme weather were indicated as the most common causes. Operators often interrupt data acquisition to maintain power-supply to the locator beacon, which is considered a crucial system.

Interviewees highlighted that monitoring buoys should have a healthy and fully charged battery pack before winter. However, this is not always possible. Buoy maintenance requires specialized ships with tight schedules and costs calculated on a daily basis. Unexpected changes in weather can easily postpone an operation or even cancel it if the time-window is over-shoot.

Even in nominal conditions, operators limit the number of onboard sensors and their sampling rate to reduce power consumption. Each sensor might have a different operating schedule to avoid overloading the power unit. Increasing the number of monitoring buoys per site is sometimes considered, increasing acquisition and maintenance costs. Interviewees expressed the need to increase battery autonomy to lift these limitations. It should be noted however, that there is a strong effort by the sensor manufacturers to reduce power consumption, and by the battery manufacturers to increase autonomy.

The PV panels used have a rated power from 50 to 150 W. Acquisition costs for moored data buoys were reported in range of 80 to 240 k€ with each sensor varying from a few thousand to 50 k€. From the operators perspective, efficient and reliable long term operation is a much desired feature. Acquisition costs were not reported as the main financial barrier, but rather the deployment, maintenance and recovery operations. It was highlighted that increasing the capital costs of monitoring systems could be offset by reducing the frequency of maintenance missions, even if the complexity of each mission slightly increases. These users perceived reducing the frequency of maintenance missions involving support ships as a priority.

Energy

This group comprises Oil&Gas and offshore renewable energy companies, technology developers and utilities. In general these types of users might be public or private entities. Although their business model and daily operations might differ significantly from the oceanography sector, the identified challenges related to data acquisition and use are similar.

The interviewees state that they might be end-users, as well as buoy operators, depending on the scale of their operations and the data made available by other entities. The monitoring equipment used is in line with the oceanography sector, and comprises buoys powered by batteries, PV panels and/or with small wind turbines. They face the same irregular data acquisition and frequent maintenance operations due to power shortages, and battery and sensor failures. Bio-fouling accumulation and failure of PV panels due to bad weather were highlighted during the interviews. Interviewees expressed the desire for reliable and easy to operate monitoring systems, with minimum maintenance and deployment requirements.

Defence

This group comprises defence-related entities. Some cover the entire value chain by integrating acquisition, processing and data usage. Others are intermediaries and integrators, and may incorporate additional processing services. Generally, this group demonstrated interest on the integration of data provided by a network of autonomous systems into existing centralized control centres. One interviewee indicated that having access to a live-feed from *in-situ* monitoring stations for shipping lanes would improve their activity. Other interviewee expressed the desire to have *in-situ* surveillance of marine protected areas. The sensor operators and the data intermediaries in this group expressed their preference for holding the intellectual property of the systems used.

Public safety

This group comprises public entities that processing data acquired externally, usually by the defence and oceanography sectors. These entities assess and forecast data that may affect public safety, such as coastal flooding, tsunamis, shipping forecasts and severe weather conditions. All the interviewees indicated that their entities are not operators of monitoring equipment, and that they only receive data for post-processing. Still, data intermittency on some observation points was reported, namely in off-shore locations,.

Transportation and fisheries

Only one interview with the transportation sector was performed. No significant data was obtained, besides that they are end-users of data and that they use the information to ensure the safety operations of maritime transport, advising for routes and possible weather conditions and potential hazards. Fishing companies rely on weather forecasting to plan operations. A challenge for this sector is the reliability of the forecasting that may cause unnecessary downtime.

Tourism

This group comprises sports/tourism companies and enthusiasts that use live weather data to perform their professional and leisure activities, including wale and bird watching, diving, and fishing. Interviews showed that this group is data oriented, as they do not intend to operate monitoring systems, but pay to access data feeds.

Interviewees generally considered the data available trough websites and mobile applications to be reliable enough for their daily near-shore activities. Challenges emerge for remote locations. These users rely on common knowledge and their experience to extrapolate near-shore data to off-shore locations. This occasionally leads to poor costumer experience when predictions fail and conditions on-site are not favourable. Some interviewees indicated that live video- and weather-streams, similar to beach and wildlife cams, in relevant locations would greatly improve their activities. These would serve has site advertising and operational planning tool.

2.4 Conclusions

The study presented in this Chapter was conceived to assess the practical limitations of *in-situ* ocean monitoring systems, namely of moored data buoys.

Nearly all sectors reported reliability issues, particularly during winter, including downtime and low or non-uniform sampling rates. These problems are typically linked to power generation and storage, transmission systems, and mooring lines. Furthermore, the high costs associated with maintenance ship operations aggravate these challenges.

Power management in offshore data buoys is a difficult task with impact over the entire data supply chain. State-of-the-art photovoltaic (PV) panels are, allegedly, only autonomy extenders and data buoys are rarely self-sufficient. Moreover, it is plausible that the intermittency of power generated with onboard PV panels in association with high power consumption is forcing the batteries to deep discharging cycles and variable charging currents, degrading their lifespan.

The interviews documented in this Chapter identify a market gap in power sources for off-grid sensing platforms as state-of-the-art power sources impose restrictions on existing applications. Furthermore, as the information technology advances, driving the demand for more complex data, augmenting the power quantity and quality of monitoring buoys becomes increasingly crucial for the integration of more sophisticated sensors and transmitters.

The wave-powered navigational buoys of the 1960's demonstrated the reliability of the OWC principle under autonomous operation in offshore environment. The inefficiency of its turbines hindered the overall power production and, presumably, a lack of alternative applications hindered the development of off-grid converters. The advancements in grid-connected electromechanical conversion of the last decades, namely in electric machines and power electronics, and the invention of biradial turbines, have increased the overall power production and quality of OWC wave energy converters. As such, the identified market gap might present a renewed opportunity for the development and commercialization of off-grid OWC wave energy converters.

Chapter 3

Incidence and slip compensation in biradial rotors

Due to the irrotational nature of a turbomachine flow in the absolute reference frame, a counter-rotating eddy appears in between rotor blades of radial machines (on the relative reference frame). This eddy causes incidence in radial turbines and slip in radial compressors, pumps, and fans. The inlet flow in a biradial rotor is centripetal while the outlet is centrifugal, resulting in two counter-rotating eddies. A model developed for conventional radial machines is used to predict the interference over inlet and outlet flow angles caused by the counter-rotating eddies and quantify it in the form of slip velocities. These velocities are then used to redefine the relationship between inlet/outlet absolute flow angles and rotor intlet/outlet blade metal angles in design conditions. The resulting relationship is employed to correct the rotor inlet/outlet blade metal angle of an existing movable-guide-vanes biradial turbine. Both the original and corrected geometries are simulated and compared using a commercial CFD code. The slip model accurately quantifies both slip and incidence in the biradial rotor analysed. For the corrected geometry, incidence and slip-related losses are decreased, and rotor outflow uniformity is increased. Diffuser performance is improved in off-design conditions, resulting in higher average turbine efficiency.

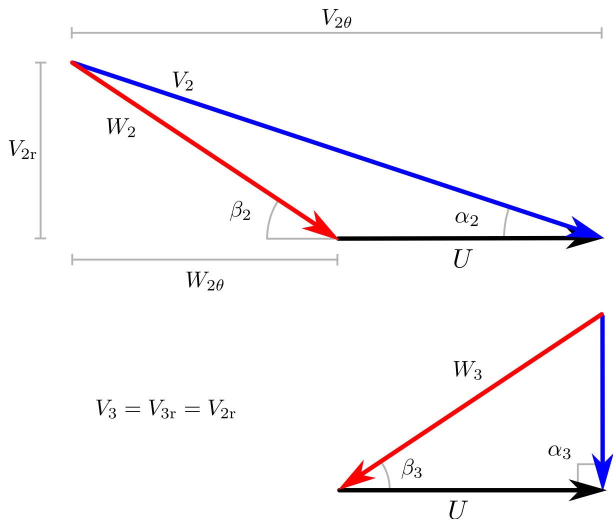

Figure 3.1: Velocity diagrams for design conditions at rotor inlet (subscript 2) and outlet (subscript 3).

3.1 Hypotheses and objectives

The typical one-dimensional velocity diagrams for the biradial rotor in design conditions [61] are shown in Fig. 3.1. Here the subscripts 2 and 3 refer to rotor inlet and outlet respectively, V is the absolute flow velocity (measured in an absolute reference frame), while W is the relative velocity (measured in a reference frame rotating with the rotor blades), α and β are the absolute and relative flow angles, respectively, with respect to the rotor peripheral velocity, $U = \Omega D/2$. The rotor rotational speed Ω is measured in radians per unit time, and D is the turbine rotor diameter.

Biradial rotor geometry and its design conditions were derived assuming inviscid flow and an infinite number of infinitesimally thin blades [61]. Under design conditions, it is desirable to have radial outlet flow (no outflow swirl), $V_{3\theta} = 0$, to minimize kinetic energy losses. As such, it follows that $V_{3r}/U = \tan\beta_3$ and, due to mass conservation, $V_{2r}/U = V_{3r}/U$. Ignoring slip due to the infinite number of blades, it comes $\beta_3 = \beta_3'$, and $\beta_2' = \beta_3'$ since the rotor is symmetric. Assuming minimum incidence losses if the inlet relative flow angle equals the blade metal angle, $\beta_2 = \beta_2'$ (again due to the infinite number of blades), comes $\beta_2 = \beta_3$, $W_2 = W_3$, and $V_{2\theta}/U = 2$ which characterizes an impulse rotor [55].

When the flow rate is changed at constant rotational speed, the rotor inlet and outlet relative flow angles (β_2 and β_3) change accordingly. Experimental testing on a movable-guide-vane (MGV) and on a fixed-guide-vane (FGV) biradial turbine shows that turbine losses are minimum for a flow rate slightly smaller than the established for design conditions [62, 64]. Altough some difference is expected due to the loss component proportional to the square of the flow rate, the experimental results suggest that flow angles different from the ones defined for design conditions in Ref. [62] might lead to higher rotor efficiency.

Publications on radial-inflow turbines show that optimum rotor inlet flow conditions do not occur when the relative flow angle coincides with the blade metal angle at the rotor inlet [75, 76], i.e. $\beta_2 = \beta_2'$. Instead, optimal conditions occur for incidence angles that can reach $\beta_2 - \beta_2' \approx 40°$ [77, 78].

For irrotational and frictionless flow entering an impeller without rotation in the absolute reference frame, the rotation is also zero at the exit in the absolute reference frame [55]. Since the impeller has a rotational speed Ω, the fluid has a rotational speed $-\Omega$ in the relative reference frame, called the counter-rotating relative eddy [55]. The combination of irrotational inlet flow with the relative counter-rotating eddy reduces the relative velocity in the blade pressure side and increases it in the suction side. Subsequently, a static pressure gradient appears in the blade-to-blade passage that deforms the streamlines towards the suction side. This effect was the basis for some of the first theories to predict slip in centrifugal machines [79, 80]. If inlet conditions are such that $\beta_2 = \beta_2'$, flow separation occurs on the pressure surface close to the leading edge.

The first research hypothesis explored in this Chapter is that the mismatch between the flow rate for minimum rotor losses and flow rate in design conditions occurs because the latter were derived under the assumption of an infinite number of infinitesimal thin blades [61]. Meaning that $\beta_3 = \beta_3'$ and $\beta_2 = \beta_2'$ [61] might be approximations with relevant impact on rotor operation. Due to a finite number of thick blades, and because the rotor is biradial, two counter-rotating eddies are expected to form in each rotor blade passage, deforming the relative streamlines, as illustrated in Fig. 3.2. They cause the flow to enter and leave the rotor with directions other than the blade metal angles, which lead to incidence losses and wasted kinetic kinetic energy respectively.

The difference between real flow deflection and hypothetical deflection from an infinite number of blades has been extensively studied for pumps, fans and compressors, and is based on the application of slip-models [55]. As for radial turbines, an incidence correction factor based

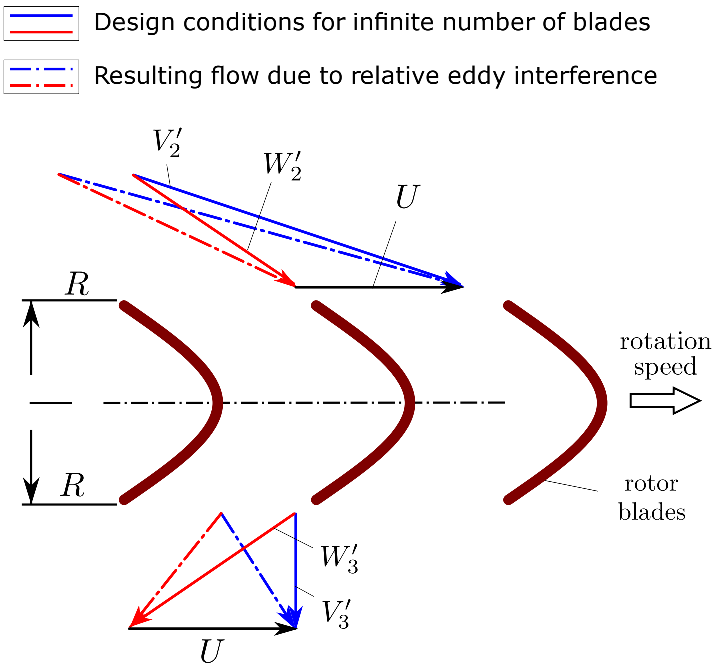

Figure 3.2: Biradial rotor plane cascade with effects of the relative eddies.

on a slip model for compressors has been reported in the literature [81]. Blade loading has also been reported to influence the incidence of radial and mixed flow turbines [82].

The second research hypothesis explored in this Chapter is that improved design operating conditions for biradial rotors can be derived from the application of a slip-factor, in an analogous approach to the literature on radial turbines and compressors.

The objective of this study is thus to increase the aerodynamic efficiency of biradial rotors by improving the prescribed design conditions of rotor geometries generated by the method described in Ref. [61].

3.2 Methods

Performance is assessed with a commercial turbomachine-oriented computational fluid dynamics software (CFD). A MGV biradial turbine with experimental data published [62] is used here as a test-case for verification and validation of the numerical model, and assessment of rotor improvements over turbine operation. The MGV version was used due to a simpler overall geometry (see Chapter 1), but note that improvements on rotor design conditions are valid for both MGV and FGV versions.

The research procedure of this study can be summarized as follows:

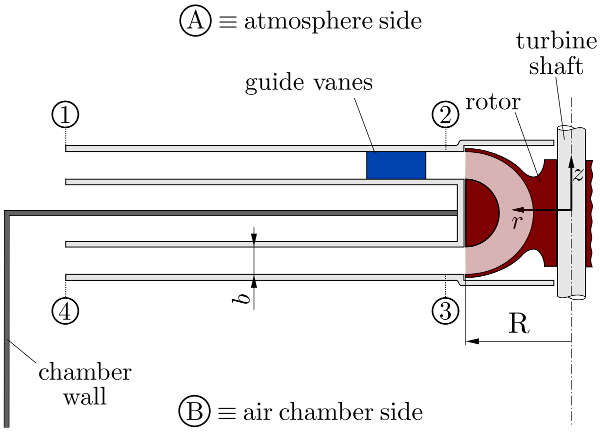

(a) MGV biradial turbine

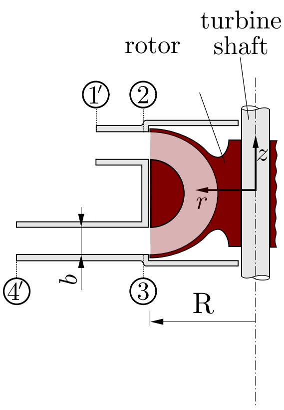

(b) Biradial rotor

Figure 3.3: Schematic representation of the simulation domain under analysis in Chapter 3.

1. simulation of a MGV biradial turbine and comparison between numerical and experimental results to assess the modelling error;
2. application of a slip model to establish conditions for minimum incidence losses at the rotor inlet and minimum kinetic energy at the rotor outlet;
3. representation of improved design conditions in chart format for simple reading;
4. determination of the rotor blade metal angles for the inlet absolute flow angle of the test-case turbine;
5. generation a rotor geometry [61] for the new blade metal angle;
6. comparison between the original and improved design conditions on the original rotor;
7. comparison between the original and improved design conditions on the new rotor;
8. performance comparison between a MGV turbine with the original and with the new rotor.

The two domains used in this Chapter for design, simulation and analysis are illustrated in Fig. 3.3. Here the section labels, k, inside circles refer to inhalation flow.

3.2.1 Improved design conditions

As previously stated, Ref. [81] presents a methodology for the design of radial-inflow turbines with minimum inlet incidence losses. The key aspect of this method is the use of the incidence velocity, $V_{2\mathrm{s}}$, analogous to the slip velocity of a radial compressor, to improve the design conditions. An analogous method was used in the present study, with a fundamental difference: since the rotor is biradial, it is expected to not only have incidence at the inlet but also slip at the rotor outlet. These effects mean that to find the inlet conditions that minimise incidence losses and the kinetic energy at the rotor exit, both incidence, $V_{2\mathrm{s}}$, and slip velocities, $V_{3\mathrm{s}}$, must be considered.

The incidence and slip velocities $V_{2\mathrm{s}}$ and $V_{3\mathrm{s}}$ were calculated using the Unified Slip Model [83] derived for radial, axial and mixed-flow machines. For biradial rotors, these velocities are function of the relative velocity for infinite number of blades W', rotational speed Ω, blade metal angle β', blade curvature, $\mathrm{d}\beta'/\mathrm{d}s$, meridional channel heigh b and its derivative with respect to the meridional mean line $\mathrm{d}b/\mathrm{d}s$, and a shape factor, F, all evaluated at the rotor inlet/outlet section k (Fig. 3.3).

The ratio between the slip velocity and rotor tip speed is defined by the sum of three terms [83],

$$\frac{V_{ks}}{U} = \frac{\pi F}{Z}\left(\sin\beta'_k + \frac{W_k}{2\Omega}\frac{\mathrm{d}\beta'}{\mathrm{d}s}\bigg|_k - \frac{2W_k\sin(2\beta'_k)}{4b\Omega}\frac{\mathrm{d}b}{\mathrm{d}s}\bigg|_k\right). \tag{3.1}$$

The first term reflects the presence of the relative eddy in the blade passage and is the dominant term for radial impellers, the second term quantifies the effect of blade loading, and the third term quantifies the variation of meridional channel height. The following relationships are derived for geometries generated by the method described in Ref. [61] and valid for blade metal angles in the range $55° \geq \beta'_3 \geq 25°$. Other rotor diameters and rotational speeds are applicable, but the remaining parameters should be as described in Ref. [62].

The shape factor

$$F = \frac{\overset{\frown}{DC}}{\overset{\frown}{AB}}, \tag{3.2}$$

is the ratio between the arc-lengths $\overset{\frown}{DC}$ and $\overset{\frown}{AB}$ illustrated in Fig. 3.4. It has the same value at the inlet and outlet due to rotor symmetry and can approximated by the cubic polynomial

$$F = 1.72\times10^{-6}\,{\beta'_3}^3 - 1.73\times10^{-4}\,{\beta'_3}^2 + 5.07\times10^{-3}\,\beta'_3 + 0.603\,, \tag{3.3}$$

with β'_3 expressed in degrees,

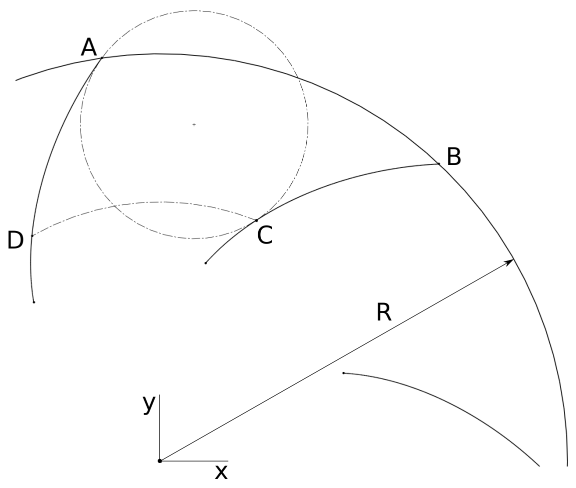

Figure 3.4: Blade mean line projection in the xy plane for a biradial rotor with $\beta' = 40°$, $F = \widehat{DC} \; / \; \widehat{AB}$.

The blade turning can be approximated by the fourth-order polynomial

$$\left.\frac{\mathrm{d}\beta'}{\mathrm{d}s}\right|_3 = -3.17 \times 10^{-6}\,{\beta'_3}^{\,4} + 5.95 \times 10^{-4}\,{\beta'_3}^{\,3} - 4.27 \times 10^{-2}\,{\beta'_3}^{\,2} + 1.45\,\beta'_3 - 2.14 \tag{3.4}$$

for the outlet and

$$\left.\frac{\mathrm{d}\beta'}{\mathrm{d}s}\right|_2 = -\left.\frac{\mathrm{d}\beta'}{\mathrm{d}s}\right|_3, \tag{3.5}$$

for the inlet, with with β'_k expressed in degrees.

The variation in channel width at the outlet can be approximated by the cubic polynomial

$$\left.\frac{\mathrm{d}b}{\mathrm{d}s}\right|_3 = -1.66 \times 10^{-5}\,{\beta'_3}^{\,3} + 2.48 \times 10^{-4}\,{\beta'_3}^{\,2} - 1.28 \times 10^{-3}\,\beta'_3 + 2.12\,, \tag{3.6}$$

while at the inlet it is

$$\left.\frac{\mathrm{d}b}{\mathrm{d}s}\right|_2 = -\left.\frac{\mathrm{d}b}{\mathrm{d}s}\right|_3, \tag{3.7}$$

with β'_3 expressed in degrees.

Following Refs. [55] and [81], the inlet velocity diagram that minimises incidence losses, considering the incidence velocity, is represented by the dashed lines in Fig. 3.5 (top) and the outlet velocity diagram that minimises kinetic energy losses, considering slip, is represented by the dashed lines in Fig. 3.5 (bottom). For both representations (top and bottom), the full lines are the corresponding theoretical velocity diagrams for an infinite number of blades. When the

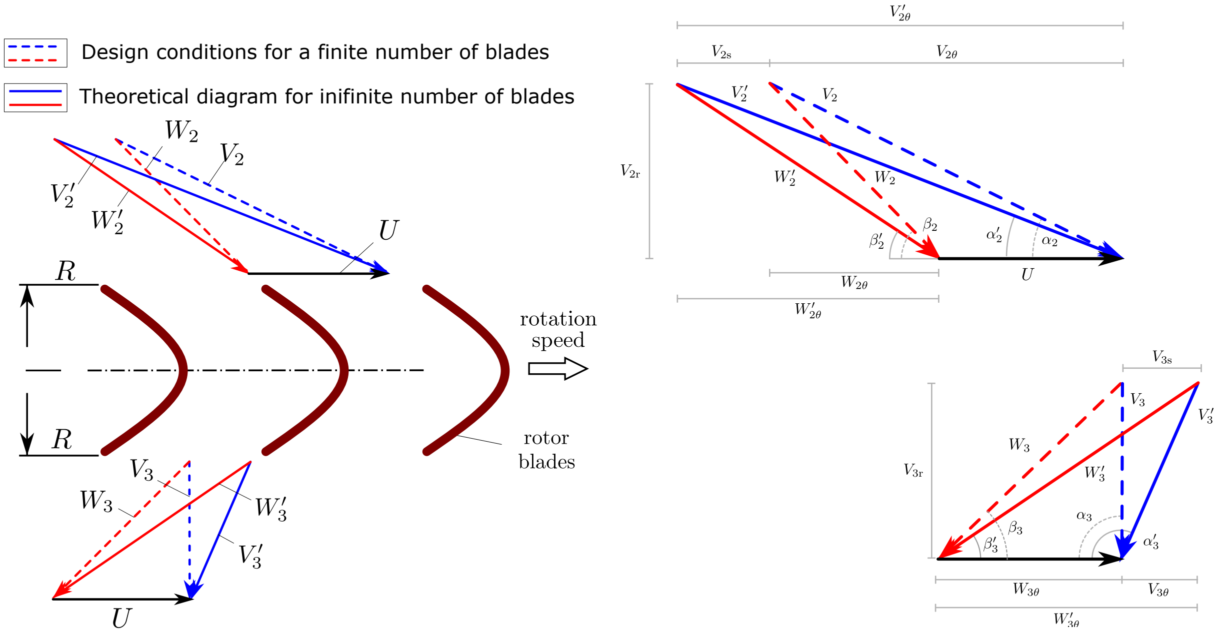

Figure 3.5: Biradial rotor inlet and outlet velocity diagrams for improved design conditions.

inlet dashed triangle is imposed as the inlet condition, inlet relative eddy aligns the relative flow with the blade, minimizing incidence losses. At the outlet, the slip caused by the respective relative eddy removes the negative swirl ($V_{2\theta} \leq 0$) resulting in the outlet outlet dashed triangle for a given blade metal angle. The calculation of the dashed triangles is described as follows.

From the definition of incidence velocity,

$$V_{2\mathrm{s}} = V_{2\theta}' - V_{2\theta} \,, \tag{3.8}$$

it is possible to calculate the inlet relative flow angle, Fig. 3.5 (top),

$$\cot \beta_2 = \cot \beta_2' - \frac{V_{2\mathrm{s}}}{V_{2\mathrm{r}}} \,, \tag{3.9}$$

the inlet absolute flow angle,

$$\cot \alpha_2 = \cot \beta_2 + \frac{U}{V_{2\mathrm{r}}} \,, \tag{3.10}$$

and the inlet tangential velocity,

$$\frac{V_{2\theta}}{U} = \frac{V_{2r}}{U} \cot \alpha_2 \,. \tag{3.11}$$

Noting that $V_{2r}/U = V_{3r}/U$, the inlet radial velocity is calculated from the outlet velocity

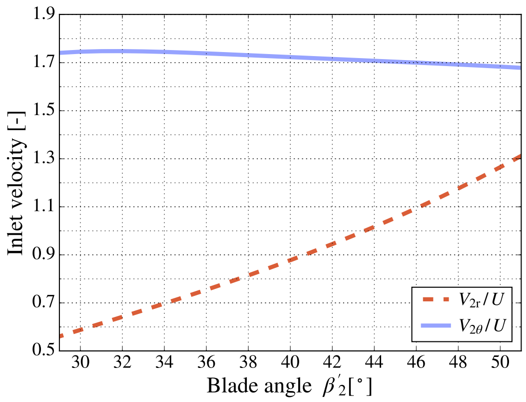

(a) Absolute velocity components V_{2r}/U and $V_{2\theta}/U$ as a function of the rotor blade inlet metal angle β_2'.

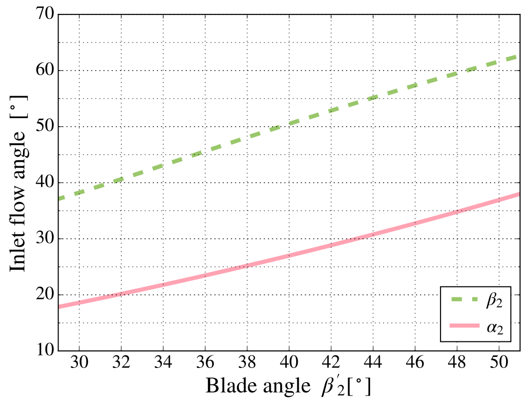

(b) Absolute and relative flow angles α_2 and β_2 as a function of the rotor blade inlet angle β_2'.

Figure 3.6: Leading edge conditions for minimum incidence losses for a biradial rotor.

diagram, Fig. 3.5 (bottom). Introducing the definition of slip velocity,

$$V_{3\mathrm{s}} = V_{3\theta} - V'_{3\theta}\,, \tag{3.12}$$

the outlet radial velocity is given by

$$\frac{V_{3r}}{U} = \frac{\dfrac{V_{3\mathrm{s}}}{U} + 1}{\cot\alpha_3 + \cot\beta_3'}\,, \tag{3.13}$$

where α_3 is a design condition, usually taken as $\alpha_3 = 90°$.

From Eqs. (3.11) and (3.13) it is possible to plot the rotor inlet flow conditions, α_2, β_2, V_{2r}/U and $V_{2\theta}/U$, as a function of the rotor inlet blade metal angle β_2', for minimum incidence losses and outlet kinetic energy ($\alpha_3 = 90°$ in Eq. (3.13)), as shown in Fig. 3.5. It can be immediately concluded that these improved design conditions are not compatible with the design condition $V_{2\theta}/U = 2$ commonly used for axial-flow impulse turbines [55] and previously used with the biradial turbine [61, 62].

3.2.2 Numerical model

The solver used was FINE/Turbo v11.1 from NUMECA International [84]. It is a three-dimensional RANS solver with an explicit time-marching multi-stage Runge-Kutta scheme and a cell centred control volume approach for spatial discretisation. All simulations were performed assuming incompressible flow and steady-state conditions, with a full multi-grid approach and the Choi-Merkle pre-conditioning [85].

In pre-conditioned computations, viscous and inviscid fluxes are determined by central discretization. For the inviscid fluxes, the solver uses a Jameson type artificial dissipation with 2nd and 4th order derivatives of the conservative variables.

Two eddy-viscosity turbulence models were used: the one-equation Spalart-Almaras model with the Spalart-Shur correction for rotation and curvature (SARC) [86]; and the two-equation Shear Stress Transport (SST) $k-\omega$ model [87]. All model constants used are the ones originally presented by their authors. Both models were applied without the use of wall functions, therefore the height of the mesh elements adjacent to the walls ensured $y^+ \leq 1$.

The version 11.1 of FINE/Turbo allows implicit residual smoothing for one equation models and incompressible flow. So, the SARC model can be used to decrease indirectly the number of iterations needed for solution convergence.

The mesh generators used are the IGG and the AutoGrid [88], both from NUMECA International. Two-dimensional structured meshes are generated in the blade-to-blade plane (see Fig. 3.7) and then mapped into the corresponding surfaces of revolution in the three-dimensional space. These surfaces are generated by a set of streamwise lines in the meridional plane (see Fig. 3.8). The inlet velocity components are imposed at the domain entry complying with the desired absolute flow angle α_2. Finally, the stacked blade-to-blade meshes are connected, resulting in a block-structured mesh for the entire three-dimensional domain (see Fig. 3.9). A similar approach is presented in Ref. [89]. The blade-to-blade mesh used in rotor simulations is shown in Fig. 3.10 according to the domain defined in Fig. 3.3b.

The mixing-plane approach was used to model the rotor-stator interface since the guide-vanes and the rotor blades have different periodicities [90]. For simulations considering only the rotor, no interface is needed, and the equations are solved in the relative frame of reference. The inlet velocity components are imposed at the domain entry complying with the desired absolute flow angle α_2.

A uniform distribution of the absolute velocity vector was assumed as inlet boundary condition. For simulations of the complete turbine, only the radial component of the velocity was imposed, while for rotor simulations both radial and tangential components were imposed. In the

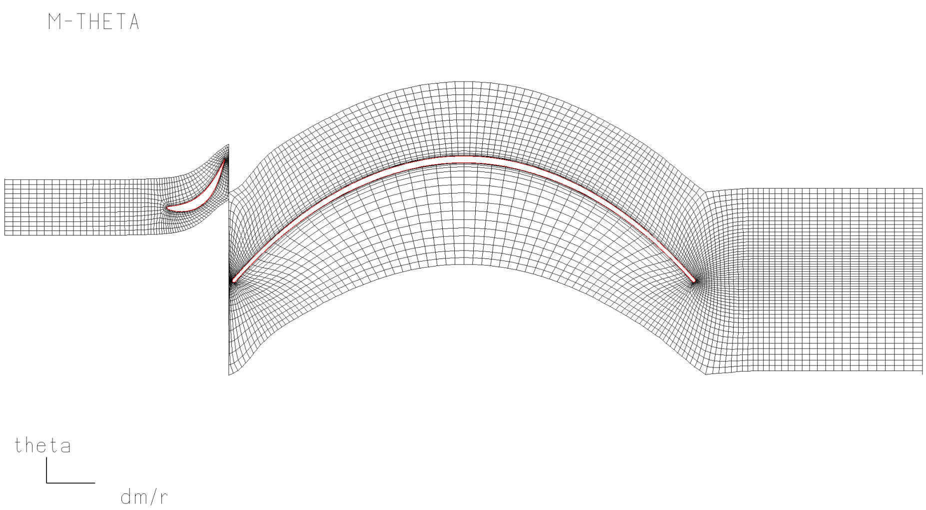

Figure 3.7: Blade-to-blade mesh for a MGV biradial turbine (Fig. 3.3a).

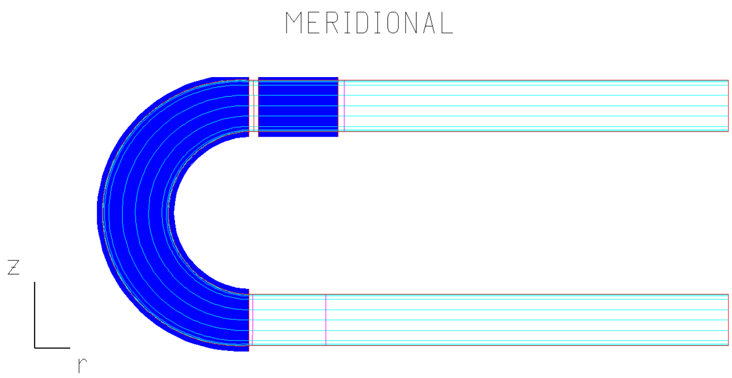

Figure 3.8: Meridional lines used for meshing a MGV biradial turbine (Fig. 3.3a).

second case, boundary conditions were calculated from the design conditions of Refs. [61, 62] or from the results of the slip/incidence model. The inlet turbulence quantities used were uniform distributions of turbulent viscosity ratio, $\nu_t/\nu = 5$, for SARC and SST models, and also turbulent intensity $T_\mathrm{u} = 0.05$ for the SST. The outlet boundary condition of uniform distribution of static pressure was imposed at a constant radius domain exit section. All walls were simulated as impermeable, and the shear stress at the wall determined directly from its definition (no wall functions).

The initial solution was a constant rothalpy distribution, along axisymmetric stream surfaces, extrapolated from the inlet conditions.

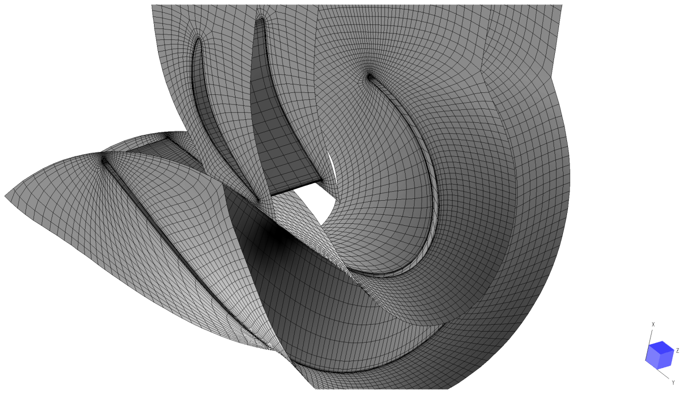

Figure 3.9: Three dimensional mesh (solid boundaries) of a MGV biradial turbine (Fig. 3.3a).

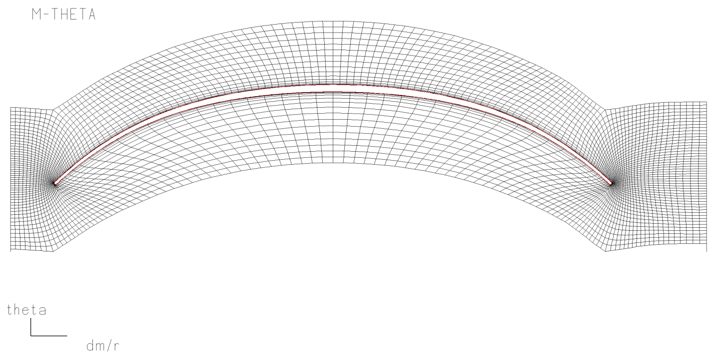

Figure 3.10: A blade-to-blade mesh for rotor flow simulations (Fig. 3.3b).

3.2.3 Performance metrics

The metrics derived for this Chapter are presented considering turbine inflow conditions, that is, from atmosphere to OWC chamber. Yet, the performance of biradial turbines is independent of the flow direction, as such, the results obtained are also valid for outflow conditions.

Section data such as the averaged flow velocity components in the radial and circumferential directions, $\bar{V}_{r_k}$ and $\bar{V}_{\theta_k}$, the flow rate Q, the averaged stagnation pressure $\bar{p}_{0_k}$, the averaged pressure $\bar{p}_k$, the kinetic energy flux per unit of volume E_k and its radial, E_{r_k}, and circumferential, E_{r_k} components at a section k, are calculated according to

$$\left\{\bar{V}_{r_k}, \bar{V}_{\theta_k}, \bar{p}_k, \bar{p}_{0_k}, E_k, E_{\mathrm{r}_k}, E_{\theta_k}\right\} = \frac{1}{Q}\int_{A_k} \left\{V_r, V_\theta, p, (p + \tfrac{1}{2}\rho V^2), \tfrac{1}{2}\rho V^2, \tfrac{1}{2}\rho V_{\mathrm{r}}^2, \tfrac{1}{2}\rho V_\theta^2\right\} |\mathbf{V}\cdot\mathbf{n}|\,\mathrm{d}A\ . \tag{3.14}$$

where ρ, p, $\mathbf{V}$, $\mathbf{n}$, and A_k are air density, pressure, absolute velocity, and outer normal vector and surface area of section k, respectively.

The averaged angle of the absolute flow with the circumferential direction is

$$\tan \bar{\alpha}_k = \frac{\bar{V}_{r_k}}{\bar{V}_{\theta_k}} \,, \tag{3.15}$$

while the averaged angle of the relative flow with the circumferential direction is

$$\tan \bar{\beta}_k = \frac{\bar{V}_{r_k}}{\bar{W}_{\theta_k}} = \frac{\bar{W}_{r_k}}{\bar{W}_{\theta_k}} \,. \tag{3.16}$$

The radial velocity component is used here because the directions of the normal vectors of sections (k, l) are purely radial. Otherwise the meridional velocity, $W_\mathsf{m} = \sqrt{W_\mathsf{r}^2 + W_\theta^2}$ would have been used in Eqs. (3.14), and the respective average in Eq. (3.15) and (3.16).

Consider a sector to be the part of the turbine geometry comprehended between two sections (k, l) with l downstream of k.

The stagnation pressure drop across a turbine sector is evaluated with the pressure coefficient,

$$\Psi_{k,l} = \frac{\bar{p}_{0_\mathsf{k}} - \bar{p}_{0_\mathsf{l}}}{\rho_1 \, \Omega^2 D^2} \,, \tag{3.17}$$

where Ω and D, are the rotational speed and rotor diameter, respectively.

The stagnation pressure loss coefficient, $\lambda_{k,l}$, is used to assess losses and compare them between two geometries, e.g. between two diffusers or two rotors. It can also used to assess multiple components simultaneously, e.g. $\lambda_{2,4}$ quantifies all the losses across both the rotor and diffuser. The stagnation pressure loss coefficient, $\lambda_{k,l}$, is derived from the pressure coefficient, $\Psi_{k,l}$. In this Chapter it is

$$\lambda_{k,l} = \Psi_{k,l} \tag{3.18}$$

for any turbine sector that does not contain the rotor, otherwise it is

$$\lambda_{k,l} = \Psi_{k,l} - \frac{\Pi}{\Phi} \,, \tag{3.19}$$

where

$$\Phi = \frac{Q}{\Omega \, D^3} \tag{3.20}$$

is the flow rate coefficient and

$$\Pi = \frac{T}{\rho_1\, \Omega^2 D^5} \tag{3.21}$$

is the torque (or power) coefficient. This is because part of the stagnation pressure drop across the rotor is converted into mechanical energy and is not a loss. Torque, T, is calculated from the change in flow angular momentum experienced between the rotor inlet and outlet, $(k, l) = (2, 3)$,

$$T = \int_{s_2} \rho r V_\theta \left|\mathbf{V} \cdot \mathbf{n}\right| \mathrm{d}s - \int_{s_3} \rho r V_\theta \left|\mathbf{V} \cdot \mathbf{n}\right| \mathrm{d}s\,. \tag{3.22}$$

Note that V_θ can be either positive or negative. The convention used in this dissertation is $V_\theta > 0$ when $\mathbf{V}_\theta$ and $\mathbf{U}$ have the same direction.

It is useful to define a kinetic energy flux coefficient across a section k,

$$\{K_k, K_{\mathsf{r}_k}, K_{\mathsf{t}_k}\} = \frac{1}{\rho_1\, \Omega^2\, D^2} \{E_k, E_{\mathsf{r}_k}, E_{\mathsf{t}_k}\}\ , \tag{3.23}$$

where $K_{\mathsf{r}_k}, K_{\mathsf{t}_k}$ refer to the radial and circumferential components of the kinetic energy flux coefficient K_k, respectively, in order to define the efficiency metrics.

The total-to-total efficiency,

$$\eta_{\mathsf{tt}_{k,l}} = \frac{\Pi}{\Phi \Psi_{k,l}}\,, \tag{3.24}$$

and the total-to-static efficiency,

$$\eta_{\mathsf{ts}_{k,l}} = \frac{\Pi}{\Phi(\Psi_{k,l} + K_l)}\,, \tag{3.25}$$

are applicable to rotors or turbine sectors (k, l) containing the rotor, e.g. a set comprising the rotor and diffuser, $\eta_{\mathsf{ts}_{2,4}}$. The difference between these two metrics is how the kinetic energy flux in section l is accounted. In the total-to-static efficiency, it is considered a loss while for the total-to-total efficiency it is not.

The efficiency definitions in Eqs. (3.24) and (3.25) can alternatively be expressed as function of the stagnation pressure loss coefficient $\lambda_{k,l}$. For the total-to-total efficiency it is

$$\eta_{\mathsf{tt}_{k,l}} = \frac{1}{1 + \dfrac{\Phi \lambda_{k,l}}{\Pi}}\,, \tag{3.26}$$

while for the total-to-static efficiency is

$$\eta_{\mathsf{ts}_{k,l}} = \frac{1}{1 + \dfrac{\Phi(\lambda_{k,l} + K_l)}{\Pi}} . \tag{3.27}$$

In OWC devices, the turbine outflow kinetic energy is lost. As such, from Eq. (3.17) and Eq. (3.23), comes the turbine available pressure head in dimensionless form. Defined here as the turbine total-to-static pressure coefficient,

$$\Psi_{\mathsf{ts}} = \Psi_{1,4} + K_4 . \tag{3.28}$$

And from Eq. (3.25), it becomes evident that the turbine efficiency operating in an OWC device is

$$\eta_{\mathsf{ts}} = \frac{\Pi}{\Phi\Psi_{\mathsf{ts}}} . \tag{3.29}$$

Sector losses and turbine outlet kinetic energy losses can also be quantified with respect to the available turbine pressure head using the relative stagnation pressure loss coefficient,

$$\Lambda_{k,l} = \frac{\lambda_{k,l}}{\Psi_{1,4} + K_4} \tag{3.30}$$

and

$$\Lambda_{4B} = \frac{K_4}{\Psi_{1,4} + K_4} , \tag{3.31}$$

respectively. For the complete turbine, it is deduced that

$$\sum_{k=1}^{4} \Lambda_{k,k+1} + \Lambda_{\mathsf{4,B}} + \eta_{\mathsf{ts}} = 1. \tag{3.32}$$

3.3 Results

A parallelized version of the CFD solver with Message Passing Interface was used in a Linux machine equipped with two Intel® Xeon® CPU E5-2609 v3 @ 1.90GHz with a total of 12 physical cores and 32 Gb of DDR4 RAM.

3.3.1 Numerical model assessment

Before any assessment to changes in rotor blade angles or the inlet flow conditions, the modelling error of the turbine total-to-static efficiency defined in Eq. (3.25) was evaluated.

The turbine model Reynolds number is Re $= \Omega D^2/\nu = 1.3\times10^6$, where ν is the air kinematic viscosity and $D = 0.488$ m is the rotor diameter. The rotor channel entry height is $b = 0.11D$ and the inlet and outlet ducts have outer diameter $D_1 = D_4 = 1.5$ m ($D_1/D = 3.074$). The guide-vane set comprises 23 stator blades that deflect the flow from the radial direction $\alpha_1 = 90°$ to $\alpha_2 = 22.8°$. The rotor has $Z = 7$ constant thickness blades, $t_\mathrm{m} = 0.007$ m, with blade metal angles of $\beta_3' = 40°$.

The first set of simulations were performed to determine the numerical parameters that most influence the solution convergence to minimise the iterative error. Mesh refinement levels were chosen by balancing the capabilities of available hardware, computational time and discretisation uncertainty. The aerodynamic analysis presented in the following sections was performed with a mesh of about 1.2 million elements, named G3, and the finest one, used for the discretisation uncertainty calculation, has 2.5 million elements, named G1. As will be seen later in this section, this mesh refinement leads to a numerical uncertainty similar to the uncertainty of the experimental results used to assess the modelling errors.

For all meshes, 20% of the cells are on the inlet block (computational domain inlet to the rotor-stator interface) and 80% on the rotor and diffuser blocks (from the rotor-stator interface to turbine outlet). The minimum mesh skewness is 26°, while 87% of cells have between 72 and 90°. The maximum spanwise angular deviation is 46°. The maximum aspect ratio is 10000, while 98% of cells have it below 1000. The maximum expansion ratio is 3.2, and 97% of cells exhibit expansion ratios between 1 and 1.8. The mesh cell aspect ratio near the turbine outlet has a significant influence on the solution iterative convergence. For cells adjacent to solid walls, the maximum cell height is 10^{-6} m on the finest mesh region, to guarantee $y^+ \leq 1$ for all tested flow rates on the coarser meshes.

The implemented pre-conditioning scheme for low Mach number flows is user controlled with the specification of the reference velocity, V_ref, and a limiter for the particle velocity, k_{v_p}, based on the local pressure. The values used are $V_\mathrm{ref} = U$ and $k_{v_p} = 0.1$.

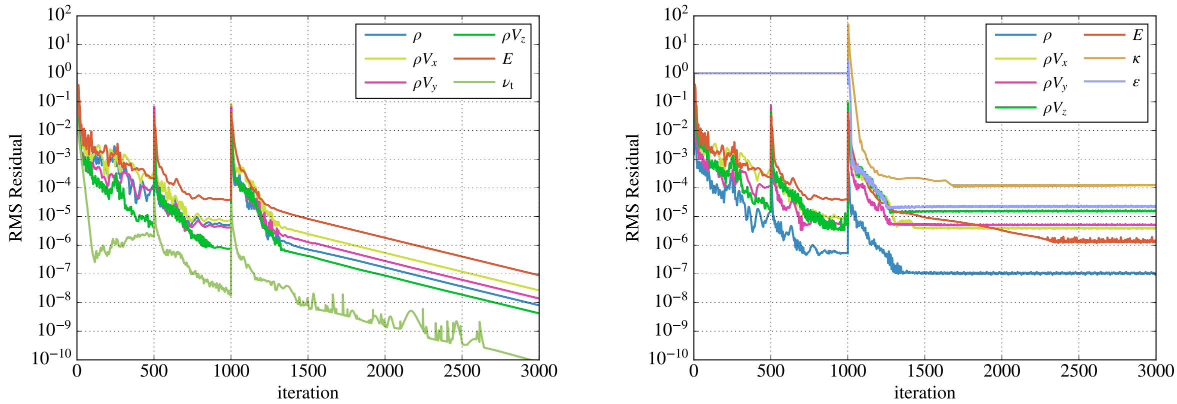

(a) SARC. (b) SST.

Figure 3.11: Iterative convergence with two eddy-viscosity models.

While time per iteration and random access memory usage was approximately the same for SARC and SST models, the SARC model was more robust, giving lower residuals than the SST model. As shown in Fig. 3.11, both models reached the reference value of 10^{-4} for all residuals.

For all simulations, iterative convergence was obtained for rotor torque and stagnation pressure head. The maximum accepted mass-flow imbalance between domain inlet and outlet was 0.5%.

The turbine total-to-static efficiency, η_{ts} at design conditions, $\Phi = 0.146$ was used to monitor convergence and to estimate the iterative uncertainty following the method described in Appendix A (Fig. 3.12). A set of six intermediate solutions, η_{ts_i}, at iteration i (Fig. 3.12a) and the corresponding residuals of the x-momentum equation (ρV_x) at iteration i (Fig. 3.11), were used to perform the least-squares fit of Eq. (A.4). Then Eq. (A.3) was used to estimate the iterative uncertainty, ξ_{itr} (Fig. 3.12b). Note that each intermediate solution corresponds to residual levels when the solution is converging. For the SARC model it corresponds to $i > 1300$, but to the SST model it is limited to $1070 < i < 1270$ due to the stagnation of the residuals.

Fig. 3.13 shows the experimental results of Ref. [62] and the numerical results obtained by the described numerical method for the two selected turbulence models. Notably, experimental results show peak efficiency well below the design flow rate of $\Phi = 0.146$. The most significant differences between the two are in the values of the maximum efficiency and the values of flow coefficient for maximum efficiency. Also, the numerical and experimental results cross for $\Phi =$

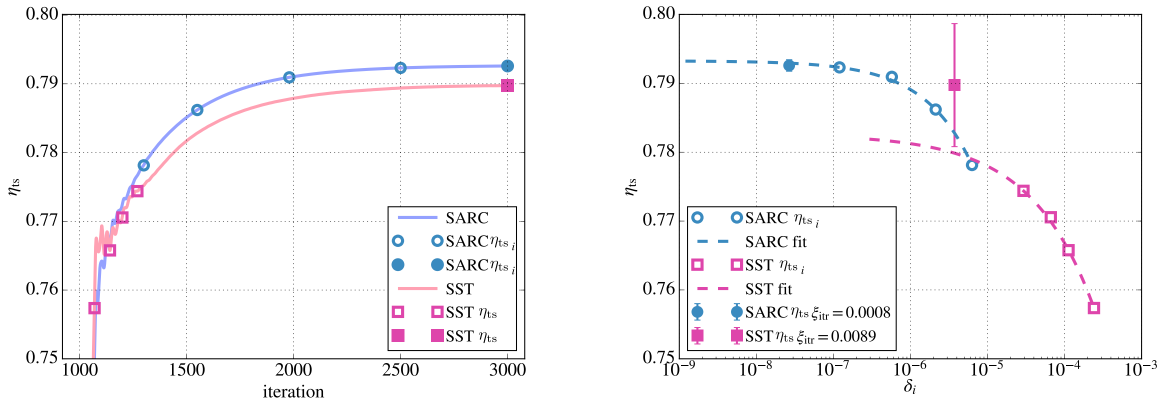

(a) Iterative convergence. (b) Iterative uncertainty.

Figure 3.12: Iterative convergence and uncertainty of the total-to-static efficiency for the turbine with $\beta_3' = 40°$.

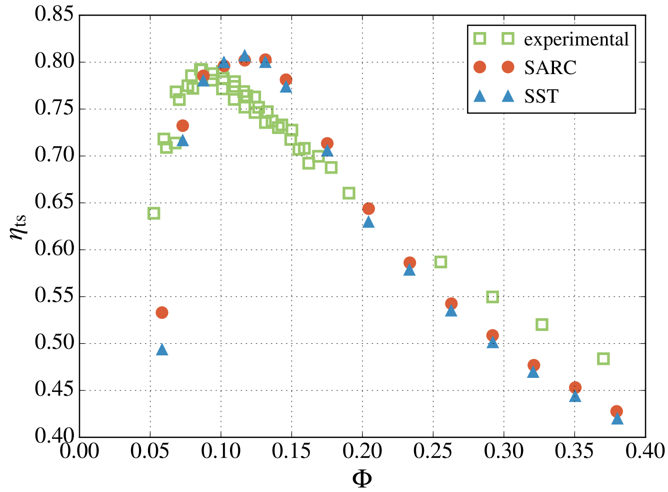

Figure 3.13: Comparison between numerical and experimental results [62] for the MVG biradial turbine: total-to-static efficiency versus flow rate coefficient.

0.2, being the experimental efficiency higher than the numerical one for $\Phi > 0.2$. This result is in agreement with the results presented in Ref. [62]. Several aerodynamic and mechanical effects might justify the differences observed, but quantification is outside the scope of the current Chapter. Inaccurate shaft bearings resistive torque calculation, in the experimental model, has a significant impact on the efficiency values at low flow coefficients [62]. Furthermore, disc friction losses (windage) and rotor flow recirculation at off-design conditions, due to non-zero reaction conditions [55, 81], were not considered in the numerical simulations.

Considering the scope of the present study, for the given geometry and settings, SARC and SST models provided identical results, but the iterative uncertainty is $\xi_{\text{itr}} = 0.0008$ for SARC, which is lower than that for SST, $\xi_{\text{itr}} = 0.0089$ (Fig. 3.12b).

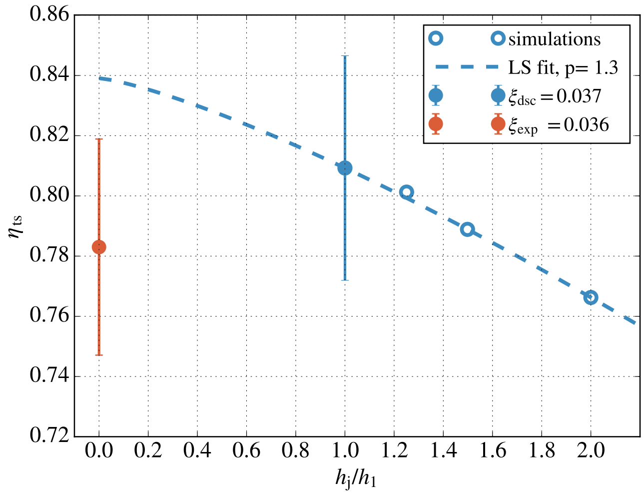

Figure 3.14: Grid refinement study of the complete turbine with $\beta_3' = 40°$.

The solver can use implicit residual smoothing to increase the Courant-Friedrichs-Lewy (CFL) number up to 1000 with one-equation turbulence models. As such, the calculation of the efficiency curve with the SARC model was significantly faster compared to the one with the SST model. The first point was calculated in design conditions and took around 3.5 hours to converge for both models. The remaining points of the SARC curve converged in 0.7 hours and 300 iterations with implicit residual smothing and using the first point as initial condition. The remaining points of the SST curve converged in 1.9 hours, also using the first point as initial condition.

Since it provided a lower iterative error and a faster convergence rate, the SARC model was used to obtain the results presented in the rest of this study.

A set of four geometrically similar meshes were created to estimate the discretisation uncertainty following the procedure described in Appendix A. The resulting discretization uncertainty $\xi_{\text{dsc}} = 0.037$ has an order of grid convergence of 1.3 and is illustrated in Fig. 3.14. The numerically calculated efficiency tends to increase with grid refinement, as also seen in this figure.

The numerical uncertainty (Appendix A) is $\xi_{\text{num}} = 0.038$, while the experimental uncertainty is $\xi_{\text{exp}} = 0.036$ [62]. Both values were taken from the best efficiency points, due to the discrepancy in design flow rate coefficients. As such, the peak total-to-static efficiency comparison error $\epsilon_{\text{cmp}} = 0.026$ with an associated validation uncertainty of $\xi_{\text{val}} = 0.052$ results in a modelling error between $0.078 \geq \epsilon_{\phi} \geq -0.026$, according to Eqs. (A.9) to (A.11).

The choice of grid refinement was a compromise between the computational cost and the resulting modelling error, ϵ_ϕ. The numerical uncertainty, ξ_{num}, can only be reduced so far before the modelling error, ϵ_ϕ, and validation uncertainty, ξ_{val}, become dominated by the experimental uncertainty, ξ_{num}, and comparison error, ϵ_{cmp} (Appendix A). Reducing the discretization uncertainty in 30%, while keeping all other results, would the decrease the validation uncertainty in 14%. Therefore, the additional cost to decrease the numerical uncertainty are justified if experimental results with lower experimental uncertainty are available.

3.3.2 Rotor performance

With the baseline case and the numerical parameters established, a set of simulations was made to assess the suitability of the Unified Slip Model as an incidence model and to assess the influence of the inlet flow angle on the rotor performance. The solver parameters used in rotor and turbine simulations were the same.

The inlet stator and its guide vanes were removed, and a short diffuser was added (see Figs. 3.3b and 3.10). The domain inlet and outlet are cylindrical surfaces with radius $r_{1'}/D = 0.666$ and $r_{4'}/D = 0.922$, respectively. There is no rotor-stator interface as the RANS equations were solved entirely in the rotating frame of reference. The inlet velocity components are imposed at the domain entry complying with the desired absolute flow angle α_2.

Fig. 3.15a shows the relative velocity vectors near the leading edge for the baseline rotor, which has the blade metal angle $\beta_3' = 40°$, for the following inlet conditions: $V_{2r}/U = 0.84$ and $V_{2\theta}/U = 2$. This plot represents the dimensionless spanwise coordinate 0.5 (0 at the hub and 1 at the shroud). Fig. 3.15a clearly shows the misalignment between the flow field and the blade inlet, and the flow separation on the suction side. This observation confirms the theoretical prediction depicted in Fig. 3.2.

Fig. 3.15b shows the relative velocity vectors for the same rotor, but with the inlet flow conditions changed to $V_{2r}/U = 0.88$ and $V_{2\theta}/U = 1.72$, in agreement with the incidence/slip model results plotted in Fig. 3.6. It is seen that the relative flow is now aligned with the blade inlet, the stagnation point is located on the leading edge, and there is no significant flow separation. This observation confirms the theoretical prediction depicted in Fig. 3.5.

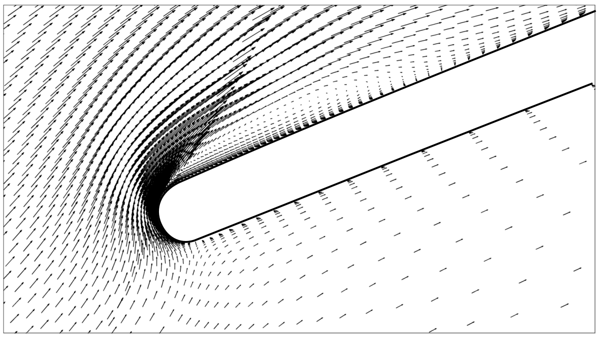

(a) $\beta_3' = 40°$, $V_{2r}/U = 0.85$ and $V_{2\theta}/U = 2$ [61].

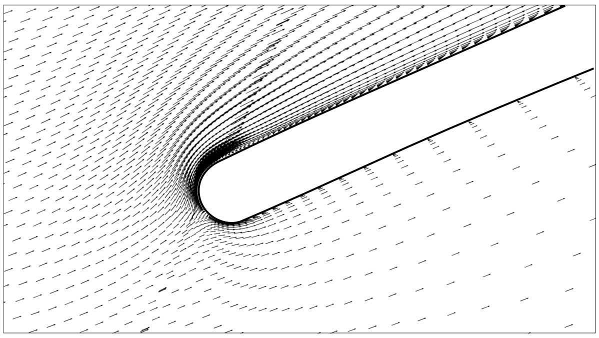

(b) $\beta_3' = 40°$, $V_{2r}/U = 0.89$ and $V_{2\theta}/U = 1.72$ (Fig. 3.6).

Figure 3.15: Rotor relative velocity vectors near the leading edge, at design conditions.

Table 3.1: Biradial rotor with $\beta_3' = 40°$ relative and absolute outlet flow angles.

$\beta_3'[°]$	Φ	$V_{2\theta}/U$	V_{2r}/U	$\beta_3[°]$	$\alpha_3[°]$
40	0.146	1.87	0.85	41.1	87.7
40	0.153	1.65	0.89	41.5	90.0

The results of Table 3.1 show that the chart on Fig. 3.6 effectively predicts the radial velocity V_{3r}/U considering the effects of slip in order to have radial outlet flow, $\alpha_3 = 90°$. These results also confirm the the theoretical prediction shown in Figs. 3.2 and 3.5. Note that the tangential velocity values, $V_{2\theta}/U$, in Table 3.1 are slightly different from the values taken from Fig. 3.6. This because the figure values were imposed at the computational domain inlet and there is viscous interaction between the flow and nozzle walls upstream of the rotor inlet.

From the results seen so far, the Unified Slip Model [83] can be effectively used as an incidence and slip model for biradial rotors. Yet, the chart on Fig. 3.6 should be used with care, as a different geometric parametrization might result in a different incidence/slip velocities V_{k_s}.

Besides the rotor with $\beta_3' = 40°$, two additional geometries with metal blade angles of $\beta_3' = 35°$ and $\beta_3' = 45°$ were analysed to assess the effects of the improved design conditions over rotor performance. The rotor $\beta_3' = 35°$ with improved design conditions and the rotor $\beta_3' = 40°$ with original design conditions share the same inlet absolute flow angle, α_2. Likewise, the same inlet absolute flow angle, α_2 is shared by the rotor $\beta_3' = 40°$ with improved design conditions and the rotor $\beta_3' = 45°$ with original design conditions.

The numerical results for the flow through the three rotors are summarised in Table 3.2. Again, the tangential velocity values, $V_{2\theta}/U$ are slightly different from the values taken from Fig. 3.6 because the nozzle walls upstream of the rotor inlet influence the flow direction.

Table 3.2: Rotor performance comparison.

$\beta'_3[°]$	$V_{2\theta}/U$	V_{2r}/U	$\alpha_2[°]$	$\alpha_3[°]$	Π/Φ	$\Psi_{\mathrm{tt}_{2-3}}$	λ_{2-3}	$\eta_{\mathrm{tt}_{2-3}}$	K_3	$\eta_{\mathrm{ts}_{2-3}}$	$\Psi_{\mathrm{tt}_{2-4'}}$	$\lambda_{3-4'}$	$\eta_{\mathrm{tt}_{2-4'}}$	$K_{4'}$	$\eta_{\mathrm{ts}_{2-4'}}$
35	1.89	0.71	20.6	87.3	0.474	0.545	0.071	0.869	0.095	0.738	0.567	0.022	0.836	0.022	0.804
35	1.68	0.74	23.6	89.5	0.421	0.484	0.063	0.870	0.092	0.728	0.501	0.017	0.840	0.028	0.796
40	1.87	0.85	24.3	87.7	0.475	0.543	0.069	0.874	0.124	0.709	0.566	0.022	0.839	0.032	0.794
40	1.65	0.89	28.2	90.0	0.422	0.483	0.061	0.873	0.126	0.690	0.502	0.019	0.840	0.043	0.775
45	1.90	1.01	28.1	88.0	0.479	0.546	0.067	0.877	0.163	0.674	0.569	0.023	0.842	0.045	0.781
45	1.65	1.07	32.9	90.0	0.423	0.486	0.062	0.872	0.176	0.636	0.508	0.023	0.833	0.069	0.734

When the inlet conditions are changed from the original to the improved ones, both the loss coefficient $\lambda_{2,3}$ and the energy coefficient Π/Φ decrease. The rotor loss coefficient $\lambda_{2,3}$ varies mainly as a result of smaller flow incidence at the rotor inlet (see Figs. 3.15a and 3.15b) despite having higher skin friction losses due to higher flowrate (compare V_{2r}/U). Π/Φ decreases due to lower inlet tangential velocity component as calculated by Eqs. (3.21) and (3.22) and higher flow rate as a result of Eq. (3.13). The rotor total-to-total efficiency is a balance between the losses, power and flow rate coefficients as in Eq. (3.26). The results show no significant changes to the total-to-total efficiency for rotors with $\beta'_3 = 35°$ and $\beta'_3 = 40°$ because the decrease of $\lambda_{2,3}$ was compensated by the decrease of Π/Φ. For the rotor with $\beta'_3 = 45°$, the variation of energy coefficient Π/Φ is larger, resulting in lower total-to-total efficiency, $\eta_{\mathrm{tt}_{2,3}}$.

The variation of the rotor total-to-static efficiency, $\eta_{\mathrm{ts}_{2,3}}$, is also dominated by the variation of energy coefficient, Π/Φ. For $\beta'_3 = 35°$, despite the decrease in both rotor losses, $\lambda_{2,3}$, and outlet kinetic energy, K_3, the energy coefficient decreases more than the two combined. These effects result in lower total-to-static-efficiency with improved design conditions. For $\beta'_3 = 40°$ and $\beta'_3 = 45°$ the total-to-static efficiency reduction is even larger due to the outlet kinetic energy increase.

Considering the rotor and the short diffuser $(k, l) = (2, 4')$, the improved conditions increase the total-to-total efficiency for $\beta'_3 = 35°$, but do not significantly change it for $\beta'_3 = 40°$ and decrease it for $\beta'_3 = 45°$. In the three cases, not only the rotor losses are smaller, but also the diffuser losses, $\lambda_{3,4}$, are smaller or similar. These results mean that the reduction of losses was only dominant over the reduction of the energy coefficient, Π/Φ for the rotor with $\beta'_3 = 35°$. For the three rotors, the domain outlet kinetic energy, $K_{4'}$, increased, which leads to a reduction of the total-to-static efficiency.

The discussion so far points to a lack of efficiency gains from changing the original design conditions to the improved ones for a given rotor blade metal angle β'_3. This is because increasing the inlet absolute flow angle α_2 reduces the power coefficient Π/Φ which dominates any reduction of incidence and kinetic energy losses. Yet, from Table 3.2 it is seen that for a given inlet absolute flow angle α_2, the rotors with improved design conditions have a higher total-to-static efficiency $\eta_{\text{ts}_{2,3}}$. This is mainly due to lower outlet kinetic energy K_3.

A final observation from the results of Table 3.2, is that decreasing the blade metal angle β_3' has a negligible effect on the total-to-total efficiency but a significant one over the total-to-static efficiency, for both $(k,l) = (2,3)$ and $(k,l) = (2,4')$. This is in agreement with the velocity diagrams plotted in Fig. 3.5. There, it can be seen that lower values of β_3' correspond to lower rotor inlet/outlet radial velocities which have a direct impact on the kinetic energy flux, Eq. (3.23) and the total-to-static efficiency, Eq. (3.27). Low rotor outlet kinetic energy favours diffuser performance, which is observable in the decrease in the ratio $K_{4'}/K_3$. The dependency of the total-to-static pressure on the blade metal angle is explored in Chapter 4.

This study started under the assumption that for a given blade metal angle β_3', a new absolute inlet flow angle α_2 would be found to increase the rotor efficiency. But the results of this Chapter show that the improved design conditions should rather be used to determine a new rotor blade metal angle β_3' for a given absolute inlet flow angle α_2. A practical application of this result is that in order to increase the efficiency of an existing turbine at its design point, it is not the guide-vanes that should be replaced to comply with the improved design conditions, but rather the rotor.

3.3.3 Turbine performance

The rotors with blade metal angles $\beta_3' = 40°$ and $\beta_3' = 35°$ were assembled with the inlet stator, guide-vanes and diffuser of the reference MGV turbine [62] to assess the influence of the inlet design conditions on turbine efficiency. When coupled with the existing guide-vanes, the rotor with $\beta_3' = 40°$, operates with the original design conditions, $V_{2\theta}/U = 2$ and $V_{2r}/U = 0.84$, at $\Phi = 0.146$, while the rotor with $\beta_3' = 35°$ operates with the improved design conditions, $V_{2\theta}/U = 1.72$ and $V_{2r}/U = 0.88$, at $\Phi = 0.126$.

The pressure head coefficient, Ψ_{ts}, power coefficient, Π, and the total-to-static efficiency, η_{ts}, are plotted as a function of the flow rate coefficient, Φ, for the two turbines in Fig. 3.16 and

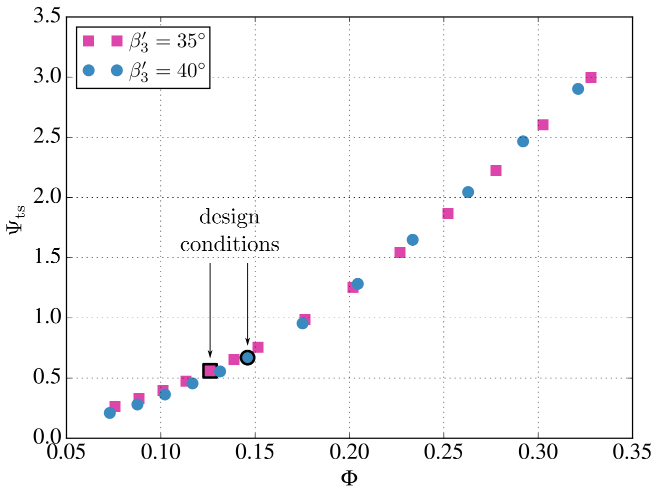

Figure 3.16: Pressure head coefficient as function of flow coefficient.

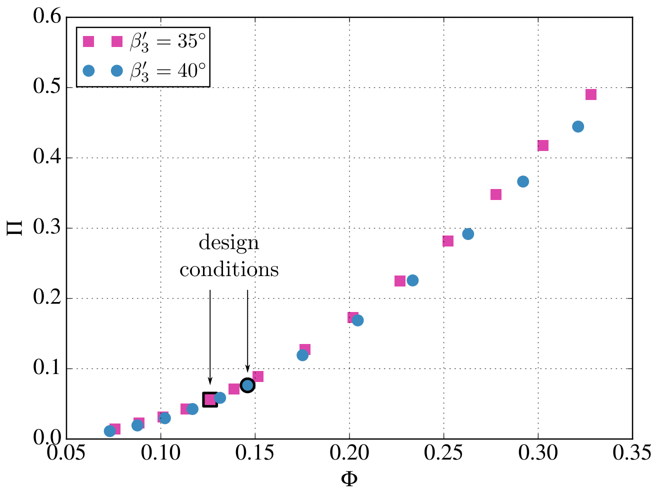

Figure 3.17: Power coefficient as function of flow coefficient.

Fig. 3.17, and Fig. 3.18 respectively.

The turbine equipped with the rotor of $\beta_3' = 35°$, operating at its design flow rate, $\Phi = 0.126$, has slightly higher efficiency, $\eta_{\text{ts}} = 0.793$, than the turbine equipped with a rotor of $\beta_3' = 40°$, at its design flow rate, $\Phi = 0.146$, for which $\eta_{\text{ts}} = 0.781$. This is in line with the results presented so far.

More significant differences are observed at higher flow rate coefficients. For values of flow coefficient $\Phi > 0.160$, the rotor with $\beta_3' = 35°$ provides a higher turbine total-to-static efficiency compared to the original rotor. To understand this behaviour, the losses in each turbine sector relative to the overall available pressure head, $\Lambda_{k,l}$, were analysed. These losses are plotted as a function of the flow rate coefficient in Fig. 3.19 where the design points of each turbine are

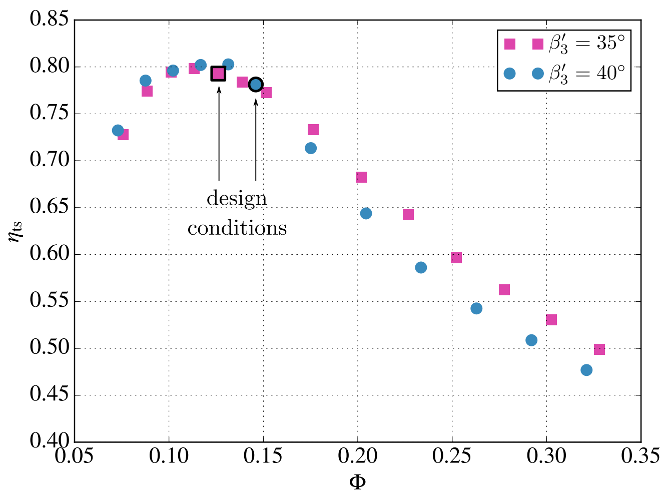

Figure 3.18: Total-to-static efficiency as function of flow rate coefficient.

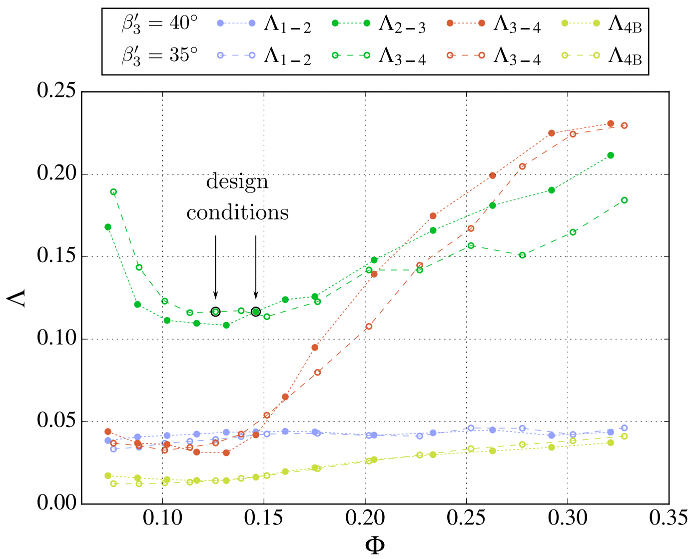

Figure 3.19: Losses distribution for a MGV biradial turbine equipped with rotors with $\beta_3' = 40°$ and $\beta_3' = 35°$

marked with a black contour.

For both turbines and across all operational points, inlet stator losses, and exit kinetic energy losses are small. The two rotors have similar losses at their design points, which is in agreement with the results of Table 3.2, but are different outside design conditions. For low flow rate coefficients, $0.08 < \Phi < 0.14$, differences in turbine losses are mainly caused by the rotor incidence losses, as losses in the remaining sectors are similar. The rotor with $\beta_3' = 35°$ has a larger flow separation near the leading edge when compared to rotor with $\beta_3' = 40°$, as seen in Fig. 3.20. These figures show the plots of the relative velocity vectors near the leading

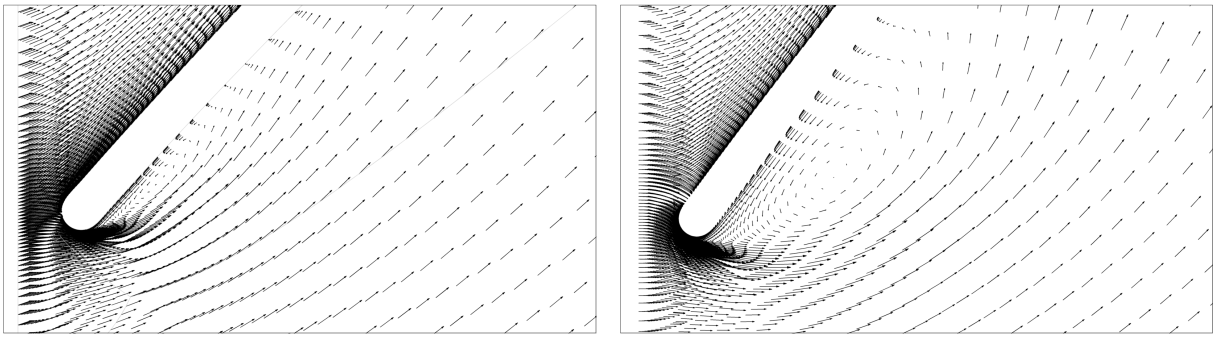

(a) For $\beta_3' = 40°$. (b) For $\beta_3' = 35°$.

Figure 3.20: Rotor relative velocity vectors near the leading edge, at $\Phi = 0.088$.

Table 3.3: Dimensionless kinetic energy flux at rotor (3) and diffuser (4) exit sections for the complete turbine.

$\beta_3'[°]$	Φ	K_3	K_{3r}	$K_{3\theta}$	K_4	K_{4r}	$K_{4\theta}$
40	0.204	0.352	0.303	0.044	0.035	0.033	0.002
35	0.202	0.326	0.258	0.064	0.033	0.029	0.004

edge, in the plane defined by the dimensionless spanwise coordinate 0.5, for a flow coefficient $\Phi = 0.088$. Rotor losses are the main contributor to differences in turbine efficiency in the range $0.20 < \Phi < 0.34$ and deserve further investigation as there are no visible differences in the flow field at the leading edge.

The diffuser performance has a significant contribution to differences in turbine efficiency in the range $0.17 < \Phi < 0.25$. High losses in diffusers can be caused by low flow uniformity in the rotor outlet. Comparing kinetic energy fluxes is one way to assess flow uniformity, since a uniform flow has smaller kinetic energy flux than a non-uniform one with the same mean velocity. Table 3.3 shows the kinetic energy coefficient defined by Eq. (3.23) at the exit section of both rotors, for $\Phi \sim 0.20$. The flow through the rotor with $\beta_3' = 40°$ has a kinetic energy 8% larger than the flow through the rotor with $\beta_3' = 35°$. Coincidently, diffuser losses with the first rotor are 30% higher than ones for the second rotor. In both cases the diffuser recovers about 90% of the rotor outlet kinetic energy.

Some qualitative conclusions about flow uniformity can also be drawn by analysing plots of the velocity profiles. Fig. 3.21 shows the contours of dimensionless radial and tangential velocity components. In this figure, z^* is the dimensionless axial coordinate, $z^* = 0$ denotes the intersection of the control surface with the shroud, $z^* = 1$ indicates the intersection of the control surface with the hub, $\theta^* = (\theta Z)/(2\pi)$ is the dimensionless pitch coordinate $(1 \geq \theta^* \geq 0)$ with

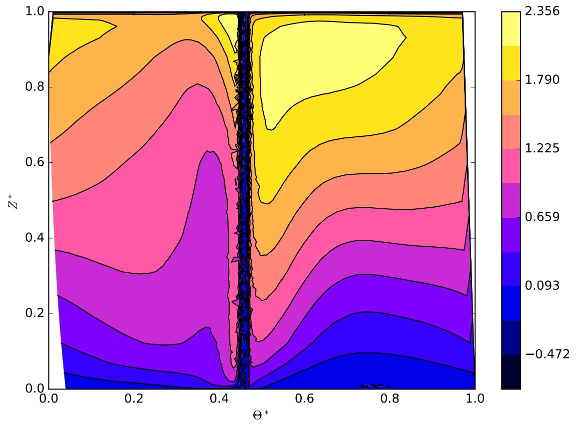

(a) Radial velocity distribution for $\beta_3' = 40°$ and $\Phi = 0.204$.

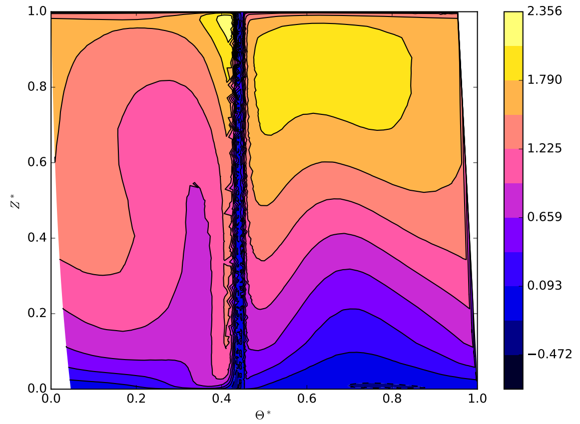

(b) Radial velocity distribution for $\beta_3' = 35°$ and $\Phi = 0.202$.

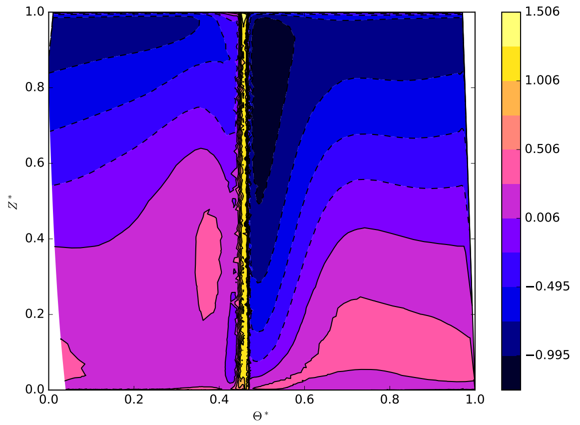

(c) Tangential velocity distribution for $\beta_3' = 40°$ and $\Phi = 0.204$.

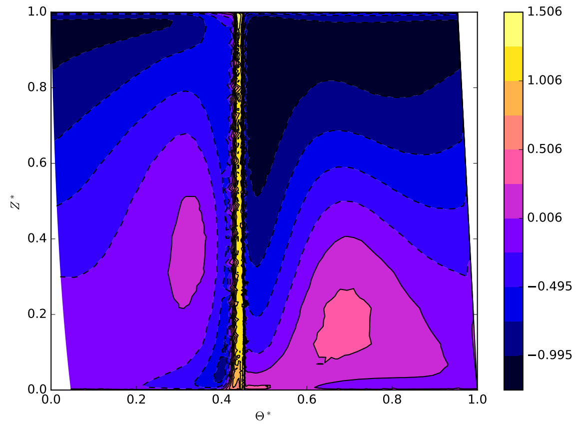

(d) Tangential velocity distribution for $\beta_3' = 35°$ and $\Phi = 0.202$.

Figure 3.21: Velocity distribution at rotor outlet: rotors with $\beta_3' = 40°$ and $\beta_3' = 35°$.

the blade located at approximately $\theta^* = 0.5$. The rotation direction is in the positive direction of θ^*. Dimensionless velocity distributions were obtained by dividing each velocity component by the transport velocity, U.

From these figures, the radial velocity distribution of the rotor with $\beta_3' = 35°$ is more uniform than the velocity distribution for the rotor with $\beta_3' = 40°$, while the opposite happens with the tangential velocity distribution. This observation is in agreement with the results presented in Table 3.3 and the energy loss distribution of Fig. 3.19.

As a confirmation that numerical errors are similar in all the geometries tested, the numerical uncertainty of the peak total-to-static efficiency of the turbine with $\beta_3' = 35°$ was calculated following the method described in Appendix A and is presented in Fig. 3.22. The iterative uncertainty is negligible, $\xi_{\text{itr}} = 0.0001$, compared with the discretisation uncertainty, $\xi_{\text{dsc}} = 0.041$

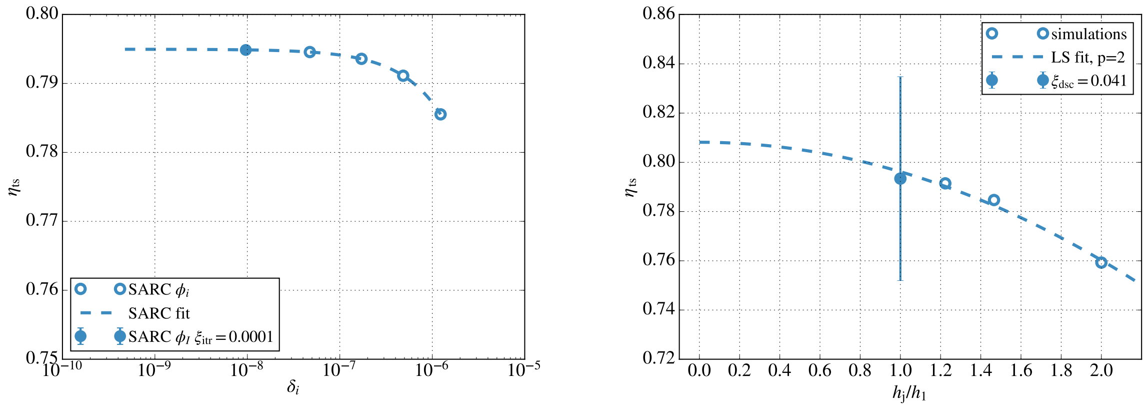

(a) Iterative uncertainty.

(b) Discretisation uncertainty.

Figure 3.22: Numerical uncertainty for the total-to-static efficiency of a MGV turbine with $\beta_3' = 35°$.

(with 1.3 observed order of grid convergence), therefore the numerical uncertainty on total-to-static efficiency is $\xi_{\text{num}} = 0.041$.

3.4 Conclusions

The biradial rotor design conditions were studied with the aim of increasing the efficiency of biradial turbines. A slip model from the literature was adapted to biradial rotors in order establish conditions for minimum incidence and outlet kinetic energy. The effects over the rotor and a MGV turbine were analysed using numerical tools.

Simulations were performed using a CFD code based on the RANS equations with two eddy-viscosity turbulence models. The baseline case was an existing biradial turbine scaled model, for which modelling errors of the design total-to-static efficiency were assessed using published experimental data.

It was found that for a given rotor blade metal angle, there is no significant gain in improving the inlet absolute flow angle. But gains appear if, for a given inlet absolute flow angle, the blade metal angle is changed to comply with the improved conditions.

As such, a new turbine rotor was designed for an existing turbine. Despite having the same peak efficiency, the improved turbine has higher average efficiency, improving the operating range.

Additionally the numerical study performed in this Chapter can be used as a reference for future simulations, namely the turbulent model and grid refinement choice.

The conclusions of Chapter 3 can be summarised as follows:

- The difference observed in peak efficiency for RANS simulations with SARC and SST is 0.5%, for the original turbine geometry.
- The SARC model is more robust and allows the application of implicit residual smoothing, which leads to faster calculation of the operating curves.
- Solutions obtained with the SARC model have one-third of the iterative uncertainty of those obtained with SST.
- For the original turbine geometry, the estimated modelling error in the design total-to-static efficiency is $\epsilon_\phi = 0.026 \pm 0.052$ using the experimental value as the reference; improving the estimation of the modelling error (diminishing the validation uncertainty) requires reductions in numerical and experimental uncertainties.
- The unified slip model successfully estimates the conditions for minimum rotor inlet losses and outlet kinetic energy.
- For biradial rotors it is not possible to simultaneously impose the design conditions for minimum incidence losses, theoretical best efficiency conditions for impulse turbines ($V_{2\theta}/U = 2$) and minimum kinetic energy at the rotor outlet ($V_{3\theta} = 0$).
- The variation of the energy coefficient has more influence on the rotor efficiency than the inlet losses and the outlet kinetic energy, for the tested geometries and inlet conditions.
- Existing rotor geometries should not be paired with new guide-vanes that provide higher absolute flow angles in order to decrease incidence. This decreases turbine efficiency, because the decrease of the power coefficient has more influence over the efficiency than the reduction of the incidence losses.
- Existing guide-vane geometries should be paired with new rotors (with lower blade metal angles) because it keeps the power coefficient, while reducing incidence losses and outlet kinetic energy.

- If the nozzle, guide-vanes, and diffuser of the reference MGV turbine are paired with a new rotor (with a lower blade metal angle), it results in a turbine with similar peak efficiency.

- If the nozzle, guide-vanes, and diffuser of the reference MGV turbine are paired with a new rotor (with a lower blade metal angle), it results in a turbine with higher average efficiency. The lower rotor outlet energy (more uniform flow distribution) increases the diffuser performance.

Turbines installed in OWC wave energy converters operate with variable rotational speed to adapt the power take-off system to the instantaneous sea conditions. Depending on the control law, the new turbine design having similar peak efficiency but improved operating range can result in a higher annual average power conversion.

Chapter 4

Constant-thickness guide-vane design for biradial turbines

The aerodynamic efficiency of FGV biradial turbines is penalized due to the inherent misalignment between the rotor outflow and the downstream guide vanes. This Chapter presents the aerodynamic design of a radial guide-vane system for self-rectifying biradial impulse turbines and the relation between guide-vane flow deflection and blockage, rotor blade angle and turbine efficiency in design conditions. The system comprises two concentric rows of constant-thickness vanes. The design method solves a multi-objective optimization problem that maximizes deflection while minimizing outflow blockage, returning a Pareto optimal set of guide vanes. A subset of these results is used to configure and assess multiple turbine geometries. Data are obtained numerically with a RANS solver. The new guide-vane system improves flow deflection over reference designs based on aerofoil-section vanes with identical blockage. A turbine efficiency of 68.2% is achieved for a guide-vane deflection of 67.3°, blockage factor of 0.61 and rotor blade angle of 35°. The new design leads to an estimated reduction of 58% on the stagnation pressure losses in the outlet guide vanes. The efficiency reached is smaller than the top performing state-of-the-art turbine. This is caused by the lower stator-to-rotor radius ratio required for the construction of the off-grid wave energy converter when compared to previous turbine designs.

4.1 Hypotheses and objectives

Current designs of FGV biradial turbines are characterized by using a large number of aerofoil-shaped guide vanes (e.g., 228 vanes in the turbine model of Ref. [63] and 256 vanes in the prototype of Refs. [64, 66]). From the manufacturing point of view, aluminium or stainless steel milled vanes provide excellent dimensional tolerances, corrosion resistance, and mechanical strength. On the other hand, milling is a more expensive process for many parts than sheet metal bending or stamping.

The study presented in Ref. [58] addresses the design and testing of a guide-vane system for axial impulse turbines. The vanes have a constant thickness, are manufactured by sheet metal bending, and the corresponding experimental results are in good agreement with the theoretical prediction. No public data is available about the production costs of biradial turbines, but previous experiences [58, 63, 64, 66] indicate that sheet bending or stamping to manufacture guide-vanes could decrease the biradial turbine production costs.

Flow stall on constant-thickness vanes occurs at lower incidence angles when compared with aerofoil-shaped vanes [55, 91]. In the case of biradial turbines, the flow admitted to the inlet guide vanes is always in the radially inwards direction, independently of the flow rate or wave cycle. Therefore, constant thickness guide vanes can be designed for zero incidences. Moreover, by being centripetal, the flow is subjected to a favourable global pressure gradient, reducing local adverse pressure gradient from blade curvature, delaying boundary layer separation, and allowing increased flow deflection (increasing swirl). As such, the first research hypothesis explored in this Chapter is that constant-thickness guide vanes can provide similar inflow deflection and have similar aerodynamic outflow stall losses compared to previous aerofoil-shaped guide-vane designs.

The work presented in Chapter 3 shows an increase in rotor total-to-static efficiency by decreasing the absolute velocity angle at the rotor inlet (with the circumferential direction). On the other hand, the research of Ref. [63] shows that by decreasing this angle, the flow blockage increases (i.e., increases the circumferential chord-to-pitch ratio of the multi-row guide vanes) and consequently increases the aerodynamic stall losses on the set of guide vanes downstream of the rotor.

Therefore, the second research hypothesis explored in this Chapter is the existence of an optimum absolute velocity angle at the rotor inlet that maximizes turbine efficiency by balancing rotor efficiency with the stall losses on the outlet set of guide vanes. A recent CFD study of a radial impulse turbine confirms that the loss in the guide vanes downstream of the rotor is critical for turbine efficiency [92]. In this study, a new rotor blade and setting angles of the guide vanes were set to reduce the losses in the guide vanes.

From the two research hypotheses, the following objectives were set:

(i) Design a guide-vane system with constant thickness vanes and compare their performance with the design based on aerofoil-shaped vanes.

(ii) Characterize the relation between turbine efficiency and the absolute velocity angle at the rotor inlet and find the angle that maximizes turbine efficiency.

4.2 Methods

Performance is assessed with a commercial turbomachine-oriented computational fluid dynamics software (CFD) with its setup based on the configuration discussed in Chapter 3. The guide-vane design uses the double-row configuration based on the experience of previous studies [63] but with a new blade shape and position calculated in this Chapter. The rotor geometry follows the state-of-the-art method [61] with blade metal angles chosen for the design conditions established in Chapter 3 and guide-vane flow deflections obtained in this Chapter.

The research procedure of this study can be summarized as follows:

1. parametric definition of a double-row guide-vane system with constant thickness radial vanes;
2. setup of a multi-objective optimization problem and respective solver;
3. design of guide-vane systems with minimum flow blockage and maximum flow deflection;
4. comparison between the new guide-vane systems and previous designs based on aerofoils;
5. determination of rotor blade metal angles for the designed guide-vane systems;

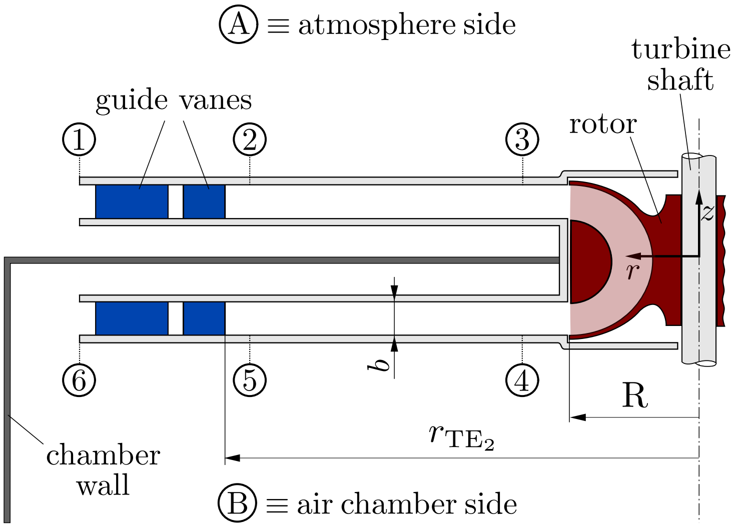

Figure 4.1: Schematic representation of the biradial turbine with fixed guide-vanes radially offset from the rotor and arranged into two concentric circular rows.

6. generation of multiple rotor geometries;

7. performance assessment of multiple turbine configurations;

8. determination of the best performing turbine configuration.

A schematic meridional view of a FGV turbine configuration used in this Chapter is illustrated in Fig. 4.1, while the respective plane cascade at the mid-span is illustrated in Fig. 4.2. Here the section labels, k, inside circles refer to inhalation flow.

4.2.1 Guide-vane geometry

The guide-vane system comprises two concentric rows of constant-thickness radial guide vanes with the camber line defined by Bézier curves [93, 94]. The vanes are span-wise uniform sections stacked in the axial direction without leaning or sweeping. These sections are designed by superposing the thickness distribution perpendicularly to the camber line, scaling, rotating to the desired stagger angle, and translating the vane inflow leading edge on the radial plane. The definitions of the following paragraphs apply to both rows of guide vanes.

The guide-vanes camber line is defined in a chord-normalized (u, v) coordinate system with second-degree Bézier curves from three control points, $\mathbf{P}_0 = (0, 0)$, $\mathbf{P}_1 = (u_1, v_1)$ and $\mathbf{P}_2 = (1, 0)$, for each guide-vane row, Fig. 4.3. The camber line begins at the origin of the

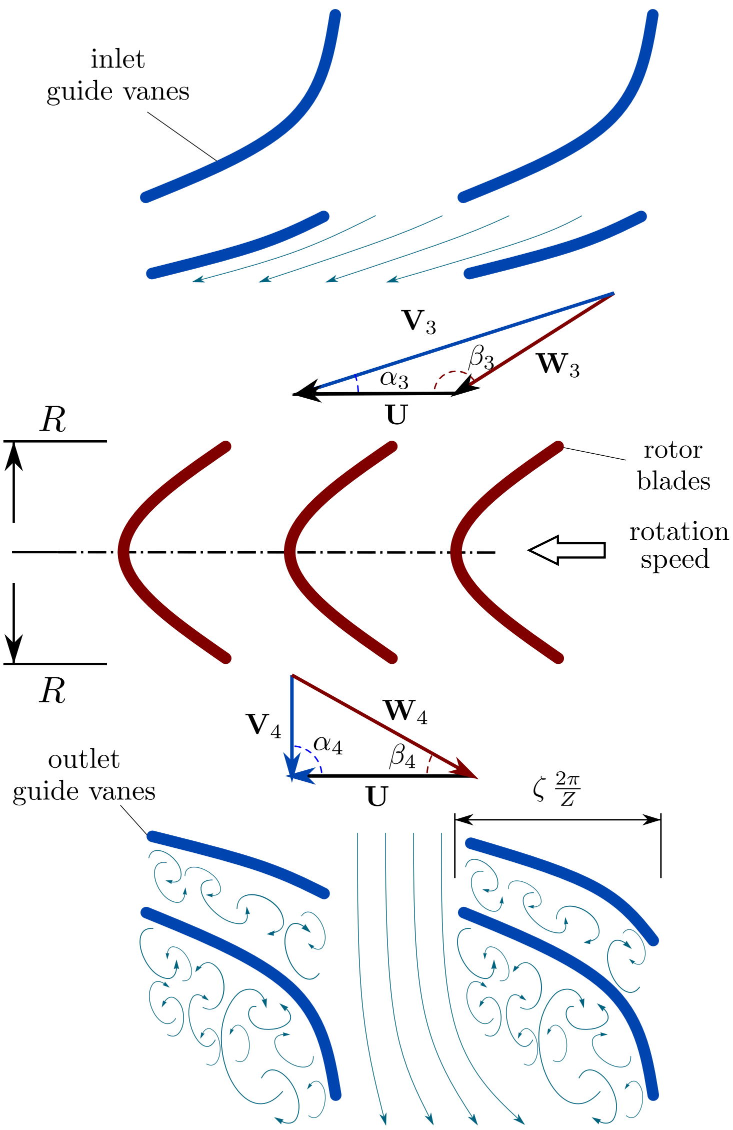

Figure 4.2: Plane cascade and velocity triangles of a FGV biradial impulse turbine. The outlet guide vanes are inherently misaligned with the rotor discharge flow velocity V_4.

referential ($\mathbf{P}_0$) and is written as a function of control points $\mathbf{P}_1$ and $\mathbf{P}_2$ as

$$\mathbf{C}(\tau) = 2\tau(1-\tau)\mathbf{P}_1 + \tau^2\mathbf{P}_2\,, \tag{4.1}$$

where τ is the dimensionless parametric variable along the camber line direction s, with $0 \leq \tau \leq 1$, and $\mathbf{P}_1$ is expressed as function of the angles δ_{LE} and δ_{TE},

$$\mathbf{P_1} = \left(\frac{\tan\delta_{\mathsf{TE}}}{\tan\delta_{\mathsf{TE}} + \tan\delta_{\mathsf{LE}}}\,,\, \frac{\tan\delta_{\mathsf{TE}}\tan\delta_{\mathsf{LE}}}{\tan\delta_{\mathsf{TE}} + \tan\delta_{\mathsf{LE}}}\right). \tag{4.2}$$

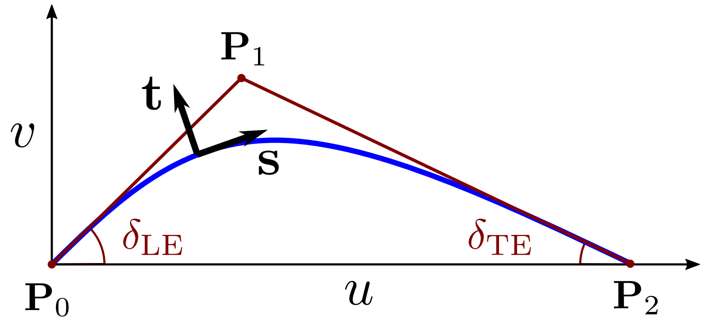

Figure 4.3: Guide-vane camber line definition with a quadratic Bézier curve.

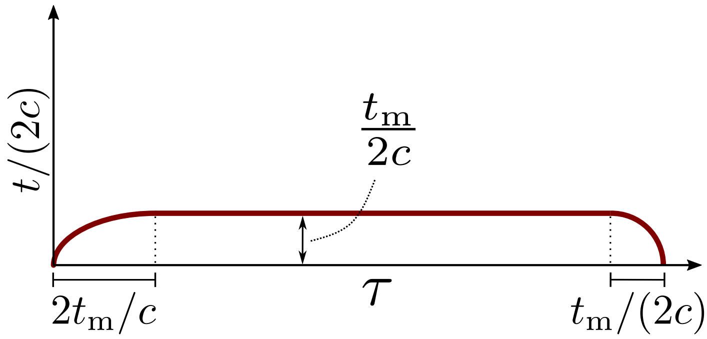

Figure 4.4: Guide-vane thickness distribution. Its maximum value is noted by t_{m}.

Unlike aerofoil-shaped, constant thickness vanes are extremely sensitive to flow separation due to incidence, mainly if a sharp leading edge is used. Other leading edge shapes, such as circular or squared, always create localized separation bubbles even with no incidence. An elliptical leading edge with an axes ratio of 4:1 was found to be a good compromise solution, while a simple circumference was used for the trailing edge, Fig. 4.4. As such, the thickness-to-chord ratio distribution as a function of coordinate τ is

$$\frac{t}{2c}(\tau) = \begin{cases} \left[\left(\frac{t_{\mathrm{m}}}{2c}\right)^2 - \left(\frac{\tau}{4} - \frac{t_{\mathrm{m}}}{2c}\right)^2\right]^{1/2} & , \tau \in \left[0\,,\, 2\frac{t_{\mathrm{m}}}{c}\right[\\ \frac{t_{\mathrm{m}}}{2c} & , \tau \in \left[2\frac{t_{\mathrm{m}}}{c}\,,\, 1 - \frac{t_{\mathrm{m}}}{2c}\right[\\ \left[\left(\frac{t_{\mathrm{m}}}{2c}\right)^2 - \left(\tau - 1 + \frac{t_{\mathrm{m}}}{c}\right)^2\right]^{1/2} & , \tau \in \left[1 - \frac{t_{\mathrm{m}}}{2c}\,,\, 1\right], \end{cases} \tag{4.3}$$

where t_{m} is the vane maximum thickness perpendicular to vane camber-line (along unit vector $\mathbf{t}$), Fig. 4.3.

The guide-vane geometry on the physical plane (x, y) illustrated in Fig. 4.5 is then

$$\mathbf{B}(\tau) = \mathbf{F} + c\,\mathbf{M}(\xi)\left[\mathbf{C}(\tau) \pm \mathbf{t}(\tau)\,\frac{t}{2c}(\tau)\right], \tag{4.4}$$

where $\mathbf{F}$ is the stacking point located on the vane inflow leading edge, defined as

$$\mathbf{F} = \left(r_{\mathsf{LE}}\cos\theta_{\mathsf{LE}}\,,\, r_{\mathsf{LE}}\sin\theta_{\mathsf{LE}}\right), \tag{4.5}$$

c is the guide vane chord, $\mathbf{M}(\xi)$ is the rotation matrix

$$\mathbf{M}(\xi) = \begin{bmatrix} \sin(\xi) & -\cos(\xi) \\ \cos(\xi) & \sin(\xi) \end{bmatrix}, \tag{4.6}$$

$\mathbf{t}(\tau)$ is the unit vector perpendicular to the camber line, and ξ is the vane stagger angle, defined here as the angle of the vane chord with the radial direction, measured at the leading edge for inflow conditions.

Note that the camber line geometry is directly related to the aerodynamic load distribution [95].

The blockage angle $2\pi\zeta/Z$ of the double-row of guide vanes can be derived from Fig. 4.5 as

$$\zeta = \frac{\max\left(\chi_1 + \theta_{\mathsf{LE}_2}, \chi_2\right)Z}{2\pi}, \tag{4.7}$$

where

$$\chi_1 = \arcsin\frac{c_1\sin\xi_1}{r_{\mathsf{TE}_1}}, \tag{4.8}$$

$$\chi_2 = \arcsin\frac{c_2\sin\xi_2}{r_{\mathsf{TE}_2}}, \tag{4.9}$$

$\theta_{\mathsf{LE}_1} = 0$, and θ_{LE_2} is the angle between the leading edges in inflow conditions of the inner and the outer closest vanes, as represented in Fig. 4.5.

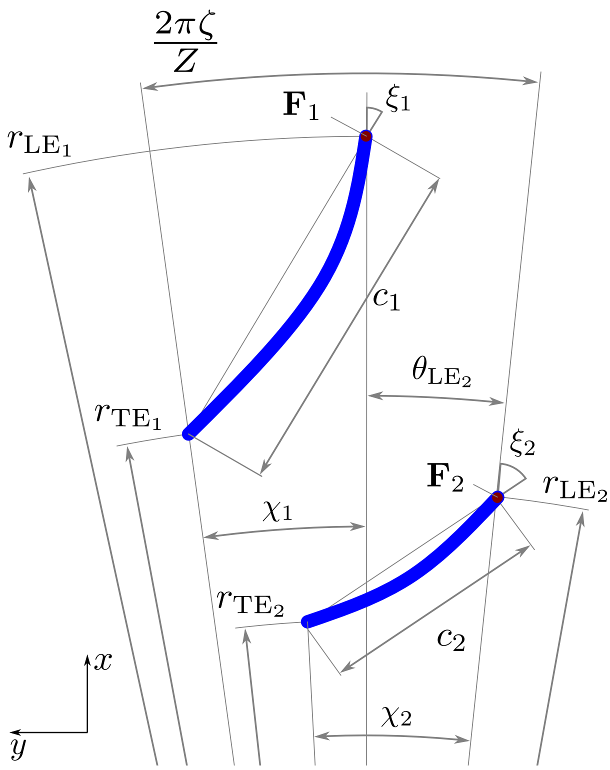

Figure 4.5: Guide-vane radial cascade definition.

4.2.2 Boundary layer monitoring

During the optimization, boundary layer separation was monitored by assessing the direction of the shear stress at the wall with respect to the main flow direction using the parameter

$$\epsilon = \tau_{\mathbf{w}} \cdot \mathbf{s}\,, \tag{4.10}$$

and the distribution of the skin friction coefficient [96]

$$c_{\mathrm{f}} = \frac{\tau_{\mathrm{w}}}{\frac{1}{2}\rho V_{\infty}^2}\,. \tag{4.11}$$

Here, $\tau_{\mathbf{w}}$ is the wall shear stress vector, **s** is the unit vector tangent to the camber line in the main flow direction, ρ is the air density, and V_∞ is the reference velocity of the undisturbed flow. Theoretically, ϵ changes sign and $c_{\mathrm{f}} = 0$ at the separation point [96] but, for the optimization, a minimum value of $c_{\mathrm{f}} = 5 \times 10^{-4}$ with $\epsilon > 0$ was used. While $\epsilon > 0$ guarantees that the boundary flow is aligned with the main flow direction, $c_{\mathrm{f}} = 5 \times 10^{-4}$ is used as a safety factor against numerical errors. Referring to the vane internal coordinate system (Fig. 4.3) and cascade geometry (Fig. 4.5), V_∞ was taken outside the boundary layer at $Zt/(2\pi r_{\mathsf{LE}_1}) = 0.112$, where the maximum height of the camber line above the chord line occurs.

4.2.3 Optimization

The goals for the guide-vane design were to (i) maximize flow deflection at the inlet guide-vane system, (ii) minimize stagnation pressure losses at the outlet guide vanes, and (iii) minimize stagnation pressure losses at the inlet guide vanes. These goals could have been used as objective functions resulting in a three-objective optimization problem. Nonetheless, the problem was reformulated to reduce optimization convergence time.

The first design goal was implemented by minimizing the inlet guide-vanes absolute flow angle with the circumferential direction at the outlet, α_2. Each geometry created by the optimization algorithm was simulated assuming inflow conditions, i.e., from section 1 to section 2 regarding Fig. 4.1.

The second design goal was fulfilled by minimizing the stator blockage factor ζ as given by Eq. (4.7) and represented in Fig. 4.5. It was experimentally observed that stagnation pressure losses in the outlet guide vanes are directly correlated to the blockage factor in an axial impulse turbine [58]. Minimization of the blockage factor is preferred because it is a pure geometric parameter. Its calculation is significantly faster than the calculation of outlet stagnation pressure losses because it does not require a CFD simulation, reducing optimization time. The author's experience with the research reported in Ref. [63] suggests that multi-row guide-vanes in the range $0.49 < \zeta < 0.81$ provide adequate flow deflection for biradial turbines. This was verified by the optimization results of the present work.

The last design goal was carried out by constraining the optimization to geometries where the boundary layers remained attached. Refs. [63, 64] show that stagnation pressure losses in inlet guide vanes with non-separated flow are much smaller than those in the rotor and outlet guide vanes. Decreasing the guide vanes blockage was prioritized even with a slight increase of stagnation pressure losses for inflow conditions. So, losses were considered minimized as long as the boundary layer remained attached.

The guide-vane design is based on a multi-objective constrained optimization problem comprising two objectives, ten decision variables, and ten restrictions. It is formalized as

$$\text{minimize } \mathbf{f}(\mathbf{x}) = (\zeta(\mathbf{x}), \alpha_2(\mathbf{x})) \tag{4.12}$$

for

$$\mathbf{x} = (c_1, \xi_1, c_2, \xi_2, \mathit{\Delta} r_{1,2}, \theta_{\mathsf{LE}_2}, \delta_{\mathsf{LE}_1}, \delta_{\mathsf{TE}_1}, \delta_{\mathsf{LE}_2}, \delta_{\mathsf{TE}_2}) \tag{4.13}$$

and subjected to

$$\begin{aligned} &0.49 < \zeta < 0.81\,, \\ &\epsilon \geq 0\,, \\ &c_{\mathsf{f}} \geq 5 \times 10^{-4}\,. \end{aligned} \tag{4.14}$$

Here,

$$\mathit{\Delta} r_{1,2} = r_{\mathsf{TE}_1} - r_{\mathsf{LE}_2} \tag{4.15}$$

is the distance between the two guide-vane rows, which was introduced as a decision variable to explore the interaction between the two rows. Restrictions on ϵ and c_{f} were applied on both sides of each guide vane for $\tau \in \left[2\frac{t_{\mathsf{m}}}{c}\,, 1 - \frac{t_{\mathsf{m}}}{2c}\right[$, which is the constant thickness part. Localized separation due to the edge geometry was considered acceptable.

The optimization problem was solved with Generalized Differential Evolution (GDE3) [97] from the open-source optimization library Pymoo v0.5.0 [98]. GDE3 is a population-based meta-heuristic algorithm based on Differential Evolution (DE) [99, 100] that considers Pareto dominance in the objective function space and constraint violation dominance, making it suitable for multi-objective constrained optimization problems.

The population comprises individuals (the geometries), which are real coded vectors of the decision variables, **x** in Eq. (4.13). The algorithm iteratively evaluates individuals (with CFD simulations) and gradually replaces them with improved ones according to the objective function (Eq. (4.12)). The process can be summarized as

1. Create an initial population of random individuals.

2. Evaluate the initial population.

3. While maximum generation number is not reached, do:

- For each individual in the population, do:
  - Create a candidate by mutation.
  - Evaluate the candidate.
  - Perform selection.
- If the population increased, truncate it.

The mutation scheme is DE/rand/1/bin from the original DE algorithm and outputs a candidate individual that is compared to its parent. The selection process then chooses how to incorporate it (or not) into the population. This process is improved over the original DE. Following Ref. [97] it is:

- If one individual is feasible and the other is infeasible, the infeasible one is rejected.
- If both individuals are infeasible, the candidate replaces the parent if it weakly dominates the parent in the constraint violation space; otherwise, the parent is kept.
- If both individuals are feasible, the candidate replaces the parent if it weakly dominates the parent in the objective function space. If the parent dominates the candidate, then the parent is kept. If neither individual dominates in the objective function space, the parent is kept, and the candidate is added to the population.

At the end of one generation, the population might have grown and has to be truncated. To do so, individuals are first ranked using nondominated sorting, and crowding distance [101]. Then, population size returns to its initial value by discarding the lower-ranked individuals.

At the end of the iterative process, a population of improved solutions is spread along a Pareto front on the objective space.

Other algorithms can be used as long as they support constrained multi-objective optimization. Reviews on evolutionary algorithms are presented in Refs. [101–104], and a performance comparison between multi-objective algorithms based on DE and other types can be found in Refs [105, 106].

4.2.4 Rotor geometry

The original rotor design methodology [61] with the design conditions for mitigation of flow incidence and slip effects presented in Chapter 3 were used. Suitable rotor geometries for the optimized guide-vanes were designed by adequate selection of the rotor inlet/outlet blade metal angle. For clarity, the procedure is summarized as follows: (i) each set of optimized guide vanes deflects the absolute velocity to an outlet angle α_2; outside the boundary layers the inflow path between the exit of the inlet guide vanes and the rotor inlet is a logarithmic-spiral due to conservation of angular momentum [55, 63]; then (ii) the absolute flow angle at the rotor inlet $\alpha_3 = \alpha_2$ is the input to calculate the corresponding rotor inlet/outlet blade metal angles $\beta_4' = \pi - \beta_3'$ in design conditions (see Chapter 3); (iii) a fixed diameter and rotational speed is chosen for all the rotors and the respective geometries are generated [61].

4.2.5 Numerical model

The flow solver used was FINE/Open v10.1 [107] from NUMECA Inc. It is an unstructured-mesh, three-dimensional, finite-volume, density-based, RANS solver with a cell-centred approach, explicit time-marching multi-stage Runge-Kutta scheme, and viscous fluxes are approximated by central differencing schemes. Inviscid fluxes were determined by central differences schemes using a Jameson-type artificial dissipation technique with second and fourth-order derivatives. Air is assumed to be a perfect gas. Simulations used a multi-grid approach, implicit residual smoothing, and Choi-Merkle pre-conditioning [85] to increase the iterative convergence rate.

Turbulence was modelled with the two-equation, eddy viscosity, Shear Stress Transport (SST) $\kappa-\omega$ model [108]. Boundary conditions at the wall result from the impermeability and no-slip condition with the shear-stress at the wall determined from its definition (no wall functions). Therefore, the dimensionless near-wall cell height complied with $y^+ < 1$.

Model for guide vane design

An unstructured mesh generator was used to avoid handling different structured mesh topologies due to the geometric freedom given by the method described in Section 4.2.1.

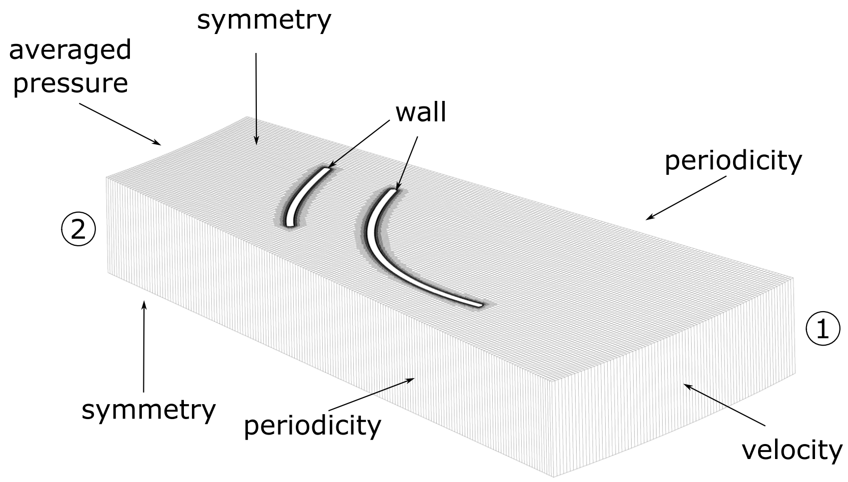

Figure 4.6: Example of mesh used for guide-vane simulations and respective boundary conditions.

Existing guide-vanes for biradial turbines are based on aerofoil-shaped vane sections stacked in the axial direction without leaning or sweeping [63]. The design method of these vanes was based on two-dimensional simulations on the mid-span blade-to-blade plane and experimental testing showd good agreement with the designed flow deflection [64]. As such, the same two-dimensional approach was followed in this work. Since the flow solver is exclusively three-dimensional, the mesh is only one cell height with symmetry conditions imposed on the faces normal to the span-wise direction.

The grids were generated with HEXPRESS, also from NUMECA Inc., which uses the volume-to-surface approach to generate non-conformal body-fitted full hexahedral unstructured meshes. A mesh used for guide-vane design is shown in Fig. 4.6.

Constant inlet turbulent intensity $T_u = 0.1$ and turbulent viscosity ratio of $\mu_t/\mu = 100$ were imposed. A correlation-based turbulence transition model [109] was added to the turbulence modelling. A uniform absolute velocity distribution was used for the inlet boundary condition and uniform static pressure distribution for the outlet.

Model for turbine assessment

Turbine performance is analysed in six sectors, each limited by two sections (k, l) as referenced to Fig. 4.1: inlet guide vanes $(1, 2)$, nozzle $(2, 3)$, rotor $(3, 4)$, diffuser $(4, 5)$, outlet guide vanes $(5, 6)$, and turbine discharge $(6, \mathrm{B})$. Both sector and global performance were derived (Section 4.2.6) from the results of separate simulations of computational domains covering

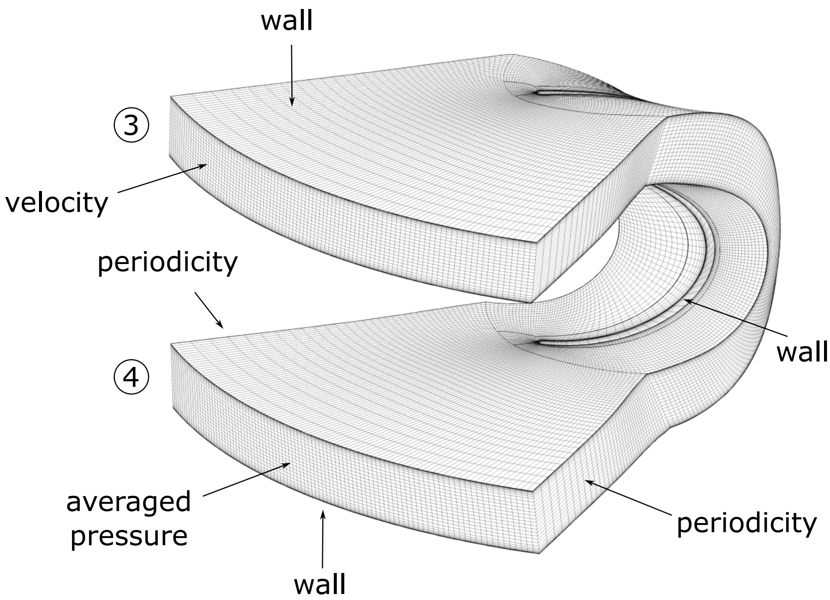

Figure 4.7: Example of mesh used for nozzle, rotor and diffuser simulations and respective boundary conditions.

sectors $(1, 2)$, $(2, 5)$ and $(5, 6)$.

Results show that a two-dimensional steady-state simulation of sectors $(1, 2)$ and $(5, 6)$ provides adequate results for losses in the scope of this study. Outlet guide-vanes $(5, 6)$ behave as bluff bodies due to the inherent misalignment with the incoming flow. Naturally, two and three-dimensional models return different results, but the difference between the two is negligible for the geometries and flow conditions considered (see Section 4.3.3). The geometries for sub-domains $(1, 2)$ were taken from selected optimization results, while sub-domains $(5, 6)$ were obtained from simulations of the same grids but with updated boundary conditions.

The outlet flow of an upstream sector was averaged in the circumferential direction (velocity and turbulence) and imposed as the inlet condition of the downstream sector. This method was used because the long nozzle and diffuser between the rotor and guide vanes smooths the flow field and the unsteady phenomena (see Section 4.3.3). An average pressure was imposed at the outlet sections.

The domain containing the nozzle, rotor and diffuser $(2, 5)$ was discretized with a structured mesh following the method described in Section 3.2.2 and is illustrated in Fig. 4.7.

Grid quality parameters and uncertainty estimation are also presented in Section 4.3.3. No turbulence transition models were used in the simulations of sectors $(2, 5)$ and $(5, 6)$.

4.2.6 Performance metrics

Due to their symmetry, the performance of biradial turbines is nominally independent of flow direction. In what follows, atmospheric inflow conditions are considered (from section 1 to 6). Despite not being a physical component, it is useful to consider the discharge as a turbine sector to account for the kinetic energy lost at the turbine outlet.

For incompressible flow, section data, such as the averaged flow velocity components in the radial and circumferential directions, $\bar{V}_{r_k}$ and $\bar{V}_{\theta_k}$, the averaged angle of the absolute flow with the circumferential direction $\bar{\alpha}_k$, the flow rate Q, the averaged stagnation pressure $\bar{p}_{0_k}$, the averaged pressure $\bar{p}_k$, and the kinetic energy flux per unit of volume E_{ke_k} at a section k, are calculated according to

$$\left\{\bar{V}_{r_k}, \bar{V}_{\theta_k}, \bar{p}_k, \bar{p}_{0_k}, E_k\right\} = \frac{1}{Q}\int_{A_k} \left\{V_r, V_\theta, p, (p + \tfrac{1}{2}\rho V^2), \tfrac{1}{2}\rho V^2\right\} |\mathbf{V}\cdot\mathbf{n}|\,\mathrm{d}A\ , \tag{4.16}$$

$$\tan\bar{\alpha}_k = \frac{\bar{V}_{r_k}}{\bar{V}_{\theta_k}}\ , \tag{4.17}$$

where ρ, p, $\mathbf{V}$, $\mathbf{n}$, and A_k are air density, pressure, absolute velocity, and outer normal vector and surface area of section k, respectively.

To account for the power lost in any sector (k, l) except for the rotor, it is convenient to use the stagnation pressure loss coefficient,

$$\lambda_{k,l} = \frac{\bar{p}_{0_k} - \bar{p}_{0_l}}{\frac{1}{2}\rho V_{\mathsf{ref}}^2}\ , \tag{4.18}$$

where V_{ref} is a reference velocity. In the present study, the average radial component of the flow velocity in sections 2 and 5 (Fig. 4.1),

$$V_{\mathsf{ref}} = \bar{V}_{r_2} = \bar{V}_{r_5} = \frac{Q}{2\pi r_2 b}\ , \tag{4.19}$$

is taken as the reference velocity, where $r_2 = r_5$ corresponds to the radius of sections 2 and 5, and b is the guide vane span (and turbine channel height), Fig. 4.1.

On the rotor sector (3,4) (Fig. 4.1), the stagnation pressure loss coefficient is

$$\lambda_{3,4} = \frac{(\bar{p}_{0_3} - \bar{p}_{0_4}) - \dfrac{T\Omega}{Q}}{\frac{1}{2}\rho V_{\text{ref}}^2}\,, \tag{4.20}$$

where T is the rotor torque computed from the angular momentum balance between sections 3 and 4,

$$T = \int_{A_3} \rho r V_\theta \, |\mathbf{V}\cdot\mathbf{n}| \, \mathrm{d}A - \int_{A_4} \rho r V_\theta \, |\mathbf{V}\cdot\mathbf{n}| \, \mathrm{d}A\,. \tag{4.21}$$

Note that V_θ can be either positive or negative. The convention used in this dissertation is $V_\theta > 0$ when $\mathbf{V}_\theta$ and $\mathbf{U}$ have the same direction.

The pressure coefficient

$$\Psi_{k,l} = \frac{\bar{p}_{0_k} - \bar{p}_{0_l}}{\rho\Omega^2 D^2} \tag{4.22}$$

accounts for the stagnation pressure drop in a sector (k,l), where D is the rotor diameter. It is easy to conclude that the drop across all sectors is

$$\Psi_{1,6} = \sum_{k=1}^{5} \Psi_{k,k+1}\,. \tag{4.23}$$

The kinetic energy E_{ke_6} at section 6 is lost, and it is helpful to consider the stagnation conditions downstream of the turbine discharge, indicated as B in Fig. 4.1 to define the turbine pressure head coefficient,

$$\Psi_{\text{ts}} = \Psi_{1,\text{B}} = \Psi_{1,6} + K_6\,, \tag{4.24}$$

where

$$K_k = \frac{E_k}{\rho\Omega^2 D^2} \tag{4.25}$$

is the kinetic energy flux coefficient at section k.

The pressure coefficient $\Psi_{k,l}$ can be calculated as a function of the stagnation pressure loss coefficient $\lambda_{k,l}$. For the rotor sector $(3,4)$ it is

$$\Psi_{3,4} = \frac{\Phi^2}{2}\left(\frac{D^2}{2\pi r_2 b}\right)^2 \lambda_{3,4} + \frac{\Pi}{\Phi}\,, \tag{4.26}$$

and for the other sectors

$$\Psi_{k,l} = \frac{\Phi^2}{2}\left(\frac{D^2}{2\pi r_2 b}\right)^2 \lambda_{k,l}\,, \tag{4.27}$$

where

$$\Pi = \frac{T}{\rho\Omega^2 D^5}\,, \tag{4.28}$$

is the turbine power coefficient, and

$$\Phi = \frac{Q}{\Omega D^3}\,, \tag{4.29}$$

the turbine flow rate coefficient.

The stagnation pressure loss coefficient $\lambda_{k,l}$ and the pressure coefficient $\Psi_{k,l}$ may seem similar but are used with different purposes. The stagnation pressure drop in a sector $\Delta p_{0_{k,l}} = \bar{p}_{0_k} - \bar{p}_{0_l}$ is equal to the stagnation pressure loss if no work is exchanged in the sector. In the rotor, part of the pressure drop is converted into work and part is lost. This is why the term $T\Omega/Q$ appears in Eq. (4.20) and Π/Φ in Eq. (4.26).

With Eqs. (4.22) to (4.29) comes the definition of rotor total-to-total efficiency,

$$\eta_{\text{tt}_{3,4}} = \frac{\Pi}{\Phi\Psi_{3,4}}\,, \tag{4.30}$$

rotor total-to-static efficiency,

$$\eta_{\text{ts}_{3,4}} = \frac{\Pi}{\Phi(\Psi_{3,4}+K_4)}\,, \tag{4.31}$$

turbine total-to-total efficiency,

$$\eta_{\text{tt}} = \frac{\Pi}{\Phi\Psi_{1,6}}\,, \tag{4.32}$$

and turbine total-to-static efficiency

$$\eta_{\text{ts}} = \frac{\Pi}{\Phi\Psi_{\text{ts}}}\,. \tag{4.33}$$

The relative stagnation pressure loss coefficient,

$$\Lambda_{\text{k,l}} = \frac{\Delta\bar{p}_{0_{\text{loss}_{\text{k,l}}}}}{\bar{p}_{0_1} - p_{\text{B}}}\,, \tag{4.34}$$

quantifies losses in a sector (k,l) as a fraction of the turbine pressure head $(1,\text{B})$ and can be calculated from the sector pressure coefficient $\Psi_{k,l}$ and other coefficients. For the rotor it is

$$\Lambda_{3,4} = \frac{\Psi_{3,4} - \Pi/\Phi}{\Psi_{\text{ts}}}\,, \tag{4.35}$$

for the outflow kinetic energy lost is

$$\Lambda_{6,\text{B}} = \frac{K_6}{\Psi_{\text{ts}}}\,, \tag{4.36}$$

and for any other sector, it is simply

$$\Lambda_{k,l} = \frac{\Psi_{k,l}}{\Psi_{\text{ts}}}. \tag{4.37}$$

It is seen again in Eq. (4.35) that only a part of the stagnation pressure drop in the rotor is a loss. It can be derived that

$$\sum_{k=1}^{5} \Lambda_{k,k+1} + \Lambda_{6,\text{B}} + \eta_{\text{ts}} = 1. \tag{4.38}$$

4.3 Results

This Chapter's results are divided into two parts. First, the analysis of the optimization results that provided new guide-vane geometries. Finally, the assessment of five turbines that were configured based on the optimization results, the rotor geometry generation method of Ref. [61] and design conditions established in Chapter 3.

4.3.1 Guide-vane design

The inlet guide vanes were designed using steady-state two-dimensional flow simulations with the optimization procedure described in Section 4.2. The geometry comprises two rows of $Z = 30$ vanes, each with a thickness $t_{\text{m}} = 0.002$ m. The outermost radius of the optimized stators is $r_{\text{LE}_1} = 0.425$ m, Fig. 4.5.

The initial population was seeded with four manually generated individuals with properties presented in Table 4.1 and twenty-four random individuals taken from the allowed range of decision variables, as listed in Table 4.2. This range was chosen based on preliminary optimization runs. An acceptable range was defined as the one that simultaneously resulted in optimization convergence without any decision variables being at their limits. When an unacceptable range

Table 4.1: Manually generated individuals inserted in the initial population.

Individual	I1	I2	I3	I4
c_1 [m]	0.088	0.095	0.103	0.114
ξ_1 [°]	24.5	26.9	28.8	28.6
c_2 [m]	0.042	0.047	0.052	0.057
ξ_2 [°]	53.0	57.4	61.3	61.7
$\Delta r_{1,2}$ [m]	-0.005	-0.005	-0.005	-0.005
θ_{LE_2} [°]	0	0	0	0
δ_{LE_1} [°]	35.5	37.9	38.8	38.7
δ_{TE_1} [°]	35.5	37.9	38.8	38.7
δ_{LE_2} [°]	13.0	12.4	10.3	10.7
δ_{TE_2} [°]	13.0	12.4	10.3	10.7

Table 4.2: Range of decision variables.

Limit	lower	higher
c_1 [m]	0.05	0.15
ξ_1 [°]	15.0	40.0
c_2 [m]	0.02	0.08
ξ_2 [°]	45.0	75.0
$\Delta r_{1,2}$ [m]	-0.01	0.01
θ_{LE_2} [°]	-0.61	0.61
δ_{LE_1} [°]	30.0	50.0
δ_{TE_1} [°]	30.0	50.0
δ_{LE_2} [°]	10.0	25.0
δ_{TE_2} [°]	5.00	20.0

was found, the run was discarded and reset from the manually seeded individuals but with updated limits.

The DE scheme used was DE/rand/1/bin and internal parameters were set according to Ref. [110]: population size of 28 individuals, differential weight $F \in [0.5, 1.0[$ with dithering [100] and crossover constant $C_{\mathrm{R}} = 0.9$. The optimization ran for 1200 generations and convergence was monitored with the hypervolume metric h_v [101] for the reference point $\mathbf{f} = (0.8, 40.0)$, Fig. 4.8.

A parallelized version of the optimization algorithm was used in a Windows machine equipped with two AMD® EPYC® CPUs 7351 @ 2.4 GHz with a total of 32 physical cores and 32 Gb of DDR4 RAM @ 2667 MHz. One physical core was assigned to each individual in the population for geometry generation, simulation and post-processing.

The algorithm performed a total of 33600 objective function evaluations. Fig. 4.9 shows the objective space with the Pareto front (circles) and the optimization results of Ref. [63] (di-

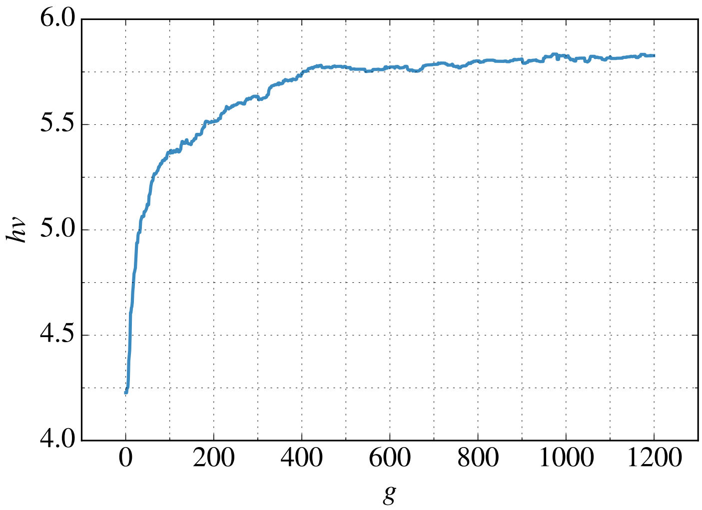

Figure 4.8: Optimization convergence of the hypervolume h_v as function of the number of generations g.

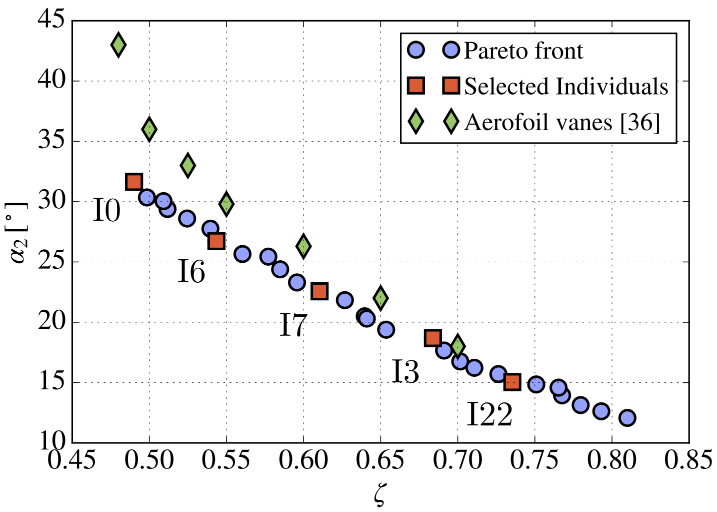

Figure 4.9: Optimized objective space (α_2, ζ) after 1200 generations. Selected individuals identified by square marks and name.

amonds). A subset of the Pareto front, named Selected Individuals, was selected for further analysis (squares). Its decision and objective spaces are presented in Table 4.3.

Despite the chord and outlet flow angle variations across the population, the flow Reynolds number at the inlet guide vanes was Re $= V_{\text{ref}}\, c_1/\nu \approx 9 \times 10^4$, taking the outermost vane as reference. The reference velocity V_{ref} was defined from Eq. (4.19) with a reference radius $r_2 = 0.28$ m, and a channel height $b = 0.03$ m, Fig. 4.1. Similarly, even with varying vane chords and radial distance between rows, $\Delta r_{1,2}$, the guide-vane set innermost radius converged to $r_{\text{TE}_2} \approx 0.322$ m, see Fig. 4.1 and Eq. (4.15).

From the objective space of Fig. 4.9, it is seen that the optimized population is well dis-

Table 4.3: Decision and objective spaces of Selected Individuals after 1200 generations.

Individual	I22	I3	I7	I6	I0
c_1 [m]	0.103	0.098	0.094	0.089	0.085
ξ_1 [°]	30.3	30.0	28.0	26.3	24.9
c_2 [m]	0.053	0.050	0.046	0.043	0.041
ξ_2 [°]	69.8	65.5	60.9	57.2	52.2
Δr_{12} [m]	-0.003	-0.003	-0.003	-0.004	-0.004
θ_{LE_2} [°]	-0.05	0.02	0.02	0.01	0.01
δ_{LE_1} [°]	39.9	39.3	39.7	38.4	38.9
δ_{TE_1} [°]	46.1	42.7	42.5	38.9	34.0
δ_{LE_2} [°]	19.9	20.0	19.8	20.0	19.4
δ_{TE_2} [°]	8.1	8.6	10.5	11.7	12.1
ζ	0.74	0.68	0.61	0.54	0.49
α_2 [°]	15.2	18.8	22.7	26.7	31.6

tributed in the allowed range for the blockage factor. The maximum absolute flow angle is $\alpha_2 = 12.1°$ for the maximum blockage, $\zeta = 0.81$, while the minimum corresponds to $\alpha_2 = 31.6°$ and $\zeta = 0.49$. The relation between these quantities is in line with the theoretical prediction [55]. Fig. 4.9 also shows that for the same blockage, the current design flow deflections are higher compared to the results of Ref. [63], especially for lower blockages and deflections.

From the decision space of Table 4.3, it is seen that the internal angle at the vanes' inflow leading edge converged to $\delta_{\mathrm{LE}_1} = 39.4\,° \pm 0.5\,°$ and $\delta_{\mathrm{LE}_2} = 19.7\,° \pm 0.3\,°$. While the parametrization is not the same as in Ref. [63], a significant difference in the results is the radial spacing between rows (Eq. (4.15)), which converged to a lower value ($\Delta r_{1,2} \approx -0.003\,\mathrm{m}$). Reduced radial spacing increases blade-to-blade interaction, which may delay boundary layer separation and favour deflection for lower blockage factors. The circumferential positioning was also defined as a decision variable. However, variations from the initial value did not provide a positive blade interaction and converged to $\theta_{\mathrm{LE}_2} \approx 0$ minimizing the blockage factor. The remaining decision variables exhibit a monotonic variation concerning the objective function. As expected, longer chords and higher camber angles improved deflection at the expense of blockage.

4.3.2 Turbine performance

The sub-set of optimized inlet guide vanes, called Selected Individuals (Fig. 4.9 and Table 4.3), were assessed in complete turbine configurations, including a nozzle, a rotor and a

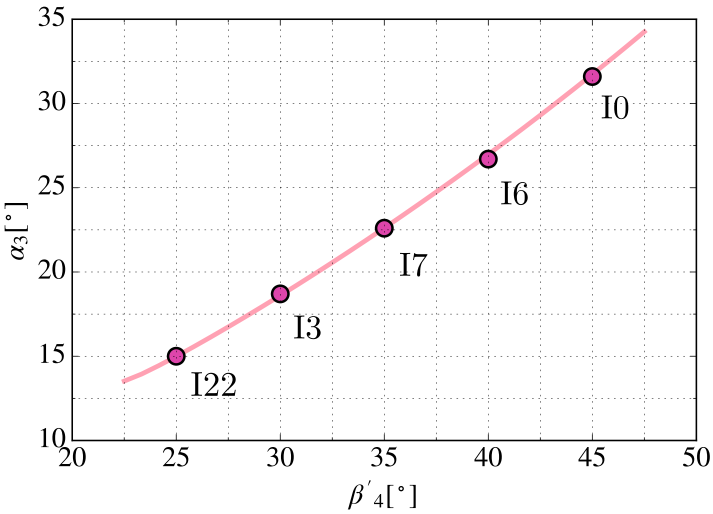

Figure 4.10: Relation between rotor blade metal angle $\beta'_4 = \pi - \beta'_3$ and absolute flow angle at the rotor inlet α_3 for design conditions (line) (from Chapter 3). Flow angles $\alpha_3 \approx \alpha_2$ and β'_4 of turbine configurations I22, I3, I7, I6 and I0 (circles).

diffuser, as represented in Fig. 4.1, following the method described in Section 4.2.4. The relation between the absolute flow leaving the guide-vanes α_2 and the rotor blade metal angle $\beta'_4 = \pi - \beta'_3$ for design conditions is derived from the results of Chapter 3 and is illustrated in Fig. 4.10 assuming $\alpha_2 \approx \alpha_3$. Since each rotor has a different blade metal angle, each turbine configuration operates at a different dimensionless flow coefficient Φ, but in design conditions (Section 4.2.4).

All rotors have seven blades with thickness $t_\mathsf{m}/R = 0.03$. The nozzle/diffuser channel width is $b/R = 0.23$ ($R = D/2$). Each turbine configuration has a stator-to-rotor radius ratio $r_{\mathsf{TE}_2}/R = 2.48$. Sections 2 and 5 have radius $r_2/R = 2.15$, Fig. 4.1. The Reynolds number based on the rotor radius, R, and its peripheral velocity, ΩR, is Re $= \Omega R^2/\nu = 2.4 \times 10^5$.

Stagnation pressure loss coefficient

Fig. 4.11 illustrates the stagnation pressure loss coefficient (Eq. (4.18)) for the inlet guide vanes $(1, 2)$, nozzle $(2, 3)$, diffuser $(4, 5)$, outlet guide vanes $(5, 6)$ and discharge flow $(6, \mathsf{B})$. To each value of ζ corresponds one turbine configuration with an optimized guide vane set according to Table 4.3 and a rotor according to Fig. 4.10 operating in design conditions. It is seen that losses increase with the blockage factor ζ in all sectors. For the inlet guide vanes, this is in line with state-of-the-art cascade flows [55]. The nozzle's flow path is approximately

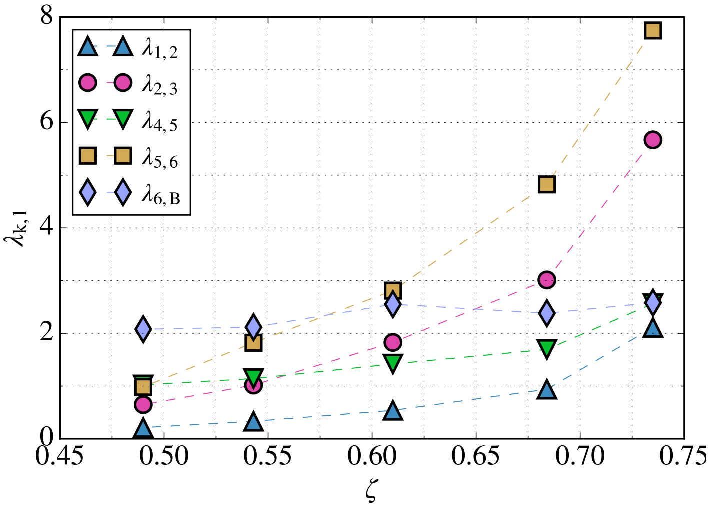

Figure 4.11: Dimensionless power losses in inlet guide vanes (1,2), nozzle (2,3), diffuser (4,5), outlet guide vanes (5,6) and outlet kinetic energy (6,B) for turbine configurations I0, I6, I7, I3 and I22 (in increasing order of ζ).

a logarithmic spiral with an internal angle α_2. As such, a higher inlet guide-vane deflection (implies higher blockage as seen in Table 4.3) translates into a longer flow path and higher loss due to viscous interaction with the nozzle walls. Losses in outlet guide vanes are dominated by the wide wakes generated by the misalignment between the vanes and the incoming flow. These losses are proportional to the body's frontal area, which is accounted for in the blockage factor ζ.

To address losses in the diffusers (Fig. 4.11), one should inspect the respective flow field. Fig. 4.12 illustrates the normalized circumferential-averaged total pressure

$$\langle \bar{p_0} \rangle^* = \frac{\langle \bar{p_0} \rangle - \min(\langle \bar{p_0} \rangle)}{\max(\langle \bar{p_0} \rangle) - \min(\langle \bar{p_0} \rangle)} \tag{4.39}$$

in two diffusers, for the configuration I0, $(\zeta, \alpha_2, \beta_4') = (0.49, 31.6°, 45°)$ and I22, $(\zeta, \alpha_2, \beta_4') = (0.74, 15.2°, 25°)$. The normalized axial and radial coordinates are $z^* = (z - z_{\text{shr}})/(z_{\text{hub}} - z_{\text{shr}})$ and $r^* = (r - r_4)/(r_5 - r_4)$, respectively. It is seen that for $\beta_4' = 25°$, the total-pressure distribution in the diffuser is less uniform, justifying the higher losses. While both cases have separation at the shroud, the effect is more widespread for the rotor with $\beta_4' = 25°$. The adverse pressure gradient is the same (from the same cross-sectional area variation). However, for $\beta_4' = 25°$, the radial velocity is lower (see the velocity triangles of Fig. 4.2), making the boundary layer more susceptible to separation.

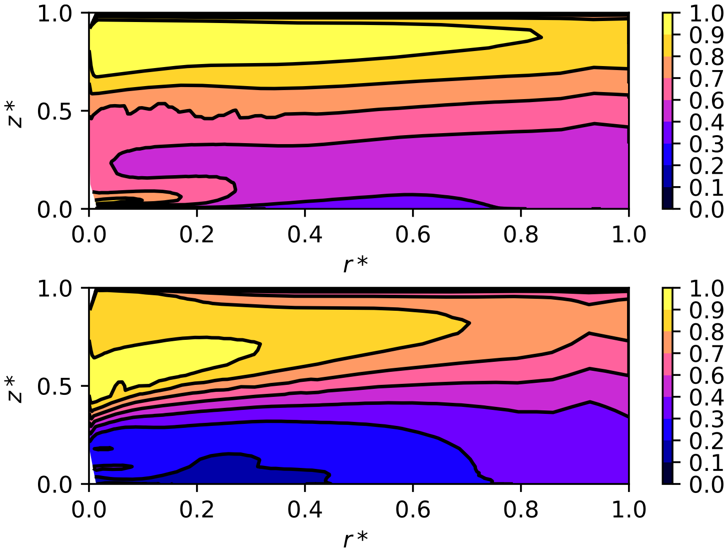

Figure 4.12: Normalized circumferential-averaged total pressure $\langle \bar{p_0} \rangle^*$ in the diffuser for turbine configurations I0 (top), with $\beta_4' = 45°$, and I22 (bottom), with $\beta_4' = 25°$.

Table 4.4: Losses comparison between turbine configuration I6 and turbine of Ref. [63].

	$\lambda_{1,3}$	$\lambda_{4,\mathrm{B}}$
Ref. [63]	0.58	12.1
Config. I6	1.35	5.08

Turbine configuration I6, $(\zeta, \alpha_2, \beta_4') = (0.54, 26.7°, 40°)$, was compared to the turbine with double rows of aerofoil shaped vanes of Ref. [63], $(\zeta, \alpha_2, \beta_4') = (0.55, 29.8°, 42.3°)$, as both have approximatelly the same blockage factor, ζ. See Table 4.5. Two factors explain the higher losses up to the rotor entry (section 3). In Ref. [63], both the inlet guide vanes and nozzle losses are calculated from a two-dimensional simulation, neglecting nozzle walls viscous losses. Additionally, aerofoils achieve better control of the velocity distribution over the guide vane and can operate at a lower $c_\mathrm{D}/c_\mathrm{L}$ than constant thickness plates. Losses after the rotor (from sections 4 to B) are significantly lower in the present design. This can be understood by considering the outlet guide vanes normalized absolute pressure distribution (Eq. (4.39)) of Fig. 4.13. It shows that the reduction of the radial distance between vane rows, $\Delta r_{1,2}$, induced a smaller wake and removed the secondary jet that forms on the suction side of the outer guide vanes in the case of Ref. [63].

Table 4.5: Losses comparison between turbine configuration I6 and turbine of Ref. [63].

	$\lambda_{1,3}$	$\lambda_{4,\mathrm{B}}$	$\lambda_{1,3}+\lambda_{4,\mathrm{B}}$
Reference	0.58	12.1	12.7
Improved	1.35	5.08	6.43

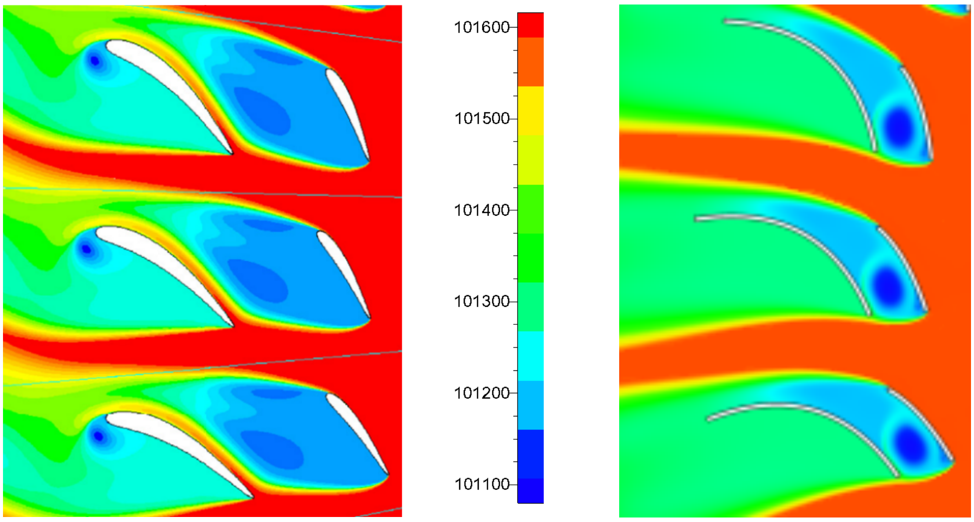

Figure 4.13: Normalized stagnation pressure distribution at the outlet guide vanes. From Ref. [63] on the left and turbine configuration I6 on the right.

Efficiency

The performance of the rotors is assessed by analysing their efficiency as defined in Eqs. (4.30) and (4.31) and considering their operation in the previously defined turbine configurations. Fig. 4.14 shows that the total-to-total efficiency decreases for $\beta_4' < 40°$. From Eq. (4.21) and Fig. 4.2 it is seen that when β_4' decreases (and by consequence, α_2), Π/Φ increases. By contrast, the rotor blades become longer and have more skin friction losses, increasing the pressure drop quantified in the coefficient Ψ. So, for $\beta_4' < 40°$ the increase in skin friction losses is larger than the increase in torque and decrease in flow rate. The total-to-static efficiency contemplates the rotor discharge kinetic energy as a loss added to the pressure coefficient Ψ (Eq. (4.31)). From Fig. 4.2 it is clear that the kinetic energy decreases with β_4', so maximum total-to-static efficiency occurs for a lower β_4' than that for maximum total-to-total efficiency. The difference between the two efficiencies quantifies the kinetic energy at the rotor outlet. For the rotors considered, maximum total-to-static turbine efficiency will occur between $\beta_4' = 25°$ and $\beta_4' = 40°$.

The efficiencies of the turbine configurations considered are compared in Fig. 4.15. It is

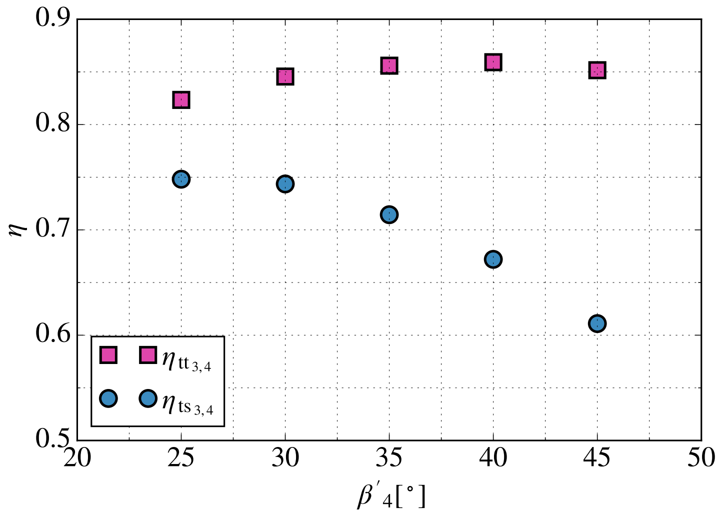

Figure 4.14: Rotor total-to-total ($\eta_{tt_{3,4}}$) and total-to-static ($\eta_{ts_{3,4}}$) efficiencies for turbine configurations I22, I3, I7, I6 and I0 (in increasing order of β'_4).

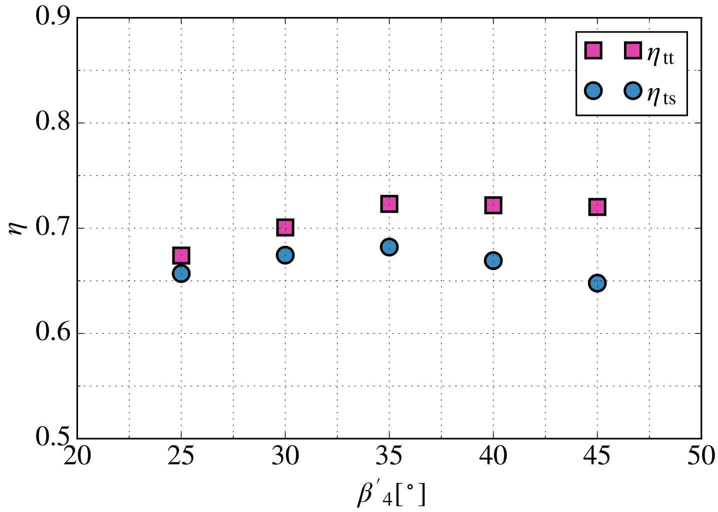

Figure 4.15: Turbine total-to-total (η_{tt}) and total-to-static (η_{ts}) efficiencies for turbine configurations I22, I3, I7, I6 and I0 (in increasing order of β'_4).

seen that a large portion of the rotor outflow kinetic energy is recovered, especially for $\beta'_4 = 40°$ and $\beta'_4 = 45°$, where the turbine η_{ts} is higher than the rotor η_{ts}. Obviously, the other turbine sectors also have their losses (turbine η_{tt} always lower than rotor η_{tt}). It is seen that for $\beta'_4 < 40°$ the other sectors introduce more losses than the kinetic energy recovered by the diffuser, since for $\beta'_4 < 40°$, the turbine η_{ts} is lower than rotor η_{ts}.

Table 4.6 compares the total-to-static efficiencies of the turbine configurations I0 and I7 with the efficiencies of the turbines with aerofoil guide vanes reported in Refs. [64] and [63]. It is seen that the efficiency increases 4.3% when comparing the turbine of Ref. [63] to the turbine configuration I0, and a decrease of 5.6% is observed between the turbine of Ref. [64] and the

Table 4.6: Efficiency comparison between turbine geometries from Refs. [63, 64] and turbine configurations I0 and I7.

	ζ	$\alpha_2[°]$	$\beta_4'[°]$	η_{ts}
Ref. [63]	0.55	29.8	42.3	0.605
Config. I0	0.49	31.6	45.0	0.648
Ref. [64]	0.65	22.2	40.0	0.738
Config. I7	0.61	22.7	35.0	0.682

turbine configuration I7. The first comparison is in line with the results presented so far, namely the significant loss reduction in the second set of guide vanes. To understand the seemingly surprising result of the second comparison, further analysis is presented.

Relative stagnation pressure loss coefficient

The normalized losses in each sector of turbine configuration I7, relative to the available pressure head, $\Lambda_{k,l}$ (Eq. (4.34) to (4.38)) , are compared to the ones from Ref. [64] in Table 4.7. In Ref. [64] there were no measurements in turbine sections $k = 5$ and 6. Despite this, it is possible to make a comparison from the available measurements. In Ref. [63] no data are available.

The relative losses in the inlet-guide-vanes $(1, 2)$ and rotor $(3, 4)$ are aligned with the results presented so far. Normalized losses for constant thickness guide-vanes are higher than in aerofoil vanes (see Section 4.3.2) and a rotor with $\beta_4' = 35°$ has lower total-to-total efficiency than one with $\beta_4' = 40°$ (see Section 4.3.2). As such, the losses in these sectors represent a higher percentage of the pressure head. By contrast, the relative loss is smaller in the nozzle $(2, 3)$ and higher on the set comprising the diffuser, outlet guide vanes and discharge $(4, \text{B})$. It is also possible to see that the increase in dimensionless partial losses after the rotor $(4, \text{B})$ dominates the difference in total-to-static efficiency between the two turbines. Such effect might be explained by the lower stator-to-rotor radius ratio of the present turbine, $r_{\text{TE}_2}/R = 2.48$, by comparison to $r_{\text{TE}_2}/R = 3.85$ in Ref. [64]. While the flow paths are shorter in the nozzle (lower $\Lambda_{2,3}$) and diffuser of the configuration I7 when compared to the turbine of Ref. [64], more kinetic energy is dissipated in the outlet guide vanes and discharge flow due to a shorter diffuser. This is because the flow at the outlet guide vanes and turbine discharge has a higher velocity. For completeness and future reference, the relative stagnation pressure loss coefficient $(\Lambda_{k,l})$ of all

Table 4.7: Relative losses comparison between the turbine of Ref. [64] and turbine configuration I7.

	$\Lambda_{1,2}$	$\Lambda_{2,3}$	$\Lambda_{3,4}$	$\Lambda_{4,\mathrm{B}}$	η_{ts}
Ref. [64]	0.010	0.052	0.110	0.090	0.738
Config. I7	0.012	0.041	0.115	0.150	0.682
Difference	0.002	-0.011	0.005	0.060	-0.056

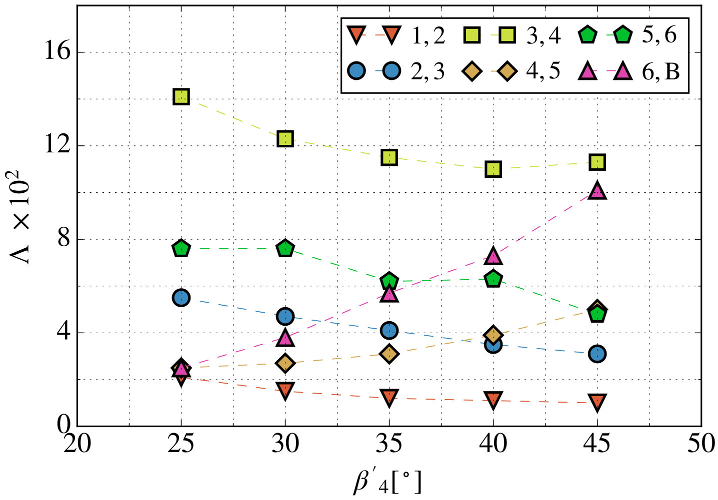

Figure 4.16: Relative stagnation pressure loss coefficients for turbine configurations I22, I3, I7, I6 and I0 (in increasing order of β'_4).

turbine configurations derived from the Selected Individuals is presented in Fig. 4.16.

4.3.3 Numerical model assessment

In this Section, the numerical modelling is assessed, namely the choices of Section 4.2.5. The case studies are Individual 7 of the optimized guide vanes and a rotor with $\beta'_4 = 35°$. As stated in Section 4.2.5, turbine performance was derived from three simulations, inlet guide vanes (1,2), rotor with nozzle and diffuser (2,5) and outlet guide vanes (5,6).

The uncertainty of a quantity of interest in a CFD solution is defined as the product of the estimated numerical error, multiplied by a safety factor, resulting in the interval around a calculated solution that contains the exact solution with 95% of confidence [111].

The uncertainty was calculated with a generalized implementation of the Grid Convergence Index. It is based on least-squares fittings on sets of four geometrically similar grids, four physical time-steps, and four residual levels of the continuity equation [112, 113]. From these, the discretization, statistical, and iterative uncertainties for the quantities of interest are derived.

Table 4.8: Comparison between two- and three-dimensional modelling uncertainty of the absolute flow angle leaving the guide vanes, α_2, and dimensionless stagnation pressure losses for Individual 7 as inlet guide vanes (inflow conditions).

	2D				3D			
h_j/h_1	α_2 [°]	$U_{\mathsf{dsc}}(\alpha_2)$ [°]	$\lambda_{1,2}$	$U_{\mathsf{dsc}}(\lambda_{1,2})$	α_2 [°]	$U_{\mathsf{dsc}}(\alpha_2)$ [°]	$\lambda_{1,2}$	$U_{\mathsf{dsc}}(\lambda_{1,2})$
1.00	22.8	0.242	0.439	0.107	23.5	0.208	0.778	0.166
1.32	22.7	0.253	0.459	0.177	23.5	0.316	0.818	0.279
1.63	22.6	0.297	0.539	0.309	23.7	0.581	0.878	0.428
1.91	22.5	0.286	0.519	0.350	23.4	0.510	0.917	0.561

The grid refinement ratio, $h_j/h_1 = (N_1/N_j)^{1/3}$, quantifies the mesh refinement, where N_1 is the number of cells in the most refined mesh and N_j the number of cells in each geometrically similar mesh. Analogously, the time refinement ratio $\Delta t_t/\Delta t_1$, quantifies the time-step refinement, where Δt_1 is the smallest time-step, and Δt_t are the other time-steps used. The normalized residual of the continuity equation $\delta_{\rho_i}/\delta_{\rho_1}$ quantifies the iterative convergence, where δ_{ρ_1} is the residual on the first iteration and δ_{ρ_i} the residual on iteration i.

Inlet guide vanes

Two and three-dimensional models of the inlet guide vanes were compared. Both cases have the same mesh distribution in the circumferential and radial directions. The two-dimensional mesh has one cell in the span-wise direction, topped by two mirror boundary conditions. The three-dimensional case has a channel height of $b/R = 0.23$ topped by two no-slip walls. In both cases, constant radial velocity and averaged static pressure were imposed as the inlet and outlet boundary conditions, respectively. The Reynolds number based on the chord of the outermost vane is Re $= V_{\mathsf{ref}}\, c_1/\nu \approx 9 \times 10^4$. Table 4.8 presents the absolute flow angle α_2 with the respective discretization uncertainty $U_{\mathsf{dsc}}(\alpha_2)$. It is seen that deflection is 0.7 to 1° higher in the two-dimensional case, which was considered acceptable. Losses are two times higher in the three-dimensional case, but as seen in Fig. 4.16, they are only 1 to 2% of the turbine's pressure head. As such, this difference does not amount to a relevant change in the turbine efficiency. For the same reason, despite the discretization uncertainty being in the same order of magnitude of the losses, the results are acceptable in the scope of this research.

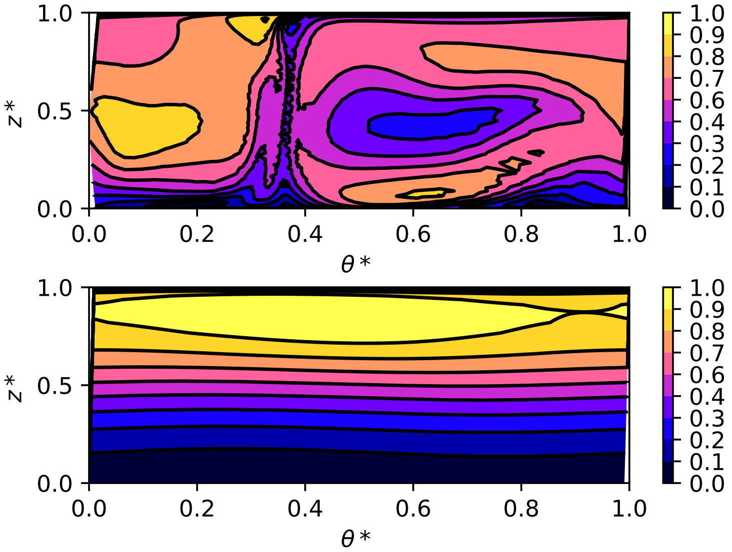

Figure 4.17: Normalized velocity magnitude V^* at the rotor outlet (top) and diffuser outlet (bottom).

Table 4.9: Discretization uncertainty results for the nozzle, rotor and diffuser simulations.

h_j/h_1	$\eta_{\text{tt}_{2,5}}$	$\eta_{\text{tt}_{3,4}}$	$\lambda_{3,4}$	$\lambda_{1,2}$	$\lambda_{4,5}$	$U_{\text{dsc}}(\eta_{\text{tt}_{2,5}})$	$U_{\text{dsc}}(\eta_{\text{tt}_{3,4}})$	$U_{\text{dsc}}(\lambda_{3,4})$	$U_{\text{dsc}}(\lambda_{1,2})$	$U_{\text{dsc}}(\lambda_{4,5})$
1.00	0.790	0.860	0.069	0.025	0.019	0.016	0.006	0.004	0.004	0.000
1.31	0.791	0.862	0.068	0.025	0.020	0.023	0.011	0.006	0.004	0.000
1.63	0.786	0.859	0.069	0.025	0.020	0.027	0.014	0.007	0.005	0.001
1.96	0.785	0.856	0.071	0.025	0.020	0.033	0.019	0.010	0.006	0.000

Nozzle, rotor and diffuser

Fig. 4.17 shows the normalized velocity magnitude,

$$V^* = \frac{V - \text{min}(V)}{\text{max}(V) - \text{min}(V)}, \tag{4.40}$$

at the rotor outlet (section 4) on top and the diffuser outlet (section 5) on the bottom. For both, $z^* = (z - z_{\text{shr}})/(z_{\text{hub}} - z_{\text{shr}})$ and $\theta^* = (\theta - \theta_{\text{ps}})/(\theta_{\text{ss}} - \theta_{\text{ps}})$ are the normalized axial and radial coordinates respectively, where the subscript ss denotes the periodic boundary on the suction side, and ps is for the pressure side. In section 5, the flow uniformity about the circumferential direction justifies using the circumferentially-averaged outlet flow of the diffuser as the outlet guide vanes inlet condition. Notice that flow periodicity on the guide vanes is different from the one on the rotor (25 vanes to 7 rotor blades).

Discretization uncertainty for this simulation is presented on Table 4.9. Here the total-to-total efficiency $\eta_{\text{tt}_{2,5}} = \Pi/(\Phi\ \Psi_{2,5})$ is applied to the sector comprising nozzle, rotor and diffuser.

Table 4.10: Comparison between two- and three-dimensional modelling uncertainty of the stagnation pressure loss coefficient of the outlet guide vanes, $\lambda_{5,6}$, and turbine discharge, $\lambda_{6,\mathrm{B}}$. Steady-state simulations.

	2D				3D			
h_j/h_1	$\lambda_{5,6}$	$U_{\mathrm{dsc}}(\lambda_{5,6})$	$\lambda_{6,\mathrm{B}}$	$U_{\mathrm{dsc}}(\lambda_{6,\mathrm{B}})$	$\lambda_{5,6}$	$U_{\mathrm{dsc}}(\lambda_{5,6})$	$\lambda_{6,\mathrm{B}}$	$U_{\mathrm{dsc}}(\lambda_{6,\mathrm{B}})$
1.00	2.87	0.12	2.23	0.37	2.79	0.34	2.87	0.31
1.32	2.87	0.19	2.23	0.57	2.83	0.44	2.79	0.51
1.63	2.81	0.37	2.55	0.95	2.83	0.57	2.67	0.76
1.91	2.95	0.37	2.41	0.99	2.89	0.64	2.57	1.01

4.3.4 Outlet guide vanes

The stagnation pressure loss coefficient of the outlet guide vanes, $\lambda_{5,6}$, and turbine discharge, $\lambda_{6,\mathrm{B}}$, and respective discretization uncertainties, $U_{\mathrm{dsc}}(\lambda_{5,6})$ and $U_{\mathrm{dsc}}(\lambda_{6,\mathrm{B}})$, are presented in Table 4.10 for the two- and three-dimensional models in steady-state. The two-dimensional meshes are identical to those used for the inlet guide vanes, but with updated boundary conditions. Constant averaged pressure was imposed as outlet condition in section 6 while constant velocity was imposed in section 5. The difference between the two models is under 2.5% for guide vane losses $\lambda_{5,6}$ and 22% for discharge losses $\lambda_{6,\mathrm{B}}$. Since discharge losses $\lambda_{6,\mathrm{B}}$ represent 6% of the pressure head available to the turbine, the significant increase of computational effort for the three-dimensional approach and the difference in total losses $\lambda_{6,\mathrm{B}}$ justify the two-dimensional approach.

Table 4.11 shows the time-averaged results for the two-dimensional model, with the same mesh and boundary conditions as in Table 4.10. By comparing the two tables, the observed difference between the two cases is at most 9% for losses in the outlet guide vanes and 14% for discharge losses. Therefore, the steady-state approach is considered sufficiently accurate, allowing much faster calculations than performing time-dependent simulations.

Numerical uncertainty

Assuming that the round-off error is negligible by using double precision (14 digits), the numerical uncertainty is the sum of the discretization and iterative uncertainties, $\xi_{\mathrm{num}} = \xi_{\mathrm{itr}} + \xi_{\mathrm{dsc}}$ [114].

The domain (2,5) covers most of the turbine dimensionless head and is used to calculate

Table 4.11: Statistical uncertainty of the outlet guide vanes and turbine discharge dimensionless stagnation pressure coefficients, $\lambda_{5,6}$ and $\lambda_{6,\mathrm{B}}$, for time-dependent simulations of Individual 7 as outlet guide vanes (outflow conditions) with two-dimensional modelling.

2D				
$\Delta t_t/\Delta t_1$	$\lambda_{5,6}$	$U_{\mathrm{sta}}(\lambda_{5,6})$	$\lambda_{6,\mathrm{B}}$	$U_{\mathrm{sta}}(\lambda_{6,\mathrm{B}})$
1.00	2.64	0.06	2.41	0.43
1.32	2.67	0.10	2.35	0.73
1.63	2.65	0.12	2.37	1.24
1.91	2.68	0.14	2.07	1.48

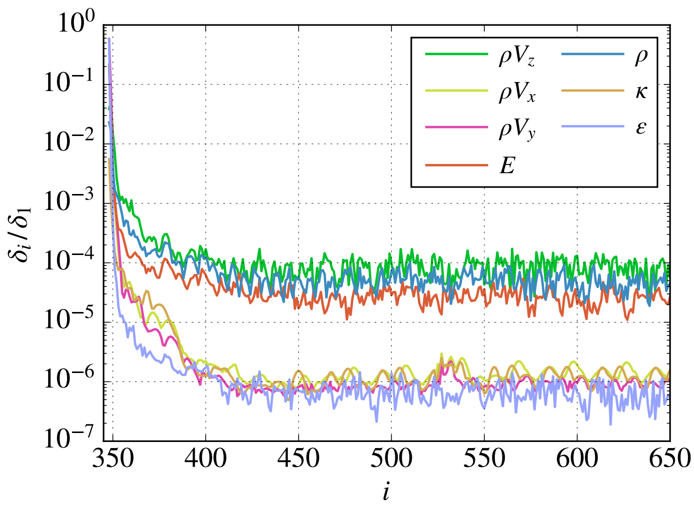

Figure 4.18: Iterative convergence of Individual 7 as outlet guide vanes (outflow conditions).

the turbine torque. Therefore, the numerical uncertainty for the total-to-total efficiency of the domain covering the nozzle, rotor and diffuser (2,5) is presented here. Iterative convergence is shown on Fig. 4.18, where is seen that the highest normalized residual on the final iteration is $\delta_{\rho V_{z_i}}/\delta_{\rho V_{z_1}} \approx 10^{-4}$. The iterative uncertainty was calculated based on the normalized residual of the continuity equation, which converged to $\delta_{\rho_i}/\delta_{\rho_1} \approx 5.8 \times 10^{-5}$ and is presented in Table 4.12.

The numerical uncertainty in the nozzle, rotor and diffuser (2,5) is $U_{\mathrm{num}}(\eta_{\mathrm{tt}_{2,5}}) \approx 0.035$.

Table 4.12: Iterative uncertainty for the total-to-total efficiency of the nozzle, rotor and diffuser (2,5), $\beta_4' = 35°$, $h_j/h_1 = 1.96$.

$\delta_{\rho_i}/\delta_{\rho_1}$	$\eta_{\mathrm{tt}_{2,5}}$	$U_{\mathrm{itr}}(\eta_{\mathrm{tt}_{2,5}})$
5.8×10^{-5}	0.785	0.002
1.6×10^{-4}	0.784	0.003
6.4×10^{-4}	0.799	0.020
1.4×10^{-3}	0.841	0.018

4.4 Conclusions

This Chapter presents the aerodynamic design and analysis of fixed-guide-vanes biradial turbines with a stator-to-rotor radius ratio $r_{\mathsf{TE}}/R = 2.48$.

The first research hypothesis was that a constant-thickness guide-vane stator could provide comparable flow deflection and blockage factors to the aerofoil-based reference cases. This hypothesis was verified, and a constant-thickness guide-vane stator with improved performance was designed.

The second research hypothesis explored was the existence of an optimum absolute flow angle at the rotor inlet that maximizes turbine efficiency by balancing rotor efficiency with stall losses on the outlet guide vanes. This hypothesis was verified, and an optimum angle was found. However, it should be noticed that this relationship is dependent on the geometric parametrization used for guide vanes and the rotor design. Other parametrizations may result in different optimum angles, especially for different stator-to-rotor radius ratios.

The conclusions taken from this Chapter can be summarized as follows:

- Flow deflection in the new inlet guide vanes is improved compared to the reference cases. For the same blockage factor ζ, deflection increases between 1 and 5° in the range $0.70 > \zeta > 0.50$.

- State-of-the-art biradial rotors have their maximum total-to-total efficiency for an inlet/exit blade metal angle $\beta_4' \approx 40°$. In contrast, the maximum total-to-static efficiency occurs for $\beta_4' \approx 25°$.

- For the tested turbine configurations, the flow deflection that maximizes turbine efficiency is $\alpha_2 = 22.7°$, which corresponds to a blockage factor $\zeta = 0.61$, and a state-of-the-art rotor with blade metal angle $\beta_4' = 35°$.

- The new design reduced the energy losses per unit of incoming kinetic energy at the outlet guide vanes by 58% for the same blockage factor.

- The improvement in outlet guide vanes performance derives from the decreased radial distance between the two rows of guide vanes, resulting in a smaller wake for the same blockage.

- Turbine configuration I0, with smaller stator-to-rotor radius ratio $r_{\mathsf{TE}}/R = 2.48$, has a total-to-static efficiency 4.3% higher than a previous turbine design with substantially larger $r_{\mathsf{TE}}/R = 3.85$.
- Turbine configuration I7, with smaller stator-to-rotor radius ratio $r_{\mathsf{TE}}/R = 2.48$ has a total-to-static efficiency 5.6% lower than a previous turbine design with substantially larger $r_{\mathsf{TE}}/R = 3.85$.
- Reducing the turbine stator-to-rotor radius ratio increases the kinetic energy (concerning the available pressure head) of the flow at the outlet guide vanes and turbine discharge. This is the reason for the efficiency drop of configuration I7 despite the reduction of losses per unit of the kinetic energy of the new guide-vane design.
- For other stator-to-rotor radius ratio and/or guide vanes geometries, maximum turbine efficiency is in the range $25° \leq \beta_4' \leq 40°$ $(15.2° \leq \alpha_2 \leq 26.7°)$.

The new guide-vane design can be scaled to find the deflection that maximizes turbine efficiency for other stator-to-rotor radius ratios. It should be noted that for turbine configuration I7, the stator-to-rotor radius ratio was decreased by 36% at the expense of 5.6% in efficiency.

Chapter 5

Improved method for biradial rotor design

The damping characteristics of OWC converters are expressed in this Chapter as a function of the turbine specific diameter. It is shown, for a given damping, that the turbine size is directly proportional to its specific diameter. The objective of this study is to obtain a new rotor geometry that simultaneously increases the turbine efficiency while decreasing its specific diameter. A new rotor geometry generation method is presented, adding more degrees of freedom to the state-of-the-art method. A commercial CFD package is then used to perform a parametric analysis using the state-of-the art geometry as a reference for performance. The effect of each geometry generation parameter over the efficiency is studied and individual optimal values are found. The rotor meridional channel width is seen to be the most influential parameter on the specific diameter. Combinations of parameter values are used to obtain improved geometries. The meridional channel width is increased in 14.5% while keeping an efficiency gain of near 1%. This low specific diameter rotor is analysed in the context of a fixed-guide-vane biradial turbine configuration. It is found that the turbine diameter can be reduced in 6.5% for the same damping characteristic, without penalising the efficiency gain.

5.1 Hypotheses and objectives

The hydrodynamic process of energy conversion of OWC WECs (wave power to air chamber pneumatic power) is dependent on the damping introduced by the air turbine [115], i.e., the relationship between the turbine pressure head, Δp, and flow rate, Q [116]. In general, the damping characteristics of air turbines depend on their shape, size and rotational speed [117]. Due to the almost quadratic damping characteristic of biradial turbines, $\Delta p \approx k_{\text{t}} Q^2$, where k_{t} is a constant related to turbine geometry and size, the rotational speed has a small or negligible effect on the flow rate for a given pressure head [64]. However, biradial turbine shape and size should be selected to maximise the efficiency of the OWC hydrodynamic process in addition to the aerodynamic process (air chamber pneumatic power to turbine shaft power). Turbomachinery theory is used here to relate these variables to operating conditions through the pressure head, $\Psi_{\text{ts}} = \Delta p/(\rho \Omega^2 D^2)$, and flow rate, $\Phi = Q/(\Omega D^3)$, coefficients [55] to give the required turbine constant,

$$k_{\text{t}} = \frac{\rho}{D^4} \frac{\Psi_{\text{ts}}(\Phi)}{\Phi^2}\,, \tag{5.1}$$

used in OWC analysis [30], where ρ is the air density, Ω the turbine rotational speed, D the turbine rotor outer diameter (size), and $\Psi_{\text{ts}}(\Phi)/\Phi^2 \approx$ constant is dependent of the turbine shape.

The biradial turbine damping constant, k_{t}, can be selected during the early stage of the WEC design phase since it is approximately independent of the turbine rotational speed, as seen in Eq. (5.1). Typically, the hydrodynamic design involves choosing the damping constant that maximizes wave-to-pneumatic power conversion [118]. For a given constant, decreasing the ratio $\Psi_{\text{ts}}(\Phi)/\Phi^2$ results in a smaller turbine and, presumably, lower manufacturing costs.

In selection of turbomachinery for conventional applications, it is common to use dimensionless parameters [55, 119, 120] such as the non-dimensional specific speed (also known as shape parameter),

$$\Omega_{\text{s}} = \left(\frac{\Phi^{\frac{1}{2}}}{\Psi_{\text{ts}}^{\frac{3}{4}}} \right)_{\Phi=\Phi_{\text{des}}}\,, \tag{5.2}$$

and the non-dimensional specific diameter,

$$D_{\text{s}} = \left(\frac{\Psi_{\text{ts}}^{\frac{1}{4}}}{\Phi^{\frac{1}{2}}} \right)_{\Phi=\Phi_{\text{des}}} , \tag{5.3}$$

that are formed by combining the pressure head coefficient, Ψ, and the flow rate coefficient, Φ, to eliminate the turbine rotor diameter, D, and speed Ω, respectively.

Cordier [55] was the first to compile data regarding the specific speed and specific diameter of hydropower turbines at best efficiency conditions. By plotting in a $(\Omega_{\text{s}}, D_{\text{s}})$ diagram, it is seen that the specific diameter, D_{s}, decreases as the specific speed, Ω_{s}, increases. It is also seen that the specific speed and diameter characterize the geometry of turbomachine (axial, radial or mixed). As such, Cordier's diagram became a usefull tool in turbomachinery preliminary design. An analogous study with self-rectifying turbines [51], but with averaged values, rather than instantaneous ones, showed the same relation between specific speed and diameter.

From Eqs. (5.1) and (5.3) it is easily deducted that the turbine damping constant can alternatively be expressed as function of the specific diameter, D_{s},

$$k_{\text{t}} = \rho \left(\frac{D_{\text{s}}}{D} \right)^{4} , \tag{5.4}$$

showing a constant ratio between the turbine rotor diameter, D, and the turbine specific diameter, D_{s}, as should be expected.

The main objective of the research presented in this Chapter is to design new biradial rotors that increase turbine efficiency and decrease the specific diameter, D_{s}.

The blade load distribution is known to affect the efficiency of turbomachines [121, 122], and has been the subject of several studies [123, 124]. The design method presented in Ref. [61] is restricted to a constant load along the streamwise direction at the blade mean line. As such, a new iteration of this method with improved control over the load distribution is implemented.

It is also hypothesised that adjusting the design pressure gradient along the streamwise direction might improve efficiency, a feature added to the design method that was also not present in Ref. [61]. Other features are discussed in Section 5.2.2.

The objectives set for this Chapter were:

- to develop a new rotor geometry generation method that controls the blade loading and streamwise pressure gradient;
- characterize the effect of the design parameters on the rotor efficiency and specific diameter;
- identify the range of specific diameters for which the rotor operates efficiently;
- obtain a rotor geometry with higher efficiency in design conditions than the reference case [62];
- obtain a rotor geometry for that decreases the specific diameter of the turbine configuration I7 presented in Chapter 4.

5.2 Methods

This study takes the design method and geometry presented in Ref. [61] and the numerical studies reported in Chapter 3 and Chapter 4 as references . It uses a three-dimensional Reynolds-Averaged Navier-Stokes (RANS) equations solver to evaluate performance.

The geometry introduced in Ref. [61] was used as the reference rotor to establish a baseline case with the generation method presented here. Then, new rotor designs were created by parametric variation, and the influence of each parameter on the rotor efficiency was evaluated. Subsequently, the parameters were combined to obtain an improved design with the specific diameter of the reference rotor and another improved design for a lower specific diameter.

The research procedure of this study can be summarized as follows:

1. identification of rotor parameters with potential influence over the specific diameter;
2. development of a new parametrised biradial rotor design method;
3. CFD analysis to the effect of parameter values over rotor efficiency;
4. design of two new rotor geometries according to the objectives;
5. CFD analysis of the new designs;
6. integration of results with data from Chapter 4.

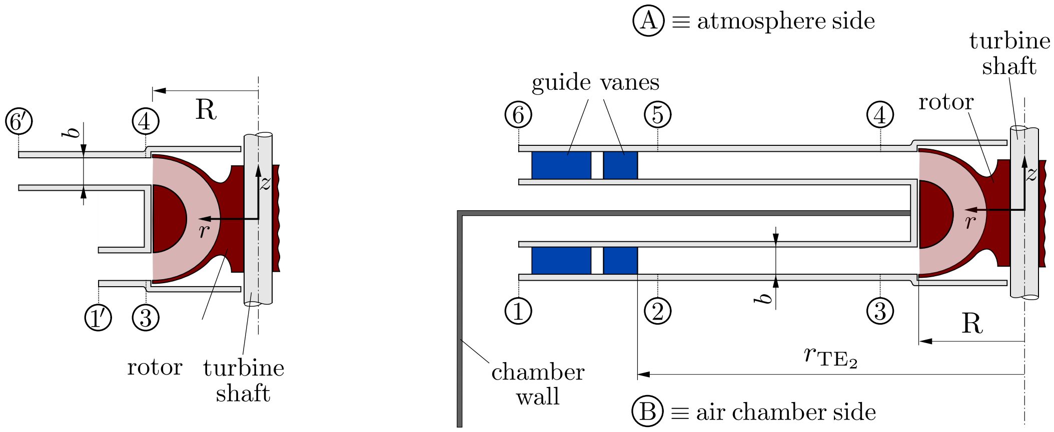

(a) Rotor domain for CFD simulations. (b) Turbine configuration I7 from Chapter 4.

Figure 5.1: Meridional view of the geometries studied in Chapter 5.

The domain used in this Chapter for design, simulation and analysis is illustrated in Fig. 5.1a. Here the section labels, k, inside circles refer to exhalation flow.

5.2.1 Specific diameter and rotor design

Classic turbomachinery one-dimensional approach is used here to express the specific diameter, D_s with respect to rotor design parameters and operating conditions.

By introducing the torque coefficient, $\Pi = T/(\rho\Omega^2 D^5)$, and turbine efficiency, $\eta_\mathrm{ts} = \Pi/(\Phi\Psi_\mathrm{ts})$ definitions in Eqs. (5.1) and (5.4), the specific diameter, D_s, can be written as

$$D_\mathrm{s}^4 = \frac{\Pi(\Phi)}{\Phi^3 \eta_\mathrm{ts}(\Phi)}\,, \tag{5.5}$$

where T is the rotor torque. It is easily seen that improving the ratio $\Psi_\mathrm{ts}(\Phi)/\Phi^2 = D_\mathrm{s}^4$ can be achieved by adjusting the turbine shape, e.g. by adjusting the rotor blade metal angles (effect over Π/Φ), reducing losses across turbine sectors (effect over η_ts) or by increasing the rotor passage width (effect over Φ). Interestingly, Eq. 5.5 shows that turbine efficiency affects not only the aerodynamic process, but also the hydrodynamic one. An efficient turbine is smaller than a less efficient one at a given OWC device with damping constant k_t.

The velocity diagrams at the entry to (subscript 3) and exit from (subscript 4) the rotor, at near design conditions, are represented in Fig. 5.2. For a rotor blade metal angle β_3' (red full), the inlet absolute velocity V_3 (blue dashed) should be imposed to compensate for the incidence/slip velocities, $V_{3\mathrm{s}}$ and $V_{4\mathrm{s}}$, resulting in zero incidence and minimum rotor outlet kinetic

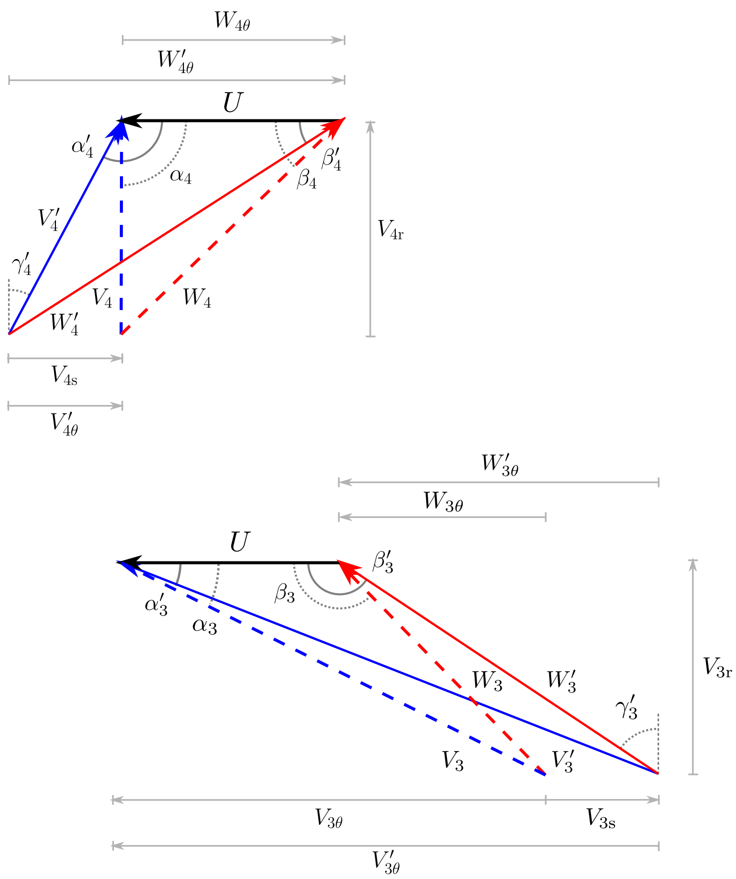

Figure 5.2: Rotor inlet and outlet velocity diagrams in design conditions. Theoretical diagrams for infinite infinitesimal thin blades in full lines and diagrams for minimization of incidence losses and outlet kinetic energy in dashed lines (see Chapter 3).

energy conditions (See Chapter 3). At the outlet, the rotor with a blade metal angle $\beta'_4 = \beta'_3$ (red full) and inlet velocity V_3 (blue dashed), discharges at an angle α_4 (blue dashed) due to the slip velocity $V_{4\text{s}}$.

From the velocity diagrams, the mechanical energy supplied to the rotor per unit mass is

$$\frac{T\Omega}{\rho Q} = \frac{\Omega D}{2} V_{3\text{r}} \left(\cot \alpha_3 - \cot \alpha_4 \right), \tag{5.6}$$

as given by the Euler turbomachinery equation [55]. Where $V_{3\text{r}} = V_{4\text{r}}$ is the rotor inlet absolute velocity, and α_3 and α_4 are the absolute flow angles at the rotor inlet and outlet, respectively. The dimensionless energy coefficient is then

$$\frac{\Pi}{\Phi} = \frac{V_{3\text{r}}}{U_3} \left(\cot \alpha_3 - \cot \alpha_4 \right), \tag{5.7}$$

where $U_3 = U_4 = \Omega D/2$ is the blade tip speed at the inlet and outlet. The flow rate coefficient is

$$\Phi = \frac{\pi}{2} \frac{V_{3\mathrm{r}}}{U_3} \frac{b}{D} , \tag{5.8}$$

where b is the rotor meridional channel width at the rotor inlet and outlet. The ratio between the rotor tip speed and the radial component of the absolute velocity at the rotor inlet/outlet can be expressed as a function of the rotor outlet conditions in the form

$$\frac{U_3}{V_{3\mathrm{r}}} = \frac{U_4}{V_{4\mathrm{r}}} = \cot\beta_4 + \cot\alpha_4 \ . \tag{5.9}$$

In Eq. (5.9) it is considered incompressible flow, incidence and slip, and the turbine's inherent symmetry resulting in $V_{3\mathrm{r}} = V_{4\mathrm{r}}$.

The specific diameter in Eq. (5.5) can then be rewritten as

$$D_{\mathrm{s}}^4 = \left(\frac{2}{\pi}\right)^2 \left(\frac{b}{D}\right)^{-2} \eta_{\mathrm{ts}}^{-1} \big(\cot\alpha_3 - \cot\alpha_4\big)\big(\cot\beta_4 + \cot\alpha_4\big) \, . \tag{5.10}$$

From Eq. (5.10), it is seen that the specific diameter D_{s} is function of b/D, β_4, α_3, α_4 and η_{ts}. Remember from Chapter 3 that flow rate and guide-vane deflection are such that incidence losses and rotor outlet kinetic energy ($\alpha_4 \approx \pi/2$) are minimum in design conditions.

Results from Chapters 3 and 4 show that small blade metal angles, β_4', favour the rotor total-to-static efficiency and, trough its influence over the turbine efficiency, η_{ts}, may decrease the specific specific diameter D_{s}. However, the blade metal angle is related to the absolute inlet flow angle, α_3, and relative outlet flow angle and, β_4', trough the incidence/slip velocities (see Chapter 3). Reducing these angles directly increases the specific diameter, D_{s}, through the terms $\cot(\alpha_3)$ and $\cot(\beta_4)$, which should be more influential than efficiency gains. As such, neither the blade metal angle, β_4', nor the absolute inlet flow angle, α_3 are tuned in the present research.

The meridional channel height to rotor diameter ratio b/D is, therefore, the main design parameter influencing the specific diameter D_{s} for constant absolute inlet flow angle, α_3, and relative outlet flow angle, β_4. Other rotor design parameters related to the flow channel and rotor blade geometries have an indirect influence on D_{s} through its effect on the turbine efficiency

η_{ts}.

To assess the efect of the new rotor designs over turbine configuration I7 of Chapter 4, data is crossed between the results of Chapter 4 and the rotor simulations of the present Chapter. The necessary equations are described in Section 5.2.4.

5.2.2 Rotor design

The biradial turbine rotor design was first introduced in Ref. [61]. Inviscid flow and infinite infinitesimal thin blades were assumed to define the blade mean three-dimensional line geometry. As a design condition, the projection of the mean line into the meridional plane is prescribed as a semi-circle, thus defining its axial and radial coordinates. The circumferential coordinate is calculated by setting the inlet/outlet blade metal angle, and imposing a linear distribution of the relative circumferential velocity along the streamwise direction (swirl) [95]. The blade's mean surfaces are a linear interpolation between two three-dimensional curves on the hub and shroud surfaces. The method begins by applying the circumferential coordinate of the mean line to the entire blade span. Then the axial and radial coordinates at the hub and shroud are calculated from mass conservation, assuming free vortex distribution for the meridional velocity, prescribing the flow channel height at the inlet/outlet, and constant relative velocity distribution in the streamwise direction.

The method discussed in this Chapter generalises the original method [61] by introducing several changes: (i) the projection of the mean line into the meridional plane is an ellipse, (ii) the swirl distribution is adjustable, (iii) the streamwise relative flow velocity follows an adjustable distribution along the mean line, and (iv) the meridional velocity distribution between the hub and shroud is better estimated.

The blade mean line projection into the meridional plane is represented in Fig. 5.3 by the ellipse arc ABC centred on point D. Point B lies on the symmetry plane, and the endpoints A and C lie at the rotor inlet and outlet, respectively. The ellipse arc has the semi-axes $\hat{\zeta}_{\text{a}}$ aligned with the axial direction and $\hat{\zeta}_{\text{b}}$ with the radial direction. Consider a point E on the ellipse perimeter, and the angle $\delta = \widehat{BDE}$, with $\delta = 0$ at point $E \equiv B$, and $\delta = \pm\pi/2$ at C and A,

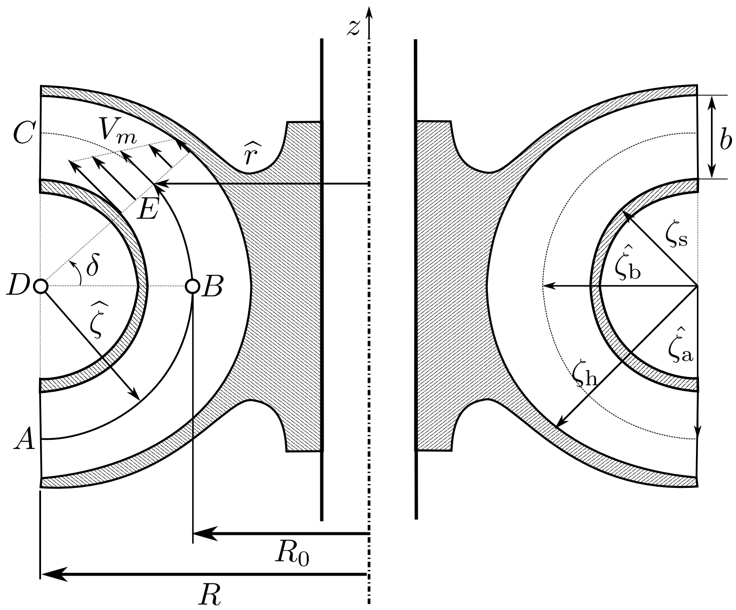

Figure 5.3: Projection into a meridional plane of the mean line of the duct formed by two neighbouring blades. Adapted from Ref. [61]

respectively (C is at the rotor outlet). The distance $\hat{\zeta}$ between points E and D is

$$\hat{\zeta}(\delta) = \left[\left(\hat{\zeta}_{\mathsf{a}} \sin\phi(\delta) \right)^2 + \left(\hat{\zeta}_{\mathsf{b}} \cos\phi(\delta) \right)^2 \right]^{1/2} , \tag{5.11}$$

where the ellipse parametric angle ϕ is expressed as a function of δ as

$$\tan\phi = \frac{\hat{\zeta}_{\mathsf{b}}}{\hat{\zeta}_{\mathsf{a}}} \tan\delta \, . \tag{5.12}$$

The radial coordinate of point E on the ellipse perimeter is an even function,

$$\hat{r}(\delta) = R - \hat{\zeta}(\delta) \cos\delta \ , \tag{5.13}$$

being $\hat{r}(\pm\pi/2) = R$ and $\hat{r}(0) = R - \hat{\zeta}_{\mathsf{b}}$. The distance between a point E on the ellipse perimeter and the symmetry plane, which contains line segment $\overline{DB}$ and is normal to the rotation axis, is

$$\hat{z}(\delta) = \hat{\zeta}(\delta) \sin\delta \ . \tag{5.14}$$

Note that $z = 0$ on the symmetry plane and $z < 0$ at the rotor inlet. Finally, the length of the elliptical arc between point A, where $s(-\frac{\pi}{2})=0$, and any point on the mean line, is given by

$$s(\delta)=\hat{\zeta}_{\mathsf{a}}\int_{\phi(-\frac{\pi}{2})}^{\phi(\delta)}\left[1-e^2\sin^2\phi\right]^{1/2}\mathsf{d}\phi\,, \tag{5.15}$$

where the eccentricity of the semi-ellipse ABC is

$$e=\left(1-\frac{\hat{\zeta}_{\mathsf{b}}}{\hat{\zeta}_{\mathsf{a}}}\right)^{\frac{1}{2}}, \tag{5.16}$$

in case $\hat{\zeta}_{\mathsf{a}}>\hat{\zeta}_{\mathsf{b}}$. Taking $s_{\mathsf{B}}=s(0)$ it is

$$s_{\mathsf{B}}\approx\frac{\pi}{2}\hat{\zeta}_{\mathsf{a}}\left(1-\frac{e^2}{4}+\frac{3e^4}{32}\right)\;. \tag{5.17}$$

The coordinates $\hat{r}$ and $\hat{z}$ of a point E, with coordinates $(\hat{r},\hat{\theta},\hat{z})$ on the blade mean line, are calculated from Eqs. (5.13) and (5.14), respectively. Determining the corresponding circumferential coordinate $\hat{\theta}$ requires further assumptions.

Consider that the rotor has infinite infinitesimal thin blades that perfectly guide the flow. Then, the blade mean-line is tangent to the relative flow velocity vector $\mathbf{W}'$. At point E, $\hat{\gamma}$ is defined as the angle between $\mathbf{W}'$ and the differential vector d$\mathbf{s}$ tangent to the ellipse arc ABC on the meridional plane S, represented in 5.3 and 5.4, i.e., γ is the angle between the relative flow velocity and the meridional direction. Moreover, d$s=\hat{\zeta}\,$dδ and $\tan\hat{\gamma}=\hat{r}\,d\hat{\theta}/ds$, which allows the circumferential coordinate $\hat{\theta}(\delta)$ definition as

$$\hat{\theta}(\delta)-\hat{\theta}(-\tfrac{\pi}{2})=\int_{-\frac{\pi}{2}}^{\delta}\frac{\tan\hat{\gamma}(\delta)}{\hat{r}(\delta)}\hat{\zeta}(\delta)\;\mathsf{d}\delta\;. \tag{5.18}$$

As the second design condition, a smooth variation for the relative flow velocity along the streamwise direction is specified as an even function of δ:

$$\hat{W}'(\delta)=\hat{W}'(-\tfrac{\pi}{2})\left[1+\kappa_w\sin\left(\pi\frac{s(\delta)}{s_B}\right)\right]\;, \tag{5.19}$$

where κ_w is a design parameter to adjust the pressure gradient along the streamwise direction $\mathbf{du}$. See Fig. 5.4.

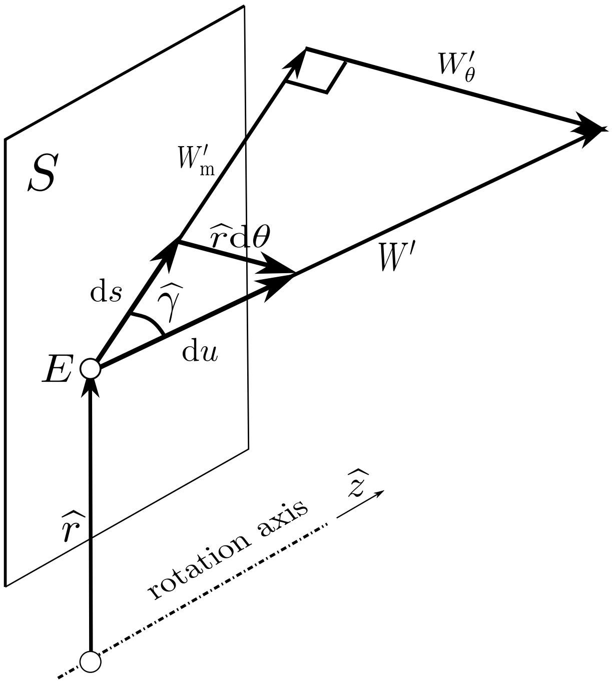

Figure 5.4: Velocity diagram at a point E on the rotor duct mean line. Plane S is the meridional plane containing E, element ds and meridional velocity $W'_{\rm m}$. The relative flow velocity $\mathbf{W}'$ makes an angle $\hat{\gamma}$ with plane S ($\gamma < 0$ for $\delta > 0$). Adapted from Ref. [61].

As the third design condition, the swirl distribution of the relative flow, $\widehat{rW}'_\theta$, is prescribed along the meridional coordinate s, as a function of δ. Since the biradial rotor is symmetric with respect to a plane that contains point B, the swirl distribution $\widehat{rW}'_\theta(\delta)$ should be an odd function and $\hat{\gamma}(0) = 0$. For $\delta \leq 0$, it is

$$\widehat{rW}'_\theta(\delta)_{AB} = R\hat{W}'(-\tfrac{\pi}{2})\sin\hat{\gamma}(-\tfrac{\pi}{2})\left(1 - f(\delta)\right). \tag{5.20}$$

Note that $\hat{W}'_\theta = \hat{W}'\sin\hat{\gamma}$ (see Figs. 5.2 and 5.4) and $f(\delta) \in [0, 1]$ is a design function that controls the swirl distribution between A and B. A cubic Bézier curve [93] is used to define $f(\delta)$ as

$$\mathbf{B}(\upsilon) = (1-\upsilon)^3\mathbf{P}_0 + 3(1-\upsilon)^2\upsilon\mathbf{P}_1 + 3(1-\upsilon)\upsilon^2\mathbf{P}_2 + \upsilon^3\mathbf{P}_3, \tag{5.21}$$

where $\mathbf{B}(\upsilon) = \left(s(\delta)/s_B\,,\, f(\delta)\right)$, with control points $\mathbf{P}_0 = (0, 0)$, $\mathbf{P}_1 = (a_1, 0)$, $\mathbf{P}_2 = (a_2, 1)$ and $\mathbf{P}_3 = (1, 1)$, and internal parametric variable $\upsilon(\delta)$. Hence,

$$f(\delta) = 3\upsilon(\delta) - 6\upsilon^2(\delta) + 4\upsilon^3(\delta)\,, \tag{5.22}$$

where $\upsilon(\delta)$ is the numerical solution of

$$\frac{s(\delta)}{s_B} = (3a_1 - 3a_2 + 1)\upsilon^3(\delta) - 6a_1\upsilon^2(\delta) + (3a_1 + 3a_2)\upsilon(\delta)\,, \tag{5.23}$$

resulting in $\widehat{rW}'_\theta(-\frac{\pi}{2}) = R\hat{W}'_A \sin\hat{\gamma}_A$ and $\widehat{rW}'_\theta(0) = 0$.

For $\delta > 0$, it is $\mathbf{B}(\upsilon) = \big(s(-\delta)/s_B\,,\, f(\delta)\big)$ and $\widehat{rW}'_\theta(\delta)_{BC} = -\widehat{rW}'_\theta(\delta)_{AB}$. Note that $\hat{W}'_\theta$ is positive in the direction of $\mathbf{\Omega}r$, and $\hat{\gamma} = \hat{\beta}' - \pi/2$, where $\hat{\beta}'$ is the blade metal angle. For $\delta < 0$, it is $\hat{W}'_\theta > 0$ and $\hat{\gamma} > 0$.

Given the design parameters a_1 and a_2 for the swirl distribution, the rotor blade angle at the mean line can be calculated as

$$\sin\hat{\gamma}(\delta) = \frac{\widehat{rW}'_\theta(\delta)}{\hat{r}(\delta)\hat{W}'(\delta)}\,, \tag{5.24}$$

concluding the necessary steps to calculate the mean line circumferential coordinate $\hat{\theta}(\delta)$ with Eq. (5.18). Remember that radial and axial coordinates, $\hat{r}$ and $\hat{z}$, are given by Eqs. (5.13) and (5.14).

The blade definition along the spanwise direction is as follows. As in Ref. [61], a constant circumferential blade coordinate along the span is adopted for a given streamwise coordinate, $\theta(\zeta, \delta) = \hat{\theta}(\delta)$. Note that this assumption is only valid for straight blade shapes along the span and without lean. Then, any point (r, z) of the blade projection on the meridional plane S is defined by the angle δ and its distance ζ to point D,

$$r(\zeta, \delta) = R - \zeta(\delta)\cos\delta \tag{5.25}$$

and

$$z(\zeta, \delta) = \zeta(\delta)\sin\delta\,. \tag{5.26}$$

To calculate $\zeta(\delta)$, a system of two equations related to the flow rate is used. For incompressible flow, the volumetric flow rate is constant along the streamwise direction and can be calculated from the velocity triangle evolution (see 5.2). It can then be expressed as a function of coordinate ζ, giving the first equation,

$$2\pi \int_{\zeta_{\mathsf{h}}(\delta)}^{\zeta_{\mathsf{s}}(\delta)} W'_{\mathsf{m}}(\zeta,\delta)\tau(\zeta,\delta)r(\zeta,\delta)\mathsf{d}\zeta = 2\pi\, R\, b\, V_{2r}\,, \tag{5.27}$$

where $b = \zeta_{\mathsf{s}}(\pm\pi/2) - \zeta_{\mathsf{h}}(\pm\pi/2)$ is the inlet/outlet channel height, and

$$\tau(\zeta,\delta) = 1 - \frac{Zt(\zeta,\delta)}{2\pi(R-\zeta\cos\delta)\cos\gamma(\zeta,\delta)}\,, \tag{5.28}$$

is a dimensionless blockage factor that takes into account the blade thickness ($\tau(\zeta,\delta) < 1$), see Ref. [61]. Here, Z is the number of rotor blades and $t(\zeta,\delta)$ is the blade thickness.

Let Γ be a surface of revolution generated by rotating the ellipse arc ABC around the rotor axis. Assume that surface Γ is a stream surface that divides the rotor into two subspaces, one adjacent to the hub and the second adjacent to the shroud. The flow rate equals one-half of the total flow rate through each one. Then, the second equation can then be written as

$$2\pi \int_{\zeta_{\mathsf{h}}(\delta)}^{\hat{\zeta}(\delta)} W'_{\mathsf{m}}(\zeta,\delta)\tau(\zeta,\delta)r(\zeta,\delta)\mathsf{d}\zeta \;\; - 2\pi \int_{\hat{\zeta}(\delta)}^{\zeta_{\mathsf{s}}(\delta)} W'_{\mathsf{m}}(\zeta,\delta)\tau(\zeta,\delta)r(\zeta,\delta)\mathsf{d}\zeta \;= 0 \tag{5.29}$$

Due to the curvature of line ABC, the velocity component $W'_{\mathsf{m}}(\zeta,\delta)$ is expected to vary with ζ. Having assumed zero blade lean, only the meridional (W'_{m}) and the circumferential (W'_θ) velocity components along the blade mean line induce centrifugal acceleration in the meridional plane [125]. Hence, on the mean line, the pressure gradient in the ζ direction is

$$\frac{1}{\rho}\frac{\mathsf{d}p(\hat{\zeta}(\delta))}{\mathsf{d}\zeta} = \frac{\hat{W}'^2_{\mathsf{m}}(\delta)}{\hat{\zeta}(\delta)} - \frac{(\hat{W}'_\theta(\delta) + \Omega\hat{r}(\delta))^2}{\hat{r}(\delta)}\cos\delta\,, \tag{5.30}$$

where ζ is the direction normal to the streamwise coordinate s on the meridional plane, Fig. 5.3. Note that the two terms of the right-hand side of Eq. (5.30) correspond to two centrifugal forces: the first one is due to the axisymmetric swirling flow, and the second one to the flow turning from centripetal to centrifugal along the rotor blade ducts.

The distribution of the meridional velocity ($W'_{\mathsf{m}}(\zeta,\delta)$) from hub to shroud is dependent on the pressure gradient normal to the stream surface, as given by Eq. (5.30), and its calculation needs further assumptions.

As a design condition, steady and inviscid relative flow is considered. Furthermore, the absolute flow in the rotor is assumed irrotational ($\nabla \times \mathbf{V} = 0$). Then [126]

$$\mathrm{d}\left(\frac{W'^2 - \Omega^2 r^2}{2}\right) + \frac{1}{\rho}\mathrm{d}p = 0\,. \tag{5.31}$$

With reference to Figs. 5.3 and 5.4, it is $\mathrm{d}r = -\mathrm{d}\zeta \cos\delta$ and $\hat{W}'_{\mathrm{m}} = \hat{W}' \cos\hat{\gamma}$. Combining Eqs. (5.30) (5.31) gives

$$\frac{\mathrm{d}W'(\hat{\zeta}(\delta))}{\mathrm{d}\zeta} = \cos\delta \sin\hat{\gamma}(\delta)\left(\frac{\hat{W}'(\delta)\sin\hat{\gamma}(\delta)}{\hat{r}(\delta)} + 2\Omega\right) - \frac{\hat{W}'(\delta)\cos^2\hat{\gamma}(\delta)}{\hat{\zeta}(\delta)}\,. \tag{5.32}$$

Inspection of Eq. (5.32) reveals that the hub to shroud velocity variation depends on the curvature radius of the duct mean line ($\hat{\zeta}(\delta)$) and the relative velocity ($\hat{W}'(\delta)$). For $\delta = 0$, it is $\hat{\gamma} = 0$, giving

$$\frac{\mathrm{d}W'(\hat{\zeta}(0))}{\mathrm{d}\zeta} = -\frac{(1+\kappa_w)\hat{W}'(-\frac{\pi}{2})}{\hat{\zeta}_{\mathrm{b}}}\,, \tag{5.33}$$

where

$$\frac{\hat{W}'(0)}{\hat{W}'(-\frac{\pi}{2})} = 1 + \kappa_w\,. \tag{5.34}$$

For $\delta = -\pi/2$ it is $\hat{\gamma} = \hat{\gamma}_{\mathrm{A}}$, and for $\delta = \pi/2$ it is $\hat{\gamma} = \hat{\gamma}_{\mathrm{C}} = -\hat{\gamma}_{\mathrm{A}}$, then

$$\frac{\mathrm{d}W'(\hat{\zeta}(\pm\pi/2))}{\mathrm{d}\zeta} = -\frac{\hat{W}'(\pm\frac{\pi}{2})\cos^2\hat{\gamma}_{\mathrm{A}}}{\hat{\zeta}_{\mathrm{a}}}\,. \tag{5.35}$$

Eqs. (5.33) and (5.35) show that the free-vortex solution assumed in the original method [61] applies only at $\delta = 0$. In this way, the meridional velocity is approximated by

$$W'_{\mathrm{m}}(\zeta,\delta) = \left(\hat{W}'(\delta) + \frac{\mathrm{d}W'(\hat{\zeta}(\delta))}{\mathrm{d}\zeta}\left(\zeta(\delta) - \hat{\zeta}(\delta)\right)\right)\cos\gamma(\zeta,\delta)\,. \tag{5.36}$$

Note that Eq. (5.32) is not a even function while the rotor must be symmetrical with respect to $\delta = 0$. To assure the rotor symmetry, the hub ($\zeta_{\mathrm{h}}(\delta)$) and shroud ($\zeta_{\mathrm{s}}(\delta)$) contours are calculated from mass balances only on the centrifugal part of the rotor ($\delta > 0$) by making $\delta = |\delta|$ in Eqs. (5.27) and (5.29). In this way, $W'_{\mathrm{m}}(\zeta,\delta)$ becomes an even function of δ.

Since the blade has a constant circumferential coordinate along the span for a given streamwise coordinate, $\theta(\zeta,\delta)=\hat{\theta}(\delta)$, the blade's mean surface is generated by a straight line through the point D that moves along the blade channel mean line and intersects the rotor axis at an angle $\pi/2-\delta$. Because the blade is twisted, the angle $\gamma(\zeta,\delta)$ is different from $\hat{\gamma}(\delta)$ for $\zeta\neq\hat{\zeta}$. Therefore

$$\tan\gamma(\zeta,\delta)=\frac{\hat{\zeta}(\delta)(R-\zeta\cos\delta)}{\zeta(R-\hat{\zeta}(\delta)\cos\delta)}\tan\hat{\gamma}(\delta)\,. \tag{5.37}$$

5.2.3 Numerical model

The flow solver used is the FINE/Turbo v15.1 from NUMECA International [84]. It is a structured-mesh three-dimensional, finite-volume, density-based RANS solver with a cell-centred approach and explicit time-marching multi-stage Runge-Kutta scheme. Viscous fluxes are approximated by central differencing schemes using a Jameson-type artificial dissipation technique with second and fourth-order derivatives. Air is assumed to be a perfect gas. Time-marching algorithms lack iterative efficiency, converging slowly when calculating low subsonic compressible flows. Choi-Merkle pre-conditioning [85] and implicit residual smoothing were used to accelerate convergence.

The flow was assumed to be fully turbulent and in steady-state conditions. Turbulence was modelled with the Spalart-Almaras model corrected for rotation and curvature effects (SARC) [86]. This model has shown good performance and accuracy in simulations of biradial rotors compared to the more complex Shear-Stress Transport model, as reported in Chapter 3. The no-slip condition was used on the walls, where the shear stress was determined from its definition. Therefore the distance of the mesh first element to the wall complies with $y^+<1$.

Uniform distributions of the absolute velocity vector and turbulent quantities ($\nu_t/\nu=5$ and $T_u=0.05$) were used as inlet boundary conditions, while a uniform pressure distribution was specified as the outlet boundary conditions. The initial flow field was derived from a constant rothalpy distribution, along axisymmetric stream surfaces across the domain, extrapolated from the inlet conditions.

A verification analysis of the reference biradial rotor simulation results was performed to support the present study (see Appendix A). The purpose was to define appropriate meshes for rotor simulations, and to estimate the uncertainty in the calculation of the rotor total-to-static

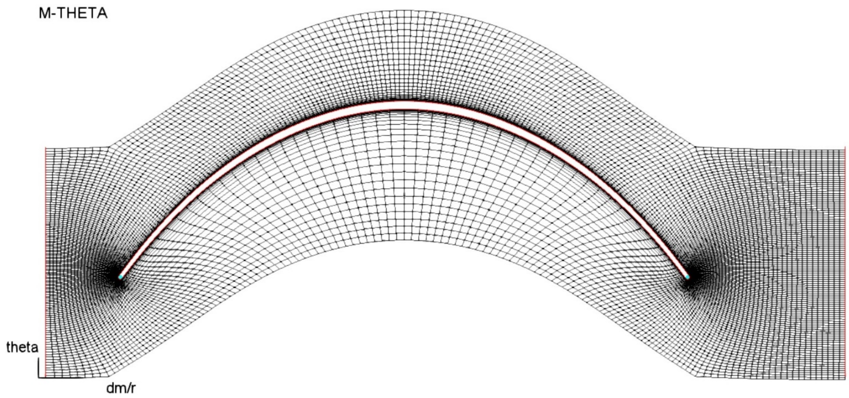

Figure 5.5: Rotor blade-to-blade mesh.

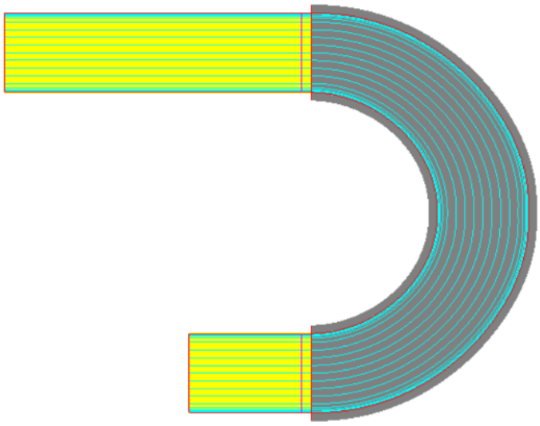

Figure 5.6: Meridional lines used for mesh generation.

efficiency (metric defined in Section 5.2.4). The round-off error was considered negligible by using double precision (14 digits) and, in such conditions, the numerical uncertainty is the sum of the discretisation and iterative uncertainties [114], $\xi_{\text{num}} = \xi_{\text{itr}} + \xi_{\text{dsc}}$.

The computational meshes were generated with IGG and Autogrid from NUMECA International [88]. The process starts with a two-dimensional structured mesh generated in the mid-span blade-to-blade plane, Fig. 5.5. This mesh is then mapped into three-dimensional surfaces of revolution [89] along the span, Fig. 5.6. Finally, the mapped two-dimensional meshes are connected, forming a multi block-structured mesh for the three-dimensional domain, Fig. 5.7.

5.2.4 Performance metrics

The biradial rotor performance analysis considers only the sector limited by sections $(k, l) = (2, 3)$, Fig. 5.1a. Outflow conditions are considered in this Chapter since performance is independent of flow direction due to symmetry.

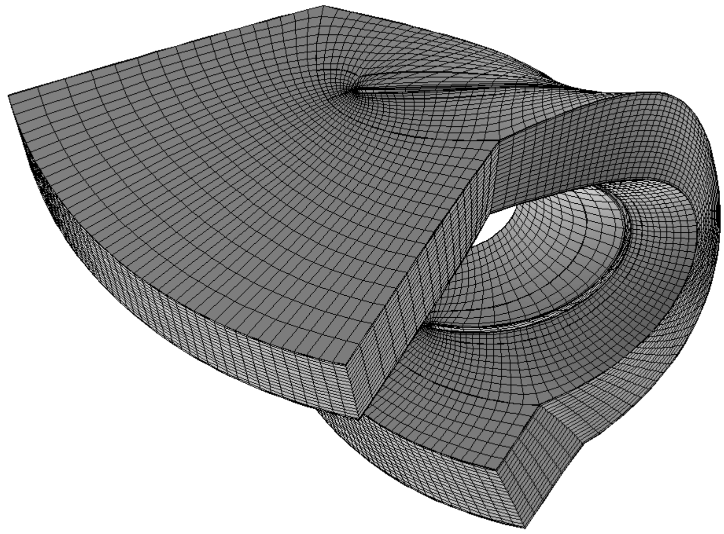

Figure 5.7: Coarse computational mesh

From the computational fluid dynamics (CFD), numerical data at a section k or l, the flow rate Q, the averaged stagnation pressure $\bar{p}_{0_k}$, and the average pressure $\bar{p}_k$, are calculated according to

$$Q = \int_{A_k} |\mathbf{V} \cdot \mathbf{n}| \, \mathrm{d}A \ , \tag{5.38}$$

and

$$\{\bar{p}_k, \bar{p}_{0_k}\} = \frac{1}{Q} \int_{A_k} \left\{p, (p + \tfrac{1}{2}\rho V^2)\right\} |\mathbf{V} \cdot \mathbf{n}| \, \mathrm{d}A \ , \tag{5.39}$$

where ρ, p, $\mathbf{V}$, $\mathbf{n}$, and A_k, are air density, pressure, absolute velocity, and outer normal vector and surface area of section k, respectively.

The rotor torque T is computed from the angular momentum balance between sections $(k, l) = (3, 4)$,

$$T = \int_{A_3} \rho r V_\theta \, |\mathbf{V} \cdot \mathbf{n}| \, \mathrm{d}A - \int_{A_4} \rho r V_\theta \, |\mathbf{V} \cdot \mathbf{n}| \, \mathrm{d}A \, , \tag{5.40}$$

where V_θ is the circumferential velocity component and r is the radius.The power coefficient is defined as

$$\Pi = \frac{T}{\rho \Omega^2 D^5} \, . \tag{5.41}$$

Introducing the rotor total-to-total pressure coefficient,

$$\Psi_{\mathrm{tt}_{3,4}} = \frac{\bar{p}_{0_3} - \bar{p}_{0_4}}{\rho \Omega^2 D^2} \ , \tag{5.42}$$

the rotor total-to-static pressure coefficient,

$$\Psi_{\text{ts}_{3,4}} = \frac{\bar{p}_{0_3} - \bar{p}_4}{\rho \Omega^2 D^2} , \tag{5.43}$$

and the flow rate coefficient,

$$\Phi = \frac{Q}{\Omega D^3} , \tag{5.44}$$

comes the definition of rotor total-to-total efficiency,

$$\eta_{\text{tt}_{3,4}} = \frac{\Pi}{\Phi \Psi_{\text{tt}_{3,4}}} , \tag{5.45}$$

and rotor total-to-static efficiency,

$$\eta_{\text{ts}_{3,4}} = \frac{\Pi}{\Phi \Psi_{\text{ts}_{3,4}}} . \tag{5.46}$$

The following equations are used to couple the performance of the guide-vane sets designed in Chapter 4 with the performance of the rotor designs of the present Chapter.

The turbine pressure head, Ψ_{ts}, is the sum of the rotor total-to-total pressure coefficient, $\Psi_{\text{tt}_{3,4}}$, taken from this Chapter, with the sum of the total-to-total pressure coefficients of other sectors, $\Psi_{\text{tt}_{1,3}} + \Psi_{\text{tt}_{4,B}}$, derived from results presented in Chapter 4,

$$\Psi_{\text{ts}} = \Psi_{\text{tt}_{1,3}} + \Psi_{\text{tt}_{3,4}} + \Psi_{\text{tt}_{4,B}} . \tag{5.47}$$

The total-to-total pressure coefficients for sections $(k, l) = (1, 3)$ and $(4, B)$ are calculated from the stagnation pressure loss coefficient, $\lambda_{k,l}$, presented in Fig. 4.11,

$$\Psi_{\text{tt}_{k,l}} = \frac{1}{2} \left(\frac{\Phi}{\Pi} \frac{D}{b} \frac{R}{r_2} \right)^2 \lambda_{k,l} , \tag{5.48}$$

where energy coefficient, Π/Φ, and the channel height to rotor diameter ratio, b/D, are taken from this Chapter. The reference section ($k = 2$) radius to rotor radius, $r_2/R = 2.15$, is kept from Chapter 4.

From Eqs. (5.3), (5.47) and (5.48) comes the specific diameter of a turbine in configuration I7,

$$D_{\mathsf{s}} = \Phi^{-1/2}\left[\Psi_{\mathsf{tt}_{3,4}} + \frac{\Phi^2}{2}\left(\frac{1}{\pi}\,\frac{D}{b}\,\frac{R}{r_2}\right)^2 \left(\lambda_{1,3} + \lambda_{4,B}\right)\right]^{1/4}. \tag{5.49}$$

5.3 Results

The study comprises three-dimensional flow simulations with a RANS equations solver to assess the effect of the design parameters described in Section 5.2.2 on the rotor performance. To facilitate the results analysis, the following definitions are introduced:

- The reference method is the geometry generation method introduced in Ref. [61].
- The reference rotor is the geometry used in Chapter 3 with $\beta_4' = 35°$ generated by the reference method.
- The generalised method is the geometry generation method introduced in this Chapter.
- The baseline values are the parameter values of the generalised method that reproduce the reference rotor in all aspects, except for the spanwise distribution of meridional velocity (Section 5.2.2).
- The baseline rotor (A) is the approximation of the reference rotor generated by the generalised method with the baseline values.
- The improved rotor (B) is generated by the generalised method for higher efficiency.
- The low specific diameter rotor (C) is generated by the generalised method for higher efficiency and decreased specific diameter.

All results are presented for a Reynolds number based on rotor peripheral velocity Re $= \Omega D^2/\nu = 1.5 \times 10^6$ (same as in Chapter 3). The maximum Mach number observed in the rotor flow was Ma $= \Omega R/c = 0.5$, where c is the speed of sound. The blade metal angle is fixed at $\beta_4' = 35°$ since it provides the highest efficiency for the turbine studied in Chapter 4 .

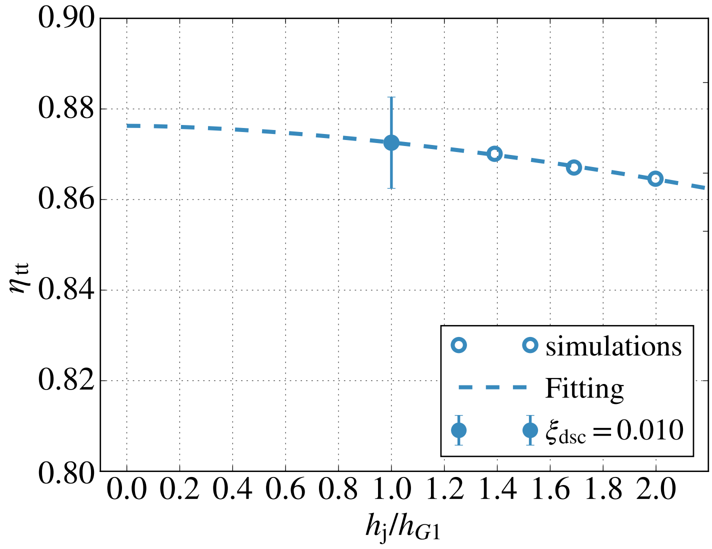

Figure 5.8: Discretisation uncertainty for the baseline rotor (A) total-to-total efficiency.

5.3.1 Uncertainty assessment

The numerical uncertainty presented here refers to calculations of the rotor total-to-total efficiency, Eq. (5.45), from simulations of the baseline rotor in design conditions.

The discretisation uncertainty, ξ_{dsc}, was calculated using four almost geometrically similar grids with grid refinement ratio $h_j/h_{\mathrm{G}_1} = (N_{\mathrm{G}_1}/N_j)^{1/3}$, where N_{G_1} is the number of cells in the most refined mesh, and N_j is the number of cells in each of the grids. Mesh refinement ratios were chosen by balancing available hardware, computational time, and discretisation uncertainty. Grid G_1 is the finest grid and contains 6.97 million cells, while G_4, the coarsest, has 0.88 million. In all grids, $y^+ < 1$ is verified on the first cells perpendicular to walls. Fig. 5.8 shows the least-squares fitting to the set of solutions obtained with the four grids (G_1 to G_4). The discretisation uncertainty of the rotor total-to-total efficiency in grid G_1 is $\xi_{\mathrm{dsc}} = 0.010$.

The iterative uncertainty, ξ_{itr}, was calculated using 70 intermediate solutions taken after initialisation and before residual stabilization (i.e. from the part of the iterative process where residual levels are decreasing). The normalized residual $\delta_{\rho V_{x i}}/\delta_{\rho V_{x 1}}$ of the momentum equation along the x-axis was used, where $\delta_{\rho V_{x 1}}$ is the residual in the first iteration and $\delta_{\rho V_{x i}}$ is the residual on each intermediate iteration. The highest normalized residual on the final iteration is $\delta_{\nu_{t i}}/\delta_{\nu_{t 1}} \approx 2 \times 10^{-6}$, as shown in Fig. 5.9 for grid G_1. In the final solution it is $\delta_{\rho V_{x i}}/\delta_{\rho V_{x 1}} \approx 2 \times 10^{-7}$ and the corresponding iterative uncertainty is $\xi_{\mathrm{itr}} = 0.018$, as shown in Fig. 5.10.

Finally, the numerical uncertainty for the rotor total-to-total efficiency is $\xi_{\mathrm{num}} = 0.028$.

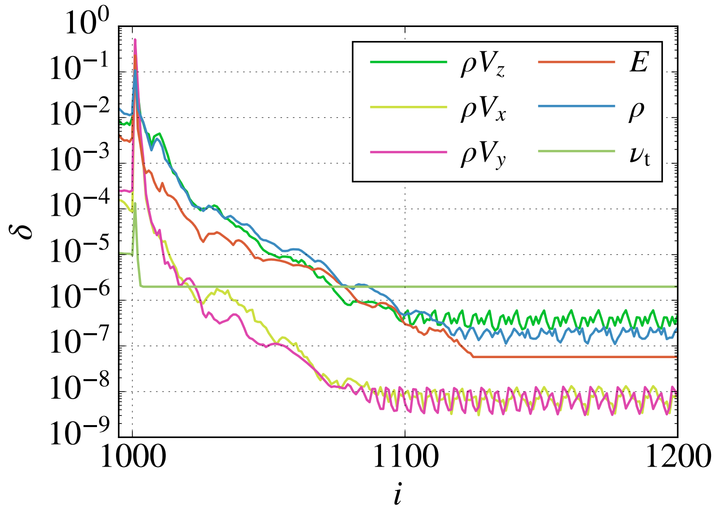

Figure 5.9: Iterative convergence of the baseline rotor (A) simulation on grid G1

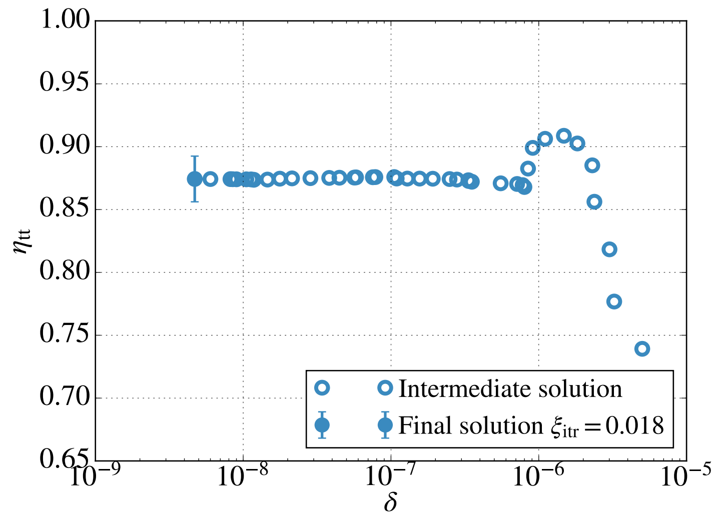

Figure 5.10: Iterative uncertainty of the baseline rotor (A) total-to-total efficiency for grid G1.

Grid G2 was used to obtain the results presented in the remainder of this study. The minimum cell skewness is 23°, while 70% of the cells are between 72° and 90°. The maximum aspect ratio is ≈ 10000. The maximum expansion ratio is 2.5, with 99.8% of the cells between 1 and 1.8.

5.3.2 Analysis of rotor design parameters

The study of the generalised method (Section 5.2.2) presented in this Section is based on parametric analysis. The parameters' values were modified one at a time while keeping the remaining ones on the baseline values, and then the effect on rotor efficiency was interpreted.

The boundary conditions are the ones used for the reference rotor according to Chapter 3.

CFD simulations were performed for each rotor design and operating conditions. The average computation time was about thirty minutes per simulation using a parallelised version of the solver with Message Passing Interface in a workstation equipped with two Intel(R) Xeon(R) Silver 4314 CPUs with a total of 32 physical cores at 2.40 GHz and 32 Gb of DDR4 RAM at 2666 MHz.

Baseline values

The baseline values generate the baseline rotor, which is a close approximation of the seven-bladed rotor ($Z = 7$) introduced in Ref. [61]. The difference lies in the distribution of meridional velocity, which follows Eq. (5.36) instead of a free vortex. Otherwise, the generalised method introduced in this study can reproduce all other parameters of the reference rotor.

The reference rotor blades have a semi-circular mean line with radius $\hat{\zeta}/D = 0.225$, Fig. 5.3, rotor inlet channel width $b/D = 0.11$, constant streamwise relative flow velocity along the channel between two consecutive blades ($\kappa_w = 0$), and swirl distribution of the relative flow as given by Eq. (5.20) with $\mathbf{P}_1 = \mathbf{P}_0 = (0, 0)$ and $\mathbf{P}_2 = \mathbf{P}_3 = (1, 1)$.

The rotor blade metal angle $\beta_4' = 35°$ was selected for the present parametric study as previous results (Chapter 4) show that the method of Ref. [61] gives maximum total-to-total rotor efficiency for $35° < \beta_4' < 40°$.

The generalised method introduced in Section 5.2.2 considers an infinite number of infinitely thin blades. Flow incidence and slip appear in biradial turbine rotors with a finite number of thick blades. Therefore, the procedure described in Chapter 3 was used to calculate the inlet flow conditions that minimise rotor inflow incidence and outflow kinetic energy. For $\beta_4' = 35°$ it is $\alpha_3 \approx 22°$ and $\alpha_4 \approx 90°$, as in Fig 5.2.

Rotor inlet/outlet channel width

The ratio between the channel inlet width and the rotor diameter, b/D, directly influences the turbine flow rate coefficient Φ and the specific diameter D_s for a given rotor blade metal angle $\beta_4' = \pi - \beta_3'$ (Eq. (5.10)). It is seen that increasing the ratio b/D results in a higher flow

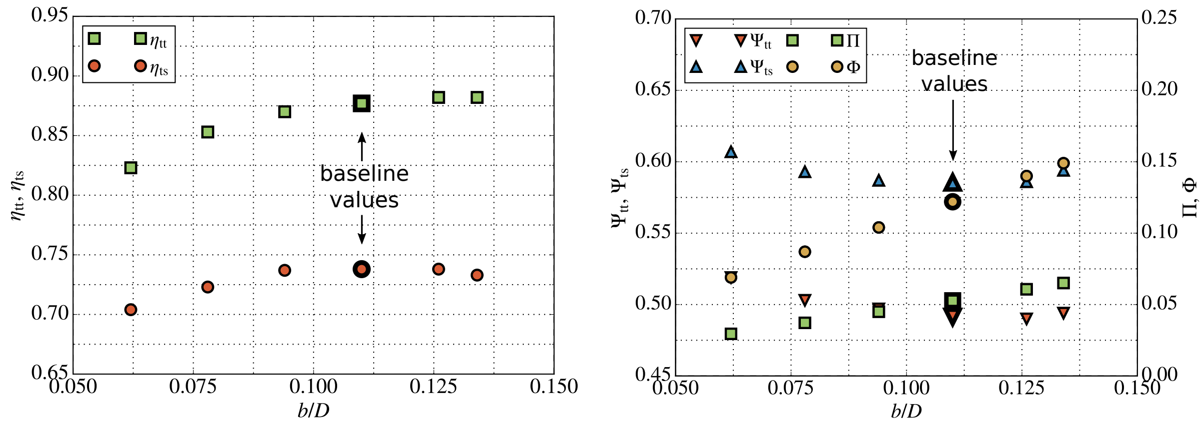

(a) Total-to-total, $\eta_{\text{tt}\,3,4}$, and total-to-static, $\eta_{\text{ts}\,3,4}$, efficiencies.

(b) Total-to-total pressure, $\Psi_{\text{tt}\,3,4}$, total-to-static pressure, $\Psi_{\text{ts}\,3,4}$, torque, Π, and flow, Φ, coefficients.

Figure 5.11: Influence of the meridional channel width to diameter ratio, b/D, on rotor performance.

rate coefficient and lower specific diameter.

Rotor performance results are presented in Fig. 5.11. These results were obtained in the range $0.062 < b/D < 0.134$, while the baseline value is $b/D = 0.11$. The channel width to rotor diameter ratio b/D has an upper limit related to $\hat{\zeta}_\text{b}$, Fig. 5.3. It is clearly seen that $\hat{\zeta}_\text{b}$ can only increase while $\zeta_\text{h}(0)$ respects the prescribed minimum distance of the rotor hub to the rotor shaft.

The results demonstrate that the value of b/D adopted for reference rotor is very close to the one corresponding to the maximum rotor total-to-static efficiency $\eta_{\text{ts}\,3,4}$. Increasing b/D causes only a slight increase in the total-to-total efficiency $\eta_{\text{tt}\,3,4}$.

Since the rotor torque increases with the increase in the flow rate, see Eq. (5.40), the power coefficient has an almost linear variation with b/D once the angle β_4 (Fig. 5.2) of the relative flow at the rotor outlet is approximately constant.

The pressure coefficient is a function of the rotor blade metal angle at the rotor inlet and outlet, $\beta'_4 = \pi - \beta'_3$, the efficiency and the flow rate coefficient. As $\beta'_4 = \pi - \beta'_3$ is constant in the present analysis, the dominant influence on the pressure coefficient variation are the flow losses, where efficiency peaks correspond to pressure coefficient valleys. The results from this parametric analysis evidence that the rotor total-to-total peak efficiency occurs in the range $0.090 < b/D < 0.125$, giving a narrow range of specific diameter, D_s, for the rotor operation with good efficiency. These values may change by adopting different rotor design parameters, but

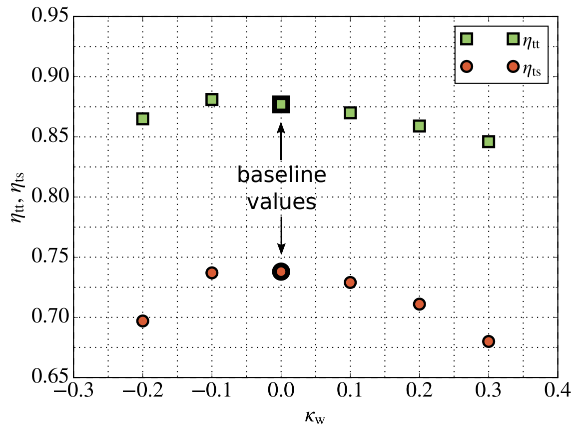

(a) Total-to-total, η_{tt}, and total-to-static, η_{ts}, efficiencies.

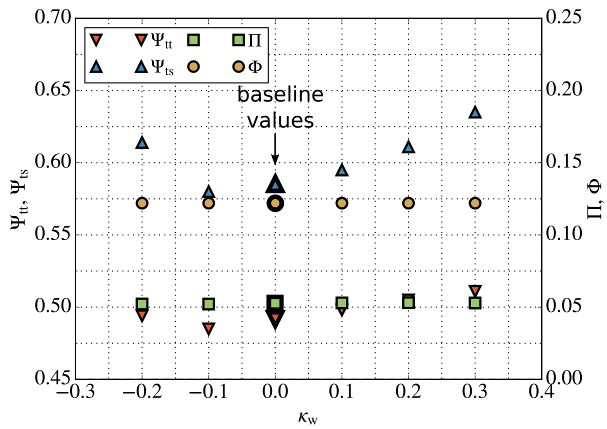

(b) Total-to-total pressure, Ψ_{tt}, total-to-static pressure, Ψ_{ts}, torque, Π, and flow, Φ, coefficients.

Figure 5.12: Influence of the relative velocity streamwise gradient parameter, κ_w, on rotor performance.

the relations stay qualitatively the same.

Mean line streamwise velocity distribution

The design parameter κ_w controls the streamwise relative velocity gradient at the mean line, as shown in Eq. (5.19). Rotor performance results are presented in Figs. 5.12 for the range $-0.2 \geq \kappa_w \geq 0.3$. The baseline value is $\kappa_w = 0$, corresponding to constant relative velocity along the mean line.

Depending on the efficiency to maximise, the optimal value for κ_w is between $-0.15 \leq \kappa_w \leq 0$. This provides a moderate acceleration of the meridional relative flow velocity in the rotor's centrifugal flow giving a small increase in the rotor's total-to-total efficiency, $\eta_{tt\,3,4}$, without significant change in the total-to-static efficiency, $\eta_{ts\,3,4}$. The κ_w parameter does not influence the flow rate, so the flow rate coefficient remains constant.

Since the relative flow angle β_4 (Fig. 5.2) at the rotor outlet is approximately constant, and the flow rate coefficient is constant, the torque coefficient is approximately constant with the variation of κ_w.

As $\beta_4' = \pi - \beta_3'$ is constant in the present analysis, the flow losses dominate the influence on the pressure coefficient variation and the efficiency peaks correspond to the pressure coefficient valleys.

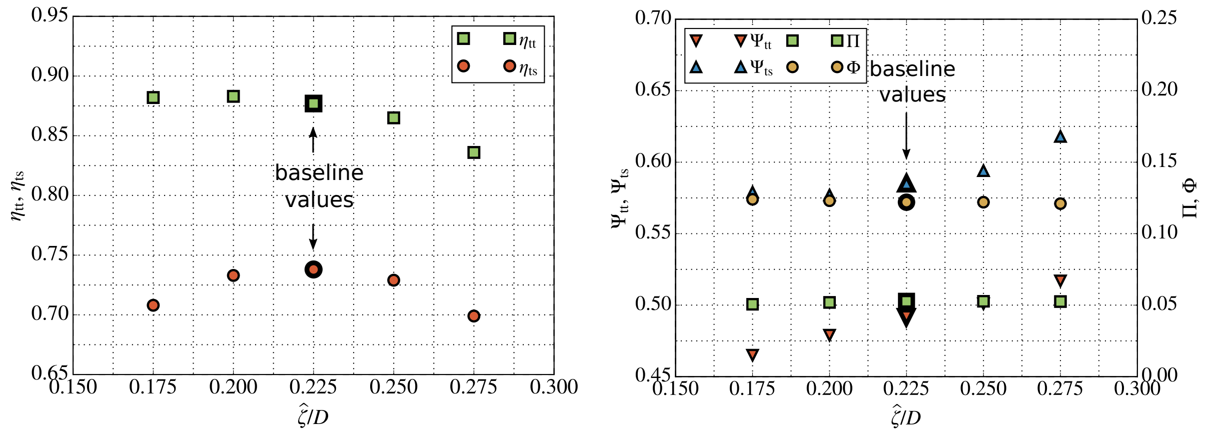

(a) Total-to-total, $\eta_{\text{tt}\,3,4}$, and total-to-static, $\eta_{\text{ts}\,3,4}$, efficiencies.

(b) Total-to-total pressure, $\Psi_{\text{tt}\,3,4}$, total-to-static pressure, $\Psi_{\text{ts}\,3,4}$, torque, Π, and flow, Φ, coefficients.

Figure 5.13: Influence of the semi-circular mean line radius, $\hat{\zeta}/D = \hat{\zeta}_\text{a}/D = \hat{\zeta}_\text{b}/D$, on rotor performance.

Semi-circular mean line

Rotor performance results for cases with semi-circular mean line, $\hat{\zeta}/D = \hat{\zeta}_\text{a}/D = \hat{\zeta}_\text{b}/D$, are presented in Fig. 5.13. These results were obtained in the range $0.175 < \hat{\zeta}/D < 0.275$, while the baseline value is $\hat{\zeta}/D = 0.225$. Similarly to Sub-Section 5.3.2, mean line radius $\hat{\zeta}$ can only increase while $\zeta_\text{h}(0)$ respects the prescribed minimum distance between the rotor hub and the rotor shaft.

The results demonstrate that the baseline value of $\hat{\zeta}/D$ is close to the one corresponding to the maximum rotor total-to-static efficiency $\eta_{\text{ts}\,3,4}$. Decreasing the value of $\hat{\zeta}/D$ causes only a slight increase in the rotor total-to-total efficiency $\eta_{\text{tt}\,3,4}$.

The optimal value of $\hat{\zeta}/D$ for efficiency is in the range $0.20 < \hat{\zeta}/D < 0.225$, depending on which efficiency type to be maximised. The $\hat{\zeta}/D$ parameter does not influence the flow rate, so the flow rate coefficient remains constant.

Since the angle β_4 (Fig. 5.2) of the relative flow at the rotor outlet is approximately constant, and the flow rate coefficient is constant, the torque coefficient is approximately constant with the variation of $\hat{\zeta}/D$. As $\beta_4' = \pi - \beta_3'$ is constant in the present analysis, the dominant influence on the pressure coefficient variation comes from the flow losses, where the efficiency peaks will correspond to the pressure coefficient valleys.

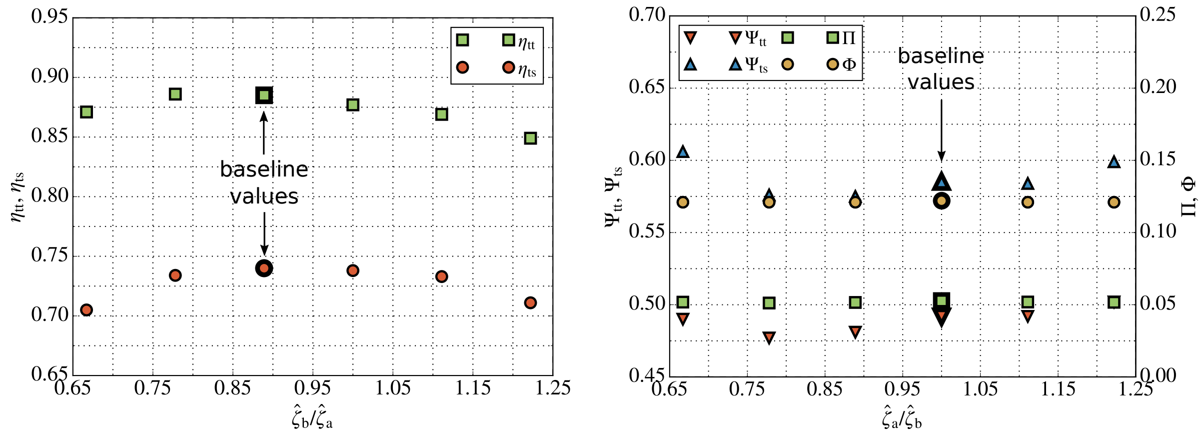

(a) Total-to-total, $\eta_{\text{tt}_{3,4}}$, and total-to-static, $\eta_{\text{ts}_{3,4}}$, efficiencies.

(b) Total-to-total pressure, $\Psi_{\text{tt}_{3,4}}$, total-to-static pressure, $\Psi_{\text{ts}_{3,4}}$, torque, Π, and flow, Φ, coefficients.

Figure 5.14: Influence of meridional mean line ellipse axes ratio, $\hat{\zeta}_b/\hat{\zeta}_a$, on rotor performance.

Ellipse arc mean line

In the generalised method, the parameter $\hat{\zeta}_b/\hat{\zeta}_a$ defines the shape of the ellipse arc mean line in the meridional plane. Rotor performance results are presented in Fig. 5.14 for the range $0.667 \le \hat{\zeta}_b/\hat{\zeta}_a \le 1.222$. The baseline value is $\hat{\zeta}_b/\hat{\zeta}_a = 1$, corresponding to a semi-circular mean line.

The results demonstrate that the value of $\hat{\zeta}_b/\hat{\zeta}_a = 1$ adopted in the reference rotor is close to the one corresponding to the maximum rotor total-to-static efficiency, and decreasing the value of $\hat{\zeta}_b/\hat{\zeta}_a$ causes only a slight increase in the rotor total-to-total efficiency.

The optimal value of $\hat{\zeta}_b/\hat{\zeta}_a$ for the efficiency is between 0.75 to 0.90, depending on the efficiency to maximise. The $\hat{\zeta}_b/\hat{\zeta}_a$ parameter does not influence the flow rate, so the flow rate coefficient is constant with its variation.

Since the angle β_4 (Fig. 5.2) of the relative flow at the rotor outlet is approximately constant and the flow rate coefficient is constant, the torque coefficient is approximately constant with the variation of $\hat{\zeta}_b/\hat{\zeta}_a$. As $\beta_4' = \pi - \beta_3'$ is constant in the present analysis, the dominant influence on the pressure coefficient variation results from the flow losses, where the efficiency peaks will correspond to the pressure coefficient valleys. These values may change by adopting different rotor design parameters, but the relations stay qualitatively the same.

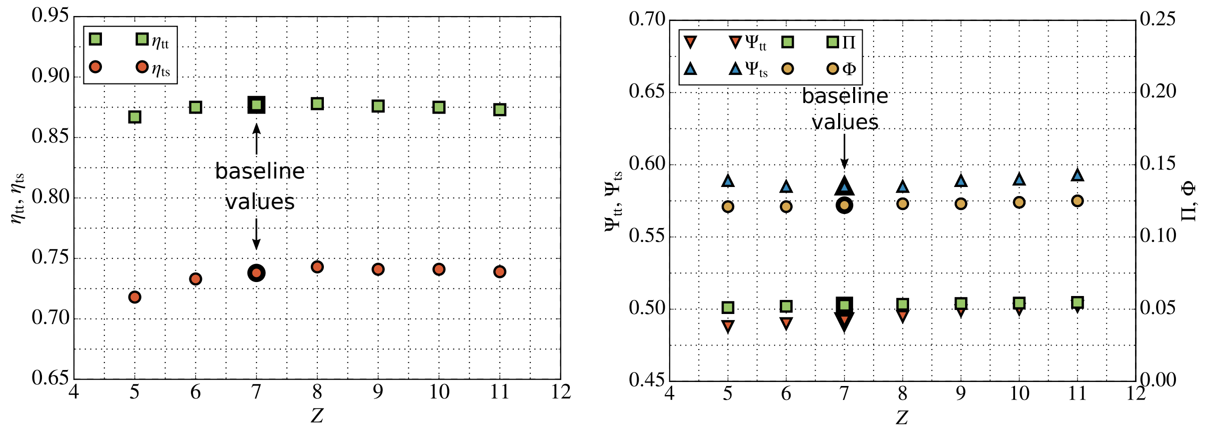

(a) Total-to-total, $\eta_{\text{tt}\,3,4}$, and total-to-static, $\eta_{\text{ts}\,3,4}$, efficiencies.

(b) Total-to-total pressure, $\Psi_{\text{tt}\,3,4}$, total-to-static pressure, $\Psi_{\text{ts}\,3,4}$, torque, Π, and flow, Φ, coefficients.

Figure 5.15: Influence of the number of rotor blades, Z, on rotor performance.

Number of rotor blades

Rotor performance results for total-to-total and total-to-static efficiencies, $\eta_{\text{tt}\,3,4}$ and $\eta_{\text{ts}\,3,4}$, total-to-total and total-to-static pressure coefficients, $\Psi_{\text{tt}\,3,4}$ and $\Psi_{\text{ts}\,3,4}$, power coefficient, Π, and flow rate coefficient, Φ, as function of the number of rotor blades, Z, are presented in Fig. 5.15.

These results were obtained in the range $5 \leq Z \leq 11$, while the baseline value is $Z = 7$. It is seen that the number of blades in the reference rotor is very close to the one corresponding to the maximum rotor total-to-total efficiency. Increasing the number of the blades to $Z = 8$ causes only slight increases in the rotor total-to-total and total-to-static efficiencies. The number of blades does not influence the flow rate, as such the flow rate coefficient was assumed constant.

Since the flow angle β_4 (Fig. 5.2) of the relative flow at the rotor outlet and the flow rate coefficient are approximately constant, the torque coefficient is also approximately constant in the considered Z range.

As $\beta'_3 = \pi - \beta'_2$ is constant in the present analysis, the pressure coefficient variation is due to the flow losses evolution, where the efficiency peaks correspond to the pressure coefficient valleys.

This parametric analysis evidences that the rotor's total-to-total peak efficiency occurs for the eight-bladed rotor ($Z = 8$). This value may change by adopting different rotor design parameters, but the relations stay qualitatively the same.

Mean line swirl distribution

A cubic Bézier curve controls the relative flow swirl distribution on the mean line through the co-ordinates of points $\mathbf{P}_1 = (a_1, 0)$ and $\mathbf{P}_2 = (a_2, 1)$, Eq. (5.21). Rotor performance results are presented in Figs. 5.16a to 5.16d for the ranges $0 \leq a_1 \leq 0.15$ and $0.5 \leq a_2 \leq 1.0$. Since the blade curvature has no influence over the flow rate, flow rate coefficient plots are omitted. The baseline values are $a_1 = 0$ and $a_2 = 1$ which correspond to a linear variation of swirl. The results demonstrate that the baseline value of $\mathbf{B}(v)$ is very close to the corresponding to maximum rotor total-to-total and total-to-static efficiencies, $\eta_{\mathsf{tt}\,3,4}$ and $\eta_{\mathsf{ts}\,3,4}$, and changing $\mathbf{P}_1$ and $\mathbf{P}_2$ co-ordinates causes about 1% increase in these efficiencies.

The optimal value of $\mathbf{B}(v)$ is for $\mathbf{P}_1 = (0.1, 0)$ and $\mathbf{P}_2 = (0.8, 1)$. This maximises both the rotor total-to-total and total-to-static efficiency. The power coefficient and angle of the absolute flow at the rotor outlet increase with the increase of both a_1 and a_2, Fig. 5.16e and 5.16f.

The variation of the outlet flow angle, α_4, confirms the influence of the blade curvature over the slip velocity as discussed in Chapter 3, see Eq. (3.1). In fact, the boundary conditions could have been updated as function of the swirl distribution parameters, a_1 and a_2, as incidence and outlet swirl might affect rotor efficiency. But for practical reasons, due to the exploratory nature of this Chapter, the followed approach was considered acceptable.

By replacing Eq. (5.9) by Eq. (3.13), and using the Unified Slip Model [83] as in Eq. (3.1), the specific diameter, D_{s}, can expressed as

$$D_{\mathsf{s}}^4 = \left(\frac{2}{\pi}\right)^2 \left(\frac{b}{D}\right)^{-2} \eta_{\mathsf{ts}}^{-1} \frac{Z\big(\cot\alpha_3 - \cot\alpha_4\big)\big(\cot\beta_4' + \cot\alpha_4\big)}{\pi F \left(\sin\beta_4' + \dfrac{W_4}{2\Omega}\dfrac{\mathsf{d}\beta'}{\mathsf{d}s}\bigg|_4 - \dfrac{2W_4\sin(2\beta_k')}{4b\Omega}\dfrac{\mathsf{d}b}{\mathsf{d}s}\bigg|_4\right)}, \tag{5.50}$$

highlighting the importance of the swirl distribution, trough the blade curvature, on the specific diameter.

5.3.3 Rotor designs

Following the study in Section 5.3.2 on the influence of each design parameter on rotor performance, it is possible to optimise a rotor geometry by solving a single or a multi-objective optimisation problem, as discussed in Chapter 4 for guide-vane design. Rotor optimisation is

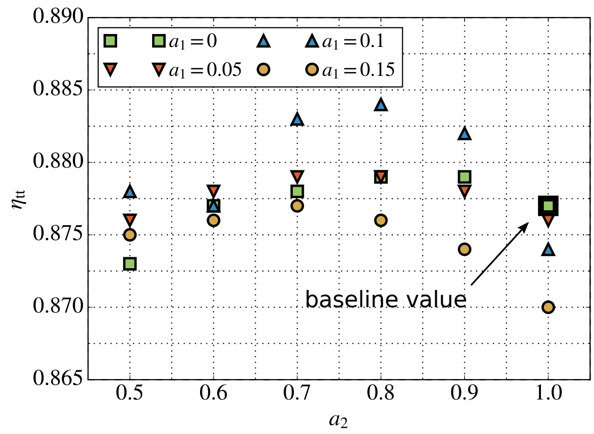

(a) Total-to-total efficiency, $\eta_{tt\,3,4}$.

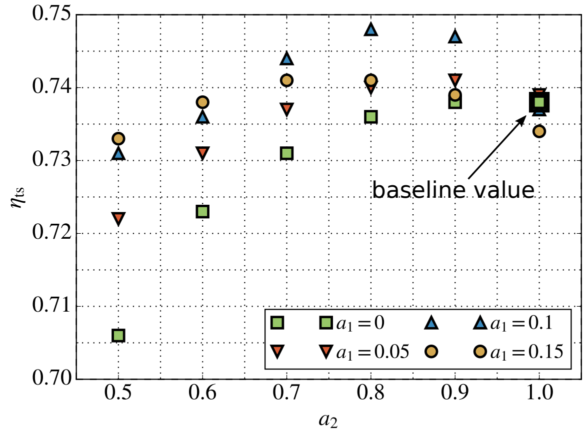

(b) Total-to-static efficiency, $\eta_{ts\,3,4}$.

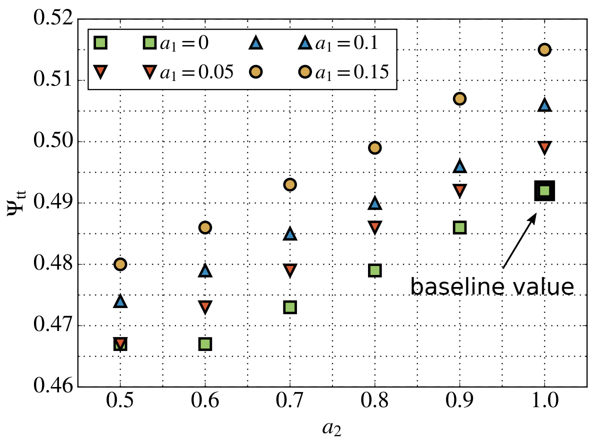

(c) Total-to-total pressure coefficient, $\Psi_{tt\,3,4}$.

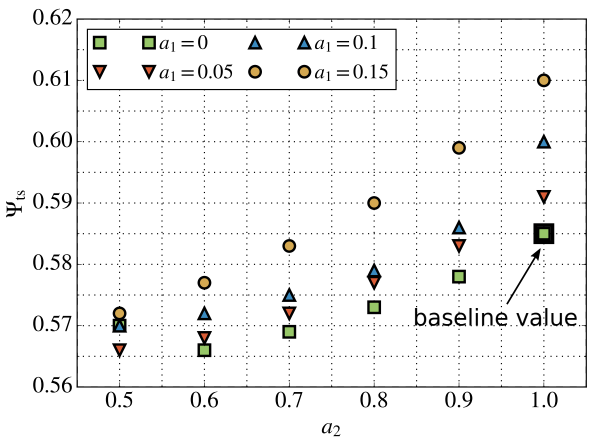

(d) Total-to-static pressure coefficient, $\Psi_{ts\,3,4}$.

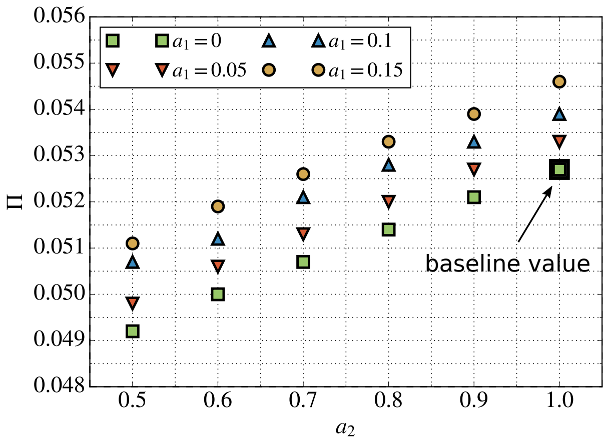

(e) Torque coefficient, Π.

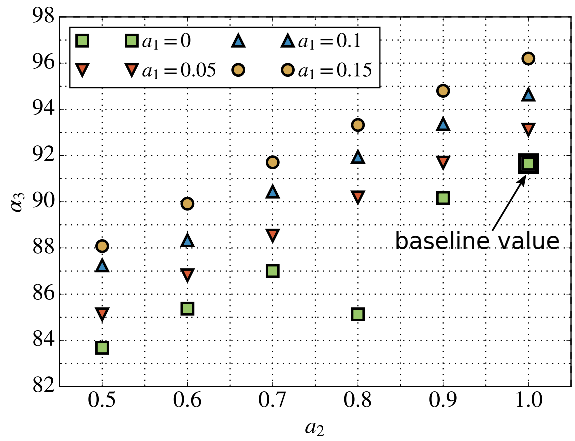

(f) Outlet absolute flow angle, α_4.

Figure 5.16: Influence of the swirl distribution parameter values, $\mathbf{P}_1 = (a_1, 0)$ and $\mathbf{P}_2 = (a_2, 1)$, on rotor performance.

outside the scope of this Chapter. Instead, the combination of design parameter values that give peak total-to-static efficiency were used to create new geometries. This approach does not necessarily result in the most efficient geometry due to the mutual interference between parameters on aerodynamic performance, which can be either positive or negative.

As seen in Section 5.3.2, b/D is the only parameter with a significant effect over the flow rate coefficient. As such, two new designs are explored: one with the design flow rate coefficient $\Phi_{\text{des}} = 0.122$ equal the baseline rotor ($b/D = 0.11$), designated as improved rotor; and other with the maximum acceptable design flow rate coefficient $\Phi_{\text{des}} = 0.140$ ($b/D = 0.126$), designated as low specific diameter rotor. All other parameter values are the ones that individually maximise total-to-static efficiency.

Improved rotor

The improved rotor is a $Z = 8$ bladed-rotor, with a rotor inlet channel width of $b/D = 0.11$, a semi-elliptical mean line with a ratio $\zeta_b/\zeta_a = 0.8$ and $\hat{\zeta}_{\text{b}}/D = 0.2$ (Fig. 5.3), with a decreasing streamwise relative flow velocity along the channel between two consecutive blades ($\kappa_w = -0.1$), and swirl distribution given by Eq. (5.20) with $\mathbf{P}_0 = (0,0)$, $\mathbf{P}_1 = (0.1,0)$, $\mathbf{P}_2 = (0.8,1)$ and $\mathbf{P}_3 = (1,1)$.

The baseline and improved rotors' operating curves for total-to-total and total-to-static efficiencies, $\eta_{\text{tt}\,3,4}$ and $\eta_{\text{ts}\,3,4}$, total-to-total and total-to-static pressure coefficients, $\Psi_{\text{tt}\,3,4}$ and $\Psi_{\text{ts}\,3,4}$, power coefficient, Π, and the outlet angles, α_4 and β_4, as a function of the flow rate coefficient, Φ, are present in Fig. 5.17. The corresponding design values are shown in Tab. 5.2. Even if incidence flow losses at rotor inlet are minimum at $\Phi = \Phi_{\text{des}}$, the flow friction losses on the channel between rotor blades increase quadratically with the flow rate coefficient Φ [126]. Therefore, maximum values of the total-to-total and total-to-static efficiencies occur for $\Phi < \Phi_{\text{des}}$.

The improved rotor gives a modest but clear aerodynamic performance improvement compared to the baseline rotor for equal or larger flow rate coefficients than in design conditions, but for lower values a decrease in efficiency is observed (Fig. 5.17a). The power coefficient evolution along the operating curve is similar for both rotors, except at the higher values of Φ, where the differences start to be considerable (Fig. 5.17b). The improved rotor presents higher values of Π at the higher values of Φ due to high α_4 and lower β_4 compared to the baseline rotor, see Fig. 5.17c and Eq. (5.6).

The growth of the angle of the absolute flow at the rotor outlet $\alpha_4(\Phi)$ in Fig. 5.17c follows the experimental observations [64] with $\alpha_4 \approx \pi/2$ near design flow rate coefficient $\Phi_{\text{des}} = 0.122$. Noticeable differences are seen in the evolutions of the relative flow angle $\beta_4(\Phi)$ at the rotor outlet, where the new design provides a lower variation of $\beta_4(\Phi)$, except for the very low flow rate coefficients. The variation of $\beta_4(\Phi)$ is caused by the variation of the slip with the flow rate, as predicted by the Unified Slip Model [83] in accordance with Eq. (3.1).

The curves of $\Psi_{\text{tt}\,3,4}(\Phi)$ and $\Psi_{\text{ts}\,3,4}(\Phi)$ are approximately quadratic functions ($\Psi \approx K\Phi^2$) as observed experimentally [64]. The differences observed in the pressure coefficients for both rotors are in line with the corresponding curves of the power coefficient $\Pi(\Phi)$ and efficiency $\eta_{3,4}(\Phi)$.

Low specific diameter rotor

The design parameter values of the low specific diameter rotor are equal to the ones from the improved rotor except for b/D. Here $b/D = 0.126$ by contrast to $b/D = 0.11$.

The operating curves of the improved and low specific diameter rotors for the total-to-total and total-to-static efficiencies, $\eta_{\text{tt}\,3,4}$ and $\eta_{\text{ts}\,3,4}$, total-to-total and total-to-static pressure coefficients, $\Psi_{\text{tt}\,3,4}$ and $\Psi_{\text{ts}\,3,4}$, power coefficient, Π, and the outlet angles α_4 and β_4 are presented in Fig. 5.18 as function of the normalized flow rate coefficient Φ/Φ_{des}. The corresponding design values are presented in Table 5.2.

The low specific diameter rotor shows similar aerodynamic performance compared to the improved rotor for the same normalized flow rate coefficient Φ/Φ_{des}. The pressure coefficients are almost coincident for both rotors, and the power coefficient is higher for the low specific diameter rotor due to its higher Φ_{des}. The flow angles $\alpha_3(\Phi/\Phi_{\text{des}})$ and $\beta_3(\Phi/\Phi_{\text{des}})$ at the rotor outlet have a similar variation for the two rotors, with more pronounced differences for $\beta_3(\Phi/\Phi_{\text{des}})$.

The specific speed of turbine configuration I7 (Chapter 4), calculated with Eq. (5.49), for each of the rotors studied in this Chapter is presented in Table 5.2. It is seen that changing

Table 5.1: Baseline (A), improved (B) and low specific diameter (C) rotors' performance metrics in design conditions.

Rotor	b/D	Φ_{des}	$\eta_{\text{tt}\,3,4}$	$\eta_{\text{ts}\,3,4}$	Π	$\Psi_{\text{tt}\,3,4}$	$\Psi_{\text{ts}\,3,4}$	$\alpha_3\,[°]$	$\alpha_4\,[°]$	$\beta_4\,[°]$	D_{s}
A	0.110	0.122	0.877	0.738	0.0527	0.492	0.585	23.6	91.6	37.1	2.54
B	0.110	0.122	0.885	0.745	0.0539	0.499	0.593	23.3	94.5	36.1	2.54
C	0.126	0.140	0.888	0.736	0.0617	0.496	0.598	23.4	93.7	36.9	2.37

Table 5.2: Baseline (A), improved (B) and low specific diameter (C) rotors' performance metrics in design conditions.

Rotor	b/D	Φ_{des}	$\eta_{\text{tt}\,3,4}$	$\eta_{\text{ts}\,3,4}$	Π	$\Psi_{\text{tt}\,3,4}$	$\Psi_{\text{ts}\,3,4}$	$\alpha_3\,[°]$	$\alpha_4\,[°]$	$\beta_4\,[°]$	D_{s}
Baseline	0.110	0.122	0.877	0.738	0.0527	0.492	0.585	23.6	91.6	37.1	2.54
Low specific diameter	0.126	0.140	0.888	0.736	0.0617	0.496	0.598	23.4	93.7	36.9	2.37

from Rotor A to Rotor C decreases the specific diameter from $D_{\text{s}_\text{A}} = 2.54$ to $D_{\text{s}_\text{C}} = 2.37$. This represents a 6.5% decrease of the rotor (and turbine) diameter for a fixed damping constant k_t, as defined by Eq. (5.4).

5.4 Conclusions

A new biradial rotor geometry generation method and new biradial rotor designs were presented and studied in this Chapter. The new method has increased control over the mean line blade loading and over the streamwise pressure gradient. A comprehensive CFD study of the rotor design parameters was performed to understand how they affect rotor performance. The new rotor designs were analysed in the context of a turbine configuration established in a previous Chapter. One of the rotor designs concerned the turbine specific speed, D_{s}, which was shown to be a useful metric in turbine design by being directly related to turbine size and damping constant, k_{t}.

The conclusions taken from this Chapter can be summarized as follows:

- the rotor blade metal angle, $\beta_4' = \pi - \beta_3'$, has a direct influence over the turbine specific diameter.
- the ratio between the channel inlet width and the rotor diameter, b/D, is the main parameter influencing the turbine specific diameter for a given rotor blade metal angle;
- other parameters have an indirect influence over the specific diameter trough the turbine

efficiency, η_{ts};

- the rotor total-to-total efficiency, $\eta_{\text{ts}\,3,4}$, was increased in near 1%;
- the biradial turbine has peak efficiency for a narrow range of the ratio between the channel inlet width and the rotor diameter, $0.09 < b/D < 0.126$;
- the diameter of a FGV biradial turbine configuration was reduced in 6.5% with one of the new designs while keeping the same efficiency gain of near 1%.

A multi-objective optimisation should follow to find the optimal combination of design parameter values that maximise the efficiency and minimise the specific diameter.

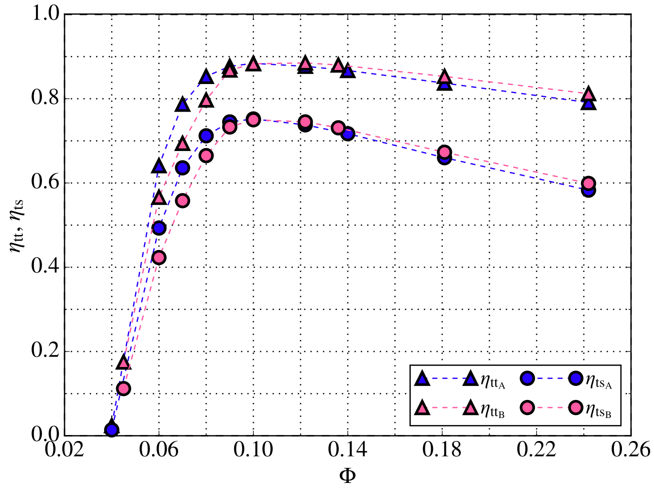

(a) Total-to-total efficiency, $\eta_{\mathrm{tt}\,3,4}$, and total-to-static efficiency, $\eta_{\mathrm{ts}\,3,4}$.

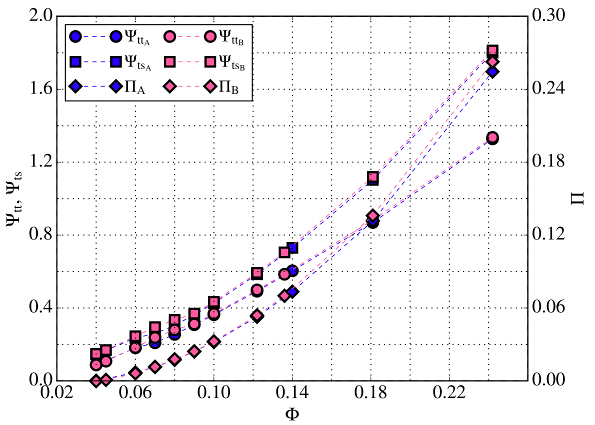

(b) Total-to-total pressure coefficient, $\Psi_{\mathrm{tt}\,3,4}$, total-to-static pressure coefficient, $\Psi_{\mathrm{ts}\,3,4}$, and torque coefficient, Π.

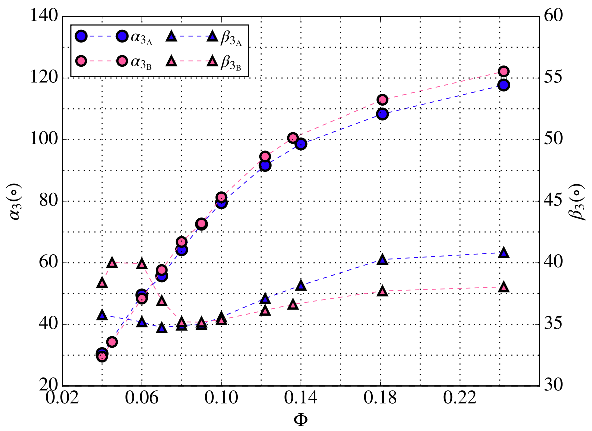

(c) Outlet absolute flow angle, α_4.

Figure 5.17: Performance comparison between baseline (A) and improved (B) rotors as function of the flow rate coefficient, Φ. ($\Phi_{\mathrm{des}} = 0.122$)

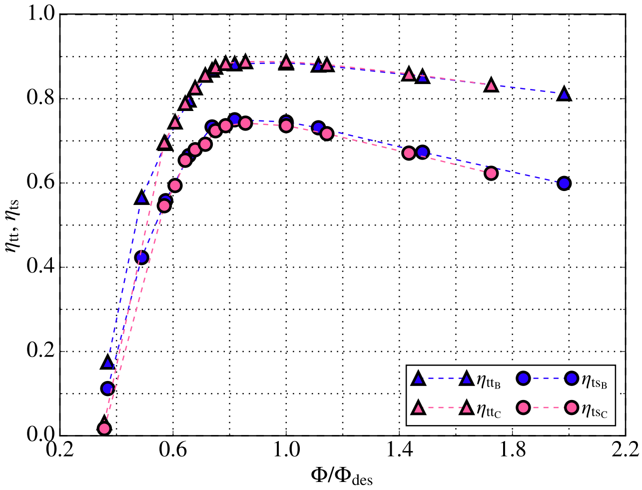

(a) Total-to-total efficiency, $\eta_{\mathrm{tt}\,3,4}$, and total-to-static efficiency, $\eta_{\mathrm{ts}\,3,4}$.

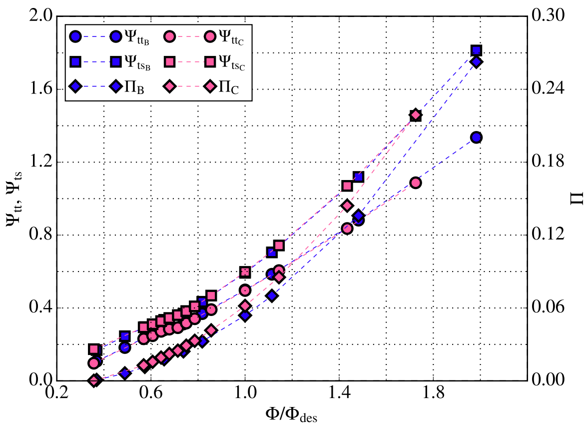

(b) Total-to-total pressure coefficient, $\Psi_{\mathrm{tt}\,3,4}$, total-to-static pressure coefficient, $\Psi_{\mathrm{ts}\,3,4}$, and torque coefficient, Π.

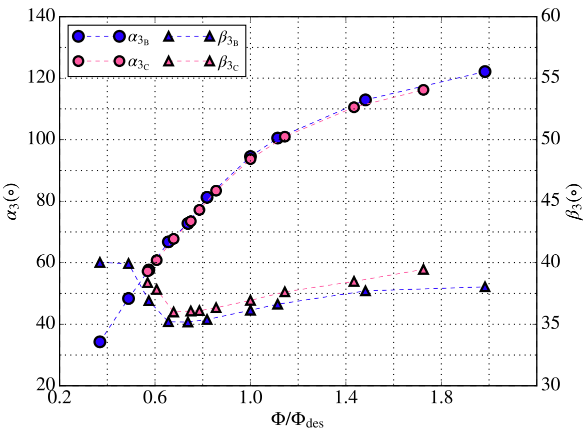

(c) Outlet absolute flow angle, α_4.

Figure 5.18: Performance comparison between improved (B) and low specific diameter (C) rotors as function of the normalized flow rate coefficient, Φ/Φ_{des}.

Chapter 6

Testing a generator and rectifier for off-grid OWC converters

This Chapter presents the experimental testing of a generator-rectifier set for off-grid oscillating-water-column wave energy converters. The set comprises a permanent magnet synchronous generator, a three-phase full-wave bridge rectifier, and a capacitive filter. It can be coupled to an impulse turbine and additional dc-to-dc converters for generator control, battery charging and stand-alone dc supply. The relationship between the generator mechanical input (torque and speed) and the rectifier electrical output (voltage and current) was mapped to integrate wave-to-wire numerical models or calculate the turbine torque from generator output in prototype testing. A speed-controlled induction motor drove the generator-rectifier assembly in a test rig while a resistor bank loaded the system. Performance was assessed based on steady-state experimental results from 127 rotational speed and resistive load pairs. Rational functions approximate the generator counter torque as a function of the rectifier output current and the rotational speed as a function of the output voltage and current. The system model approximates the measured generator-rectifier efficiency with differences below 1% for the most representative resistive loads. For an operating range between 20 and 100% of the generator's continuous duty counter torque, the power factor varies between 0.92 and 0.95, and the generator-rectifier efficiency is between 0.83 and 0.93. The maximum observed direct-axis current is 8% of the demagnetization limit. At the maximum tested speed of 3000 r/min, the generator-rectifier set has a continuous duty electrical power of 1.6 kW with 91% efficiency.

6.1 Objectives

Squirrel-cage induction machines are often used as generators (SCIG) in wind [127] and wave energy converters [128] due to their reliability and off-the-shelf availability. These generators draw reactive power from the electrical grid to generate voltage and supply active power [129]. Active rectifiers are typically used in both cases. Alternatively, self-excitation of induction generators is achievable by coupling a capacitor bank to the generator terminals and using proper control algorithms for reactive power generation from residual rotor magnetism. Passive rectifiers can then be used, provided that dc-to-dc converters are used for power regulation [130].

Permanent-magnet synchronous generators (PMSG) are brushless self-excited machines in which permanent magnets produce the magnetic flux [131]. Active or passive rectifiers can be used with PMSGs [128], but they should be carefully sized to avoid over-voltage at a high rotational speed. A mechanical brake or shut-off valve should be installed with the turbine and used in energetic sea states.

The magnets on PMSGs are more susceptible to corrosion than squirrel-cage rotors of induction generators [132]. Additionally, magnetic circuits are subject to saturation, overheating and demagnetization. These factors should be considered when selecting the environmental protection index and control scheme of the generator.

Other commonly studied generators for wind and wave power conversion [127, 128] are the doubly-fed induction and the wound-rotor synchronous generators (electrically-excited synchronous generators). However, the need for slip rings and brushes implies regular maintenance, which is undesirable in offshore systems. Brushless versions of these machines exist but are more complex and costly.

The literature review shows that Wells turbines require active rectifiers due to the lack of self-starting capability (see Chapter 1). In this case, the ruggedness of SCIGs and their lower sensitivity to the corrosive environment makes them a good choice. The self-starting capability of impulse turbines provides flexibility in the choice of generator and power converter.

Diode-based (passive) rectifiers are inexpensive compared to active rectifiers but allow less power control [127]. Diodes introduce harmonics in the generator phases which distort the power signal, creating a torque ripple and decreasing the power factor [133]. Generators and power converters are rated by voltage and current regardless of power factor. Their size, cost and efficiency are then inverse to the power factor for a given mechanical power.

A PMSG and a full-wave bridge rectifier, controlled by a dc-to-dc power converter, is a simple topology for off-grid generation but at the expense of lower efficiency and higher risk of rotor demagnetization. It was was extensively studied for small wind turbines [134–136], and, to some extent, to point absorbers with linear PMSGs, but few studies have addressed this topology applied to the OWC principle so far [137]. An OWC wave energy converter with a PMSG and a diode rectifier to charge batteries and supply a desalination plant through an inverter was built and commissioned [138]. More recently, an OWC wave energy converter with a Wells turbine and a PMSG powering a stand-alone dc micro-grid was studied numerically [139], but the need for self-starting capability must still be addressed.

The objective of this Chapter is to obtain the operational performance of a setup comprising a PMSG, a three-phase full-bridge rectifier and a capacitive filter, based on experimental data, for given sets of input rotational speed and resistive load in steady-state. This Chapter's discussion is focused on the practical aspects of implementing the proposed system rather than on the fundamentals of electric machinery and power electronics.

The first research outcome is the assessment of the power factor, efficiency and proximity to demagnetization conditions, which are the main shortcomings of using a PMSG with a passive rectifier.

The development cycle of OWC wave energy converters from concept to full-scale deployment follows a well-defined path: conceptualization, sub-system design, wave-to-wire numerical modeling, hydrodynamic wave tank testing and turbo-generator dry-testing, scaled sea trials, and full-scale sea trials [140].

Wave-to-wire models have become essential tools for the design, selection and integration of components by coupling different physical domains in the same simulation, such as hydrodynamics, aerodynamics and electronics [141]. These models are also fundamental for the financial evaluation of a WEC design as they enable the estimation of the power production on a given deployment site. The successive experimental tests up to commercialization are used to improve the accuracy of the wave-to-wire models and to prove the concept in increasingly demanding conditions.

The second research outcome of this Chapter are the PMSG and rectifier performance maps to be used in the design and operation of OWC converters. These can be easily integrated into wave-to-wire models for the sizing and selection of components such as the turbine and power converters. The measured system efficiency includes all the generator and rectifier losses, making it a valuable tool for controller design and estimating power production.

Most variables related to the performance of OWC turbo-generators are measured with robust and compact sensors except for torque. Torque meters are mounted between the turbine and generator shafts, increasing the assembly size and creating a weak structural point susceptible to the energetic transient regimes associated with wave energy conversion. As such, a method to calculate the turbine torque from generator parameters was established to dismiss torque meters in prototype testing.

6.2 Materials and methods

Turbine and dc-to-dc converters at the rectifiers output terminals are outside the scope of this Chapter. In the present study, the mechanical power input was supplied by an induction motor while the load at the rectifier's output was emulated with a resistive load bank.

The set comprising the PMSG, rectifier and capacitor filter was characterized in steady-state to map the generator efficiency and power factor, and verify the proximity to rotor demagnetization regimes based on manufacturer information. The relationship between the mechanical input (torque and speed) and the rectifier output (voltage and current) was fitted with analytical functions for easy integration with wave-to-wire models and prototype testing procedures [142].

The integration of steady-state test results into time-dependent wave-to-wire models is based on the assumption that generator-rectifier performance under time-varying conditions may be represented by a set of steady-state performances covering a sufficiently large range of these conditions with a sufficiently large resolution. The validity of this assumption is dependent on the ratio between two frequencies: (a) a representative wave frequency f_{wave} and (b) the generated voltage frequency $f_{\text{e}} = m\,\Omega/(2\pi)$, where m is the number of generator pole pairs, and Ω is its rotational speed. The validity condition is met if f_{e} is very large compared with f_{wave}, which generally occurs in OWC converters. In the Mutriku OWC-breakwater plant equipped with biplane Wells turbines, it is $f_{\text{wave}} = 0.1\,\text{s}^{-1}$ and $\Omega = 300\,\text{rad/s}$ [49]. Assuming four pole pair generators, the electrical frequency is $f_{\text{e}} = 190\,\text{s}^{-1}$ and $f_{\text{e}}/f_{\text{wave}} = \mathcal{O}[10^3]$.

6.2.1 Turbo-generator dynamics

The generator should apply a counter torque defined by the turbo-generator controller when turbine torque is produced. In most situations, the counter torque should be such that the turbo-generator achieves a rotational speed for operation in maximum efficiency or maximum power [143]. The dynamics of the mechanical power transmission is described by

$$J\frac{\mathrm{d}\Omega(t)}{\mathrm{d}t} = T_{\text{turb}}(t) - T_{\text{gen}}(t)\,, \tag{6.1}$$

where J is the turbine and generator rotors' moment of inertia, Ω is the rotational speed, t is time, T_{turb} is the turbine torque and T_{gen} is the generator counter torque.

In a wave-to-wire modelling with a PMSG and a passive rectifier it is crucial to calculate the output voltage and current. Considering that the turbine is fully characterized, its torque $T_{\text{turb}}(t)$ is calculated from the rotational speed and chamber pressure. The generator current imposes the counter torque, $T_{\text{gen}}(t)$, and can be regulated by a dc-to-dc converter, and respective controller, at the rectifier's output terminals. The voltage is mainly a function of the rotational speed, but the generator load also influences it. Therefore, to integrate the PMSG and rectifier in a wave-to-wire model, the relationships $\bar{T}_{\text{gen}}(I_{\text{dc}})$ and $U_{\text{dc}}(\bar{\Omega}, I_{\text{dc}})$ must be established, where $\bar{T}_{\text{gen}}$, $\bar{\Omega}$, I_{dc} and U_{dc} are the average generator counter-torque, average rotational speed, and average rectifier ouput current and voltage, respectively.

Consider the post-processing of operational values from a PMSG with a rectifier at sea, where the flow rate, rotational speed, dc voltage and current time series are known. From the relationship $T_{\text{gen}}(I_{\text{dc}})$, the turbine torque, $T_{\text{turb}}(t)$, can be easily calculated using Eq. (6.1).

6.2.2 Generator testing procedure and instrumentation

The generator test-rig is schematically represented in Fig. 6.1. The prime mover was a three-phase Efacec two-pole $7.4\,\text{kW}$ squirrel cage induction motor controlled by a Danfoss VLT

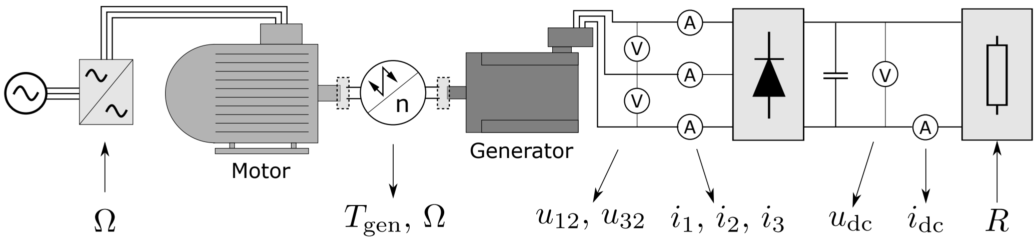

Figure 6.1: Schematic representation of the test-rig, test parameters and measured variables.

Table 6.1: Test-rig sensor's range and accuracy.

Variable	Sensor	Range	Accuracy
Torque	ST TorqSense RWT410	± 8 Nm	$\pm 0.25\%$ of range
Speed	ST TorqSense RWT410	± 20000 r/min	± 1 r/min
Current	MPS MCS1803-05	± 5 A	$\pm 1.5\%$ of reading
Voltage	LEM LV 25-P	± 500 V	$\pm 0.9\%$ of reading
Temperature	SEW PT1000	-50 to $+200$°C	$\pm 1\%$ of reading

Midi Drive FC 280 variable frequency drive. A three-phase full-wave bridge rectified the generator's ac power. A capacitive filter and a manually adjustable resistive load bank were connected to the rectifier's output terminals.

The generator performance metrics were calculated under steady-state conditions for several resistive loads and rotational speeds (R, Ω). The rotational speed was imposed on the induction motor by the variable frequency drive, while the load was imposed by adjusting the total resistance of the load bank.

A total of ten variables were measured as illustrated in Fig. 6.1: torque, rotational speed, two phase-to-phase voltages, three-phase currents, a winding temperature, a dc voltage and current. The sensors used, their accuracy and measuring range are presented in Table 6.1.

The torque meter, coupled between the motor and generator shafts, has a surface acoustic wave torque sensor and an optical rotary speed sensor. The former was calibrated using a lever arm mechanism, while the latter was calibrated with an optical tachometer with an absolute accuracy of 0.05 r/min. The voltages and currents were measured with Hall effect sensors calibrated with 0.1% accuracy. The winding temperature was measured with a platinum resistance temperature detector embedded in the generator and an external voltage divider.

The sensors' output voltage signals were logged with a National Instruments USB-6211 data acquisition board and the NI-DAQmx Python API. This board has 16 single-ended analogue voltage inputs with 16-bit resolution and an aggregate sampling rate of 250 kHz.

Table 6.2: Generator technical data [144].

speed class [r/min]	2000
maximum operating speed [r/min]	6000
mechanically permitted speed [r/min]	7200
standstill torque [Nm]	6.5
standstill current [A]	3.5
maximum current [A]	12.2
phase inductance [mH]	17.4
phase resistance (20°C) [Ω]	3.27
electrical time-constant [ms]	5.32
phase-to-phase open-circuit rms voltage [Vmin/r]	0.128
number of poles [-]	8

After calibration and system warm-up, the first load was set by adjusting the resistance on the load bank, and the first test rotational speed was set on the variable frequency drive. Data was logged for 30 s, after which the speed was increased. A new data set was logged, and the speed-increase/logging process was repeated until the maximum motor rotational speed of 3000 r/min or the generator's continuous duty current was reached. The motor was then stopped, the zero of the torque meter was confirmed, the next load was set, and the data logging procedure was repeated for successive increasing rotational speeds.

6.2.3 Permanent magnet synchronous generator

The generator tested was a SEW Eurodrive CM3C71S three-phase synchronous servomotor [144]. It has surface mounted rotor magnets, a concentrated stator winding in star connection, a three-wire terminal interface and a sinusoidal back electromotive force (EMF). The machine parameters are summarized in Table 6.2.

The maximum continuous duty generator rms phase current, I_{S1}, is shown in Fig. 6.2 as a function of the rotational speed. This value is valid up to an ambient temperature of $40°$C and altitude of 1000 m. Outside this range, the generator should be derated. The generator can temporarily operate above the continuous duty limit, up to the maximum current, provided the winding temperature is monitored and kept below $145°$C.

The average generator counter torque, $\bar{T}_{\mathsf{gen}}$, and the average rotational speed, $\bar{\Omega}$, over a

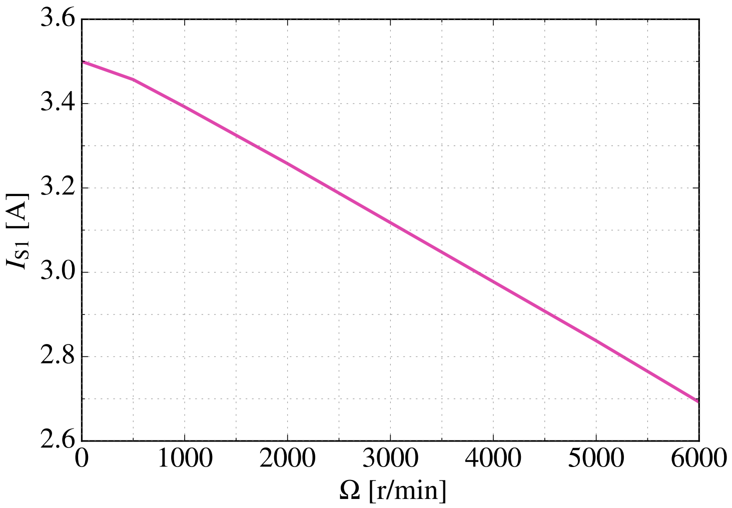

Figure 6.2: CM3C71S (class 2000 r/min) maximum continuous duty current for an ambient temperature below $40°$C. Derived from manufacturer data [144].

measurement time interval $t_\mathrm{b} - t_\mathrm{a}$ is

$$\{\bar{T}_\mathrm{gen}, \bar{\Omega}\} = \frac{1}{t_\mathrm{b} - t_\mathrm{a}} \int_{t_\mathrm{a}}^{t_\mathrm{b}} \{T_\mathrm{gen}(t), \Omega(t)\}\, \mathrm{d}t\,, \tag{6.2}$$

The instantaneous mechanical power is the product of the generator counter torque, $T_\mathrm{gen}(t)$, by the rotational speed, $\Omega(t)$. Thus, the average mechanical power over the measurement period is

$$\overline{T_\mathrm{gen}\Omega} = \frac{1}{t_\mathrm{b} - t_\mathrm{a}} \int_{t_\mathrm{a}}^{t_\mathrm{b}} T_\mathrm{gen}(t)\Omega(t)\mathrm{d}t\,. \tag{6.3}$$

The average active power, $\bar{P}_\mathrm{gen}$, over the measurement period is

$$\bar{P}_\mathrm{gen} = \frac{1}{t_\mathrm{b} - t_\mathrm{a}} \int_{t_\mathrm{a}}^{t_\mathrm{b}} \big(u_{12}(t)i_1(t) + u_{32}(t)i_3(t)\big)\, \mathrm{d}t\,, \tag{6.4}$$

where i_1 and i_3 are the instantaneous currents in phases 1 and 3, and u_{12} and u_{32} are the instantaneous voltages between phases 1 and 2, and 3 and 2, respectively [145].

The generator average efficiency, $\bar{\eta}_\mathrm{gen}$ is the ratio between the average active power and the average mechanical power,

$$\bar{\eta}_\mathrm{gen} = \frac{\bar{P}_\mathrm{gen}}{\overline{T_\mathrm{gen}\,\Omega}}\,. \tag{6.5}$$

Since the load is symmetric, the rms value of the phase currents and phase-to-phase voltages are $I_1 = I_2 = I_3$ and $U_{12} = U_{32} = U_{13}$, respectively, and the average generator apparent power [145], $\bar{S}_{\text{gen}}$, is

$$\bar{S}_{\text{gen}} = \sqrt{3}\, U_{12}\, I_1 \,. \tag{6.6}$$

The power factor PF is defined here as the true power factor [133], which is the product of the displacement power factor, PF_{d}, by the distortion factor, PF_{h}, or the ratio of the average active power, $\bar{P}_{\text{gen}}$, by the average apparent power, $\bar{S}_{\text{gen}}$,

$$PF = PF_{\text{d}}\, PF_{\text{h}} = \frac{\bar{P}_{\text{gen}}}{\bar{S}_{\text{gen}}} \,. \tag{6.7}$$

The distortion power factor PF_{d} accounts for the displacement between the fundamental phase voltage and current,

$$PF_{\text{d}} = \frac{\bar{P}_{\text{gen}_{\text{f}}}}{\bar{S}_{\text{gen}_{\text{f}}}} \,, \tag{6.8}$$

caused by inductive and/or capacitive loads. The subscript f refers to the fundamental frequency. A Fourier transform with flat-top windowing was applied to the phase-to-phase voltages and phase currents to obtain their fundamental components. Then the fundamental average active ($\bar{P}_{\text{gen}_{\text{f}}}$) and apparent powers ($\bar{S}_{\text{gen}_{\text{f}}}$) were calculated with the analogous versions of Eqs. (6.4) and (6.6) using $u_{12_{\text{f}}}$ $u_{32_{\text{f}}}$, $i_{1_{\text{f}}}$, $i_{2_{\text{f}}}$, $U_{12_{\text{f}}}$ and $I_{1_{\text{f}}}$ in a time window approximately centred at $(t_{\text{b}} - t_{\text{a}})/2$ and comprising twenty periods of the fundamental phase 1 current.

The distortion power factor PF_{h} accounts for the effect of non-linear loads such as diodes over the total power factor [133]. Its relation with the total harmonic distortion of the voltage and current signals, THD, is given by

$$PF_{\text{h}} = \frac{1}{\sqrt{1 + THD_{\text{u}}}}\, \frac{1}{\sqrt{1 + THD_{\text{i}}}} \,, \tag{6.9}$$

where the subscripts u and i refer to voltage and current, respectively. Considerations about the distortion of the individual signals are outside the scope of the present study. As such, the distortion power factor,

$$PF_{\text{h}} = \frac{PF}{PF_{\text{d}}} \,, \tag{6.10}$$

is used here as the global metric for the harmonic content of the generator power.

The direct- and quadrature-axis currents, i_{d} and i_{q}, should be monitored to avoid rotor demagnetization. The dq transformation [146] with the direct axis aligned with phase 1 is

$$\begin{bmatrix} i_\mathsf{d} \\ i_\mathsf{q} \end{bmatrix} = \frac{2}{3} \begin{bmatrix} \cos(\theta_\mathsf{e}) & \cos(\theta_\mathsf{e} - \frac{2}{3}\pi) & \cos(\theta_\mathsf{e} + \frac{2}{3}\pi) \\ -\sin(\theta_\mathsf{e}) & -\sin(\theta_\mathsf{e} - \frac{2}{3}\pi) & -\sin(\theta_\mathsf{e} + \frac{2}{3}\pi) \end{bmatrix} \begin{bmatrix} i_1 \\ i_2 \\ i_3 \end{bmatrix} . \tag{6.11}$$

The rotating frame position, θ_e, is derived from the fundamental phase 1 current in the present study,

$$\theta_\mathsf{e} = \omega_{1_\mathsf{f}} t \, , \tag{6.12}$$

where ω_{1_f} is the fundamental frequency calculated with a Fourier transform and flat-top windowing. Again, the time window used for Eqs. (6.11) and (6.12) was approximately centered at $(t_\mathsf{b} - t_\mathsf{a})/2$ due to the windowing scheme, and comprised twenty periods of the fundamental phase 1 current with $\theta_\mathsf{e} = 0$ for $i_{1_\mathsf{f}} = 0$.

The direct- and quadrature-axis currents are constant for purely sinusoidal currents. However, their rms values, I_d and I_q, are used in the present study due to the harmonic content introduced by the rectifying bridge. As with sinusoidal phase currents,

$$I_1 = I_2 = I_3 = \sqrt{(I_\mathsf{d}^2 + I_\mathsf{q}^2)/2} \, . \tag{6.13}$$

According to the manufacturer's recommendation, the direct-axis current, I_d, should be lower than 40% of the rated maximum phase current (Table 6.2) for a hot machine, and lower than 50% for a cold one, to avoid demagnetization [147].

The generator counter torque in a synchronous generator with surface-mounted magnets can be approximated by

$$T_\mathsf{gen} = \sqrt{\frac{3}{2}} E i_\mathsf{q} \, , \tag{6.14}$$

where E is the generator back EMF, expressed here as the rms value of the phase-to-phase voltage in Vs/rad [148]. A diode rectifier does not provide control over the currents, and, as such, the generator operates with $i_\mathsf{d} \neq 0$ as a result of the harmonic content imposed by itself, the rectifier and other loads. It can be seen from Eqs. (6.13) and (6.14) that for a given operation point (torque and rotational speed set), rectification with a diode rectifier leads to higher phase

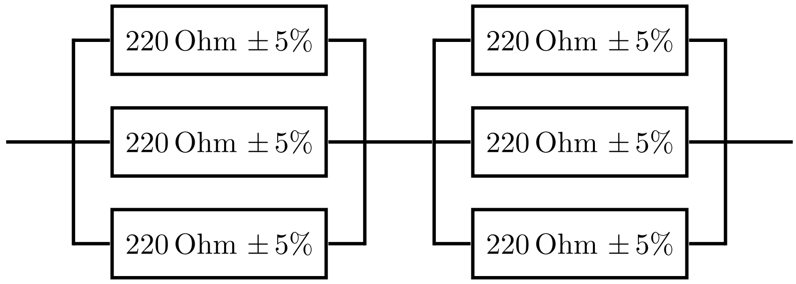

Figure 6.3: Resistor bank setup $k = 6$.

currents than rectification with a switched rectifier controlled for $i_\mathrm{d} \approx 0$, resulting in higher ohmic losses [148].

6.2.4 Rectifier, capacitor and resistor bank

The three-phase rectifier used is an IXYS VUO35-12NO7, rated at 1200 V and 30 A. Its average efficiency is given by

$$\bar{\eta}_\mathrm{rec} = \frac{\bar{P}_\mathrm{dc}}{\bar{P}_\mathrm{gen}}\,, \tag{6.15}$$

where $\bar{P}_\mathrm{gen}$ is the generator average active power calculated by Eq. (6.4), and $\bar{P}_\mathrm{dc}$ is the average rectifier output power calculated by

$$\bar{P}_\mathrm{dc} = \frac{1}{t_\mathrm{b} - t_\mathrm{a}} \int_{t_\mathrm{a}}^{t_\mathrm{b}} u_\mathrm{dc}(t) i_\mathrm{dc}(t)\,\mathrm{d}t\,. \tag{6.16}$$

For the remainder of this study, I_dc and U_dc refer to the average current and voltage at the rectifier's terminals instead of the rms values at the generator's terminals, I_{12} and U_{12}.

A capacitor is installed between the rectifier and the dc load to reduce the generator counter torque ripple and current harmonics at the expense of deteriorating the distortion power factor, PF_d. It is a MKP DC-LSI film capacitor from TDK/EPCOS, rated at 1200 V and 50 A with a capacitance of $50\,\mu$F.

The resistor bank comprises six TE1500B220RJ ceramic-core wire-wound 220 Ohm resistors with a tolerance of 5 % and rated at 2.5 kW. Table 6.3 summarizes the available combinations in manual operation, and Fig. 6.3 exemplifies the connection for setup R_6.

Table 6.3: Resistor bank setups.

Setup k	R_k [Ohm]	Resistors in use	Sets in series	Per-set parallel resistors
1	37	6	1	6
2	44	5	1	5
3	55	4	1	4
4	73	3	1	3
5	110	2	1	2
6	147	6	2	3
7	220	1	1	1
8	330	6	3	2
9	440	2	2	1
10	660	3	3	1
11	880	4	4	1
12	1100	5	5	1
13	1320	6	6	1

The efficiency of the system comprising the generator, rectifier and capacitor is

$$\bar{\eta}_{\text{sys}} = \frac{\bar{P}_{\text{dc}}}{\bar{T}_{\text{gen}}\Omega} \,. \tag{6.17}$$

6.3 Results

The results section is organized as follows. The relationship between the mechanical (torque and speed) and electrical variables (dc voltage and current) is established and fitted with analytical functions for integration with wave-to-wire modelling and experimental post-processing. This relationship is expressed here as a function of the current at the rectifier's output terminals, I_{dc} and the rotational speed, Ω. In a real application, the current can be regulated by a dc-to-dc converter and the rotational speed can be continuously monitored. Then the generator and rectifier performance is addressed, namely the power factor, efficiency, and demagnetization current, as a function of the counter torque.

Data was obtained from 127 steady-state operating points, (Ω, R), as shown in Fig. 6.4 with the resulting torque $\bar{T}_{\text{gen}}$.

Balanced loads and uniform generator phase properties were assumed. Therefore, phases 1 and 2 were used to express phase-associated values. Results labelled with the superscript * were normalized with relevant properties commonly found on electrical machines' nameplates

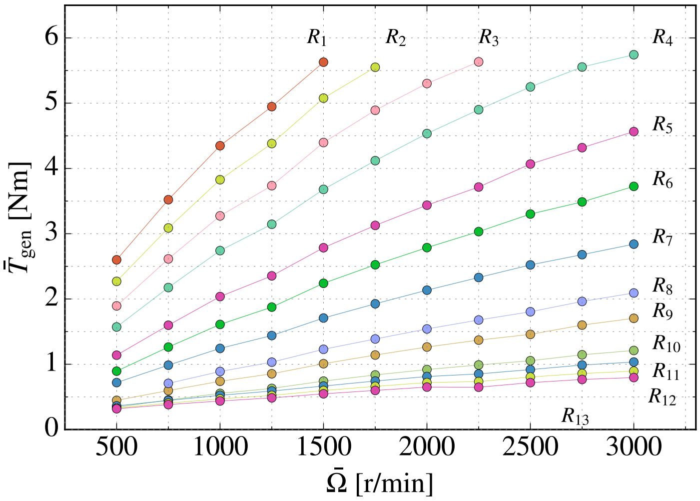

Figure 6.4: Operating points for generator and rectifier tests. R_1 to R_{13} denote the load bank resistances according to Table 6.3.

Table 6.4: Reference values for test results normalization.

T_{ref} [Nm]	Ω_{ref} [rad/s]	I_{ref} [A]	U_{ref} [V]	R_{ref} [Ohm]
6.5	628.3	3.5	128	36.6

and data-sheets, as indicated in Table 6.4. The reference torque (T_{ref}) is the continuous-duty standstill torque in motor operation. The maximum operational speed is the reference rotational speed (Ω_{ref}). The reference current (I_{ref}) is the continuous-duty standstill current in motor operation. The reference voltage (V_{ref}) is the open-circuit voltage at 1000 r/min in generator operation. The reference resistance (R_{ref}) is the ratio of the reference voltage to the reference current.

The generator normalized torque, $\bar{T}^*_{\text{gen}} = \bar{T}_{\text{gen}}/T_{\text{ref}}$, can be expressed as a function of the normalized current, $I^*_{\text{gen}} = I_{\text{gen}}/I_{\text{ref}}$, as illustrated in Fig. 6.5, and approximated by

$$\bar{T}^*_{\text{gen}} = \frac{d_1 I^*_{\text{dc}} + d_2}{I^*_{\text{dc}} + d_3}, \tag{6.18}$$

where d_1, d_2 and d_3 are the fitting coefficients listed in Table 6.5.

The relationship between the normalized dc voltage $U^*_{\text{dc}} = U_{\text{dc}}/U_{\text{ref}}$ and the normalized rotational speed, $\bar{\Omega}^*$, was fitted with

$$U^*_{\text{dc}_k} = \frac{e_{1,k}\bar{\Omega}^*}{\bar{\Omega}^* + e_{2,k}}, \tag{6.19}$$

with coefficients $b_{i,k}$ given in Table 6.6 for constant normalized resistances, $R^*_k = R_k/R_{\text{ref}}$,

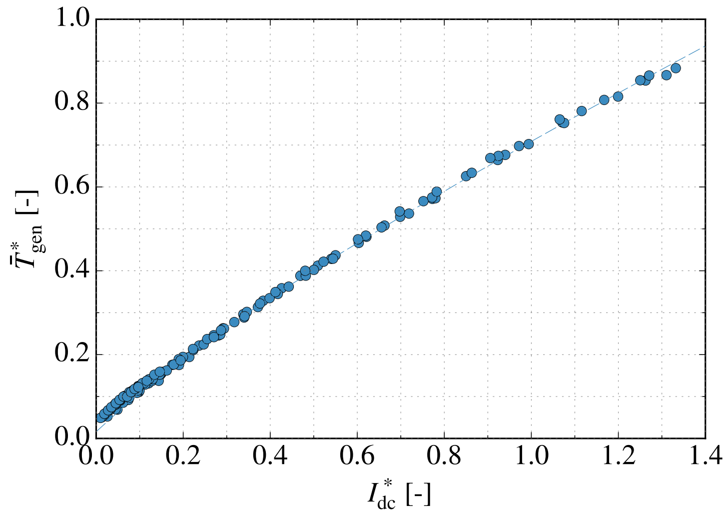

Figure 6.5: Normalized generator torque, $\bar{T}^*_{\text{gen}}$, as a function of normalized current, I^*_{dc}. The solid symbols and the dashed line correspond to experimental results and to the fitting given by Eq. (6.18), respectively.

Table 6.5: Coefficients for Eq. (6.18).

d_1	d_2	d_3	R-squared
4.13	0.1741	5.5052	0.9995

corresponding to the bank setup indicated in Table 6.3. Their respective R-squared values are also listed.

In situations where the calculation of instantaneous values from data acquired in steady-state conditions is acceptable (recall the assumption presented in Sec. 6.2), the results of Eqs. (6.18) and (6.19) can be used as follows. At an instant t, the normalized rotational speed of the turbo-generator, Ω^*, is given by Eq. (6.1) from $t-\Delta t$, where Δt is the simulation time-step, and the regulation of the dc-to-dc converters results in a rectifier output current, i_{dc}. The pair (Ω^*,i^*_{dc}) is then used to evaluate T^*_{gen} from Eq. (6.18) and u^*_{dc} from Eq. (6.19). Finally, Eq. (6.1) is solved for the rotational speed to be used in time $t + \Delta t$.

The efficiency of the generator-rectifier set is plotted in Fig. 6.7 to assess the quality and usefulness of Eqs. (6.18) and (6.19). Recalling Eq. (6.17), full symbols indicate system efficiency, $\bar{\eta}_{\text{sys}}$, calculated from measurements, $\bar{P}_{\text{dc}}$ and $\overline{T_{\text{gen}}\Omega}$, and dashed lines are derived from the fittings of Eqs. (6.18) and (6.19) with

$$\bar{\eta}_{\text{sys}} = \frac{I_{\text{dc}}U_{\text{dc}}}{\bar{\Omega}\bar{T}_{\text{gen}}} . \tag{6.20}$$

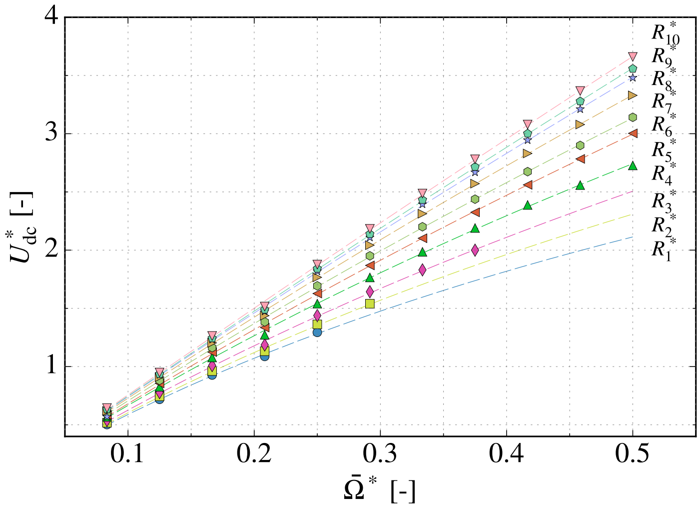

Figure 6.6: Normalized dc voltage, U^*_{dc}, versus the normalized rotational speed, Ω^*, for selected normalized resistances, R^*_k. The solid symbols and the dashed lines correspond to the experimental results and Eq. (6.19), respectively.

Table 6.6: Coefficients for Eq. (6.19).

k	R^*_k	$e_{1,k}$	$e_{2,k}$	R-squared
1	1.01	6.00	0.920	0.9984
2	1.20	7.88	1.206	0.9985
3	1.50	10.05	1.505	0.9991
4	2.00	12.38	1.757	0.9995
5	3.01	19.90	2.821	0.9997
6	4.02	22.32	3.060	0.9997
7	6.02	31.37	4.206	0.9997
8	9.02	46.54	6.176	0.9996
9	12.03	62.38	8.254	0.9997
10	18.05	91.44	11.98	0.9997

Results are plotted for selected bank resistances corresponding to setups indicated in Table. 6.3. It can be seen that the maximum efficiency occurs for normalized rotational speeds between $0.35 \leq \bar{\Omega}^* \leq 0.5$ increasing with the bank resistance up to $R^* = R^*_4$, below which the efficiency decreases. The fitting-derived efficiency shows good agreement with the measurements. Deviations of around 1% are observed for most bank resistances which are considered a good approximation considering the uncertainty of the measurements and fittings. For R^*_8 and R^*_{10}, this value can reach 3%.

The generator efficiency is illustrated in Fig. 6.8 as a function of the mechanical inputs. It varies with the counter torque and rotational speed, as expected. The maximum observed efficiency occurs for a counter torque in the range $0.4 < \bar{T}^*_{\text{gen}} < 0.75$ at the maximum test

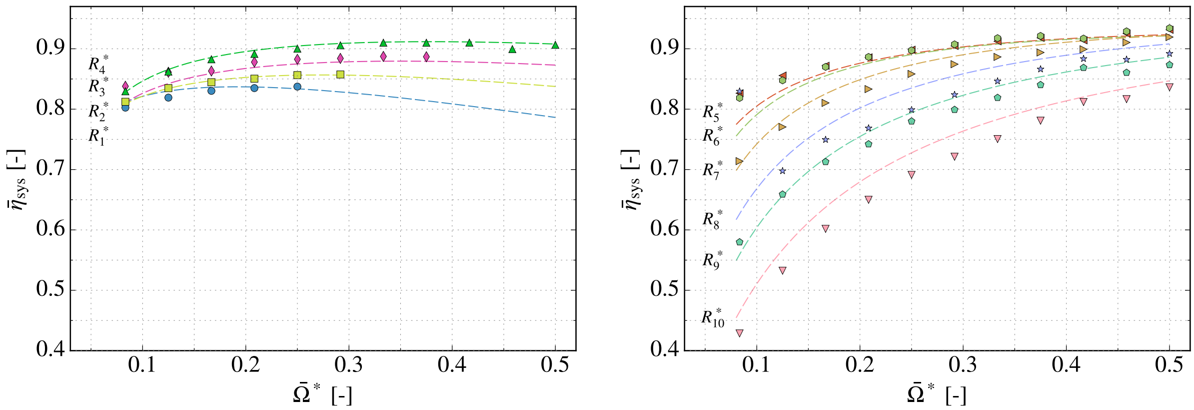

(a) R_1^* to R_4^*.

(b) R_5^* to R_{10}^*.

Figure 6.7: Generator-rectifier set efficiency, $\bar{\eta}_{\text{sys}}$, versus the normalized rotational speed, $\bar{\Omega}^*$, for selected normalized resistances, R_k^*. The solid symbols and the dashed lines correspond to experimental results and to Eq. (6.20), respectively.

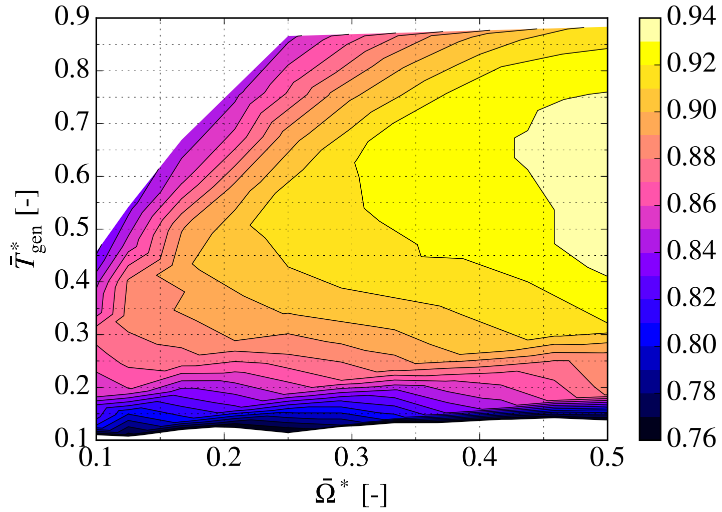

Figure 6.8: Generator efficiency map as a function of the normalized rotational speed, $\bar{\Omega}^*$, and torque, $\bar{T}^*_{\text{gen}}$.

speed. It is unknown if the observed maximum efficiency corresponds to the actual maximum because the test rig motor could not be driven above its synchronous speed.

The rectifier efficiency is illustrated in Fig. 6.9 as a function of the mechanical inputs. It shows that the rectifier efficiency is mostly independent of the rotational speed and is ruled by the generator counter torque. The efficiency increases continuously with torque, reaching $\bar{\eta}_{\text{rec}} = 0.95$ at $\bar{T}^*_{\text{gen}} \approx 0.3$, up to an observed maximum of $\bar{\eta}_{\text{rec}} = 0.99$ at $\bar{T}^*_{\text{gen}} \approx 0.9$. The observed maximum may be less than the real maximum because the generator limited the maximum test current, which is lower than the rectifier-rated current. This observation suggests that it may be possible to match the generator's maximum efficiency torque range with another rectifier's

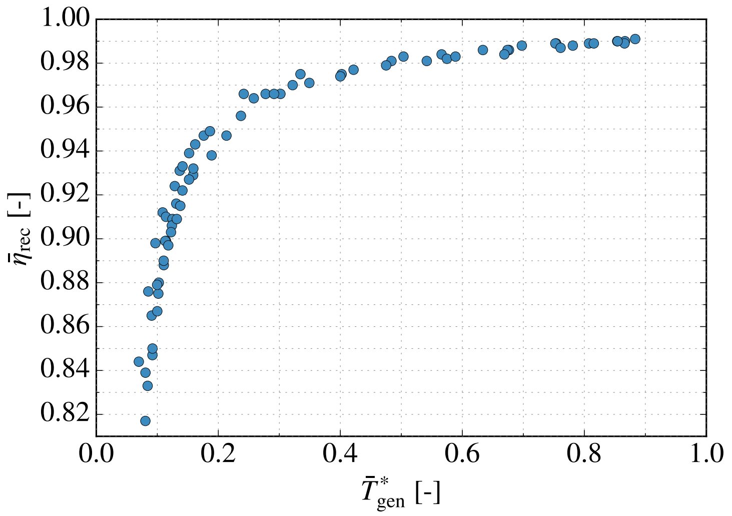

Figure 6.9: Relationship between rectifier efficiency, $\bar{\eta}_{\text{rec}}$, and normalized generator torque, $\bar{T}^*_{\text{gen}}$.

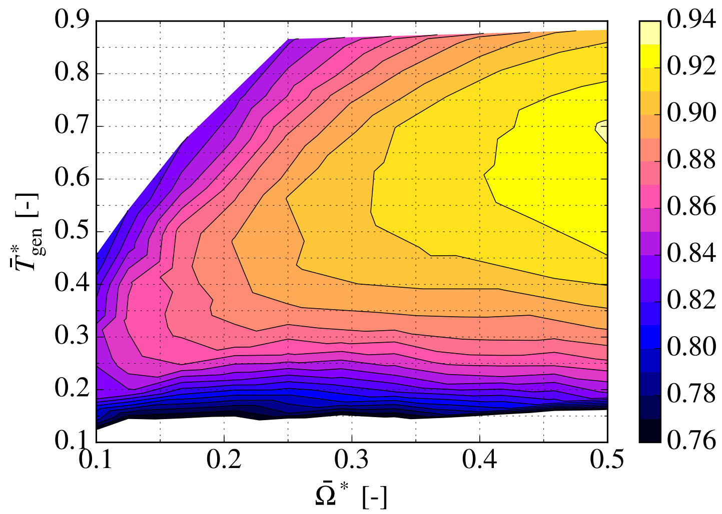

Figure 6.10: Generator-rectifier set efficiency map as a function of the normalized rotational speed, $\bar{\Omega}^*$, and torque, $\bar{T}^*_{\text{gen}}$.

range if it has a lower rated current than the tested rectifier.

The total generator-rectifier efficiency, $\bar{\eta}_{\text{sys}}$, is illustrated in Fig. 6.10 for different mechanical inputs. Naturally, Eq. (6.17) can be rewritten as $\bar{\eta}_{\text{sys}} = \bar{\eta}_{\text{gen}}\bar{\eta}_{\text{rec}}$. As such, the generator-rectifier efficiency follows the same overall trend of the generator efficiency concerning rotational speed in high counter torque regimes. In contrast, the rectifier efficiency dominates in lower counter torque regimes and the variation with speed is attenuated. The maximum efficiency, $\bar{\eta}_{\text{sys}} \approx 0.93$, is observed at $\bar{T}^* \approx 0.7$ and $\bar{\Omega}^* = 0.5$. Again, the true maximum efficiency is unknown due to the test-rig rotational speed limit.

The generator total, displacement, and distortion power factors are primarily independent

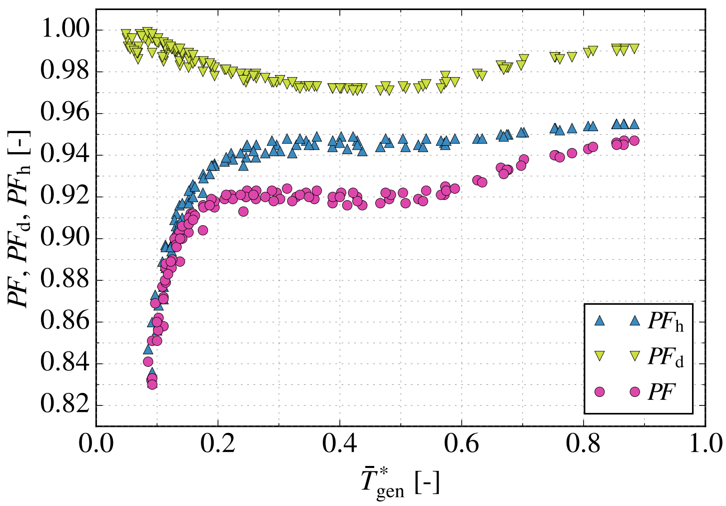

Figure 6.11: Relationship between generator total power factor, PF, distortion power factor, PF_{d}, harmonic power factor, PF_{h}, and normalized torque, T^*_{gen}.

of the rotational speed as plotted in Fig. 6.11 as a function of the generator counter torque. The harmonic content caused by the rectifier's non-linearity and lack of current control has a more significant influence over the total power factor than the phase displacement caused by the capacitive filter. Three distinct zones can characterize the total power factor for the proposed generator-rectifier set. For $0 < \bar{T}^*_{\mathrm{gen}} \leq 0.2$, the power factor increases with torque from very low values due to low harmonic power factors, while the displacement power factor is near its maximum. For $0.2 < \bar{T}^*_{\mathrm{gen}} \leq 0.5$, the power factor remains approximately constant around $PF_{\mathrm{d}} \approx 0.92$ with a slight decrease with torque due to the displacement power factor reaching its minimum value of $PF_{\mathrm{d}} = 0.97$ at $\bar{T}^*_{\mathrm{gen}} \approx 0.45$. In contrast, the distortion power factor remains constant. For $\bar{T}^*_{\mathrm{gen}} > 0.5$, the total power factor increases consistently with torque up to the maximum observed value of $PF \approx 0.948$ as both displacement and distortion power factors increase with torque.

The normalized direct- and quadrature-axis currents are depicted in Fig. 6.12 versus the normalized torque. It is seen that the normalized quadrature-axis current increases with the normalized torque in line with Eq. (6.14). As per the manufacturer's recommendation, the direct-axis current should be $I^*_{\mathrm{d}} < 1.4$ to avoid rotor demagnetization. Results show that the normalized direct-axis current converged asymptotically to $I^*_{\mathrm{d}} \approx 0.11$, indicating a low demagnetization risk for the chosen generator-rectifier set. However, the experiments were performed under steady-state conditions, and the presented results do not exclude the occurrence of

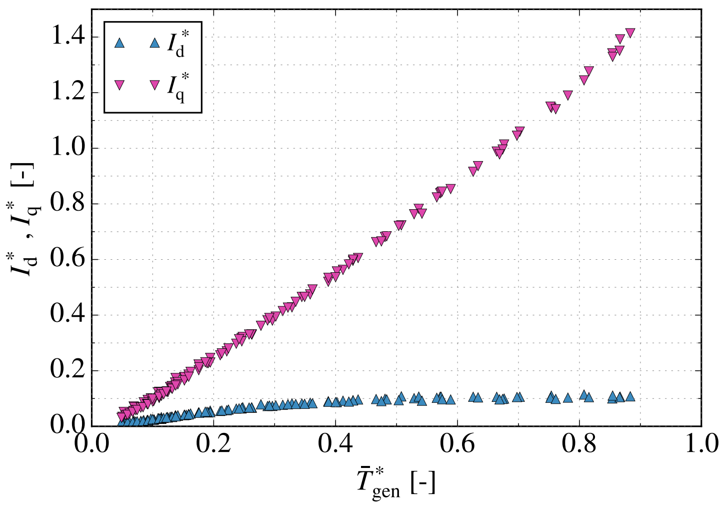

Figure 6.12: Relationship between normalized direct-, I_d^*, and quadrature-axis, I_q^*, currents and torque, T_{gen}^*.

direct-axis current peaks during transient conditions.

The relationship between torque ripple and filter capacitance was excluded from the present research.

6.4 Conclusion

This Chapter presents the steady-state operational performance of a setup comprising a permanent magnet synchronous generator (PMSG), a three-phase full-bridge rectifier and a capacitive filter for 127 experimental data sets acquired in a dedicated test rig.

The relationships between the generator's mechanical input and the rectifier's electrical output were established and approximated with functions of the direct current and rotational speed. The direct current was the main influence over the generator counter-torque and is assumed to be regulated by at least one dc-to-dc converter in wave energy applications. The rotational speed is assumed to be continuously monitored in these applications and is the primary influence over the dc voltage, with a slight influence of the direct current. The efficiency of the generator-rectifier set was calculated using the derived relationships and was compared to the measurements. The comparison error was around 1% for most cases, with an observed maximum of 3%. This outcome emphasizes the potential for incorporating these derived relationships into more comprehensive wave-to-wire models for designing oscillating-water-column

(OWC) wave energy converters or forecasting power production in techno-economic assessments.

Still, for the selected components and considering an operating range between 20 and 100% of the generator continuous duty torque, the power factor is in the interval 0.92 to 0.95, and the generator-rectifier efficiency varies between 0.83 and 0.93 for the same torque range but depending on the rotational speed. These results are considered satisfactory, especially compared to induction generators of similar size and given the simplicity of bridge rectifiers.

Regarding the risk of rotor demagnetization, the results indicate that if hypothetical transient peaks are mitigated, the proposed generator and rectifier can operate continuously without the risk of rotor demagnetization. Further testing with mechanical input variations typical of OWC converters should follow to define the control algorithms.

The generator-rectifier pairing could be improved, as a lower-rated rectifier can potentially have the same maximum efficiency torque range as the generator.

Chapter 7

Power electronic converter design for off-grid OWC wave energy converters

This Chapter introduces a low-power off-grid oscillating water column wave energy converter comprising a spar buoy, a biradial turbine, a permanent magnet generator, a full-wave bridge rectifier and a lead-acid battery bank. The research aims at the preliminary design of a power electronic converter for interfacing the rectifier with the battery bank. The power-take-off system was modelled in Simulink/MATLAB and its performance was assessed considering a wave climate characteristic off the Port of Leixões, Portugal. The chamber pressure, the turbine, generator and rectifier performance were taken from experimental data sets. A simplified battery model was derived from the manufacturer's data-sheet. An ideal switched-mode step-down dc-to-dc converter operating in discontinuous conduction mode regulates battery charging and service load supply. This converter, in parallel with an ideal braking chopper, adjusts the generator counter torque by regulating the current through the rectifier. Twelve system variables were recorded for selected pairs of the input pressure and the step-down converter design coefficient. The duty-cycle range, the inductance and the braking resistance were calculated. The results show that around 400 W of electrical power is available at the rectifier's terminals during the most frequent sea states. The system was rated at 1.4 kW from the batteries maximum charging power. A control strategy was proposed and tested with simulations in time-dependent conditions. Results show that the controllers can protect the turbo-generator from over-current and over-speed, and limit the step-down converter output current.

7.1 Objectives

Equipping off-grid wave energy converters (WEC) with an internal batteries is recommended to smooth the intermittency of wave energy and ensure a continuous power supply to its service loads. Battery charging is a complex process, requiring different voltage and current schemes depending on the battery type (lithium-ion, lead-acid, etc.) and its state-of-charge.

A turbine driving a permanent magnet synchronous generator (PMSG) coupled to a full-wave bridge rectifier and a dc-to-dc converter is a simple off-grid power generation system. However, a diode rectifier is a passive component and does not provide control over transmitted power. Excluding mechanical or pneumatic regulators, an additional power converter is needed to regulate the output power.

As seen in Chapter 6, the rectifier output current is proportional to the generator counter torque while the voltage is proportional to the rotational speed with a slight influence of the current. In a system consisting solely of a turbine, a PMSG, a diode rectifier, and a battery, the generator counter torque is regulated by the battery's internal resistance, while the battery charging voltage exhibits significant variation in response to the OWC chamber pressure changes.

This Chapter presents a power electronic converter for off-grid direct-current power supply with an OWC converter, a biradial turbine, a permanent magnet generator and diode rectifier. The research objective is to perform preliminary component and control strategy design for internal battery charging and turbo-generator operation. The main contributions of this Chapter are the converter and controller specifications, which serve as the foundation for future detailed design and component procurement for experimental testing.

The power electronic interface between the diode rectifier and the battery bank is depicted in Fig. 7.1. It comprises a buck converter between the rectifier and the internal battery bank, and a chopper between the rectifier and a braking resistance. The service loads are connected to the battery bank. The OWC pneumatic power drives the turbine, while the combined action of the buck converter and the braking chopper regulates the rectifier's output impedance, governing the current drawn and the generator counter torque. A buck converter [149] was chosen under the assumption that the rectifier's output voltage, U_{dc}, is higher than the battery

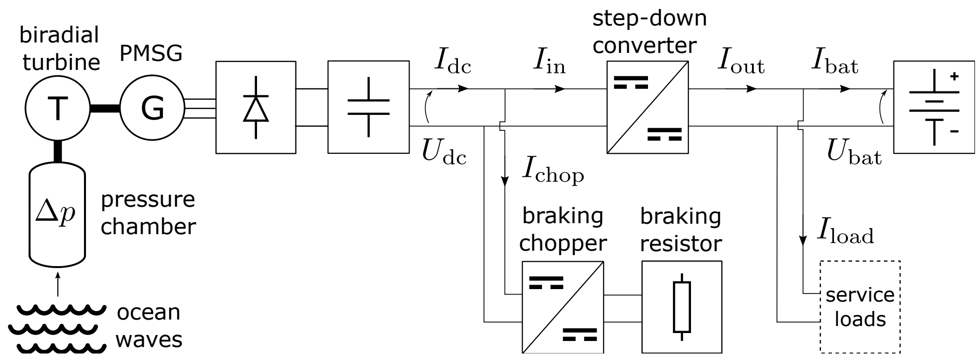

Figure 7.1: Proposed off-grid OWC turbo-generator, power electronic interface and batteries.

voltage, U_{bat}, during the majority of the operational time. Alternatively, a boost or a buck-boost converter should be considered. Versions of these converters with galvanic isolation exist and are recommended for practical implementation. Still, a non-isolated ideal buck converter was considered as the first approach.

The buck converter regulates the current supply to the battery and service loads. During energetic sea-states, the power consumption might not be sufficient to maintain the turbo-generator within the rotational speed safety-limit. Without power consumption, the turbo-generator accelerates until its open-circuit losses match the pneumatic power input. This situation poses risks to the system, including centrifugal stress, vibration, and over-voltage. A pulse-width-modulated (PWM) braking chopper supplies an adjustable dump load to draw rectifier current and maintain a generator counter torque.

Consider the power variation across an ideal buck converter operating between two voltage levels, U_{dc} and U_{bat}, as a function of the input voltage, U_{dc}, and duty cycle d_{buck}, depicted in Fig. 7.1. Naturally, there is no transmitted power when $V_{\text{dc}} < V_{\text{bat}}$. A buck converter can operate in discontinuous conduction mode (DCM) or continuous conduction mode (CCM), depending on whether the inductor current falls to zero during a switching cycle. In DCM, the power curve is a quadratic function of the input voltage, U_{dc}, for any duty cycle, d_{buck}. The maximum power points of an impulse turbine follow a quadratic curve with respect to the rotational speed for any given chamber pressure [150]. Since the rectifier output voltage is proportional to the speed [149], the first research hypothesis explored here is the possibility of tracking the maximum power points with a constant or near-constant duty cycle with a buck converter in DCM.

The control strategy lies in the notion that power generation is determined by the batteries'

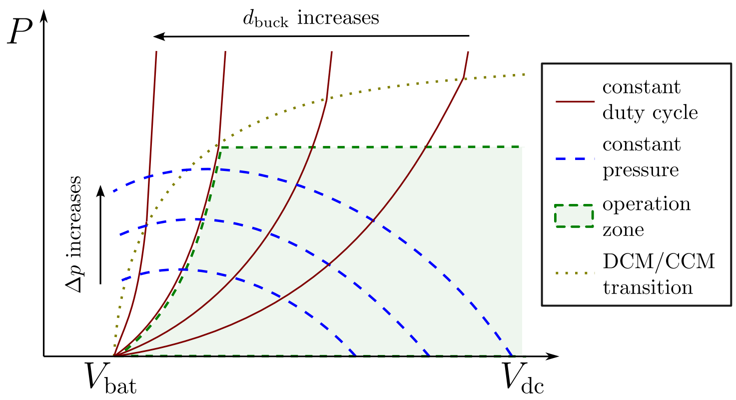

Figure 7.2: Power across and ideal buck converter operating between two voltage levels, V_{dc} and V_{bat}, as a function of the input voltage, V_{dc}, and duty cycle d_{buck}.

state-of-charge (SOC) and service load fluctuations. Consequently, an off-grid converter operates under maximum power production for a fraction of the total operational time. However, it should quickly and effectively switch between low-power and maximum-power production regimes.

Considering Fig. 7.2, the operation under constant chamber pressure can be divided into a zone with a lower voltage than the maximum power point, and a zone with a higher voltage. Normal operation occurs in the higher voltage zone, where the power varies from maximum to zero (turbo-generator runaway). Adjusting the power production is achieved by changing the buck duty cycle. As such, a simple feedback loop can control the battery charging by regulating the buck duty cycle as a function of the battery bank voltage or the current. When more charging current is needed, the duty cycle is increased. However, the duty cycle should be limited. There are situations where the pneumatic power input is lower than the electrical power required by the service loads or battery. In these situations, the duty cycle increases above the value for maximum power production. Additionally, a rated power limit is needed to protect the WEC's components. The air chamber pressure and rectifier output voltage could be possible alternatives for controller saturation reference variables and should be the subject of future research.

7.2 Methods

The power take-off system (PTO) was modelled and simulated in Simulink/MATLAB. The sub-component modelling combines experimental test-results of OWC buoy, turbine, generator and rectifier, battery manufacturer data and theoretical models for chopper and step-down converter. The electrical components were simulated with averaged value models, neglecting the rippling effects caused by the rectifier, transistor switching, capacitor and inductor charging/discharging.

A first set of simulations in steady-state conditions was performed for a range of input pressures and step-down converter coefficients to design the system and a control strategy for a defined turbine, generator, rectifier, and battery bank. Then a second set of simulations in time-dependent conditions was performed to test the controllers ability to prevent generator over-current and over-speed and limit the step-down converter output current.

7.2.1 Applications

A reference application for the off-grid converter was derived from the requirements to charge an Iver3 Standard AUV by L3Harris Ocean Server [151], see Table 7.1. This AUV is used by civilian and military organizations [152, 153]. It uses inertial navigation, and has a side scan sonar and a magnetometer which enable hydrographic, search and recovery, and environmental monitoring missions. The recommended charging power is the specified minimum charging power with an additional 90 W to keep the vehicle's non-propulsion systems running [20]. A recent review on docking stations for AUV charging reports efficiencies ranging from 80 to 92% [154]. Assuming a docking station with 83% efficiency the recommended charging power for the Iver3 is 300 W.

7.2.2 OWC spar buoy

A spar buoy was purposely designed for this off-grid wave energy converter [34] and was tank-tested at 1:10 scale for regular and irregular waves [35]. Its shape and dimensions are illustrated in Fig. 7.3.

The hydrodynamic damping of an OWC equipped with an impulse turbine depends on the

Table 7.1: Iver3 AUV physical and electrical parameters, adapted from [20].

lenght [m]	1.52 to 2.16
hull diameter [m]	0.147
mass [kg]	27 to 38.5
autonomy [h]	8 to 14
recharge time [h]	5
internal battery capacity [Wh]	800
charging power [W]	160
required power in dock [W]	250

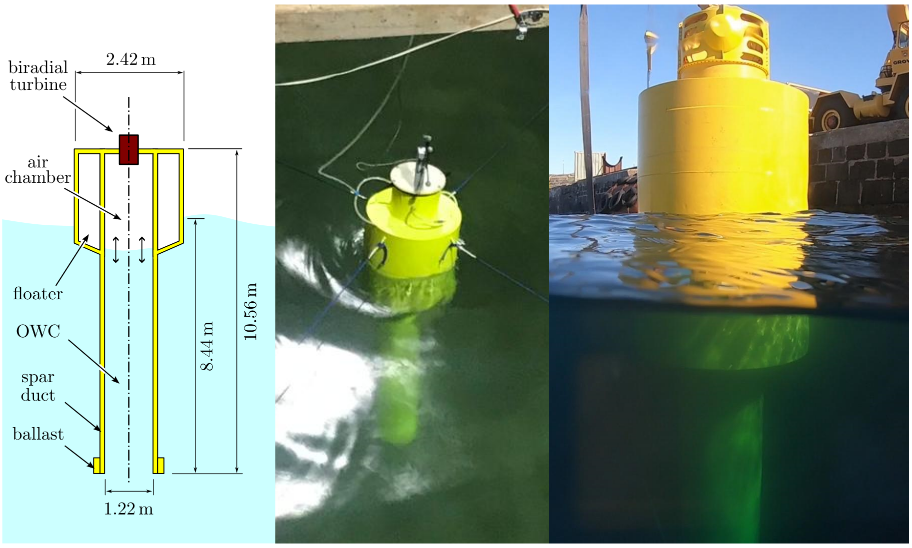

Figure 7.3: Off-grid OWC spar buoy dimensions [35].

turbine diameter and is approximately independent of its rotational speed [69]. As such, the OWC chamber relative pressure taken from experimental testing [35] can be used as the PTO model input. The nearly quadratic damping of impulse turbines is often emulated by replacing the turbine with a calibrated round orifice on the pressure chamber wall in OWC testing [30].

The pneumatic power of an OWC device is given by

$$P_{\mathsf{pneu}} = \frac{\dot{m}}{\rho} \Delta p \,, \tag{7.1}$$

where ρ is the air density Δp is the chamber relative pressure and $\dot{m}$ is the mass flow rate trough the turbine. If the turbine is replaced by a round orifice, comes

$$\dot{m} = \frac{\pi}{4} C_{\mathsf{d}} d_{\mathsf{o}}^2 \sqrt{2\rho} |\Delta p|^{-\frac{1}{2}} \Delta p \,, \tag{7.2}$$

where C_{d} is the discharge coefficient, and d_{o} is the orifice diameter. By rearranging Eqs. (7.1)

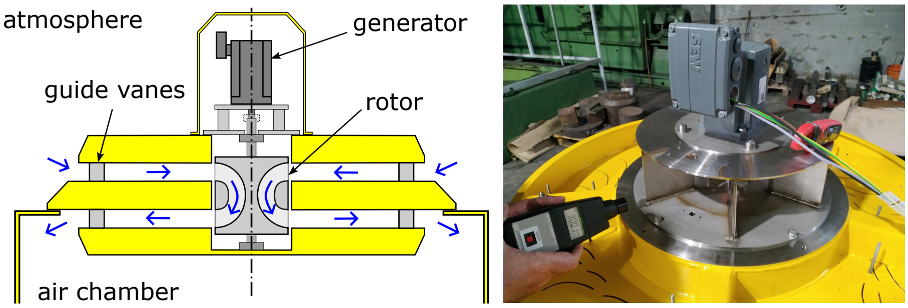

Figure 7.4: Turbo-generator for off-grid conversion.

and (7.2), the chamber pressure can be expressed as a function of the pneumatic power and orifice properties,

$$|\Delta p| = \frac{\rho^2}{4}\left(\frac{4P_{\mathsf{pneu}}}{\pi C_{\mathsf{d}} d_{\mathsf{o}}^2}\right)^{2/3}. \tag{7.3}$$

Equations (7.1), (7.2) and (7.3) are valid for instantaneous values.

The root-mean-square of the chamber pressure corresponding to each sea state was approximated by taking the associated average pneumatic power from the spar buoy power matrix and utilizing it in equation (7.3). The wave climate off the Port of Leixões, in the West coast of mainland Portugal, was then used to compile the pressure values into classes for which the probability of occurrence was calculated. The most relevant classes were used as the pressure input values for the PTO simulations.

7.2.3 Turbo-generator

Considering a direct rigid connection between the turbine and the generator, the rotational speed, Ω, results from the balance between the turbine torque, T_{turb}, induced by the OWC flow and the generator counter torque, T_{gen}, regulated by the joint action of the two dc-to-dc converters, Fig. 7.1. It is

$$J\frac{\mathrm{d}\Omega(t)}{\mathrm{d}t} = T_{\mathsf{turb}}(t) - T_{\mathsf{gen}}(t)\,, \tag{7.4}$$

where J is the total rotational inertia of the turbine and generator rotors, and t is time.

The turbine has a rotor diameter $D = 0.26$ m and is geometrically similar to the grid-connected 30 kW fixed-guide-vane biradial turbine [66]. Neglecting effects related to Reynolds number variations, the performance of geometrically similar turbines is characterized by the pressure,

$$\Psi = \frac{\Delta p}{\rho \Omega^2 D^2}\,, \tag{7.5}$$

torque (or power),

$$\Pi = \frac{T_{\text{turb}}}{\rho \Omega^2 D^5}\,, \tag{7.6}$$

and flow rate,

$$\Phi = \frac{Q}{\Omega D^3}\,, \tag{7.7}$$

coefficients. As such, the turbine torque to be used with Eq. 7.4 is given by

$$T_{\text{turb}} = \Pi(\Psi)\rho\Omega^2 D^5\,. \tag{7.8}$$

The relationship between the torque coefficient, Π, and the pressure coefficient, Ψ, is approximated by the polynomial

$$\Pi(\Psi) = b_1\Psi^4 + b_2|\Psi|^3 + b_3\Psi^2 + b_4|\Psi| + b_5\,, \tag{7.9}$$

with $b_1 = 5.4442 \times 10^{-4}$, $b_2 = -8.3127 \times 10^{-3}$, $b_3 = 5.0681 \times 10^{-2}$, $b_3 = 9.5067 \times 10^{-1}$ and $b_4 = 9.5067 \times 10^{-1}$, for the chosen turbine geometry and derived from experimental testing [66]. The flow rate coefficient, Φ, is related to the pressure coefficient by the fitting function

$$\Phi = \text{sign}(\Psi)\big(a_1 + a_2\sqrt{a_3\,|\Psi| + a_4}\,\big)\,, \tag{7.10}$$

with $a_1 = -6.5848 \times 10^{-2}$, $a_2 = 1.2551 \times 10^{-5}$, $a_3 = 4.6 \times 10^{8}$ and $a_3 = 2.7525 \times 10^{7}$, also valid for the chosen turbine geometry. The turbine efficiency is derived from the other dimensionless coefficients,

$$\eta_{\text{turb}} = \frac{\Pi}{\Phi\Psi}\,. \tag{7.11}$$

Variations in turbine rotational speed lead to changes in the ratio between the flow rate and pressure head (turbine damping), influencing the hydrodynamic energy conversion process of OWC WECs. However, in biradial impulse turbines it is seen that $K = \Psi/\Phi^2$ is approximately constant [64, 66]. Then, the relationship between pressure and flow rate of biradial turbines is

$$\Delta p \approx \left(\frac{\rho K}{D^4}\right) Q^2 \,. \tag{7.12}$$

This result shows that the rotational speed of biradial impulse turbines has a negligible effect on the turbine damping and, as such, on the hydrodynamic energy conversion process. Note that $\Delta p(Q)$ is approximately a quadratic function, justifying the turbine emulation with a round orifice in OWC testing refered in Section 7.2.2.

The generator is a SEW Eurodrive CM3C71S three-phase synchronous servomotor, see Table. 6.2 and the rectifier an IXYS VUO35-12NO7 standard module. The pair is modelled here as a single unit following the experimental characterization of the relationship between the mechanical input (torque and rotational speed) and electrical output (direct current and voltage) presented in Chapter 6.

The relationship between the normalized generator counter torque, T^*_{gen}, and the normalized rectifier output current, I^*_{dc} was found to be well fitted by the rational function

$$T^*_{\text{gen}} = \frac{d_1 I^*_{\text{dc}} + d_2}{I^*_{\text{dc}} + d_3} \,. \tag{7.13}$$

Likewise, the rectifier normalized output voltage, $U^*_{\text{dc}_k}$, is also well fitted by a rational function of the normalized rotational speed, Ω^*, and with a slight influence from the normalized rectifier load, $R^*_k = U^*_{\text{dc}}/I^*_{\text{dc}}$,

$$U^*_{\text{dc}_k} = \frac{e_{1,k}\bar{\Omega}^*}{\bar{\Omega}^* + e_{2,k}} \,. \tag{7.14}$$

The fitting coefficients d_1, d_2, d_3, $e_{1,k}$ and $e_{2,k}$ for Eqs. 7.13 and 7.14 are indicated in Tables 6.5 and 6.6, respectively, and the normalization reference values for Eqs. 7.13 and 7.14 are given in Table 6.4.

7.2.4 Power electronic converter

A non-isolated switched-mode step-down converter [149] is designed to operate in discontinuous condution mode (DCM). Its average output current, I_{out}, when operating between two voltage sources, U_{dc} and U_{bat}, is

$$I_{\text{out}} = \frac{d_{\text{buck}}^2}{2fL}\left(\frac{U_{\text{dc}}^2}{U_{\text{bat}}} - U_{\text{dc}}\right), \tag{7.15}$$

where d_{buck} is the converter switching duty cycle, f is the switching frequency and L is the converter inductance. From the unitary efficiency assumption, $U_{\text{dc}}I_{\text{in}} = U_{\text{bat}}I_{\text{out}}$, comes the input current,

$$I_{\text{in}} = \frac{d_{\text{buck}}^2}{2fL}\left(U_{\text{dc}} - U_{\text{bat}}\right). \tag{7.16}$$

The step-down design coefficient is defined here as

$$K_{\text{buck}} = \frac{d_{\text{buck}}^2}{2fL}. \tag{7.17}$$

At the boundary between discontinuous and continuous conduction mode (CCM), the average output current is

$$I_{\text{out}_{\text{lim}}} = \frac{d_{\text{buck}}}{2fL}\left(U_{\text{dc}} - U_{\text{bat}}\right). \tag{7.18}$$

As such, Eqs. (7.15) and (7.16) are valid only if $I_{\text{out}} < I_{\text{out}_{\text{lim}}}$.

The braking chopper is modelled here as an ideal switch in series with a resistor. The current through the braking resistor is

$$I_{\text{chop}} = \frac{d_{\text{chop}}}{R}U_{\text{dc}}, \tag{7.19}$$

where d_{chop} is the chopper switching duty cycle and R is the braking resistance.

Note that the joint action of the dc-to-dc converters regulates the generator counter torque as seen by Eq. (7.13) and Fig. 7.1,

$$I_{\text{dc}} = I_{\text{in}} + I_{\text{chop}}, \tag{7.20}$$

and that the step-down converter regulates the current to the battery and loads,

$$I_{\text{out}} = I_{\text{bat}} + I_{\text{load}}. \tag{7.21}$$

7.2.5 Battery bank

The battery bank comprises four series-connected Mastervolt gel batteries MVG 12/85 [155] rated at 12 V with a nominal capacity of $C_{20} = 85$ Ah at 25°C for a current $I_{20} = 4.25$ A. Gel batteries are often used as service batteries in off-grid systems despite being more expensive than absorbent glass mat (AGM). Charging follows the three-step procedure, also known as IUoU. The charge parameters presented here are tuned for the battery model and connection chosen.

The first step is the bulk phase, and starts when the bank voltage drops below $U_{\text{blk}} = 47.6$ V. All battery loads should be removed and the charging current set to a constant value in the range $20 \leq I_{\text{blk}} \leq 25.5$ A. A maximum of 42.5 A is possible at the expense of the batteries' useful life. The bulk phase should end when the bank voltage reaches 57 V. This value can be adjusted depending on the batteries' temperature to prolong their useful life.

The second step is the absorption phase or constant-voltage boost stage. The bank should be in over-voltage at $U_{\text{abs}} = 57$ V while the charging current decreases. The absorption phase continues until 6% of the maximum charging current is reached, $I_{6\%} = 1.5$ A.

Finally there is the float phase. The bank voltage should be kept at $U_{\text{flt}} = 55.2$ V while the bank current is allowed to vary between the maximum charge and discharge currents imposed by the state-of-charge and existing service loads. If the bank voltage drops below U_{blk}, the service load supply should be interrupted, and the charger returned to the bulk phase.

7.2.6 Control

A closed-loop control scheme regulates the battery charging by varying the step-down converter duty cycle as represented in Fig. 7.5. The process variable is either the battery bank current or voltage, depending on the charging stages described in Section 7.2.5. The set-point error is fed to a proportional-integral (PI) controller whose output signal is the duty cycle, d_{buck}. The manipulated variable is the step-down converter output current, I_{out}, as defined in Eq. (7.15). The service loads are disturbances on the charging process, as they consume part of the step-down converter output current. If the service load current, I_{load}, is larger than the step-down output current, I_{out}, the battery discharges. Consider Eqs. (7.13), (7.15), (7.16), (7.20)

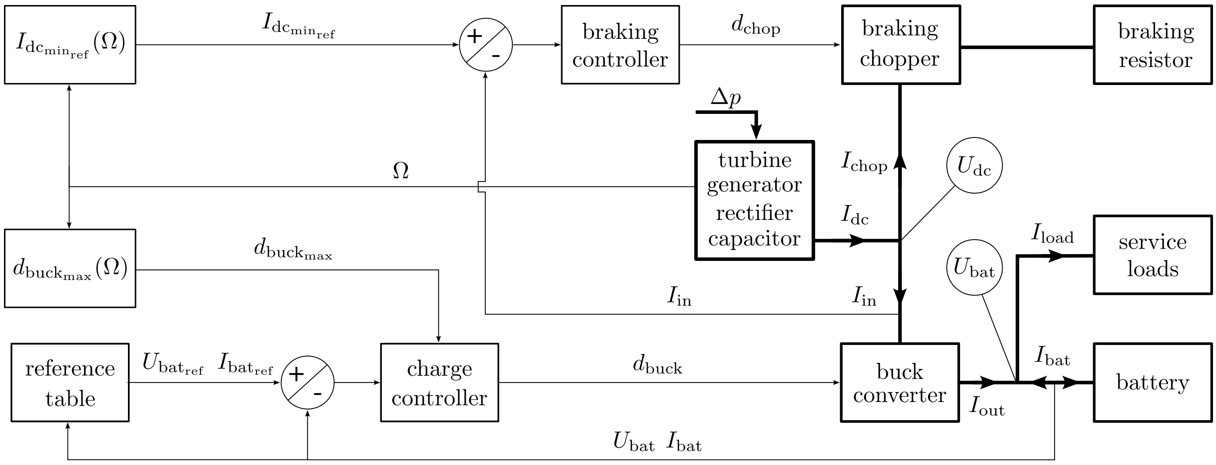

Figure 7.5: Converter control scheme.

and (7.21). Note that without dump or service loads, $I_{\text{chop}} = 0$ and $I_{\text{load}} = 0$, the generator counter torque becomes entirely dependent on the battery charging process. Both the generator counter torque and the step-down converter output current are proportional to the duty cycle. As such, it becomes necessary to define an upper saturation limit for the controller output to limit these currents. This limit was derived from the steady-state simulations presented in Section 7.3. Battery discharging and service load protection is outside the scope of this study.

An open-loop control scheme regulates the dump load by acting on the braking chopper as represented in Fig. 7.5. It passes current through the braking resistor when the step-down converter input current falls below a threshold, imposing a minimum rectifier output current and generator counter torque by consequence. This control scheme indirectly keeps the turbo-generator below the specified rotational speed because the response of the electrical system is faster than that of the mechanical one. The dump load replaces the battery charging and service loads before the turbo-generator over-speeds. Consider again Eqs. (7.13), (7.15), (7.16), (7.20) and (7.21), but now assume $I_{\text{bat}} = 0$ and $I_{\text{load}} = 0$. It is seen that there is no generator counter torque because $I_{\text{dc}} = 0$ unless $I_{\text{chop}} \neq 0$. The process variable for this control loop is the rectifier output current, I_{dc}. Here the reference chopper current, I_{chop} is the difference between the minimum rectifier output current as function of the rotational speed, $I_{\text{dc}_{\text{min}}}(\Omega)$, and the step-down converter input current, I_{in}. The controller output signal is the braking chopper duty cycle, d_{chop}, calculated with Eq. (7.19) and the manipulated variable is the braking chopper current, I_{chop}. Eqs. (7.19) and (7.20) show that while $I_{\text{in}} > I_{\text{dc}_{\text{min}}}$, the controller should impose $d_{\text{chop}} = 0$, and $0 < d_{\text{chop}} < 1$ otherwise. It is necessary to define an adequate braking resistance, R, to guarantee the necessary chopper current for the expected range of voltages, U_{dc}. The minimum rectifier output current and braking resistance were derived from the simulations in steady-state conditions presented in Section 7.3. The modelling error associated to Eq. (7.19) is not expected to severely influence the turbine rotational speed, as such, an open-loop control scheme was considered sufficiently accurate for chopper operation.

7.2.7 Simulation setup

Simulations in steady-state and time dependent conditions were performed with different objectives. The former to design the power electronic converter and the latter to test the control strategy.

Steady-state conditions

A series of simulations in steady-state conditions were performed for a range of OWC chamber pressures, Δp, and step-down converter design coefficients, $K_{\text{buck}} = d^2_{\text{buck}}/(2fL)$.

The Simulink model is illustrated in Fig. 7.6 and is described as follows. Note that the description and illustration of the block's input/output ports were simplified for clarity. Other ports and blocks were used, namely for variable measurement and recording. The battery bank was modelled as a constant voltage source, where $U_{\text{bat}} = U_{\text{float}} = 55.2\,$V, connected in series with a resistor that models the battery bank internal resistance, $R_{\text{bat}} = 2.48 \times 10^{-4}\,$Ohm. Custom function blocks defined the turbine, generator and rectifier equations. These components were then inserted in a sub-assembly block with the chamber pressure, Δp, and rectifier output current, I_{dc}, as inputs and the rectifier output voltage, U_{dc}, as output. The step-down converter was modelled with a custom function block using the design coefficient, K_{buck}, the rectifier output voltage, U_{dc} and the battery voltage, U_{bat} as inputs, and the converter's input and output currents as the block's output, I_{in} and I_{out}, respectively. It was not necessary to simulate the braking chopper and the service loads for this set of simulations. Making $I_{\text{load}} = 0$ and $I_{\text{chop}} = 0$, it comes $I_{\text{dc}} = I_{\text{in}}$ and $I_{\text{bat}} = I_{\text{out}}$. The turbine-generator-rectifier, the step-down converter, and the battery blocks were connected with a Simscape Specialized Power Systems grid.

Twelve variables were recorded in addition to the two inputs, Δp and K_{buck}: turbine dimen-

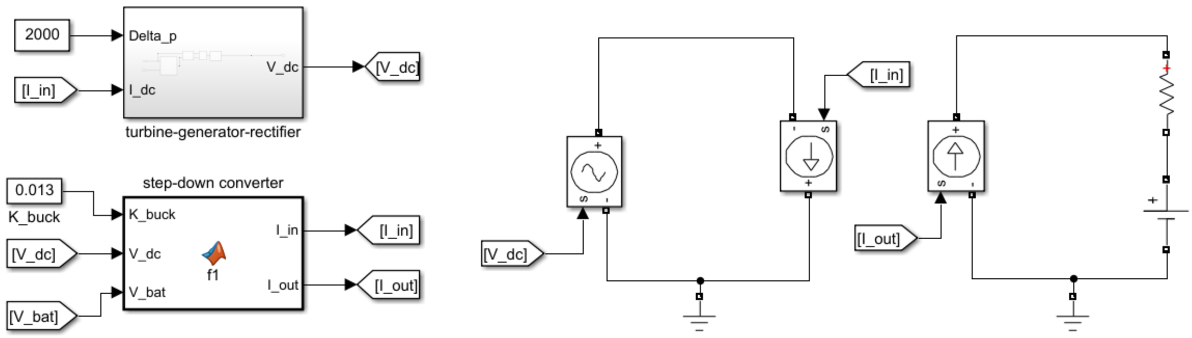

Figure 7.6: MATLAB/Simulink model for simulations in steady-state conditions (simplified).

sionless coefficients, Ψ, Φ, Π and η_{turb}, flowrate, Q, rotational speed, Ω, turbine and generator torque, T_{turb} and T_{gen}, rectifier output voltage and current, U_{dc} and I_{dc}, generator-rectifier efficiency, η_{gr}, and battery current, I_{bat}. Note that since $I_{\text{chop}} = I_{\text{load}} = 0$, it is $I_{\text{dc}} = I_{\text{in}}$ and $I_{\text{bat}} = I_{\text{out}}$.

Time-dependent conditions

A set of simulations with time-dependent conditions was performed to test the step-down converter controller saturation and braking chopper operation described in Sec. 7.2.6. The numerical model depicted in Fig. 7.6 was updated to inclue two controlled current sources for the chopper and service loads as illustrated in Fig. 7.7. An additional custom function block models the chopper and its controller. The step-down converter custom function block was updated with the frequency, f_{buck}, and the inductance, L, and the design coefficient K_{buck} was replaced by the duty cycle, d_{buck} as an input. An additional sub-system models the respective closed-loop controller.

7.3 Results

The probability distribution, ϕ, of the OWC spar buoy pneumatic chamber root-mean-square pressure, rms(Δp), for a discharge coefficient $C_{\text{d}} = 0.683$, orifice diameter $d_{\text{o}} = 0.16\,$m and considering the deployment off the Port of Leixões [35], on the West coast of mainland Portugal, is illustrated in Fig. 7.8. It is seen that 30% of the sea states for this location result in a root-mean-square pressure between 1 and 1.5 kPa. During 65% of the time, the pressure is $0.5 < \text{rms}(\Delta p) < 2.0\,$kPa. These results were used to define the pressure ranges for the simu-

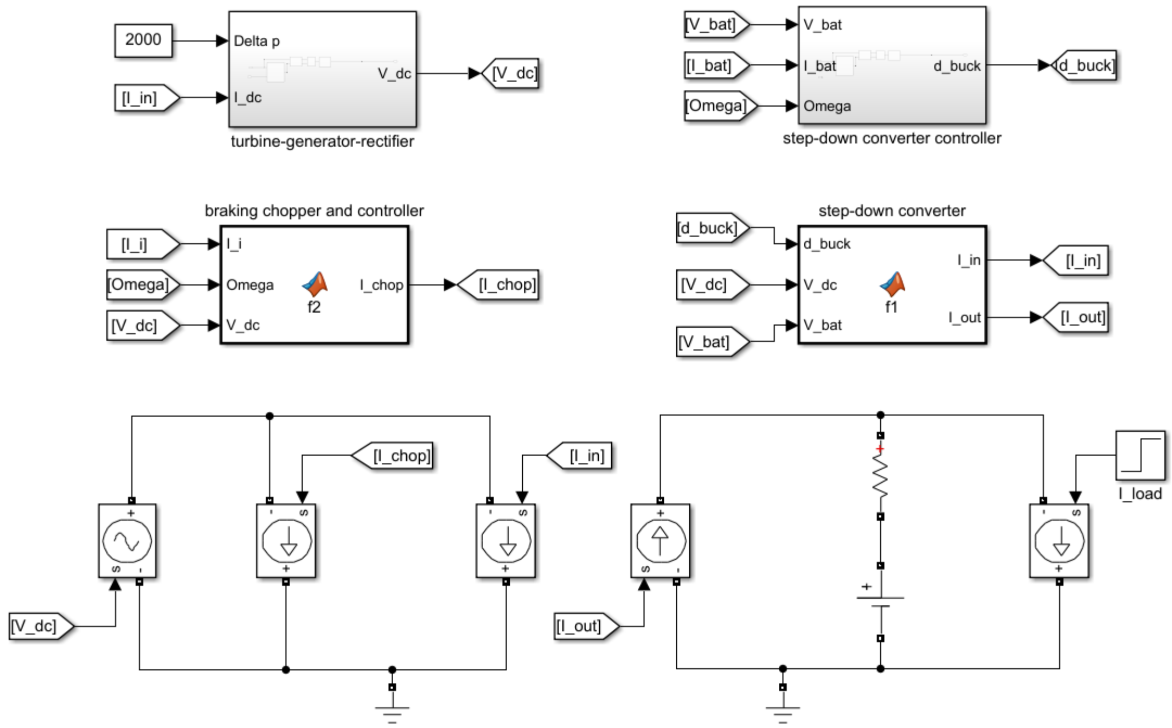

Figure 7.7: MATLAB/Simulink model for simulations in time-dependent conditions (simplified).

lations.

7.3.1 Steady-state conditions

The characterization study was performed for six OWC chamber pressures in the range $0.5 < \Delta p < 5.0$ kPa and eleven step-down converter design coefficients in the range $0 < K_{\text{buck}} < 33 \times 10^{-3}$ Ohm^{-1}, in a total of seventy-two $(\Delta p, K_{\text{buck}})$ pairs. Every simulation ran until steady-state was achieved for all recorded variables. The results were compiled into two charts for sizing the step-down converter, the braking chopper and defining the control laws. Fig. 7.9 relates the rectifier output power, P_{dc}, and voltage, U_{dc}, and Fig. 7.9 relates it with the turbo-generator rotational speed, Ω. The points sets labelled 0.5 to 5 kPa result from the characterization study by varying K_{buck} while keeping the chamber pressure, Δp equal to the respective label value. The remaining lines are related to specific operational conditions relevant for the system design.

Based on the results depicted in Figs. 7.8 and 7.9, it is anticipated that the electric power availability at the rectifier's terminals will roughly vary between 100 and 850 W for approximately 75% of the time. Additionally, the most likely pressure range, with a probability of 31%, provides

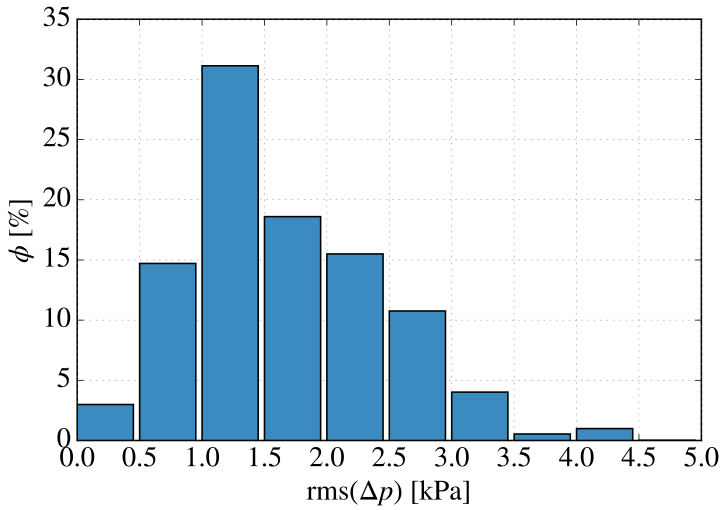

Figure 7.8: Probability distribution of the OWC chamber rms pressure.

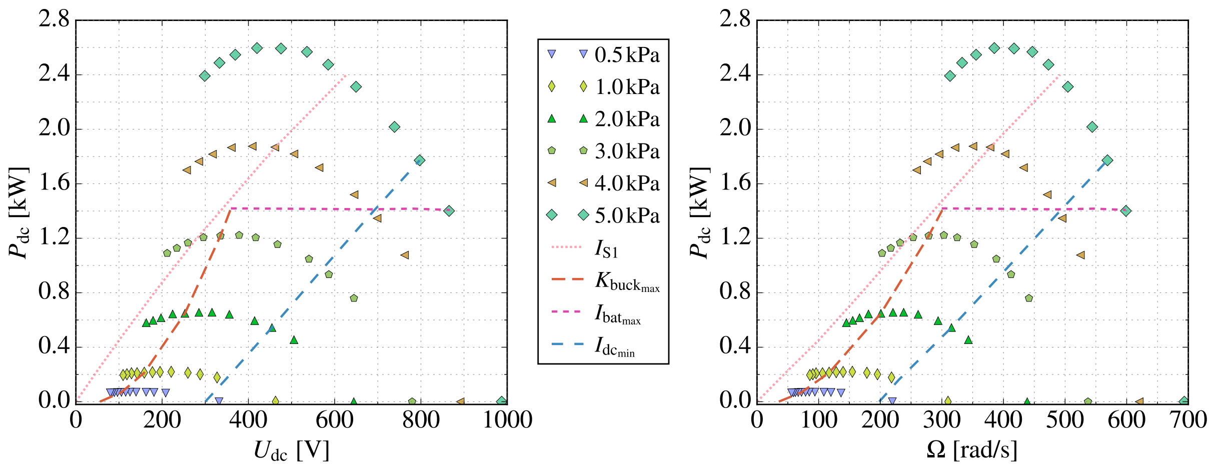

Figure 7.9: Relationship of rectifier output power, $P_{\mathrm{dc}} = I_{\mathrm{dc}}U_{\mathrm{dc}}$, with voltage, U_{dc} (left), and rotational speed, Ω (right), for a range of input pressures, Δp, the generator current limit, I_{S1}, the converter design coefficient $K_{\mathrm{buck_{max}}} = 0.013\,\mathrm{Ohm}^{-1}$, the maximum battery bank charging power, $I_{\mathrm{bat}} = 25.5\,\mathrm{A}$, and the established minimum rectifier output current, $I_{\mathrm{dc_{min}}}$.

power in the range of 200 to 400 W. This outcome indicates promising potential for the wave energy converter under investigation to supply AUVs, such as the Iver3 briefly presented in Sec. 7.2.1. However, it is crucial to interpret these findings as preliminary due to the approximations discussed in Sec. 7.2.2 and the fact that the presented results were obtained under steady-state conditions.

The horizontal line labelled $I_{\mathrm{bat_{max}}}$ illustrates the rectifier output power for the maximum battery charging current under the assumption of an ideal step-down converter. Naturally, some variation to the shape and location of this curve is expected with more advanced modelling. Still, it is a practical first approach for defining the converter rated power.

The line labelled $K_{\text{buck}_{\text{des}}}$ illustrates the power for constant step-down converter design coefficient, $K_{\text{buck}} = 0.013\,\text{Ohm}^{-1}$. This value was chosen for the design because the line intersects the maximum battery charging current curve, $I_{\text{bat}_{\text{max}}}$, closely below the generator current limit, I_{S1} curve, and approximately follows the maximum power points. Recalling the transition between DCM and CCM, Eq. (7.18) can be rewritten to provide the duty cycle,

$$d_{\text{buck}} = \frac{K_{\text{buck}}}{I_{\text{out}_{\text{lim}}}} \left(U_{\text{dc}} - U_{\text{bat}} \right) . \tag{7.22}$$

An output current at the transition point of $I_{\text{out}_{\text{lim}}} = 28\,\text{A}$ was chosen for precaution. Simulation results reveal that a converter with $K_{\text{buck}} = K_{\text{buck}_{\text{des}}} = 0.013\,\text{Ohm}^{-1}$ achieves this current at $\Delta p = 3.35$ kPa with a rectifier voltage of $U_{\text{dc}} = 378\,\text{V}$. As such, from Eq. (7.22), the converter maximum duty cycle is $d_{\text{buck}} = 0.15$. A frequency $f = 30\,\text{kHz}$ was assumed based on the conventional power transistor modules, micro-controllers and gate drivers available in the market. Then, from the definition of the converter design coefficient, $K_{\text{buck}} = d^2_{\text{buck}}/(2fL)$, comes its inductance $L = 29\,\mu\text{H}$.

As discussed in Sec. 7.2.6, the step-down converter duty cycle, d_{buck}, should be limited to avoid generator and battery over-current. Setting the limit to $d_{\text{buck}} = 0.15$ keeps the currents below their respective rated values if the speed is $\Omega < 300\,\text{rad/s}$, see Fig. 7.9. Above this threshold, the battery maximum charging current is the limiting factor. Consequently, a maximum duty cycle varying with the rotational speed was imposed. The relationship between the duty cycle and rotational speed for the results labelled $I_{\text{bat}_{\text{max}}}$ is plotted in Fig. 7.10. It is approximated by the analytical function

$$d_{\text{buck}_{\text{max}}}(\Omega)[-] = \begin{cases} 0.15 & , 0 \leq \Omega \leq 300\,\text{rad/s} \\ 330.51\Omega^{-1.352} & , \Omega > 300\,\text{rad/s} \end{cases} \tag{7.23}$$

with a coefficient of determination R-squared $= 0.9982$ for $\Omega > 300\,\text{rad/s}$, defining the upper saturation limit for the step-down converter controller. Imposing a maximum duty cycle as a function of the rotational speed below 300 rad/s would track the maximum power points more effectively. However, this value is an adequate first approach to be adjusted after deriving the

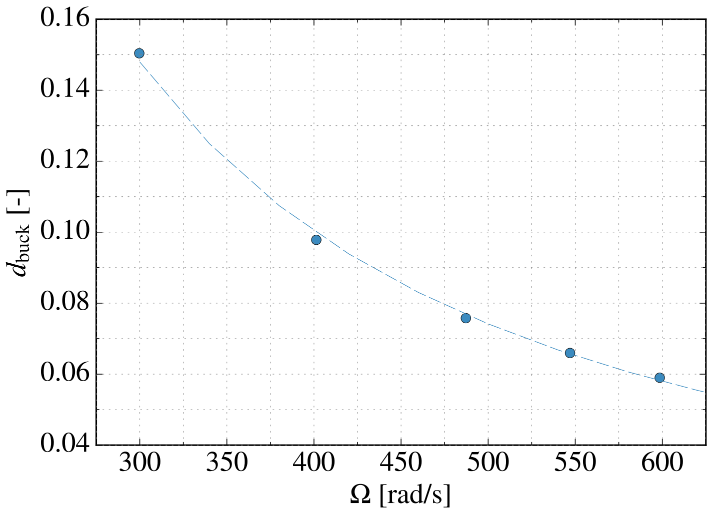

Figure 7.10: Relationship between step-down converter duty cycle, d_{buck}, and rotational speed, Ω, for a battery charging current $I_{\text{bat}} = I_{\text{bat}_{\text{max}}} = 25.5$ A.

converter efficiency, inductance and operating frequency from experimental testing. It should be noted that the limit for $\Omega > 300$ rad/s prevents battery charging over-current, but also prevents the maximum charging current to be reached if there are connected service loads, I_{load}. This is due to the limit being imposed on the step-down converter output current, I_{out}, which simultaneously supplies the battery and service loads during the float stage (see Eq. 7.21 and Sec. 7.2.5). It should be noted that the duty cycle may be too low for practical implementation, but it is implicit that considering a PMSG with a lower back electromotive force would increase the duty cycle and should be focus of future investigation.

The minimum rectifier output current was derived by prescribing a linear variation of the rectifier output power between $P_{\text{dc}} = 0$ at $U_{\text{dc}} = 300$ V and $P_{\text{dc}} = 1.78$ kW at $U_{\text{dc}} = 800$ V, as represented by the lines labelled $I_{\text{dc}_{\text{min}}}$ in Figs. 7.9 and 7.9. The resulting minimum current as function of the rectifier output voltage is

$$I_{\text{dc}_{\text{min}}} = 3.56 - \frac{1069}{U_{\text{dc}}} \quad [\text{SI units}]. \tag{7.24}$$

The required braking resistance is calculated by recalling the braking chopper current definition of Eq. (7.19),

$$R = d_{\text{chop}} \left(\frac{3.56}{U_{\text{dc}}} - \frac{1069}{U_{\text{dc}}^2} \right)^{-1} \quad [\text{SI units}]. \tag{7.25}$$

Considering that $0 \leq d_{\text{chop}} \leq 1$, the allowable resistance range is $0 \leq R \leq 337.4$ Ohm (neglect-

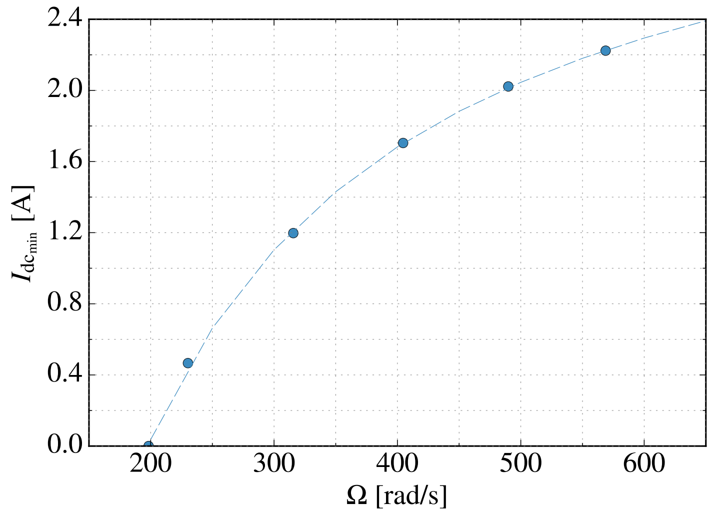

Figure 7.11: Relationship between the minimum rectifier output current, $I_{\text{dc}_{min}}$, and the generator rotational speed, Ω, for the prescribed minimum rectifier output power.

ing $R < 0$). A resistance of $R = 220\,$Ohm was selected

The relationship between the minimum rectifier output current, $I_{\text{dc}_{\text{min}}}$, and the turbo-generator rotational speed, Ω, is illustrated in Fig. 7.11 and was fitted with the function

$$I_{\text{dc}_{\text{min}}}(\Omega)[\text{A}] = \begin{cases} 0 & , \; 0 \leq \Omega \leq 200\,\text{rad/s} \\ \dfrac{3.632\Omega - 717.7}{\Omega + 36.99} & , \; \Omega > 200\,\text{rad/s}\,, \end{cases} \tag{7.26}$$

with a coefficient of determination R-squared $= 0.9995$. This function provides the chopper controller with the set-points to guarantee a minimum current at the rectifier output terminals.

7.3.2 Time-dependent conditions

This section covers three time-dependent simulations. The step-down converter PI controller has a parallel structure with the proportional and integral coefficients being $K_{\text{P}} = 0.05$ and $K_{\text{I}} = 0.5$, respectively. The battery is kept in the float stage with the PI controller reference of $V_{\text{float}} = 55.2\,V$. The tests are performed at constant input pressure, with step changes in the service loads providing the system perturbation. The first two simulations cover the effectiveness of the step-down converter controller saturation and the third tests the braking chopper controller reference defined in Eqs. (7.23) and (7.26), respectively.

The results from the first step-down converter saturation limit test are plotted in Fig. 7.12.

The simulation was performed at a constant input pressure of $\Delta p = 3$ kPa. The system starts in equilibrium with a service load of $P_{\text{load}} = 1$ kW at $\Omega = 370$ rad/s and $V_{\text{dc}} = 450$ V (see Fig. 7.9). At the instant $t = 10$ s, a service load step-variation from 1 to 1.5 kW is imposed. This setup was chosen to test the controller saturation below $\Omega = 300$ rad/s. The battery voltage decreases marginally and the step-down converter controller responds by increasing the duty cycle as intended. As a consequence, the generator torque increases and turbo-generator supplies the entirety of the load during deceleration. The duty cycle, d_{buck}, eventually reaches the imposed limit, $d_{\text{buck}} = 0.15$, and since the rotational speed continues to decrease, the battery starts supplying the load while the turbo-generator stabilizes at $P_{\text{dc}} = 1.25$ kW, $\Omega = 275$ rad/s, $V_{\text{dc}} = 450$ V and $K_{\text{buck}} = 0.013\,\text{Ohm}^{-1}$ (see Fig. 7.9). The results demonstrate that the system achieved the expected steady-state after the load perturbation and that the duty cycle was effectively limited. However the rectifier output current during rotor deceleration shows that the generator's should be carefully sized and equipped with thermal protection. The maximum current during the event was $I_{\text{dc}} = 4$ A.

The results from the second step-down converter saturation limit test are plotted in Fig. 7.13. The simulation was performed at a constant input pressure of $\Delta p = 4$ kPa. The system starts in equilibrium with a service load of $P_{\text{load}} = 2$ kW at $\Omega = 527$ rad/s and $V_{\text{dc}} = 721$ V (see Fig. 7.9). At the instant $t = 10$ s, a service load step-variation from 1 to 2 kW is introduced. This setup was chosen to test the controller saturation above $\Omega = 300$ rad/s. The battery voltage decreases marginally and the step-down converter controller responds by increasing the duty cycle as intended. As a consequence, the generator torque increases and the turbo-generator decelerates. The duty cycle, d_{buck}, eventually reaches the imposed limit, $d_{\text{buck}} = 0.077$, and the battery starts supplies part of the load while the turbo-generator stabilizes at $P_{\text{dc}} = 1.4$ kW, $\Omega = 485$ rad/s, $V_{\text{dc}} = 668$ V and $K_{\text{buck}} = 0.035\,\text{Ohm}^{-1}$ (see Fig. 7.9). The results demonstrate that the system achieved the expected steady-state after the load perturbation and that the duty cycle was effectively limited to the maximum rectifier output power. However, as discussed in Sec. 7.3.1, the duty cycle is likely too small for effective implementation.

The results from the braking chopper operation test are plotted in Fig. 7.14. The simulation was performed at a constant input pressure of $\Delta p = 3$ kPa. The system starts in equilibrium with a service load of $P_{\text{load}} = 1.2$ kW at $\Omega = 345$ rad/s and $V_{\text{dc}} = 476$ V (see Fig. 7.9). At the instant $t = 10$ s, a service load step-variation from 1.2 kW to 0 is introduced. The battery voltage increases marginally and the step-down converter controller responds by decreasing the duty cycle as intended. As a consequence, the generator torque decreases and the turbo-generator accelerates. The duty cycle, d_{buck}, eventually reaches, $d_{\text{buck}} = 0$, at which point, there is no step-down converter output current. Yet, as d_{buck} decreases, the braking chopper duty cycle increases and the turbo-generator output current is sent to the braking resistor, stabilizing at $P_{\text{dc}} = 0.96$ kW, $\Omega = 410$ rad/s, $V_{\text{dc}} = 644$ V (see Fig. 7.9). The results demonstrate that the system achieved the expected steady-state after the load perturbation and that the braking chopper effectively limited the rotational speed.

7.4 Conclusions

An off-grid oscillating-water-column wave energy converter (WEC) equipped with a biradial impulse turbine, a permanent magnet generator, a diode rectifier and an internal battery bank for intermediate energy storage was introduced. The objective of this Chapter was to design a power electronic converter and respective controllers as an interface between the rectifier and the batteries.

A converter configuration was devised consisting in a dc-to-dc step-down converter, operating in discontinuous conduction mode, in parallel with a resistance-connected chopper. The step-down converter supplies the batteries and service loads and the chopper brakes the turbo-generator. Two controllers manage the system.

The complete power-take-off system was simulated in Simulink/MATLAB in the context of a deployment site off the Port of Leixões, Portugal, to select the power electronic converter internal components and establish the control laws. The systems' response was tested in simulations with time-dependent loads.

For operation off the Port of Leixões, Portugal, it is anticipated that the electric power available at the rectifier's terminals will range between 100 to 850 W for approximately 75% of the time and in the range of 200 to 400 W for around 31% of the time. This outcome indicates a promising potential for the wave energy converter under investigation to supply ocean monitoring equipment and AUVs. The converter power was rated at 1.4 kW based on the maximum recommended battery charging power, as a first approach, but a higher value is achievable at the expense of the batteries lifespan.

The step-down converter duty-cycle range, frequency and inductance were obtained for part procurement. However the calculated duty-cycle range below 0.15 might be too low for practical implementation. Using a generator with lower back electromotive force should increase this value and should be considered in future studies.

A control strategy was devised and its viability was confirmed to avoid generator over-current and over-speed, and limit the step-down converter output power to protect the batteries.

Future investigation should comprise the experimental testing of the power converter to derive its efficiency curves as a function of the load and voltage. This data can be easily integrated in the simulation setup to provide more comprehensive results. The setup can also be adapted for different deployment sites, buoys, mechanical and electrical components to assess their impact on the proposed power electronic converter.

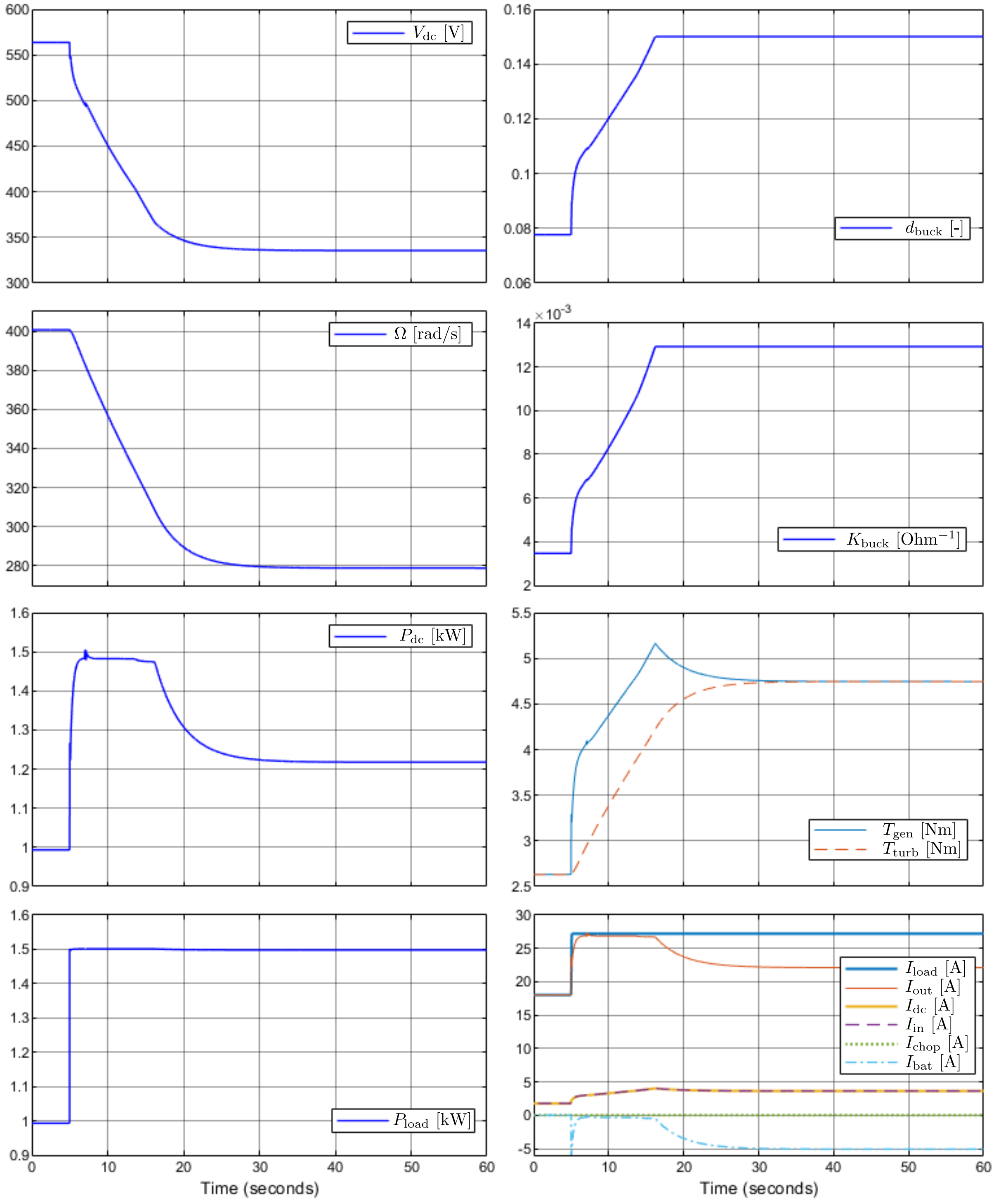

Figure 7.12: Time variation of the rectifier output voltage, U_{dc} and power, P_{dc}, turbo-generator rotational speed, Ω, step-down converter duty cycle, d_{buck} and design coefficient, K_{buck} for a service load step-variation from 1 to 1.5 kW at a constant input pressure of $\Delta p = 3$ kPa.

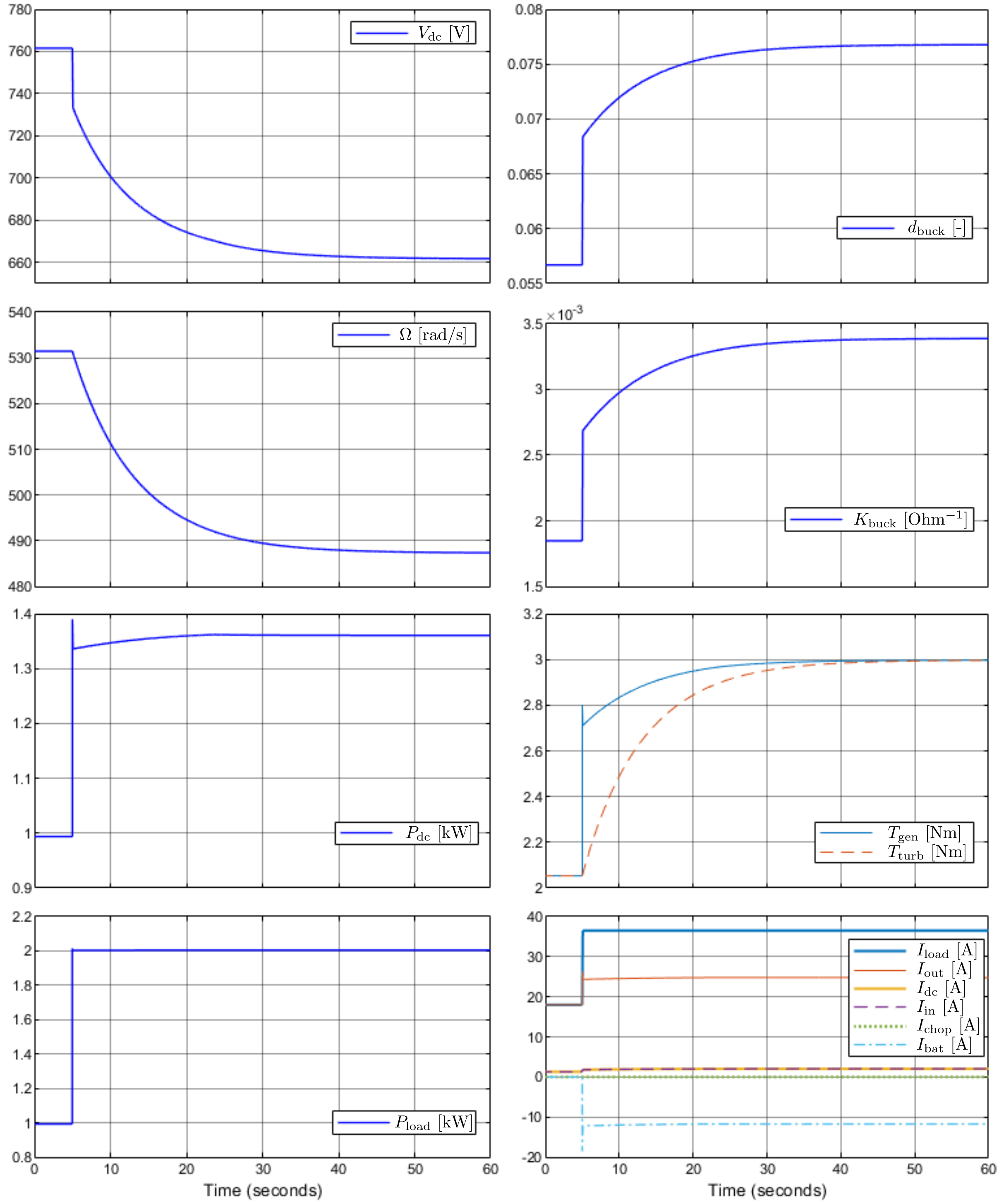

Figure 7.13: Time variation of the rectifier output voltage, U_{dc} and power, P_{dc}, turbo-generator rotational speed, Ω, step-down converter duty cycle, d_{buck} and design coefficient, K_{buck} for a service load step-variation from 1 to 2 kW at a constant input pressure of $\Delta p = 4$ kPa.

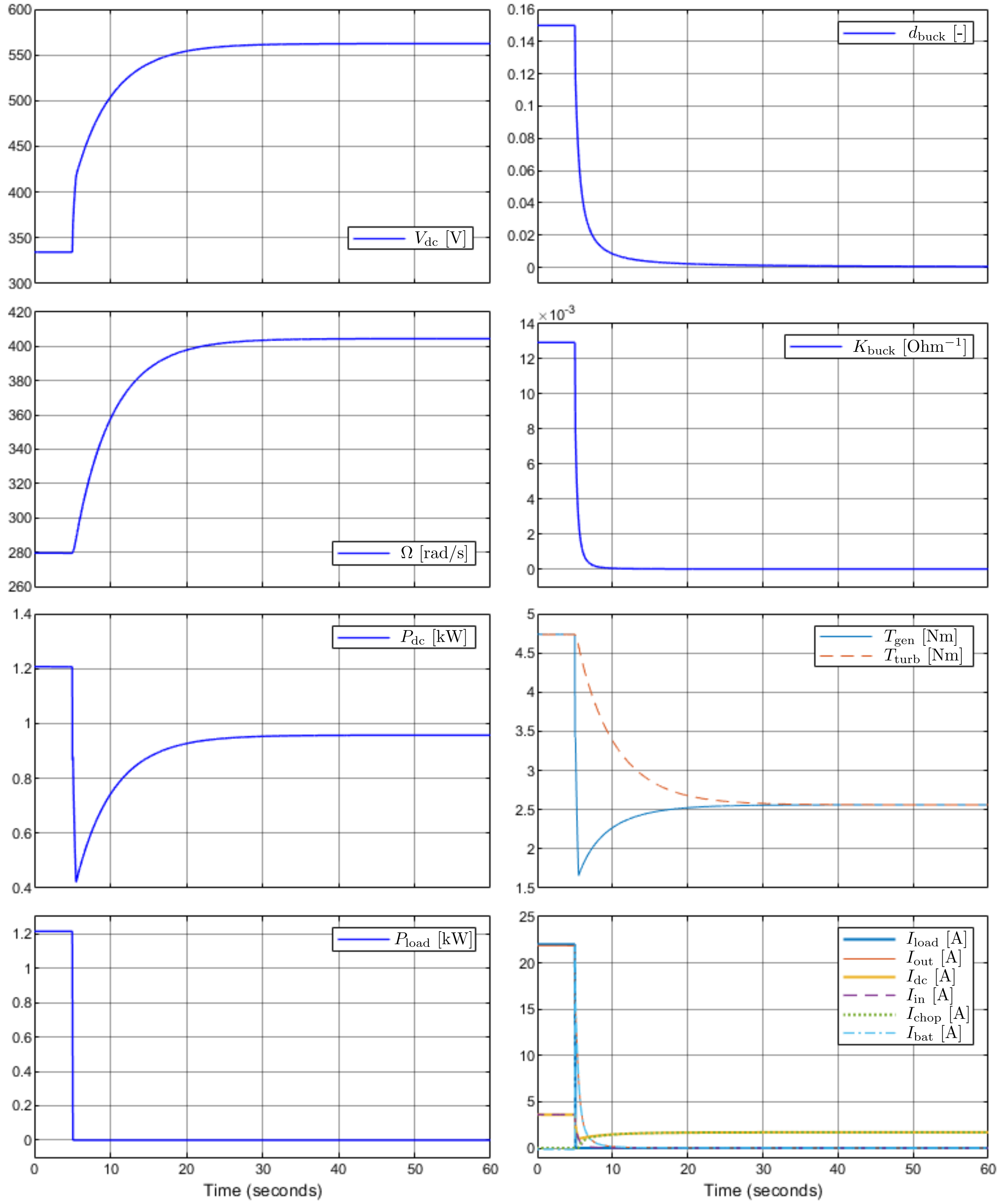

Figure 7.14: Time variation of the rectifier output voltage, U_{dc} and power, P_{dc}, turbo-generator rotational speed, Ω, step-down converter duty cycle, d_{buck}, and braking chopper duty cycle, d_{chop}, for a service load step-variation from 1.2 kW to 0 at a constant input pressure of $\Delta p = 3$ kPa.

Chapter 8

Conclusion and future work

The concept of off-grid wave energy conversion is emerging as a potential driver for the development of the Blue Economy. The doctoral research presented here is an integral part of Instituto Superior Tecnico's effort to design, manufacture and test a full-scale oscillating water column wave energy converter to power off-grid electrical systems. Interviews with ocean monitoring equipment professionals, taken at the beginning of the research, confirmed the project's relevance and applicability and contributed with valuable knowledge to set functional requirements for the converter. Scientific monitoring and maritime surveillance are perceived as fields where wave energy conversion may have an immediate impact, namely by powering sensors and transmitters directly, or by charging autonomous vehicles.

The core of this doctoral research was the design, manufacturing and testing of turbo-generator aerodynamic and electromechanical components for the IST's off-grid wave energy converter. The grid-connected design tested in the scope of the OPERA project was iteratively modified to increase its performance and ensure compatibility with the new application. The conclusions drawn from each modification are summarized at the end of the respective chapter and will not be repeated here. Instead, an overview of the project's breakthroughs achieved with this doctoral work is discussed.

The buoy-design team established the hydrodynamic damping for the converter from which a scaling factor was derived and applied to the OPERA turbine design. After adjustments due to structural requirements, the resulting geometry had a stator diameter of 1144 mm. It comprised a total of 256 aerofoil-shaped vanes, where the smallest ones had a length of 36 mm by

Table 8.1: Evolution of the turbine design.

	OPERA	scaled-OPERA	Chapter 4	Chapter 5
rotor diameter [mm]	488	260	260	243
stator diameter [mm]	2146	1144	850	795
GV number	256	256	120	120
outer GV chord [mm]	112	60	94	88
inner GV chord [mm]	68	36	46	43
outer GV thick. [mm]	13.4	7.2	2.0	1.9
inner GV thick. [mm]	8.2	4.3	2.0	1.9
process	milling	milling	bending	bending
turbine efficiency	71%	71%	65%	65%

4 mm of maximum thickness. It was realized that this diameter was too large to be mounted on the OWC buoy and that such small vanes would have poor aerodynamic performance and high manufacturing costs. These challenges motivated a new design with a smaller stator-to-rotor radius ratio and fewer but larger constant-thickness vanes. Since it was expected that a smaller stator-to-rotor radius ratio would penalize the turbine efficiency, measures for decreasing energy losses were also implemented. Additionally, an improved rotor design method was developed in order to increase the rotor efficiency and further decrease turbine size and costs. Table 8.1 summarizes the evolution of the turbine design. It can be seen that from the scaled-OPERA version to the Chapter 4 version, the number of guide vanes decreased 53%, the vanes became manufacturable by sheet bending and have 58% fewer stagnation pressure losses for the rotor outflow (see Chapter 4). The turbine had a further size reduction in Chapter 5 without penalties to the efficiency.

Decreasing the stator-to-rotor radius ratio penalized the efficiency, but it is worth noting that from the scaled-OPERA version to the Chapter 5 version, the stator diameter decreased 31% and the respective circular area decreased 52%. This parameter is critical for the structural integrity of a biradial turbine, since it is roughly the area where the OWC pressure is applied to the frame. A smaller area needs less structural reinforcement for the same maximum stress and thus decreases manufacturing costs.

Induction generators, like the one utilized in the OPERA project, draw reactive power from the electrical grid to generate voltage and supply active power. However, in off-grid systems, batteries with inverters are commonly used as the source of reactive power. Nevertheless, the reliance on batteries may present reliability concerns, especially in light of the reports discussed in Chapter 2 from moored data buoy operators on the limited lifespan of batteries in solar-powered buoys.

To address this issue, permanent magnet generators were considered a more viable choice for off-grid generation, as they can take full advantage of the self-starting capability of biradial turbines, resulting in a totally self-starting turbine and generator set. Furthermore, their increased efficiency compared to induction generators can help offset the efficiency losses resulting from the mechanical adaptations previously discussed.

In the context of electric machine adaptations, servomotors, such as the one tested in Chapter 6, emerged as a favourable choice due to their widespread availability in the market, environmental protection index, and notably, their high maximum speed rating compared to generators for small wind turbines. This combination of characteristics makes servomotors a well-suited choice in this particular application. However, it is essential to note that servomotors are generally more expensive compared to induction motors.

The OPERA prototype uses an industrial variable frequency drive (VFD) to interface the generator and the grid. It is a back-to-back power electronic converter for four quadrant operation and a grid-side inverter for generated power supply. Industrial VFDs can be adapted to perform a similar role in off-grid generation, but require further modifications in this specific context. While the grid-side inverter is not necessary, three characteristics remain indispensable: physical access to the DC bus, four quadrant operation for bidirectional power flow, and the ability to self-start the control module from the DC bus.

A step-down converter, similar to the one discussed in Chapter 7, would be needed to convert the DC-bus voltage, typically 400 V, to the battery voltage and regulate the charging process. This design would offer the advantage of a constant input voltage, allowing for precise parameter tuning. However, it should be noted that the efficiency of step-down converters is inversely proportional to the input/output voltage ratio, and that the converter designed in Chapter 7 featured a lower input voltage during the most frequent sea-states. The added advantage of a lower input/output voltage ratio increases if a permanent magnet generator with a lower back electromotive force is considered. Further investigation is recommended to compare this aspect on the two solutions.

The usefulness of a brake resistor was shown in Chapter 7, and an equivalent braking chopper could be connected to the VFD DC bus in line with the industrial motor braking units.

Regarding rectification, vector control techniques can be employed when using an industrial VFD, enabling a permanent magnet generator to operate at near unitary power factor, which offers several advantages as discussed in Chapter 6. Diode rectifiers are simple, cost-effective, reliable and compact, complying with the general requirements of low-power off-grid generation. In Chapter 6, the shortcomings of diode rectifiers were addressed. The characterization study showed satisfying results in terms of power factor, efficiency and risk of generator demagnetization, but the influence of the step-down converter over these parameters is yet to be addressed. Again, further investigation is recommended.

The control challenges faced by off-grid systems differ from those of grid-connected ones. Within the OPERA project, the primary control strategy was focused on maximum power point tracking, accompanied by safety measures to avoid over-power and over-speed during energetic sea-states. However, in off-grid generation the state-of-charge of batteries and the service loads significantly influence the turbo-generator operation, as seen in Chapter 7. Given that the turbo-generator's power output depends on the system loads and input pressure, it is expected to operate predominantly away from its maximum power points. Consequently, the model presented in Chapter 7 should be further developed to assess the system response to time-varying OWC chamber pressures. Understanding this response will be instrumental in optimizing the control strategy and harnessing the full potential of the OWC technology for off-grid generation.

Appendix A

Verification and validation of CFD results

All simulations involving the use of numerical methods have an associated numerical error. The uncertainty of a quantity of interest in a CFD solution is defined as the product of the estimated numerical error, ϵ_{num}, multiplied by a safety factor, F, resulting in the interval, $\pm\, \xi_{\text{num}}$, around a calculated solution, ϕ_{num}, that contains the exact solution, ϕ_{exc}, with 95% of confidence [111],

$$\phi_{\text{num}} - \xi_{\text{num}} \leq \phi_{\text{exc}} \leq \phi_{\text{num}} + \xi_{\text{num}} \,. \tag{A.1}$$

The numerical error, ϵ_{num}, has three contributions: round-off, ϵ_{rnd}, iterative, ϵ_{itr}, and discretisation, ϵ_{dsc}.

In careful performed simulations, the numerical error is dominated by the discretisation error [114]. This is achieved by using double-precision (14 digits) to obtain negligible round-off errors and an iterative convergence criterion that reduces the iterative error to at least one order of magnitude below the discretisation error [114].

In cases where the iterative error can not be neglected, the numerical uncertainty has contributions from the iterative and discretisation errors, which should be added arithmetically [114],

$$\xi_{\text{num}} = \xi_{\text{itr}} + \xi_{\text{dsc}} \,. \tag{A.2}$$

The iterative uncertainty, ξ_{itr}, is determined by multiplying a safety factor, F_{itr}, by an estimate of the iterative error, ϵ_{itr},

$$|\xi_{\text{itr}}| = F_{\text{itr}}|\epsilon_{\text{iter}}| = F_{\text{itr}}|\phi_I - \phi_{\text{itr}}| \,. \tag{A.3}$$

This estimate is given by the difference between two solutions:

(i) the final solution obtained at the end of the iterative process, ϕ_I, on which the quantities of interest have stabilised and the residuals are at least of the order 10^{-4} (I denotes the final iteration number);

(ii) the estimate of the solution without iterative error, ϕ_{itr}, which is used instead of a solution converged to machine accuracy for practical reasons.

To calculate ϕ_{itr}, a least-squares fit of the exponential function

$$\phi_{\text{i}} = \phi_{\text{itr}} + C_1\, e^{\,\ln(\delta_i)\, C_2} \tag{A.4}$$

to a set of J intermediate solutions, ϕ_i, is used [113]. In this equation, C_1 and C_2 are constants and δ_i is a residual of a relevant equation related to the solution ϕ_i. These intermediate solutions are taken from the part of the iterative process where residual levels are decreasing (i.e. after initialisation and before stabilisation).

The discretisation uncertainty ξ_{dsc} of a numerical solution, ϕ_{num}, is also determined by multiplying a safety factor, F_{dsc}, by an estimate of the discretisation error,

$$|\xi_{\text{dsc}}| = F_{\text{dsc}}|\epsilon_{\text{dsc}}| = F_{\text{dsc}}|\phi_I - \phi_{\text{dsc}}| \,. \tag{A.5}$$

The estimate of the solution without discretisation error, ϕ_{dsc}, is based on mesh refinement studies, following the solution verification methodology established in Ref. [112] using the Richardson's extrapolation

$$\phi_j = \phi_{\text{dsc}} + C_3 \left(\frac{h_j}{h_{\text{G1}}}\right)^{C_4} , \tag{A.6}$$

where C_3 and C_4 are constants. The extrapolation was made with a least-square fit of the numerical solutions calculated in M geometrically similar meshes, ϕ_j. Here, the mesh density is represented by the parameter h_j/h_{G1} that relates the typical cell size in each mesh,

$$h_j = \overline{H}_j^{1/3} = \left(\frac{\sum_{n=1}^{N} H_n}{N} \right)_j^{1/3} , \tag{A.7}$$

with the typical cell size in the finest mesh, h_{G1}, where $\sum_{n=1}^{N} H_n$ is the grid total volume, H_{n} the mesh cell volume, $\overline{H}$ the mean mesh cell volume and N the total number of mesh cells, giving

$$\frac{h_j}{h_{\mathrm{G1}}} = \left(\frac{N_{\mathrm{G1}}}{N_j} \right)^{1/3} . \tag{A.8}$$

A set of $M = 4$ meshes (G1 to G4) was used to estimate the numerical uncertainty, with G1 being the finest and G4 being the coarsest. The meshes used for different geometries have the same number of elements in each surface, but with somewhat different distribution. This is to accommodate the geometrical differences and keep the mesh quality parameters.

When comparing experimental and numerical results, it is essential to take into consideration that the experimental results also have an associated uncertainty. Using the V&V 20 Standard [156], the error of the quantity of interest calculated by the CFD code, ϵ_ϕ, shall be inside an interval bounded by the comparison error, ϵ_{cmp}, and the validation uncertainty, ξ_{val},

$$\epsilon_{\mathrm{cmp}} - \xi_{\mathrm{val}} \leq \epsilon_\phi \leq \epsilon_{\mathrm{cmp}} + \xi_{\mathrm{val}} , \tag{A.9}$$

with

$$\epsilon_{\mathrm{cmp}} = \phi_{\mathrm{num}} - \phi_{\mathrm{exp}} \tag{A.10}$$

and

$$\xi_{\mathrm{val}} = \sqrt{\xi_{\mathrm{num}}^2 + \xi_{\mathrm{exp}}^2} . \tag{A.11}$$

Appendix B

Turbo-generator manufacturing

Appendix B shows photos of the turbo-generator taken during manufacturing.

Figure B.1: Biradial turbine chassis lower sub-assembly.

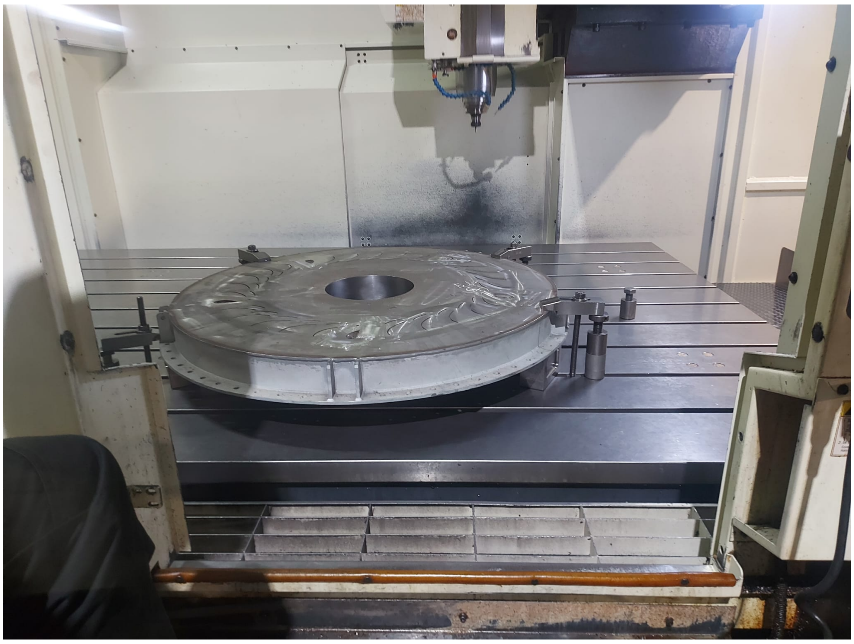

Figure B.2: Biradial turbine chassis central sub-assembly guide-vane slot milling.

Figure B.3: Biradial turbine chassis central sub-assembly and guide vanes.

Figure B.4: Biradial turbine rotor, shaft and bearing housing.

Figure B.5: Biradial turbine chassis and rotor sub-assemblies.

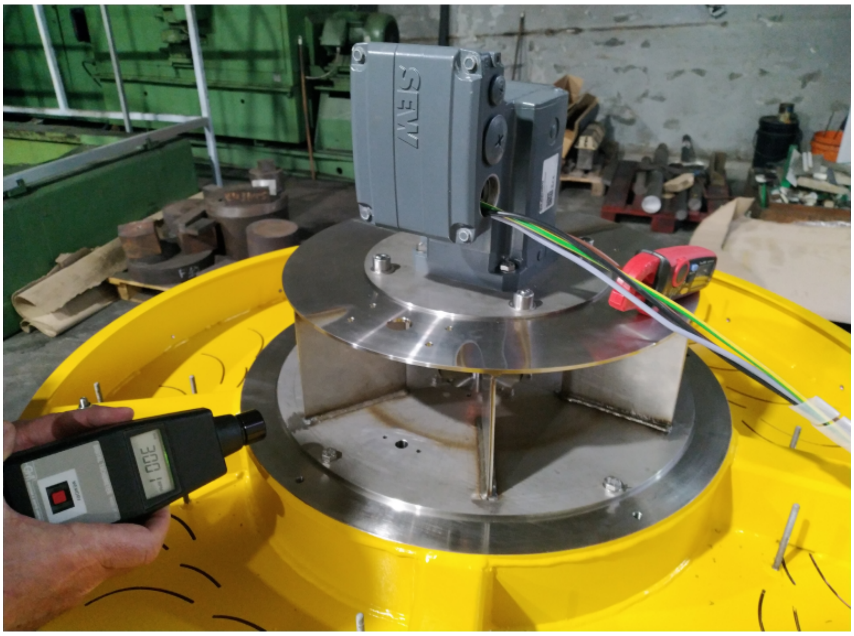

Figure B.6: Biradial turbine conformity speed-test.

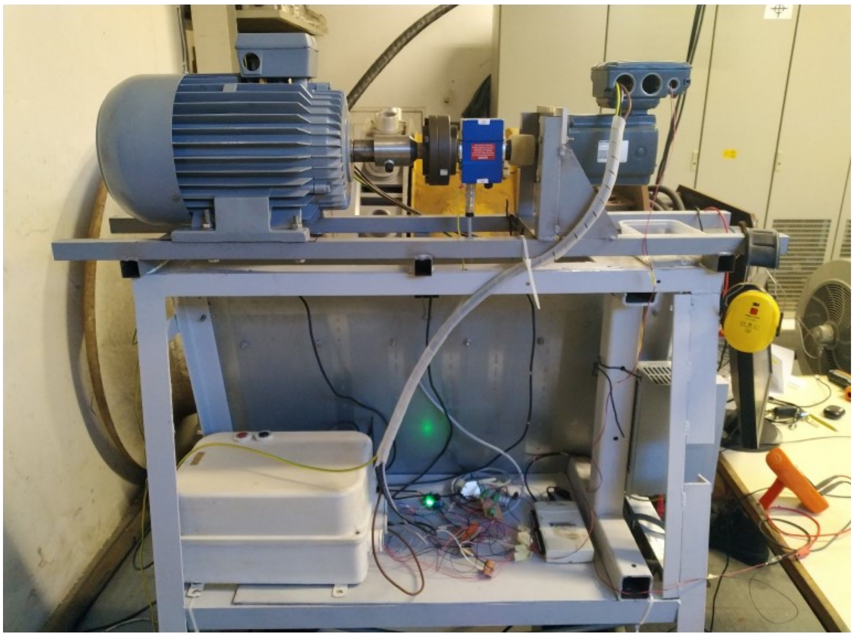

Figure B.7: Generator and rectifier test-bench.

References

[1] OECD. *The Ocean Economy in 2030*. OECD Publishing, Paris, France, 2016. doi:/10.1787/9789264251724-en.

[2] UN. *Blue Economy Concept Paper*. United Nation Environment Programme, 2013. URL https://www.unep.org/resources/report/blue-economy-concept-paper.

[3] EU. *Sustainable blue economy*. European Comission, 2021. URL https://oceans-and-fisheries.ec.europa.eu/ocean/blue-economy/sustainable-blue-economy_en.

[4] EU. *Recovery plan for Europe*. European Comission, 2020. URL https://commission.europa.eu/strategy-and-policy/recovery-plan-europe_en.

[5] EU. *European Green Deal*. European Comission, 2019. URL https://commission.europa.eu/strategy-and-policy/priorities-2019-2024/european-green-deal_en.

[6] EU. *Blue Growth*. European Comission, 2020. URL https://s3platform.jrc.ec.europa.eu/blue-growth.

[7] DGPM. *National Ocean Strategy 2021-2030*. Direcção-Geral de Política do Mar, Lisbon, Portugal, 2021. URL https://www.dgpm.mm.gov.pt/enm-21-30.

[8] A. Silva. *Visão Estratégica para o Plano de Recuperação Económica de Portugal 2020-2030*. XXII Governo da República Portuguesa, Lisbon, Portugal, 2021. URL https://www.dgpm.mm.gov.pt/enm-21-30.

[9] F. Davidson, A. Alvera-Azcárate, A. Barth, G. B. Brassington, E. P. Chassignet, E. Clementi, P. De Mey-Frémaux, P. Divakaran, C. Harris, F. Hernandez, P. Hogan, L. R.

Hole, J. Holt, G. Liu, Y. Lu, P. Lorente, J. Maksymczuk, M. Martin, A. Mehra, A. Melsom, H. Mo, A. Moore, P. Oddo, A. Pascual, A.-C. Pequignet, V. Kourafalou, A. Ryan, J. Siddorn, G. Smith, D. Spindler, T. Spindler, E. V. Stanev, J. Staneva, A. Storto, C. Tanajura, P. N. Vinayachandran, L. Wan, H. Wang, Y. Zhang, X. Zhu, and Z. Zu. Synergies in operational oceanography: The intrinsic need for sustained ocean observations. *Frontiers in Marine Science*, 6, 2019. ISSN 2296-7745. doi:10.3389/fmars.2019.00450.

[10] C. Whitt, J. Pearlman, B. Polagye, F. Caimi, F. Muller-Karger, A. Copping, H. Spence, S. Madhusudhana, W. Kirkwood, L. Grosjean, B. M. Fiaz, S. Singh, S. Singh, D. Manalang, A. S. Gupta, A. Maguer, J. J. H. Buck, A. Marouchos, M. A. Atmanand, R. Venkatesan, V. Narayanaswamy, P. Testor, E. Douglas, S. de Halleux, and S. J. Khalsa. Future vision for autonomous ocean observations. *Frontiers in Marine Science*, 7, 2020. ISSN 2296-7745. doi:10.3389/fmars.2020.00697.

[11] B. Guo and J. V. Ringwood. A review of wave energy technology from a research and commercial perspective. *IET Renewable Power Generation*, 15:3065–3090, 10 2021. doi:10.1049/RPG2.12302.

[12] R. Green, A. Copping, R. J. Cavagnaro, D. Rose, D. Overhus, and D. Jenne. Enabling power at sea: Opportunities for expanded ocean observations through marine renewable energy integration. Institute of Electrical and Electronics Engineers Inc., 10 2019. doi:10.23919/OCEANS40490.2019.8962706.

[13] D. Clemente, P. Rosa-Santos, and F. Taveira-Pinto. On the potential synergies and applications of wave energy converters: A review. *Renewable and Sustainable Energy Reviews*, 135:110162, 1 2021. doi:10.1016/J.RSER.2020.110162.

[14] A. LiVecchi, A. Copping, D. Jenne, A. Gorton, R. Preus, G. Gill, R. Robichaud, R. Green, S. Geerlofs, S. Gore, D. Hume, W. McShane, C. Schmaus, and H. Spence. *Powering the Blue Economy: Exploring Opportunities for Marine Renewable Energy in Maritime Markets*. U.S. Department of Energy, Office of Energy Efficiency and Renewable Energy, Washington, D.C., 2019. URL `https://www.energy.gov/eere/water/blue-economy-applications`.

[15] OES. *Blue Economy and its Promising Markets for Ocean Energy*. IEA Technology Collaboration Programme for Ocean Energy Systems (OES), 2020. URL `https://www.ocean-energy-systems.org/publications/oes-documents/market-policy-/document/blue-economy-and-its-promising-markets-for-ocean-energy-2020-/`.

[16] OES. *Alternative Markets for Ocean Energy*. IEA Technology Programme for Ocean Energy Systems, 2021. URL `https://www.ocean-energy-systems.org/publications/oes-documents/market-policy-/document/alternative-markets-for-ocean-energy/`.

[17] T. Zhao, M. Xu, X. Xiao, Y. Ma, Z. Li, and Z. L. Wang. Recent progress in blue energy harvesting for powering distributed sensors in ocean. *Nano Energy*, 88:106199, 2021. ISSN 2211-2855. doi:https://doi.org/10.1016/j.nanoen.2021.106199.

[18] X. Wang, J. Shang, Z. Luo, L. Tang, X. Zhang, and J. Li. Reviews of power systems and environmental energy conversion for unmanned underwater vehicles. *Renewable and Sustainable Energy Reviews*, 16:1958–1970, 5 2012. doi:10.1016/J.RSER.2011.12.016.

[19] B. Tian and J. Yu. Current status and prospects of marine renewable energy applied in ocean robots. *International Journal of Energy Research*, 43:2016–2031, 5 2019. doi:10.1002/ER.4371.

[20] B. P. Driscol, L. A. Gish, and R. G. Coe. A scoping study to determine the location-specific WEC threshold size for wave-powered AUV recharging. *IEEE Journal of Oceanic Engineering*, 46:1–10, 1 2021. ISSN 15581691. doi:10.1109/JOE.2020.2973032.

[21] D. Clemente, P. Rosa-Santos, T. Ferradosa, and F. Taveira-Pinto. Wave energy conversion energizing offshore aquaculture: Prospects along the Portuguese coastline. *Renewable Energy*, 204:347–358, 2023. doi:10.1016/j.renene.2023.01.009.

[22] L. Rusu and C. Guedes Soares. Wave energy assessments in the Azores islands. *Renewable Energy*, 45:183–196, 2012. ISSN 0960-1481. doi:10.1016/j.renene.2012.02.027.

[23] D. Silva, P. Martinho, and C. Guedes Soares. Wave energy distribution along the Portuguese continental coast based on a thirty three years hindcast. *Renewable Energy*, 127:1064–1075, 2018. ISSN 0960-1481. doi:10.1016/j.renene.2018.05.037.

[24] A. F. O. Falcão. Wave energy utilization: A review of the technologies. *Renewable and Sustainable Energy Reviews*, 14(3):899–918, 2010. ISSN 1364-0321. doi:10.1016/j.rser.2009.11.003.

[25] N. Khan, A. Kalair, N. Abas, and A. Haider. Review of ocean tidal, wave and thermal energy technologies. *Renewable and Sustainable Energy Reviews*, 72:590–604, 2017. ISSN 1364-0321. doi:10.1016/j.rser.2017.01.079.

[26] J. P. Kofoed. *The Wave Energy Sector*, pages 17–42. Springer International Publishing, Cham, 2017. ISBN 978-3-319-39889-1. doi:10.1007/978-3-319-39889-1_2.

[27] T. V. Heath. A review of oscillating water columns. *Philosophical Transactions of the Royal Society A: Mathematical, Physical and Engineering Sciences*, 370:235–245, 1 2012. doi:10.1098/RSTA.2011.0164.

[28] N. Delmonte, D. Barater, F. Giuliani, P. Cova, and G. Buticchi. Review of oscillating water column converters. *IEEE Transactions on Industry Applications*, 52(2):1698–1710, 2016. doi:10.1109/TIA.2015.2490629.

[29] A. F. O. Falcão and J. C. C. Henriques. Oscillating-water-column wave energy converters and air turbines: A review. *Renewable Energy*, 85:1391–1424, 1 2016. doi:10.1016/J.RENENE.2015.07.086.

[30] J. C. C. Portillo, J. C. C. Henriques, L. M. C. Gato, and A. F. O. Falcão. Model tests on a floating coaxial-duct OWC wave energy converter with focus on the spring-like air compressibility effect. *Energy*, 263:125549, 2023. ISSN 0360-5442. doi:10.1016/j.energy.2022.125549.

[31] I. McLeod and J. V. Ringwood. Powering data buoys using wave energy: A review of possibilities. *Journal of Ocean Engineering and Marine Energy*, 8(3):417–432, 2022. doi:10.1007/s40722-022-00240-3.

[32] D. Ross. *Power from the Waves*. Oxford University Press, USA, 1995.

[33] R. Ahamed, K. McKee, and I. Howard. Advancements of wave energy converters based on power take off (PTO) systems: A review. *Ocean Engineering*, 204:107248, 2020. ISSN 0029-8018. doi:10.1016/j.oceaneng.2020.107248.

[34] J. C. C. Henriques, J. C. C. Portillo, L. M. C. Gato, R. P. F. Gomes, D. N. Ferreira, and A. F. O. Falcão. Design of oscillating-water-column wave energy converters with an application to self-powered sensor buoys. *Energy*, 112:852–867, 10 2016. doi:10.1016/J.ENERGY.2016.06.054.

[35] C. L. G. Oikonomou, R. P. F. Gomes, and L. M. C. Gato. Unveiling the potential of using a spar-buoy oscillating-water-column wave energy converter for low-power stand-alone applications. *Applied Energy*, 292:116835, 6 2021. doi:10.1016/J.APENERGY.2021.116835.

[36] N. Mathias, R. N. Marini, T. Morais, P. Luís, M. Vaz, and P. Rosa-Santos. Response of a self-powered offshore floating support structure with an OWC for powering a LIDAR device. *Ocean Engineering*, 220:108366, 2021. ISSN 0029-8018. doi:10.1016/j.oceaneng.2020.108366.

[37] A. P. A. Duarte. Modelling and analysis of a backward bent duct buoy WEC for oceanographic applications. Master's thesis, Instituto Superior Técnico, Universidade de Lisboa, 2018. URL `https://fenix.tecnico.ulisboa.pt/cursos/memec/dissertacao/846778572211876`.

[38] T. A. S. Lopes. Construction and experimental testing of an oscillating water column device of the BBDB type. Master's thesis, Instituto Superior Técnico, Universidade de Lisboa, 2018. URL `https://fenix.tecnico.ulisboa.pt/cursos/memec/dissertacao/846778572211879`.

[39] O. R. Chowdhury, H. Kim, D. Park, Y. Cho, C. Shin, and J. Park. Development of a simple and innovative wave energy harvester suitable for ocean sensor network application. *Int. J. Smart Home*, 9(11):197–210, 2015.

[40] M. Boland, T. Kelly, R. Carolan, B. Walsh, and T. Dooley. Scale model testing of the WASP-a novel wave measuring buoy. In *Proceedings of 13th European wave and tidal energy conference, Napoli, Italy*, pages 1531–1, 2019. URL `http://www.bolandengineering.ie/resources/Design&construction%20of%20a%20prototype%20WASP.pdf`.

[41] R. Carolan, B. Walsh, M. Boland, T. Dooley, and T. Kelly. The design and construction of a prototype WASP-a novel wave measuring buoy. In *Proceedings of 13th European wave and tidal energy conference, Napoli, Italy*, pages 1594–1, 2019. URL `http://www.bolandengineering.ie/resources/Design&construction%20of%20a%20prototype%20WASP.pdf`.

[42] A. Hamilton, F. Cazenave, D. Forbush, R. G. Coe, and G. Bacelli. The MBARI-WEC: a power source for ocean sensing. *Journal of Ocean Engineering and Marine Energy*, 7: 189–200, 5 2021. doi:10.1007/s40722-021-00197-9.

[43] RW. Smart Power Buoy by Resen Waves ApS. `https://www.resenwaves.com/wave-energy-data-communications/the-technology/`. Accessed on February, 2024.

[44] OPT. PB3 PowerBuoy by Ocean Power Technologies. `https://oceanpowertechnologies.com/platform/opt-pb3-powerbuoy/`. Accessed on February, 2024.

[45] Y. Masuda. An experience of wave power generator through tests and improvement. In D. V. Evans and A. F. O. de Falcão, editors, *Hydrodynamics of Ocean Wave-Energy Utilization*, pages 445–452, Berlin, Heidelberg, 1986. Springer Berlin Heidelberg. ISBN 978-3-642-82666-5.

[46] B. S. Lopes, L. M. C. Gato, A. F. O. Falcão, and J. C. C. Henriques. Test results of a novel twin-rotor radial inflow self-rectifying air turbine for OWC wave energy converters. *Energy*, 170:869–879, 2019. ISSN 0360-5442. doi:10.1016/j.energy.2018.12.078.

[47] L. Rodríguez, B. Pereiras, M. García-Diaz, J. Fernández-Oro, and F. Castro. Flow pattern analysis of an outflow radial turbine for twin-turbines-OWC wave energy converters. *Energy*, 211:118584, 2020. ISSN 0360-5442. doi:10.1016/j.energy.2020.118584.

[48] A. F. O. Falcão and L. M. C. Gato. *Comprehensive Renewable Energy*, volume 8, chapter Air Turbines, pages 111–149. Elsevier, 2012.

[49] J. S. Alves, L. M. C. Gato, A. F. O. Falcão, and J. C. C. Henriques. Experimental investigation on performance improvement by mid-plane guide-vanes in a biplane-rotor Wells turbine for wave energy conversion. *Renewable and Sustainable Energy Reviews*, 150: 111497, 2021. ISSN 1364-0321. doi:10.1016/j.rser.2021.111497.

[50] R. Starzmann. *Aero-acoustic analysis of Wells turbines for ocean wave energy conversion*. PhD thesis, Universität Siegen, Düsseldorf, Germany, 2012. Fortschr.-Ber. VDI Reihe 7, Nr. 500, VDI Verlag.

[51] A. F. O. Falcão, J. C. C. Henriques, and L. M. C. Gato. Self-rectifying air turbines for wave energy conversion: A comparative analysis. *Renewable and Sustainable Energy Reviews*, 91:1231 – 1241, 2018. ISSN 1364-0321. doi:10.1016/j.rser.2018.04.019.

[52] D. O'Sullivan, J. Griffiths, M. G. Egan, and A. W. Lewis. Development of an electrical power take off system for a sea-test scaled offshore wave energy device. *Renewable Energy*, 36(4):1236–1244, 2011. doi:https://doi.org/10.1016/j.renene.2010.10.007.

[53] S. Raghunathan. The Wells air turbine for wave energy conversion. *Progress in Aerospace Sciences*, 31(4):335–386, 1995. ISSN 0376-0421. doi:https://doi.org/10.1016/0376-0421(95)00001-F.

[54] T. Setoguchi, S. Santhakumar, H. Maeda, M. Takao, and K. Kaneko. A review of impulse turbines for wave energy conversion. *Renewable Energy*, 23:261–292, 6 2001. doi:10.1016/S0960-1481(00)00175-0.

[55] S. L. Dixon and C. Hall. *Fluid Mechanics and Thermodynamics of Turbomachinery*. Butterworth-Heinemann, Oxford, UK, 7th edition, 2014. ISBN 978-0-12-415954-9.

[56] M. Takao, T. Setoguchi, K. Kaneko, S. Raghunathan, and M. Inoue. Noise characteristics of turbines for wave power conversion. *Proceedings of the Institution of Mechanical Engineers, Part A: Journal of Power and Energy*, 216(3):223–228, 2002. doi:10.1243/095765002320183540.

[57] F. Thiebaut, D. O'Sullivan, P. Kracht, S. Ceballos, J. Lopez, C. Boake, J. Bard, N. Brinquete, J. Varandas, L. M. C. Gato, R. Alcorn, and A. W. Lewis. Testing of a floating OWC device with movable guide vane impulse turbine power take-off. In *Proceedings of the 9th European Wave and Tidal Energy Conference*, Southampton, UK, 2011. EWTEC 2011.

[58] L. M. C. Gato, A. A. D. Carrelhas, and A. F. A. Cunha. Performance improvement of the axial self-rectifying impulse air-turbine for wave energy conversion by multi-row guide vanes: Design and experimental results. *Energy Conversion and Management*, 243: 114305, 9 2021. ISSN 0196-8904. doi:10.1016/J.ENCONMAN.2021.114305.

[59] T. Setoguchi, M. Takao, K. Kaneko, S. Nagata, and K. Toyata. Effect of end plates on the performance of an impulse turbine for wave energy conversion. *Journal of Fluid Science and Technology*, 3(3):450–457, 2008. doi:10.1299/jfst.3.450.

[60] Y. Cui, Z. Liu, X. Zhang, C. Xu, H. Shi, and K. Kim. Self-Starting Analysis of an OWC Axial Impulse Turbine in Constant Flows: Experimental and Numerical Studies. *Applied Ocean Research*, 82:458–469, 2019. doi:https://doi.org/10.1016/j.apor.2018.11.014.

[61] A. F. O. Falcão, L. M. C. Gato, and E. P. A. S. Nunes. A novel radial self-rectifying air turbine for use in wave energy converters. *Renewable Energy*, 50:289–298, 2013. ISSN 0960-1481. doi:10.1016/j.renene.2012.06.050.

[62] A. F. O. Falcão, L. M. C. Gato, and E. P. A. S. Nunes. A novel radial self-rectifying air turbine for use in wave energy converters. Part 2. Results from model testing. *Renewable Energy*, 53:159–164, 2013. ISSN 0960-1481. doi:10.1016/j.renene.2012.11.018.

[63] L. M. C. Gato, A. R. Maduro, A. A. D. Carrelhas, J. C. C. Henriques, and D. N. Ferreira. Performance improvement of the biradial self-rectifying impulse air-turbine for wave energy conversion by multi-row guide vanes: Design and experimental results. *Energy*, 216:119110, 2021. ISSN 0360-5442. doi:10.1016/j.energy.2020.119110.

[64] A. A. D. Carrelhas, L. M. C. Gato, J. C. C. Henriques, and A. F. O. Falcão. Experimental study of a self-rectifying biradial air turbine with fixed guide-vanes arranged into two concentric annular rows. *Energy*, 198:117211, 2020. ISSN 0360-5442. doi:10.1016/j.energy.2020.117211.

[65] J. C. C. Henriques, L. M. C. Gato, V. La Sala, and A. A. D. Carrelhas. Acoustic noise emission of air turbines for wave energy conversion: Assessment and analysis. *Renewable Energy*, 212:897–907, 2023. ISSN 0960-1481. doi:10.1016/j.renene.2023.05.078.

[66] A. A. D. Carrelhas, L. M. C. Gato, J. C. C. Henriques, A. F. O. Falcão, and J. Varandas. Test results of a 30 kW self-rectifying biradial air turbine-generator prototype. *Renewable and Sustainable Energy Reviews*, 109:187–198, 7 2019. ISSN 1364-0321. doi:10.1016/J.RSER.2019.04.008.

[67] BiMEP, Biscay Marine Energy Platform. `https://www.bimep.com/en/`. Accessed: August, 2022.

[68] OPERA - Open Sea Operating Experience to Reduce Wave Energy Cost, Contract 654444, European Commission, 2016- 2019. `http://opera-h2020.eu/`. Accessed: August, 2022.

[69] L. M. C. Gato, J. C. C. Henriques, and A. A. D. Carrelhas. Sea trial results of the biradial and Wells turbines at Mutriku wave power plant. *Energy Conversion and Management*, 268:115936, 2022. ISSN 0196-8904. doi:10.1016/j.enconman.2022.115936.

[70] IDOM. MARMOK-A-5 by IDOM. `https://www.idom.com/en/project/wave-energy-converter-prototype-marmok-a-5/`. Accessed on February, 2024.

[71] T. Tanhua, A. McCurdy, A. Fischer, W. Appeltans, N. Bax, K. Currie, B. DeYoung, D. Dunn, E. Heslop, L. K. Glover, J. Gunn, K. Hill, M. Ishii, D. Legler, E. Lindstrom, P. Miloslavich, T. Moltmann, G. Nolan, A. Palacz, S. Simmons, B. Sloyan, L. M. Smith, N. Smith, M. Telszewski, M. Visbeck, and J. Wilkin. What we have learned from the framework for ocean observing: Evolution of the global ocean observing system. *Frontiers in Marine Science*, 6, 2019. doi:10.3389/fmars.2019.00471.

[72] D. M. Legler, H. J. Freeland, R. Lumpkin, G. Ball, M. J. McPhaden, S. North, R. Crowley, G. J. Goni, U. Send, and M. A. Merrifield. The current status of the real-time in situ global ocean observing system for operational oceanography. *Journal of Operational Oceanography*, 8(sup2):s189–s200, 2015. doi:10.1080/1755876X.2015.1049883.

[73] Copernicus Marine Service. What is Operational Oceanography? https://marine.copernicus.eu/explainers/operational-oceanography. Accessed on February, 2024.

[74] M. J. Bell, T. H. Guymer, J. D. Turton, B. A. MacKenzie, R. Rogers, and S. P. Hall. Setting the course for UK operational oceanography. *Journal of Operational Oceanography*, 6 (2):1–15, 2013. doi:10.1080/1755876X.2013.11020146.

[75] N. H. Woolley and A. P. Hatton. Viscous flow in radial turbomachine blade passages. In *Conference on Heat and Fluid Flow in Steam and Gas Turbine Plant*, pages 175–181, Coventry, England, 1973. IMechE.

[76] A. Sugimoto, K. Nakamura, and K. Matsumoto. An experimental investigation of flow in blade passage of radial inflow turbine. *Bulletin of JSME*, 18(126):1432–1439, 1975. doi:10.1299/jsme1958.18.1432.

[77] H. E. Rohlik. Turbine design and application, Chapter 10: Radial-inflow turbines. Technical Report NASA-SP-290-Vol-1-3, NASA Lewis Research Center, Cleveland, OH, United States, 1994.

[78] C. Rodgers and R. Geiser. Performance of a High-Efficiency Radial/Axial Turbine. *Journal of Turbomachinery*, 109(2):151–154, 04 1987. ISSN 0889-504X. doi:10.1115/1.3262077.

[79] A. Stodola. *Steam and gas turbines: with a supplement on the prospects of the thermal prime mover*, volume 2. McGraw-Hill, 1927.

[80] J. D. Stanitz. Some Theoretical Aerodynamic Investigations of Impellers in Radial- and Mixed-Flow Centrifugal Compressors. *Transactions of the American Society of Mechanical Engineers*, 74(4):473–497, 07 2022. ISSN 0097-6822. doi:10.1115/1.4015817.

[81] A. Whitfield and N. C. Baines. *Design of Radial Turbomachines*. Longman Scientific and Technical, Harlow, U.K., 1 edition, 1990. ISBN 0-582-49501-6.

[82] H. Chen and N. C. Baines. The aerodynamic loading of radial and mixed-flow turbines. *International Journal of Mechanical Sciences*, 36(1):63–79, 1994. ISSN 0020-7403. doi:10.1016/0020-7403(94)90007-8.

[83] X. Qiu, D. Japikse, J. Zhao, and M. R. Anderson. Analysis and Validation of a Unified Slip Factor Model for Impellers at Design and Off-Design Conditions. *Journal of Turbomachinery*, 133(4), 04 2011. ISSN 0889-504X. doi:10.1115/1.4003022. 041018.

[84] NUMECA Inc. FINE/Turbo. `https://www.numeca.com/product/fineturbo`, . Accessed on February, 2024.

[85] Y. H. Choi and C. L. Merkle. The application of preconditioning in viscous flows. *Journal of Computational Physics*, 105:207–223, 4 1993. ISSN 0021-9991. doi:10.1006/JCPH.1993.1069.

[86] M. L. Shur, M. K. Strelets, A. K. Travin, and P. R. Spalart. Turbulence modeling in rotating and curved channels: Assessing the Spalart-Shur correction. *AIAA Journal*, 38(5):784 – 792, 2000. doi:10.2514/2.1058.

[87] F. R. Menter. Two-equation eddy-viscosity turbulence models for engineering applications. *AIAA Journal*, 32(8):1598–1605, 1994. doi:10.2514/3.12149.

[88] NUMECA Inc. Automesh. `https://www.numeca.com/product/automesh`, . Accessed on February, 2024.

[89] R. I. Lewis. *Vortex Element Methods for Fluid Dynamic Analysis of Engineering Systems*. Cambridge University Press, Cambridge, UK, 1st edition, 1991. ISBN 0-521-01754-8.

[90] J. D. Denton. The Calculation of Three-Dimensional Viscous Flow Through Multistage Turbomachines. *Journal of Turbomachinery*, 114(1):18–26, 01 1992. ISSN 0889-504X. doi:10.1115/1.2927983.

[91] I. H. Abbott and A. E. Von Doenhoff. *Theory of wing sections: including a summary of airfoil data*. Courier Corporation, 2012.

[92] M. Saad, M. G. Díaz, B. Pereiras, and J. González. Optimized geometry design of a radial impulse turbine for OWC wave energy converters. *Applied Ocean Research*, 111: 102650, 2021. ISSN 0141-1187. doi:10.1016/j.apor.2021.102650.

[93] P. E. Bézier. How Renault uses numerical control for car body design and tooling. In *SAE Technical Paper*. SAE International, 1968. doi:10.4271/680010.

[94] A. R. Forrest. Interactive interpolation and approximation by Bézier polynomials. *Computer-Aided Design*, 22(9):527–537, 1990. ISSN 0010-4485. doi:10.1016/0010-4485(90)90038-E.

[95] J. E. Borges, L. M. C. Gato, and R. M. R. J. Pereira. Iterative use of a time-marching code for designing turbomachine blade rows. *Computers & Fluids*, 25:197–216, 1996. doi:10.1016/0045-7930(95)00038-0.

[96] H. Schlichting. *Boundary-Layer Theory*. McGraw Hill, New York, 7th edition, 1979. ISBN - 0-07-055334-3.

[97] S. Kukkonen and J. Lampinen. GDE3: the third evolution step of generalized differential evolution. In *2005 IEEE Congress on Evolutionary Computation*, volume 1, pages 443–450 Vol.1, 2005. doi:10.1109/CEC.2005.1554717.

[98] J. Blank and K. Deb. Pymoo: Multi-Objective Optimization in Python. *IEEE Access*, 8: 89497–89509, 2020. doi:10.1109/ACCESS.2020.2990567.

[99] R. Storn and K. Price. Differential Evolution - A Simple and Efficient Heuristic for Global Optimization over Continuous Spaces. *Journal of Global Optimization*, 11:341–359, 1997. doi:10.1023/A:1008202821328.

[100] *The Differential Evolution Algorithm*, pages 37–134. Springer Berlin Heidelberg, Berlin, Heidelberg, 2005. doi:10.1007/3-540-31306-0_2.

[101] K. L. Du and M. N. Swamy. *Search and optimization by metaheuristics: Techniques and algorithms inspired by nature*. Springer International Publishing, 7 2016. ISBN 9783319411927. doi:10.1007/978-3-319-41192-7.

[102] C. A. C. Coello, G. B. Lamont, and D. A. V. Veldhuizen. *Evolutionary Algorithms for Solving Multi-Objective Problems*, volume 5. Springer US, 2nd edition, 2007. doi:10.1007/978-0-387-36797-2.

[103] A. Arias-Montano, C. A. C. Coello, and E. Mezura-Montes. Multiobjective evolutionary algorithms in aeronautical and aerospace engineering. *IEEE Transactions on Evolutionary Computation*, 16(5):662–694, 2012. doi:10.1109/TEVC.2011.2169968.

[104] S. Das, S. S. Mullick, and P. N. Suganthan. Recent advances in differential evolution-an updated survey. *Swarm and Evolutionary Computation*, 27:1–30, 4 2016. doi:10.1016/j.swevo.2016.01.004.

[105] T. Tušar and B. Filipič. Differential evolution versus genetic algorithms in multiobjective optimization. In S. Obayash, K. Deb, C. Poloni, T. Hiroyasu, and T. Murata, editors, *Evolutionary Multi-Criterion Optimization. EMO 2007. Lecture Notes in Computer Science*, volume 4403, pages 257–271. Springer, 2007. doi:10.1007/978-3-540-70928-2_22.

[106] L. C. T. Bezerra, M. López-Ibáñez, and T. Stützle. A large-scale experimental evaluation of high-performing multi- and many-objective evolutionary algorithms. *Evolutionary Computation*, 26:621–656, 2018. ISSN 15309304. doi:10.1162/EVCO_A_00217.

[107] NUMECA Inc. FINE/Open with OPENLABS. `https://www.numeca.com/product/fineopen`, . Accessed on February, 2024.

[108] F. R. Menter. Two-equation eddy-viscosity turbulence models for engineering applications. *AIAA Journal*, 32:1598–1605, 1994. doi:10.2514/3.12149.

[109] R. B. Langtry and F. R. Menter. Correlation-based transition modeling for unstructured parallelized computational fluid dynamics codes. *AIAA Journal*, 47:2894–2906, 12 2009. doi:10.2514/1.42362.

[110] K. Zielinski, P. Weitkemper, R. Laur, and K. D. Kammeyer. Parameter study for differential evolution using a power allocation problem including interference cancellation. pages 1857–1864, 2006. doi:10.1109/cec.2006.1688533.

[111] P. J. Roache. *Fundamentals of Verification and Validation*. Hermosa Publishers, Albuquerque, U.S.A., 2009. ISBN 0913478121.

[112] L. Eça and M. Hoekstra. A procedure for the estimation of the numerical uncertainty of CFD calculations based on grid refinement studies. *Journal of Computational Physics*, 262:104–130, 2014. ISSN 0021-9991. doi:10.1016/j.jcp.2014.01.006.

[113] L. Eça, G. Vaz, S. L. Toxopeus, and M. Hoekstra. Numerical Errors in Unsteady Flow

Simulations. *Journal of Verification, Validation and Uncertainty Quantification*, 4(2), 2019. ISSN 2377-2158. doi:10.1115/1.4043975. 021001.

[114] L. Eça and M. Hoekstra. Evaluation of numerical error estimation based on grid refinement studies with the method of the manufactured solutions. *Computers & Fluids*, 38(8): 1580–1591, 2009. ISSN 0045-7930. doi:10.1016/j.compfluid.2009.01.003.

[115] R. Carballo and G. Iglesias. A methodology to determine the power performance of wave energy converters at a particular coastal location. *Energy Conversion and Management*, 61:8–18, 2012. doi:10.1016/j.enconman.2012.03.008.

[116] I. López, R. Carballo, and G. Iglesias. Site-specific wave energy conversion performance of an oscillating water column device. *Energy Conversion and Management*, 195:457–465, 2019. doi:10.1016/j.enconman.2019.05.030.

[117] R. Curran and L. M. C. Gato. The energy conversion performance of several types of wells turbine designs. *Proceedings of the Institution of Mechanical Engineers, Part A: Journal of Power and Energy*, 211(2):133–145, 1997. doi:10.1243/0957650971537051.

[118] J. C. C. Portillo, P. F. Reis, J. C. C. Henriques, L. M. C. Gato, and A. F. O. Falcão. Backward bent-duct buoy or frontward bent-duct buoy? review, assessment and optimisation. *Renewable and Sustainable Energy Reviews*, 112:353–368, 2019. ISSN 1364-0321. doi:10.1016/j.rser.2019.05.026.

[119] J. H. Horlock. *Axial Flow Turbines - Fluid Mechanics and Thermodynamics*. Butterworths, London, UK, 2nd edition, 1966. ISBN 978-1-11-951808-2.

[120] S. A. Korpela. *Principles of Turbomachinery*. Wiley, Honoboken, USA, 2nd edition, 2020. ISBN 978-1-11-951808-2.

[121] R. H. Aungier. *Turbine Aerodynamics: Axial-Flow and Radial-Flow Turbine Design and Analysis*. ASME Press, 01 2006. ISBN 0791802418. doi:10.1115/1.802418.

[122] R. H. Aungier. *Centrifugal Compressors: A Strategy for Aerodynamic Design and Analysis*. ASME Press, 01 2000. ISBN 9780791800935. doi:10.1115/1.800938.

[123] *Performance Improvement of a Centrifugal Compressor Stage by Increasing Degree of Reaction and Optimizing Blade Loading of a 3D-Impeller*, volume Volume 7: Turbomachinery, Parts A and B of *Turbo Expo: Power for Land, Sea, and Air*, 06 2009. doi:10.1115/GT2009-59588.

[124] S. Pakle and K. Jiang. Design of double curvature radial turbine blades for a micro gas turbine. *Applied Mathematical Modelling*, 67:529–548, 2019. ISSN 0307-904X. doi:10.1016/j.apm.2018.10.020.

[125] R. A. Van den Braembussche. *AVT-143 RTO, AVT/VKI lecture series - Optimization of Radial Impeller Geometry*. 2006. URL `http://https://www.sto.nato.int/publications/STOEducationalNotes/RTO-EN-AVT-143/EN-AVT-143-13.pdf`.

[126] M. Schobeiri. *Turbomachinery flow physics and dynamic performance*. 2nd edition, 2012. doi:10.1007/978-3-642-24675-3.

[127] Z. Alnasir and M. Kazerani. An analytical literature review of stand-alone wind energy conversion systems from generator viewpoint. *Renewable and Sustainable Energy Reviews*, 28:597–615, 2013. doi:https://doi.org/10.1016/j.rser.2013.08.027.

[128] I. López, J. Andreu, S. Ceballos, I. Martínez de Alegría, and I. Kortabarria. Review of wave energy technologies and the necessary power-equipment. *Renewable and Sustainable Energy Reviews*, 27:413–434, 2013. doi:https://doi.org/10.1016/j.rser.2013.07.009.

[129] R. Bansal. Three-phase self-excited induction generators: an overview. *IEEE Transactions on Energy Conversion*, 20(2):292–299, 2005. doi:10.1109/TEC.2004.842395.

[130] A. S. Satpathy, N. K. Kishore, D. Kastha, and N. C. Sahoo. Control scheme for a stand-alone wind energy conversion system. *IEEE Transactions on Energy Conversion*, 29(2): 418–425, 2014. doi:10.1109/TEC.2014.2303203.

[131] D. G. Dorrell, M.-F. Hsieh, M. Popescu, L. Evans, D. A. Staton, and V. Grout. A review of the design issues and techniques for radial-flux brushless surface and internal rare-earth permanent-magnet motors. *IEEE Transactions on Industrial Electronics*, 58(9): 3741–3757, 2011. doi:10.1109/TIE.2010.2089940.

[132] D. L. O'Sullivan and A. W. Lewis. Generator selection and comparative performance in offshore oscillating water column ocean wave energy converters. *IEEE Transactions on Energy Conversion*, 26(2):603–614, 2011. doi:10.1109/TEC.2010.2093527.

[133] A. Kalair, N. Abas, A. R. Kalair, Z. Saleem, and N. Khan. Review of harmonic analysis, modeling and mitigation techniques. *Renewable and Sustainable Energy Reviews*, 78: 1152–1187, 2017. ISSN 1364-0321. doi:10.1016/j.rser.2017.04.121.

[134] K.-Y. Lo, Y.-M. Chen, and Y.-R. Chang. MPPT battery charger for stand-alone wind power system. *IEEE Transactions on Power Electronics*, 26(6):1631–1638, 2011. doi:10.1109/TPEL.2010.2088405.

[135] C. N. Bhende, S. Mishra, and S. G. Malla. Permanent magnet synchronous generator-based standalone wind energy supply system. *IEEE Transactions on Sustainable Energy*, 2(4):361–373, 2011. doi:10.1109/TSTE.2011.2159253.

[136] J. C. Y. Hui, A. Bakhshai, and P. K. Jain. An energy management scheme with power limit capability and an adaptive maximum power point tracking for small standalone pmsg wind energy systems. *IEEE Transactions on Power Electronics*, 31(7):4861–4875, 2016. doi:10.1109/TPEL.2015.2478402.

[137] E. Ozkop and I. H. Altas. Control, power and electrical components in wave energy conversion systems: A review of the technologies. *Renewable and Sustainable Energy Reviews*, 67:106–115, 2017. doi:https://doi.org/10.1016/j.rser.2016.09.012.

[138] N. Sharmila, P. Jalihal, A. Swamy, and M. Ravindran. Wave powered desalination system. *Energy*, 29(11):1659–1672, 2004. doi:10.1016/j.energy.2004.03.099.

[139] S. Seo, J. Kim, E. Muljadi, R. M. Nelms, and H. Moeljanto. Holistic design of small-scale oscillating water column in stand-alone dc microgrid. In *2022 IEEE Energy Conversion Congress and Exposition (ECCE)*, pages 1–8, 2022. doi:10.1109/ECCE50734.2022.9947376.

[140] J. C. C. Portillo, K. M. Collins, R. P. F. Gomes, J. C. C. Henriques, L. M. C. Gato, B. D. Howey, M. R. Hann, D. M. Greaves, and A. F. O. Falcão. Wave energy converter phys-

ical model design and testing: The case of floating oscillating-water-columns. *Applied Energy*, 278:115638, 2020. ISSN 0306-2619. doi:10.1016/j.apenergy.2020.115638.

[141] L. Ciappi, I. Simonetti, A. Bianchini, L. Cappietti, and G. Manfrida. Application of integrated wave-to-wire modelling for the preliminary design of oscillating water column systems for installations in moderate wave climates. *Renewable Energy*, 194:232–248, 2022. ISSN 0960-1481. doi:10.1016/j.renene.2022.05.015.

[142] A. A. D. Carrelhas, L. M. C. Gato, J. C. C. Henriques, and G. D. Marques. Estimation of generator electrical power output and turbine torque in modelling and field testing of owc wave energy converters. *Energy Conversion and Management: X*, 19:100384, 2023. ISSN 2590-1745. doi:10.1016/j.ecmx.2023.100384.

[143] M. Rosati, J. C. C. Henriques, and J. V. Ringwood. Oscillating-water-column wave energy converters: A critical review of numerical modelling and control. *Energy Conversion and Management: X*, 16:100322, 2022. doi:10.1016/j.ecmx.2022.100322.

[144] *CM3C63 - CM3C100 Synchronous Servomotors*. SEW Eurodrive, 2020. `https://download.sew-eurodrive.com/download/pdf/29194652.pdf`.

[145] H. Späth. A general purpose definition of active current and non-active power based on German standard DIN 40110. *Electrical Engineering*, 89:167–175, 2007. doi:10.1007/s00202-005-0333-z.

[146] C. J. O'Rourke, M. M. Qasim, M. R. Overlin, and J. L. Kirtley. A geometric interpretation of reference frames and transformations: dq0, Clarke, and Park. *IEEE Transactions on Energy Conversion*, 34(4):2070–2083, 2019. doi:10.1109/TEC.2019.2941175.

[147] *CM3C63 - CM3C100 Synchronous Servomotors*. SEW Eurodrive, 2022. Private communication on installation and operation.

[148] S. Umans, A. Fitzgerald, and C. Kingsley. *Electric Machinery: Seventh Edition*. McGraw-Hill Higher Education, 2013. ISBN 9780077428501.

[149] N. Mohan, T. M. Undeland, and W. P. Robbins. *Power Electronics. Converters, Applications and Design*. John Wiley and Sons, Inc, third edition, 2003.

[150] J. C. C. Henriques, J. C. C. Portillo, W. Sheng, L. M. C. Gato, and A. F. O. Falcão. Dynamics and control of air turbines in oscillating-water-column wave energy converters: Analyses and case study. *Renewable and Sustainable Energy Reviews*, 112:571–589, 2019. ISSN 1364-0321. doi:10.1016/j.rser.2019.05.010.

[151] Iver3 Standard System AUV. `https://www.l3harris.com/all-capabilities/iver3-standard-system-auv`. Accessed on May 2023.

[152] H. C. Brown, M. S. Lawrence, J. V. Sloat, and J. S. Fajans. Toward Longitudinal Reef Health Monitoring in the Florida Keys National Marine Sanctuary using Iver AUVs. In *OCEANS 2019 MTS/IEEE SEATTLE*, pages 1–7, 2019. doi:10.23919/OCEANS40490.2019.8962630.

[153] M. L. Incze. Lightweight Autonomous Underwater Vehicles (AUVs) performing coastal survey operations in REP 10A. *Ocean Dynamics*, 61(11):1955–1965, 2011. doi:10.1007/s10236-011-0446-z.

[154] C. R. Teeneti, T. T. Truscott, D. N. Beal, and Z. Pantic. Review of wireless charging systems for autonomous underwater vehicles. *IEEE Journal of Oceanic Engineering*, 46 (1):68–87, 2021. doi:10.1109/JOE.2019.2953015.

[155] Mastervolt MVG 12/85. `https://www.mastervolt.com/products/mvg-12v-gel/mvg-12-85-gel/`. Accessed on May 2023.

[156] ASME V&V 20–2009. *Standard for Verification and Validation in Computational Modeling of Fluid Dynamics and Heat Transfer*. American Society of Mechanical Engineers, New York, USA, 2009. ISBN 9780791832097.